IMPERIAL

Nonlinear Dynamics of Geometrically Exact Beams Modelled under the Special Euclidean Lie Group Formulation

Amir Kamyar Bagheri

Department of Mechanical Engineering
Imperial College London

Submitted in part fulfilment of the requirements for the degree of
Doctor of Philosophy of Imperial College London
and the Diploma of Imperial College London

August 2024

Statement of Originality

I hereby confirm that the work presented in this thesis is my own. All else is appropriately referenced.

Copyright Declaration

The copyright of this thesis rests with the author. Unless otherwise indicated, its contents are licensed under a Creative Commons Attribution-Non Commercial 4.0 International Licence (CC BY-NC).
Under this licence, you may copy and redistribute the material in any medium or format. You may also create and distribute modified versions of the work. This is on the condition that: you credit the author and do not use it, or any derivative works, for a commercial purpose.
When reusing or sharing this work, ensure you make the licence terms clear to others by naming the licence and linking to the licence text. Where a work has been adapted, you should indicate that the work has been changed and describe those changes.
Please seek permission from the copyright holder for uses of this work that are not included in this licence or permitted under UK Copyright Law.

"That whose existence is necessary must necessarily be one essence."
Avicenna

Acknowledgements

Firstly, I would like to express my deepest gratitude to my supervisor, Dr. Ludovic Renson, for his unwavering support and invaluable guidance and mentorship throughout my research journey. Ludovic always found time to meet and discuss this work and I would leave every meeting with more inspiration and motivation, and for that I am truly grateful. I particularly acknowledge his support in the final months leading up to the submission of this thesis.

I am also profoundly grateful to Dr. Valentin Sonneville, whose expertise and patient guidance have been critical to the completion of this thesis. His extensive knowledge of Lie groups and his ability to explain complex concepts with infectious enthusiasm have been instrumental in shaping my understanding of the field. I fondly reflect on the memories of visiting him at the Technical University of Munich and for the countless discussions we had over coffee and Spezi.

My sincere thanks also go to my colleagues and friends at Imperial College and the staff who work tirelessly behind the scenes to ensure everything runs smoothly. I am particularly grateful to Mr. Peter Higgs, whose support for my research and seamless handling of administrative tasks allowed me to focus fully on my work.

To the love of my life, my wife Sara, words cannot express my gratitude for your constant support, love, and encouragement. Your unwavering belief in me, even when I doubt myself, continues to motivate me and drive me. The sacrifices you have made for me are beyond measure, and for that I am forever grateful.

Finally, I wish to thank my sister and brother, Kimiya and Kiyarash, and especially my parents, Abbas and Roshanak, for always being there for me. As I write this acknowledgement I warmly recall my childhood memories of going to my dad's PhD graduation ceremony, and my mum's PhD viva, being inspired to one day achieve the same as they have. My father in particular has always been my role model, and I can only hope that this achievement has made them proud. This thesis is dedicated to them.

Abstract

The dynamic analysis of flexible slender beams, which exhibit significant geometric nonlinearities due to large displacements and rotations, is critical for various industrial applications, including the aerospace, automotive, and renewable energy sectors. The use of mathematically rigorous and geometrically exact formulations, such as those based on Lie groups, is essential in modelling geometric nonlinearities accurately. However, current state-of-the-art dynamic analysis tools cannot be used on the nonlinear configuration space of Lie groups and require adaptation. This thesis addresses this challenge by developing both a single shooting and a multiple shooting method, together with a pseudo-arclength continuation method, which is compatible with geometrically exact beam formulations based on the Special Euclidean Lie group $SE(3)$. Due to the correct kinematic representation of displacements and rotations in the Lie group framework of rigid body motion, and the local frame representation of the beam equations, the $SE(3)$ model is geometrically exact and inherently shear locking free. The adapted shooting and continuation methods developed in this thesis enable the $SE(3)$ model to be used in industrial applications. These methods are used herein to compute nonlinear normal modes and forced responses of geometrically nonlinear structures, in addition to performing stability analysis and bifurcation detection. The results affirm the suitability of the $SE(3)$ formulation in modelling large amplitude motions, and confirm the effectiveness of the shooting and continuation methods in capturing nonlinear dynamic phenomena such as bifurcations and mode interactions with high accuracy, paving the way for its application in industrial design and analysis. This thesis therefore contributes to filling a critical gap in current industrial modelling capabilities, providing a rigorous and efficient approach for analysing nonlinear dynamics of flexible structures.

Keywords: Geometric nonlinearity, nonlinear dynamics, $SE(3)$ Lie group, shooting, pseudo-arclength continuation.

Contents

Acknowledgements **7**

Abstract **9**

Nomenclature **19**

1 Introduction **29**

2 Fundamentals and Literature Review **35**

2.1 Introduction . . . 36
2.2 Nonlinear Normal Modes . . . 36
2.2.1 Properties of NNMs . . . 37
2.2.2 Computation of NNMs . . . 37
2.2.3 Recent works on NNMs . . . 39
2.2.4 Computation of NNMs with Shooting and Pseudo-arclength Continuation 39
2.3 Geometrically Exact Beam Formulations . . . 42
2.4 3D Finite Element Beam Model with von Kármán Strains . . . 46
2.4.1 von Kármán Strains . . . 47
2.4.2 Finite Element Discretisation . . . 48
2.4.3 Numerical Time Integration: Newmark Method . . . 54
2.5 Conclusion . . . 57

3 Lie Groups **59**

3.1 Introduction to Lie Groups . . . 60
3.1.1 Definition . . . 60
3.1.2 Group Action . . . 60
3.1.3 Lie Algebra . . . 61
3.1.4 Left and Right Invariant Vector Fields . . . 63
3.1.5 Exponential and Logarithm Maps . . . 64
3.1.6 Adjoint Representation . . . 65
3.1.7 Commutativity of Cross Derivatives . . . 68
3.1.8 Derivative of the Exponential and Tangent Operator . . . 69
3.2 Rotation Group $SO(3)$ . . . 70

3.2.1 Rigid Body Velocities on $SO(3)$ . . . 71
3.3 Rigid Body Motion Group $SE(3)$ . . . 73
3.3.1 Rigid Body Velocities on $SE(3)$ . . . 76
3.4 Equation of Motion of a Free Rigid Body . . . 78
3.4.1 Problem Definition . . . 78
3.4.2 $SE(2)$ Lie group framework . . . 79
3.4.3 Kinetic Energy . . . 80
3.4.4 Kinematic Joints . . . 82
3.4.5 Constraint Equation . . . 85
3.4.6 Constraint Gradient . . . 86
3.4.7 Elastic Potential Energy . . . 88
3.4.8 Full Equation of Motion . . . 88
3.5 Beam Equations Formulated on the $SE(3)$ Group . . . 89
3.5.1 Derivatives . . . 91
3.5.2 Equations of Motion . . . 96
3.5.3 Finite Element Discretisation . . . 98
3.5.4 Derivatives . . . 99
3.5.5 Discretised Equations of Motion . . . 101
3.6 Time Integration . . . 105
3.7 Advantages of the $SE(3)$ Beam Model . . . 108
3.8 Conclusion . . . 109

4 Nonlinear Dynamics of 2D Beams Formulated on the $SE(2)$ Group 111
4.1 Introduction . . . 112
4.2 Shooting Adaptation to Lie Group Formulation . . . 112
4.3 Continuation Adaptation to Lie Group Formulation . . . 115
4.3.1 Prediction Step and Relative Increments . . . 115
4.3.2 Correction Step and Orthogonality Condition . . . 116
4.4 Sensitivities . . . 118
4.4.1 Computation of the Monodromy . . . 120
4.5 Phase Condition . . . 121
4.6 Comparison of SE & von Kármán Beams on 2D Cases . . . 122
4.6.1 Straight Clamped-Clamped Beam: NNM1 . . . 122
4.6.2 Straight Clamped-Clamped Beam: NNM2 . . . 123
4.6.3 Shallow Arch: NNM1 . . . 125
4.6.4 Shallow Arch: NNM2 . . . 125
4.6.5 Straight Cantilever Beam: NNM1 . . . 127
4.6.6 Straight Cantilever Beam: NNM2 . . . 129
4.7 Convergence Analysis . . . 130
4.8 Conclusion . . . 133

5 Multiple Shooting on the $SE(3)$ Group with Application to 3D Beams 135
5.1 Introduction . . . 136
5.2 Multiple Shooting Formulation . . . 137
5.2.1 Alternative Multiple Shooting Equations . . . 139
5.2.2 Initial Periodic Orbit . . . 140
5.3 Application to a Two Degree of Freedom Oscillator . . . 141
5.4 Adaptation of the Multiple Shooting Method to Lie Group Formulations . . . 143
5.4.1 Periodicity Equation . . . 143
5.4.2 Sensitivities . . . 144
5.5 Right-Angled Beam: NNM1 . . . 146
5.5.1 Single shooting . . . 146
5.5.2 Multiple shooting . . . 150
5.6 Challenges and Suggestions . . . 150
5.6.1 Large Dimensionality . . . 150
5.6.2 Continuation Step Size . . . 151
5.6.3 Continuation Orthogonality Condition . . . 151
5.6.4 Relative Increments . . . 152
5.6.5 Initial Accelerations . . . 152
5.7 A Global Periodicity Condition . . . 152
5.7.1 Sensitivities of the Global Periodicity Condition . . . 154
5.7.2 Advantages of the Global Periodicity Condition . . . 155
5.8 Computational Savings and Parallel Implementation . . . 156
5.9 Conclusion . . . 156

6 Forced Continuation of Periodic Solutions of Beams on $SE(2)$ and $SE(3)$ 159
6.1 Introduction . . . 160
6.2 Continuation Procedure . . . 160
6.2.1 Sensitivity to Period . . . 161
6.3 Geometrically Exact Damping . . . 162
6.3.1 Damping Based on Strain Rate . . . 162
6.3.2 Kelvin-Voigt Damping . . . 163
6.4 Bifurcations and Stability of Periodic Orbits . . . 166
6.4.1 Branch Switching and Symmetry Breaking Bifurcation . . . 168
6.5 2D Cantilever Beam . . . 169
6.5.1 Primary Resonance Frequency Response . . . 170
6.5.2 Secondary Resonance Frequency Response . . . 174
6.6 3D Cantilever Beam . . . 179
6.7 2D Vertical Cantilever Beam . . . 184
6.7.1 Continuation Challenges . . . 185
6.7.2 Sine Sweep Results . . . 186
6.8 Conclusion . . . 191

7 Nonlinear Dynamics of Flexible Aircraft Structures **193**
7.1 Introduction . . . 194
7.2 High-Aspect-Ratio Wing . . . 195
7.3 Box Wing Aircraft Structure . . . 199
7.3.1 Clamped Configuration . . . 200
7.3.2 Free Configuration . . . 205
7.4 Conclusion . . . 211

8 Conclusion **213**

A Euler-Rodrigues Motion Parametrisation **219**

B Derivative of Joint Motion Frames **223**

C Some Lie Group Identities and Relationships **225**
C.1 Identity . . . 225
C.2 Identity . . . 225
C.3 Identity . . . 225
C.4 Derivative of the Adjoint . . . 225

D Box Wing Aircraft Geometry Data **227**

References **229**

List of Tables

7.1 Natural frequencies of box wing aircraft in clamped configuration 200
7.2 Natural frequencies of box wing aircraft in free configuration with XY supports . 206
7.3 Natural frequencies of box wing aircraft in free configuration with XZ supports . 209

D.1 Nodal coordinates of box wing aircraft 227

List of Figures

2.1 3D von Kármán beam element . . . 49

3.1 Illustration of a Lie group and its Lie algebra . . . 62
3.2 Composition with the exponential map on a Lie group . . . 66
3.3 Rigid body motion frame . . . 73
3.4 Unforced undamped elastic pendulum . . . 79
3.5 Kinematic joint . . . 83
3.6 Description of beam kinematics . . . 90
3.7 Lie groups of rigid body motion . . . 91

4.1 Constant body velocity in circular motion . . . 114
4.2 Geometry of 2D test cases . . . 122
4.3 First NNM of clamped-clamped beam . . . 123
4.4 Second NNM of clamped-clamped beam . . . 124
4.5 First NNM of shallow arch . . . 126
4.6 Second NNM of shallow arch . . . 127
4.7 First NNM of cantilever beam . . . 129
4.8 Deformed beam shape of first NNM of cantilever beam . . . 129
4.9 Second NNM of cantilever beam . . . 130
4.10 Time history of second NNM of cantilever beam . . . 131
4.11 Convergence of clamped-clamped and cantilever beam . . . 132
4.12 Displacement convergence of clamped-clamped beam . . . 133

5.1 Schematic illustration of the multiple shooting method . . . 138
5.2 Schematic illustration of the 2 DoF system . . . 141
5.3 First NNM of cubic spring: single vs multiple shooting . . . 142
5.4 Multiple shooting time series of cubic spring . . . 142
5.5 Multiple shooting orbit corrections for cubic spring . . . 143
5.6 First NNM of right-angled beam . . . 147
5.7 Deformed beam shape of first NNM of right-angled beam . . . 147
5.8 Deformed beam shape of first NNM of right-angled beam - planar views . . . 148
5.9 First NNM of right-angled beam - velocities . . . 148
5.10 Modal analysis of first NNM of right-angled beam . . . 149
5.11 Frequency spectrum of first NNM of right-angled beam . . . 149
5.12 FEP of first NNM of right-angled beam, single vs multiple shooting . . . 150

6.1 Beam differential element . . . 166
6.2 Configuration diagram of undeformed 2D cantilever beam . . . 170
6.3 FRC of 2D cantilever beam - mode 1 . . . 171
6.4 FRC bifurcations of 2D cantilever beam - mode 1 . . . 172
6.5 Time simulations of 2D cantilever beam - mode 1 . . . 172

6.6 Deformed shape of 2D cantilever beam - mode 1 . . . 173
6.7 FRC of 2D cantilever beam - mode 1 cascade . . . 174
6.8 FRC of 2D cantilever beam - mode 2 . . . 175
6.9 FRC bifurcations of 2D cantilever beam - mode 2 . . . 176
6.10 Locus of Floquet multipliers of 2D cantilever beam - mode 2 . . . 177
6.11 Deformed shape of 2D cantilever beam - mode 2 . . . 178
6.12 Time simulations of 2D cantilever beam - mode 2 . . . 179
6.13 Configuration diagram of undeformed 3D cantilever beam . . . 180
6.14 FRC of 3D cantilever beam . . . 181
6.15 Deformed shape of 3D cantilever beam - mode 1 . . . 181
6.16 FRC bifurcations of 3D cantilever beam . . . 182
6.17 FRC of 3D cantilever beam with 1:1 internal resonance . . . 183
6.18 FRC of 3D cantilever beam with 1:1 internal resonance - 2D projections . . . 183
6.19 Deformed shapes of 3D cantilever beam . . . 184
6.20 Configuration diagram of undeformed vertical cantilever beam . . . 185
6.21 Vertical cantilever sine sweep . . . 187
6.22 Vertical cantilever projection onto linear modes . . . 188
6.23 Vertical cantilever sine sweep up and down . . . 189
6.24 Vertical cantilever accelerations wavelet transform . . . 189
6.25 Vertical cantilever position wavelet transform . . . 190
6.26 Deformed shape of vertical cantilever beam . . . 191

7.1 Schematic of high-aspect-ratio wing . . . 196
7.2 Static solution of beam under various tip masses . . . 196
7.3 FRC of HARW - mode 1 . . . 197
7.4 FRC of HARW - mode 2 . . . 198
7.5 Time simulation of HARW - mode 2 . . . 198
7.6 Box wing aircraft geometry . . . 200
7.7 Box wing aircraft static response . . . 200
7.8 FRC of box wing aircraft, fuselage response - mode 4 . . . 201
7.9 FRC of box wing aircraft, wing response - mode 4 . . . 202
7.10 FRC of box wing aircraft, MAC - mode 4 . . . 203
7.11 FRC bifurcations of box wing aircraft - mode 4 . . . 203
7.12 Deformed shape of box wing aircraft - mode 4 . . . 204
7.13 Time simulation of box wing aircraft - mode 4, period-doubling . . . 204
7.14 Time simulation of box wing aircraft - mode 4, Neimark-Sacker . . . 205
7.15 FRC of box wing aircraft in free configuration - Z force . . . 207
7.16 FRC of box wing aircraft in free configuration - X force . . . 207
7.17 FRC of box wing aircraft in free configuration - MAC plot . . . 208
7.18 Deformed box wing aircraft shape at resonance peaks - Z force . . . 208
7.19 Deformed box wing aircraft shape at resonance peaks - X force . . . 208
7.20 FRC of box wing aircraft in free configuration - Y force . . . 210
7.21 Deformed box wing aircraft shape at resonance peaks - Y force . . . 211

Nomenclature

$(\bullet)^\vee$ Inverse map from the Lie algebra $\mathfrak{g}$ to $\mathbb{R}^m$.

$[\boldsymbol{\omega}]_\times$ Skew-symmetric matrix constructed from $\boldsymbol{\omega} \in \mathbb{R}^3$.

$[X, Y]$ Lie bracket of elements X and Y in the Lie algebra, defined as $XY - YX$.

$\alpha_m, \alpha_f, \gamma, \beta$ Numerical parameters of the generalised-α time integration scheme.

$\bar{\mathbf{h}}_j(0)$ Relative twist increments with reference to the previous converged continuation step.

$\bar{q}_A$ Homogeneous coordinates in $\mathbb{R}^4$ of a point on a rigid body relative to frame A.

$\bar{q}_B$ Homogeneous coordinates in $\mathbb{R}^4$ of a point on a rigid body relative to frame B.

$\boldsymbol{\Phi}_e$ Shape functions for an element.

$\boldsymbol{\sigma}$ Second Piola-Kirchhoff stress tensor.

$\boldsymbol{B}_i$ Matrix of shape function derivatives.

$\boldsymbol{C}^e$ Von Kármán beam element damping matrix.

$\boldsymbol{K}^e$ Von Kármán beam element stiffness matrix.

$\boldsymbol{M}^e$ Von Kármán beam element mass matrix.

$\boldsymbol{P}^e$ Vector of applied external forces on the von Kármán beam element.

$\boldsymbol{q}^e$ Vector of nodal displacements and rotations for a von Kármán beam element.

$\boldsymbol{R}^e$ Von Kármán beam element rotation matrix.

$\boldsymbol{U}^e$ Vector of displacement fields for a von Kármán beam element.

$\boldsymbol{\chi}$ Twist vector in $\mathbb{R}^3$, representing elements of $\mathfrak{se}(2)$ in vector form.

$\boldsymbol{\epsilon}$ Deformation gradient in the current configuration along the beam's neutral axis.

$\boldsymbol{\gamma}$ Axial and shear strains along the beam's neutral axis.

$\boldsymbol{\kappa}$ Torsion and bending curvatures along the beam's neutral axis.

$\boldsymbol{\lambda}$ Lagrange multiplier vector for enforcing constraints.

$\boldsymbol{\omega}^b$ Angular velocity of the body as viewed in the body frame.

$\boldsymbol{\omega}^s$ Angular velocity of the body as viewed in the spatial frame.

$\boldsymbol{\omega}_L$ Left-invariant angular velocity, equal to $\boldsymbol{\omega}^b$.

$\boldsymbol{\xi}$ Twist vector in $\mathbb{R}^6$, representing elements of $\mathfrak{se}(3)$ in vector form.

$\mathbf{A}$ Full-rank linear mapping from $\mathfrak{h}$ to $\mathfrak{g}$, relating Lie subgroup and Lie group algebras.

$\mathbf{a}_L$ Left-invariant vector field associated with the derivative of $\mathcal{X}$, as given by $d_a(\mathcal{X}) = \mathcal{X}\tilde{\mathbf{a}}_L$.

$\mathbf{A}_P$ Matrix mapping the prismatic joint parameter to the Lie algebra $\mathfrak{se}(2)$.

$\mathbf{A}_R$ Matrix mapping the revolute joint parameter to the Lie algebra $\mathfrak{se}(2)$.

$\mathbf{B}$ Boolean matrix identifying velocity degrees of freedom in continuation phase condition.

$\mathbf{B}_i$ Boolean matrix for the phase condition on the i-th partition.

$\mathbf{b}_i$ Derivative of the state transition map with respect to the period for the i-th partition.

$\mathbf{C}^L$ Element damping matrix.

$\mathbf{C}_T$ Tangent damping matrix.

$\mathbf{d}$ Relative configuration vector representing the twist between nodes A and B.

$\mathbf{D}(q)$ Matrix satisfying $\widetilde{\mathbf{D}(q)\mathbf{w}} = q^{-1}\tilde{\mathbf{w}}q$.

$\mathbf{D}(s,u,v)$ Matrix relating deformation gradients to the Green-Lagrange strain tensor.

$\mathbf{d}_\Omega$ Rotational component of the relative configuration vector $\mathbf{d}$.

$\mathbf{d}_U$ Translational component of the relative configuration vector $\mathbf{d}$.

$\mathbf{F}$ Vector of the applied forcing amplitude.

$\mathbf{f}_\Omega$ Rotational component of the deformation gradient.

$\mathbf{f}_U$ Translational component of the deformation gradient.

$\mathbf{GL}(s,u,v)$ Green-Lagrange strain tensor at a point (s,u,v) on the beam.

$\mathbf{gl}(s,u,v)$ Vector form of the Green-Lagrange strain components.

$\mathbf{g}_{ext}$ External forces and moments.

$\mathbf{g}_{ine}$ Inertial forces.

$\mathbf{g}_{int}$ Internal forces.

$\mathbf{H}$ Homogeneous transformation matrix in $SE(3)$ and $SE(2)$.

$\mathbf{h}$ Twist increments in $\mathfrak{se}(3)$ mapping the reference beam to the deformed configuration.

$\mathbf{H}_j^\star(0)$ Converged solution of deformed initial configuration for continuation step j.

$\mathbf{H}_A$ Material frame at node A of a finite element.

$\mathbf{H}_B$ Material frame at node B of a finite element.

$\mathbf{H}_G$ Ground frame transformation matrix in $SE(2)$.

$\mathbf{H}_J$ Frame of relative motion of a kinematic joint J connecting frames A and B.

$\mathbf{H}_M$ Pendulum tip mass frame in $SE(2)$.

$\mathbf{H}_\Phi$ Constraint matrix ensuring consistency between the frames of the tip mass and the joints.

$\mathbf{H}_{AB}$ Homogeneous transformation matrix in $SE(3)$ from frame B to frame A.

$\mathbf{H}_{JP}$ Transformation frame of the prismatic joint.

$\mathbf{h}_{JP}$ Lie algebra element representing the motion of the prismatic joint in $\mathfrak{se}(2)$.

$\mathbf{h}_{jP}$ Relative extension of the prismatic joint.

$\mathbf{H}_{JR}$ Transformation frame of the revolute joint.

$\mathbf{h}_{JR}$ Lie algebra element representing the motion of the revolute joint in $\mathfrak{se}(2)$.

$\mathbf{h}_{jR}$ Relative angle of the revolute joint.

$\mathbf{I}$ Identity matrix.

$\mathbf{i}_s, \mathbf{i}_u, \mathbf{i}_v$ Unit vectors defining the beam's local reference frame.

$\mathbf{J}_j$ Jacobian matrix at continuation step j.

$\mathbf{K}$ Stiffness matrix.

$\mathbf{K}^L$ Element stiffness matrix.

$\mathbf{K}_\Omega$ Torsional and bending stiffness terms, diagonal components of the stiffness matrix $\mathbf{K}$.

$\mathbf{K}_T$ Tangent stiffness matrix

$\mathbf{K}_U$ Axial and shear stiffness terms, diagonal components of the stiffness matrix $\mathbf{K}$.

$\mathbf{M}$ Mass matrix.

$\mathbf{m}(s)$ Resultant moment vector, integrated over the cross section.

$\mathbf{M}^L$ Element mass matrix.

$\mathbf{M}_T$ Tangent mass matrix.

$\mathbf{N}$ Contribution of translational and rotational deformations to the position field derivative.

$\mathbf{n}(s)$ Resultant force vector, integrated over the cross section.

$\mathbf{O}_0(s)$ Rotation matrix defining the beam's reference orientation.

$\mathbf{P}(\mathbf{d})$ Matrix relating the variation of the relative configuration vector $\mathbf{d}$ to the combined infinitesimal motion vector $\delta\mathbf{h}_{AB}$.

$\mathbf{Q}(x, \mathbf{d})$ Matrix relating the infinitesimal motion field $\delta\mathbf{h}(x)$ to the nodal motion vector $\delta\mathbf{h}_{AB}$.

$\mathbf{R}$ Rotation matrix in the $SO(3)$ group.

$\mathbf{r}(s)$ Resultant vector of internal forces and moments, integrating stress over the cross section.

$\mathbf{R}_{2\times2}$ Rotation matrix in $SE(2)$, representing planar orientation.

$\mathbf{R}_{AB}$ Rotation matrix describing the orientation of frame B relative to frame A.

$\mathbf{s}$ Vector form of the second Piola-Kirchhoff stress tensor.

$\mathbf{S}(s, u, v)$ Second Piola-Kirchhoff stress tensor at a point on the beam.

$\mathbf{S}_T$ Time integration iteration matrix.

$\mathbf{T}(\boldsymbol{\tau})$ Tangent operator, mapping $\mathfrak{g} \mapsto \mathfrak{g}$.

$\mathbf{T}^\star(x, \mathbf{d})$ Scaled tangent operator.

$\mathbf{T}_{SE(3)}$ Tangent operator on the $SE(3)$ group.

$\mathbf{T}_{SO(3)}$ Tangent operator on the $SO(3)$ group.

$\mathbf{u}$ Translation vector in $\mathbb{R}^3$, part of the Lie algebra $\mathfrak{se}(3)$.

$\mathbf{u}^b$ Body translational velocity as viewed in the body frame, relative to the spatial frame.

$\mathbf{u}^s$ Body translational velocity as viewed in the spatial frame, relative to the spatial frame.

$\mathbf{u}_L$ Left-invariant translational velocity, equal to $\mathbf{u}^b$.

$\mathbf{V}$ Viscosity tensor representing viscoelastic effects.

$\mathbf{v}$ Velocity in $\mathfrak{se}(3)$.

$\mathbf{v}^*$ Velocities for the full joint configuration.

$\mathbf{V}^\star$ Application of the Adjoint map to the difference of local velocities.

$\mathbf{v}_j^\star(0)$ Converged solution of initial velocity for continuation step j.

$\mathbf{v}_\Omega$ Rotational velocity vector of the beam's cross section in the local frame.

$\mathbf{v}_j$ Velocity vector of the joint parameters in $\mathfrak{h}$.

$\mathbf{v}_L$ Left-invariant velocity vector, defined in the body (local) frame.

$\mathbf{v}_M$ Body velocity of the pendulum tip mass in $SE(2)$.

$\mathbf{v}_R$ Right-invariant velocity vector, defined in the global (inertial) frame.

$\mathbf{v}_U$ Translational velocity vector of the beam's neutral axis in the local frame.

$\mathbf{x}$ Position vector in $\mathbb{R}^3$.

$\mathbf{x}_j$ Initial condition vector and period at continuation step j.

$\mathbf{x}_p(s, u, v)$ Position vector of point p in the deformed configuration.

$\mathbf{x}_{2\times1}$ Translation vector in $SE(2)$, representing planar position.

$\boldsymbol{\omega}$ Vector in $\mathbb{R}^3$, representing rotational velocity.

$\boldsymbol{\psi}$ Local periodicity condition.

$\boldsymbol{\varphi}$ Global periodicity condition.

$\boldsymbol{P}_j$ Tangent vector at the jth continuation step.

$\boldsymbol{u}$ Unit vector in $\mathbb{R}^3$ representing the axis of rotation, where $\boldsymbol{\omega} = \boldsymbol{u}\theta$.

$\boldsymbol{u}_j$ Component of the continuation tangent vector corresponding to $\boldsymbol{X}$.

$\boldsymbol{X}(0)$ Initial condition vector in phase space.

$\boldsymbol{x}_i$ Intermediate state at the end of the ith partition interval.

$\boldsymbol{y}(u, v)$ Vector containing the coordinates u and v along the cross-section axes of the beam.

$\circ$ Group composition operator, combining elements of the Lie group.

Δs_i Length of the partition interval i.

Δ Derivative used for linearisation in Newton-Raphson iterations.

δ Variation operator.

$\delta\mathbf{h}$ Infinitesimal motion vector.

$\delta\mathbf{h}^*$ Infinitesimal motions for the full joint configuration.

$\delta\mathbf{h}_\Phi$ Infinitesimal variation vector in $\mathbb{R}^3$, computed from $\mathbf{H}_\Phi$.

$\delta\mathbf{h}_M$ Infinitesimal variation vector for the tip mass configuration.

$\delta\mathbf{h}_{AB}$ Infinitesimal motion vector defined from the variation of the nodal frames.

$\delta\mathbf{h}_{JP}$ Infinitesimal variation vector for the prismatic joint.

$\delta\mathbf{h}_{jP}$ Infinitesimal variation vector for the prismatic joint motion variable r_j.

$\delta\mathbf{h}_{JR}$ Infinitesimal variation vector for the revolute joint.

$\delta\mathbf{h}_{jR}$ Infinitesimal variation vector for the revolute joint motion variable θ_j.

$\delta\boldsymbol{\epsilon}$ Variation of the deformation gradient vector.

η Shear viscosity of the viscoelastic Kelvin-Voigt solid.

γ, β Quadrature parameters for the Newmark method.

$\hat{V}_F$ Diagonal matrix of effective axial and shear viscosity terms.

$\hat{V}_M$ Diagonal matrix of effective torsional and bending viscosity terms.

λ_j Component of the continuation tangent vector corresponding to T.

$\mathcal{E}$ Identity element of the Lie group $\mathcal{G}$.

$\mathcal{G}$ Lie group, consisting of all possible group elements.

$\mathcal{H}$ Lie subgroup of Lie group $\mathcal{G}$.

$\mathcal{K}$ Kinetic energy.

$\mathcal{V}_{ext}$ External forces.

$\mathcal{V}_{int}$ Internal strain energy.

$\mathcal{X}, \mathcal{Y}$ Elements of the Lie group $\mathcal{G}$.

$\mathfrak{g}$ Lie algebra associated with Lie group $\mathcal{G}$.

$\mathfrak{h}$ The Lie algebra associated with the subgroup $\mathcal{H}$.

$\mathfrak{se}(3)$ Lie algebra of the $SE(3)$ group.

$\mathfrak{so}(3)$ Lie algebra of the $SO(3)$ group.

$\mathrm{Ad}_{\mathcal{X}}(\widetilde{\boldsymbol{\tau}})$ Adjoint action of $\mathcal{X}$ on $\widetilde{\boldsymbol{\tau}}$, mapping $\mathfrak{g} \to \mathfrak{g}$.

$\mathrm{ad}_{\widetilde{\boldsymbol{\mu}}}(\widetilde{\boldsymbol{\nu}})$ adjoint map in the Lie algebra, defined using the Lie bracket as $\mathrm{ad}_{\widetilde{\boldsymbol{\mu}}}(\widetilde{\boldsymbol{\nu}}) = [\widetilde{\boldsymbol{\mu}}, \widetilde{\boldsymbol{\nu}}]$.

$\mathrm{D}_{\bullet}$ Directional derivative in the direction of $(\bullet)$.

$\mu_1, \mu_2, \ldots, \mu_{n-1}$ Non-trivial Floquet multipliers.

μ_n Trivial Floquet multiplier for periodic solutions, $\mu_n = 1$.

ν Poisson ratio of the material.

$\odot$ Bialternate product operator.

Ω Forcing frequency.

Φ Alternative vectorial map used as an approximation to the logarithm map for $SE(2)$.

ϕ Mapping function representing the state vector evolution over time.

$\Phi_q \mathbf{A}$ Constraint gradient matrix.

ψ_f Test function for fold bifurcation.

$\psi_{\mathbf{H}}$ Increment vector of local periodicity condition.

$\psi_{\mathbf{v}}$ Velocity vector of local periodicity condition.

ψ_{fl} Test function for flip bifurcation.

ψ_{NS} Test function for Neimark-Sacker bifurcation.

ρ Material density of the beam.

τ_B Bending relaxation time constant.

τ_E Extension relaxation time constant.

τ_S Shear relaxation time constant.

θ Angular position of pendulum tip mass in polar coordinates.

θ_j Angle of the revolute joint in the pendulum system.

$\underline{\underline{\boldsymbol{\epsilon}}}$ Assembled deformation gradient matrix of full beam structure.

$\underline{\underline{\mathbf{C}}}$ Assembled damping matrix of full beam structure.

$\underline{\underline{\mathbf{g}_{ext}}}$ Assembled matrix of integrated external forces of full beam structure.

$\underline{\underline{\mathbf{H}}}$ Assembled matrix of material frames of full beam structure.

$\underline{\underline{\mathbf{K}}}$ Assembled stiffness matrix of full beam structure.

$\underline{\underline{\mathbf{M}}}$ Assembled mass matrix of beam structure.

$\underline{\underline{\mathbf{P}}}$ Assembled $\mathbf{P}(\mathbf{d})$ matrix of full beam structure.

$\underline{\mathbf{v}}$ Assembled matrix of nodal velocities of full beam structure.

$\underline{tv}$ Velocity sensitivity with respect to the period T.

$\underline{tw}$ Spatial sensitivity with respect to the period T.

$\underline{t}$ Sensitivity of the final states with respect to the period T.

$\underline{v}$ Rows of the monodromy matrix corresponding to velocity derivatives.

$\underline{w}$ Rows of the monodromy matrix corresponding to spatial derivatives.

$\varphi_{\mathbf{H}}$ Increment vector of global periodicity condition.

$\varphi_{\mathbf{v}}$ Velocity vector of global periodicity condition.

$\vec{e}_X, \vec{e}_Y, \vec{e}_Z$ Unit vectors defining the global coordinate system.

$\vec{e}_x, \vec{e}_y, \vec{e}_z$ Unit vectors defining the local coordinate system of the element.

$\widehat{(\bullet)}$ Hat operator, mapping a vector in $\mathbb{R}^m$ to an $m \times m$ matrix.

$\widehat{\boldsymbol{\mu}}\boldsymbol{\nu}$ Matrix-vector product, equivalent to $\mathrm{ad}_{\boldsymbol{\mu}}(\boldsymbol{\nu})$.

$\widetilde{(\bullet)}$ Linear map (isomorphism) from $\mathbb{R}^m$ to the Lie algebra $\mathfrak{g}$.

$\widetilde{\boldsymbol{\mu}}, \widetilde{\boldsymbol{\nu}}$ Matrices in the Lie algebra $\mathfrak{g}$.

$\widetilde{\boldsymbol{\rho}}$ Matrix in the Lie algebra, associated with right-hand group composition.

$\widetilde{\boldsymbol{\sigma}}$ Matrix in the Lie algebra, associated with left-hand group composition.

$\widetilde{\boldsymbol{\tau}}$ Matrix in the Lie algebra, parametrising the Lie group.

$\widetilde{\mathbf{a}}_L$ Matrix in the Lie algebra representing the left-invariant vector field associated with derivative with respect to parameter a.

$\widetilde{\mathbf{f}}$ Deformation gradient in $\mathfrak{se}(3)$.

$\widetilde{\mathbf{h}_J}$ An element in the Lie algebra $\mathfrak{g}$.

$\widetilde{\mathbf{h}_j}$ An element in the Lie algebra $\mathfrak{h}$ containing joint parameters.

$\widetilde{\mathbf{v}}(s)$ Left-invariant velocity field in $\mathfrak{se}(3)$ along neutral axis of the beam.

$\widetilde{\mathbf{v}}^b_{AB}$ Body velocity in $\mathfrak{se}(3)$ of frame B relative to frame A.

$\widetilde{\mathbf{v}}^s_{AB}$ Spatial velocity in $\mathfrak{se}(3)$ of frame B relative to frame A.

$\widetilde{\mathbf{v}}_L$ Left-invariant velocity vector in $\mathfrak{se}(3)$, equivalent to the body velocity.

$\widetilde{\mathbf{w}}$ Lie algebra element representing the derivative of q.

ξ Coordinate along the length of the von Kármán finite element, with $\xi \in [0, l]$.

ζ Bulk viscosity of the viscoelastic Kelvin-Voigt solid.

ζ_j Angle between the tangent vectors $\boldsymbol{P}_{j-1}$ and $\boldsymbol{P}_j$.

A Element cross-sectional area.

$d_a(\mathcal{X}), d_b(\mathcal{X})$ Left-invariant derivatives of $\mathcal{X}$ with respect to a and b.

$D_T\boldsymbol{\psi}$ Derivative of the periodicity function with respect to the period.

$D_X\boldsymbol{\psi}$ Derivative of the periodicity function with respect to the states.

$D_{\exp}(\widetilde{\boldsymbol{\tau}})$ Derivative of the exponential map at $\widetilde{\boldsymbol{\tau}}$.

D_{KV} Dissipation function for the viscoelastic Kelvin-Voigt beam model.

E Modulus of elasticity.

G Shear modulus.

h Time step size for the time integration scheme.

$h_{\mathcal{X}}$ Conjugation map, defined as $h_{\mathcal{X}}(\mathcal{Y}) = \mathcal{X}\mathcal{Y}\mathcal{X}^{-1}$.

I Second moment of area.

J Polar moment of inertia.

j_e Jacobian of the transformation from x to ξ.

k, l Dimensions of $\mathfrak{g}$ and $\mathfrak{h}$ respectively.

k_θ Angular stiffness constant of planar pendulum problem.

k_r Radial stiffness constant of planar pendulum problem.

l Element length.

$L_{\mathcal{X}}$ Left translation map defined as $L_{\mathcal{X}}(\mathcal{Y}) = \mathcal{X}\mathcal{Y}$.

M Monodromy matrix.

m Mass per unit length of the beam element.

N Number of system degrees of freedom.

p Phase condition function.

p_{AB} Position vector in $\mathbb{R}^3$ of body frame B relative to spatial frame A.

q_A Position in $\mathbb{R}^3$ of a point q on the rigid body relative to the spatial frame A.

q_B Position in $\mathbb{R}^3$ of a point q on the rigid body relative to the body frame B.

r Radial distance of pendulum tip mass in polar coordinates.

$R_{\mathcal{X}}$ Right translation map defined as $R_{\mathcal{X}}(\mathcal{Y}) = \mathcal{Y}\mathcal{X}$.

r_j Extension of the prismatic joint in the pendulum system.

r_t Radius of gyration about the longitudinal axis of the beam.

s Parametric variable along the beam reference curve.

s_i Partition points of the multiple shooting unit interval.

$SE(2)$ Special Euclidean group representing rigid body transformations in $\mathbb{R}^2$.

$SE(3)$ Special Euclidean group representing rigid body transformations in $\mathbb{R}^3$.

$SO(3)$ Special Orthogonal group representing rotations in 3D space.

T Period of periodic solution.

t Time variable.

u_i Displacement in the ith direction.

V Total strain energy for the von Kármán beam.

$v_{\bar{q}_A}(t)$ Velocity of point q_A in the spatial frame A in homogeneous coordinates.

$v_{\bar{q}_B}(t)$ Velocity of point q_B in the body frame B in homogeneous coordinates.

$v_{q_A}(t)$ Velocity of point q_A in the spatial frame A.

$v_{q_B}(t)$ Velocity of point q_B in the body frame B.

W Strain energy density for the von Kármán beam.

x Coordinate along the length of the finite element, with $x \in [0, l]$.

x_j Coordinate in the jth direction.

z_j Continuation step size.

q Configuration state of the system for time integration, represented by the frame variable.

Chapter 1

Introduction

New designs of mechanical structures are increasingly lighter and more flexible and exhibit geometric nonlinearities due to the presence of large displacements and rotations. Geometric nonlinearity has become an increasingly pressing concern in industrial applications in recent years, as it leads to complex nonlinear vibration phenomena that cannot be accurately predicted using traditional finite element models and nonlinear dynamics software in current use. Flexible slender beams are an example of geometrically nonlinear structures which are ubiquitous in industrial and engineering systems, with applications ranging from dynamics of cables [67], rotating blades of onshore and offshore wind turbines [125], [172], [249], and flexible medical soft robots [202], to rotating blades of turbo engines and helicopter rotor blades [80], [136], [240], wings of flexible aircraft [42], [165], [173], and nanotubes and microcantilevers found in microelectromechanical systems (MEMS) [51], [108], [135]. Further industrial applications of beams include nonlinear dynamics of deep-water offshore moored floating platforms [85], contact and friction modelling [153], fracture of materials and modelling of composite structures under delamination [175], cable systems in the automotive industry [40], pipes conveying fluids in the power industry and power plants [174], among many more industrial applications [110]. The large displacements and rotations of these structures result in complex nonlinear vibration phenomena that can lead to unexpected deformations and stresses, which could result in earlier fatigue and even premature failure of components if not accounted for properly. Modelling highly flexible and complex structures, especially those encountered in industry, necessitates the use of formulations that can accurately and efficiently capture their nonlinear behaviour.

Common nonlinear dynamics phenomena observed in geometrically nonlinear structures include energy transfer [77], [235], mode bifurcations [182], [189], localisation [233], isolated responses [118], [140], and modal interactions [115], [170]. These phenomena pose significant challenges for accurately predicting the dynamic response of structures and complicate the experimental validation of models, making it a critical issue in the design and analysis of industrial components. For instance, energy transfer can lead to internal resonance between modes, where modes which are well-separated in frequency may still interact, resulting in unexpected vibrations. Isolated responses also pose significant challenges from both design and experimentation perspectives. Failure to correctly characterise and compute isolated responses has important

consequences, as they could merge with the main response branch of the structure, causing sudden and dramatic changes in resonance frequency and response amplitude. This could lead to accelerated fatigue, a reduction in the operational lifespan of components, or even design failure.

The accurate and effective prediction and modelling of these nonlinear phenomena requires accurate and broadly applicable methods that are both mathematically rigorous and numerically efficient. In the context of slender beams in large-amplitude motions, geometrically exact formulations exist that have been developed and used over decades (see review paper by Meier et al. [139]). These displacement-based models are based on absolute variables, including positions and rotations, which are used to formulate the dynamic beam behaviour. The correct representation of rigid body motion and the mathematically precise handling of rotations and displacements are often overlooked in these formulations. This leads to numerical models whose foundational kinematic assumptions and descriptions of rigid body motions are either approximate, due to truncation of nonlinear terms, or geometrically incompatible with the nonlinear configuration space of rigid body motions. Furthermore, problems such as strain objectivity and numerical issues such as shear locking are commonplace, as well documented in the literature [27], [44], [54], [112]. Although alternative geometrically exact formulations have been developed to address these challenges, they generally fail to incorporate a fully accurate kinematic description of rigid body motion in 3D space. Consequently, these models often resort to ad hoc methods or more complicated numerical representations in order to maintain objectivity and avoid shear locking (see Chapter 2 for a comprehensive review of the formulations.)

There is therefore a strong motivation for using more accurate beam formulations for the modelling and analysis of nonlinear dynamics of structures, which are efficient and can be used in industrially significant applications. Geometrically exact beam models formulated on the Special Euclidean Lie group $SE(3)$ [208] offer the only formulation that is grounded in a precise and mathematically rigorous description of rigid body motion in three dimensions. Unlike classical beam theories which treat positions and rotations as independent variables, the $SE(3)$ model is based on a deep coupling between the two variables, which aligns with the mathematical structure of rigid body motion. The model is naturally locking-free and intrinsic in nature, and maintains strain invariance under rigid body motion [210].

Developing computational analysis methods to be used with geometrically exact models formulated on the $SE(3)$ framework will enable the use of significantly more accurate and numerically efficient tools for nonlinear vibration analysis much earlier in the design process, generating greater insight into the structure's dynamics, and offering a more accurate modelling of nonlinear dynamic phenomena.

Motivation

The motivation of this thesis is to develop sophisticated methods for the analysis of nonlinear dynamics of geometrically exact beams formulated on the $SE(3)$ Lie group. In particular, the objective is to adapt current state-of-the-art analysis methods to be used with Lie group models,

such that they preserve the fundamental geometric properties associated with the nonlinear configuration space of the Lie group. Many numerical methods have been developed in the literature for the analysis of nonlinear dynamics of mechanical systems that are applicable to complex and large-scale structures [62], [182], [248]. However, these methods cannot be readily used on geometrically exact formulations based on the $SE(3)$ Lie group. The $SE(3)$ group is a nonlinear manifold, meaning that vector space operations such as addition and subtraction, which presuppose a Euclidean embedding and flat surface geometry, cannot be directly applied. Therefore, numerical tools which have been developed for the nonlinear dynamic analysis of structures need to be modified to be used with a Lie group formulation.

In developing and adapting these methods to fulfil the aims of this thesis, we also demonstrate the suitability of the $SE(3)$ formulation in modelling extremely large displacements and rotations, and capturing nonlinear dynamic phenomena accurately. It is noted that we do not aim to validate the $SE(3)$ model, as that objective has been met in previous works in the field [17], [94]. Our focus is therefore on the adaptation of existing numerical tools in nonlinear dynamic analysis to facilitate their use with Lie group models. The main novelty of this work also lies in this objective, as, to the best of our knowledge, Lie group models have not previously been used for nonlinear dynamics analysis of geometrically nonlinear structures. A secondary aim of this work is to provide a step-by-step introduction to the theory of Lie groups and the $SE(3)$ finite element formulation, particularly for structural dynamicists. The theory of Lie groups is often seen as prohibitively complex, and this work seeks to demystify the subject and make it more accessible to those in the field.

Lie group theory, specifically the $SE(3)$ group, has found extensive application in the field of computational multibody system dynamics aimed at kinetic analysis of complex mechanical systems [146]. Rigid bodies perform what is known as screw motion in three dimensions, and Lie group theory provides a geometric and analytic foundation for efficient modelling of rigid body mechanisms. It has been used widely in the context of rigid multibody systems and joint kinematics [35], [50], [143], [144], offering a geometric description of relative motion between adjacent bodies. Group theory has also enjoyed extensive application in the field of robotics, where it is used to model the rigid body motion of robotic arms and joints, enabling precise control and simulation of complex robotic mechanisms [82], [111], [117], [162], [163]. The theory has also been used extensively in the context of flexible multibody systems, accounting for the combined description of flexibility and large-amplitude rigid body motion [64], [186], [242]. Indeed, the $SE(3)$ beam model used in this thesis, is an example of a flexible body undergoing deformations and large displacements and rotations.

The relevance of the $SE(3)$ model in industrial applications is evident in a wide range of engineering disciplines, such as those mentioned in the introduction, where accurate representation of rigid body motion is essential to simulate the complex nonlinear dynamics of slender beam structures. This underscores the versatility and suitability of the $SE(3)$ formulation in addressing the complex demands of modern industrial engineering applications, and highlights the importance of this thesis' objective in developing the numerical models necessary for

nonlinear vibration analysis of structures formulated on the Lie group framework.

Research Questions

To address the challenges and gaps identified, this thesis seeks to answer the following research questions:

1. **How can numerical tools for nonlinear dynamic analysis be adapted to operate within the $SE(3)$ framework, enabling rigorous and efficient analysis of geometrically nonlinear structures with industrial relevance?**

2. **To what extent does the $SE(3)$ formulation improve the modelling of nonlinear dynamic phenomena, such as large displacements, bifurcations, and modal interactions?**

Thesis Outline

- Chapter 2 introduces the concept of nonlinear normal modes and explores their fundamental properties. Recent contributions in the literature are reviewed and discussed. This is followed by a review of the literature on geometrically exact beam formulations, along with a brief overview of the advantages of the Lie group formulation on $SE(3)$ compared to classical beam models. Following the preliminary introduction to the $SE(3)$ model, which is formulated thoroughly in Chapter 3, the nonlinear finite element equations of a beam with von Kármán strains are developed, which serves as a model for comparison with the $SE(3)$ formulation in Chapter 4.

- Chapter 3 gives a step-by-step introduction to the theory of Lie groups, incorporating various examples to facilitate comprehension of the mathematical concepts. Aiming to offer a suitable introduction for structural dynamicists, the equations of motion of a free rigid body are developed, effectively integrating Lie group theory into the formulation of mechanical problems. This chapter concludes with a review of the geometrically nonlinear beam equations formulated on the $SE(3)$ group, presenting the method in a more gradual and structured manner to enhance understanding. The main contributions of this chapter therefore lie in its novel approach to making these advanced concepts more accessible.

- Chapter 4 presents computational results of nonlinear normal modes of a range of 2D geometrically nonlinear beams. The Special Euclidean formulation in two dimensions, namely the $SE(2)$ group, is used to model the structures, and is compared with the von Kármán beam formulated in Chapter 2. The adaptations required to the shooting and pseudo-arclength continuation methods to enable their use within the Lie group framework are discussed, which marks a novel contribution of this chapter.

- Chapter 5 introduces the multiple shooting method for computing periodic responses and offers a comprehensive review of its formulation, giving an example of its application to

a two degree of freedom nonlinear oscillator. The adaptations required to the multiple shooting method to enable its use with the $SE(3)$ Lie group model are discussed. The application of the multiple shooting method to a 3D right-angled beam modelled under the $SE(3)$ formulation faced some challenges, which are discussed at length, and aim to be addressed in future studies. Finally, a global periodicity condition on the nonlinear $SE(3)$ manifold is developed. The adaptations of the multiple shooting method, and the formulation of the global periodicity condition, underscore the novel contributions of this chapter.

- Chapter 6 presents results on the forced response of geometrically nonlinear beams formulated on the $SE(2)$ and $SE(3)$ groups using shooting and continuation. A discussion on the implementation of a geometrically exact damping model within Lie group formulations is given. Through the use of numerical techniques, such as sine sweeps and continuation, the forced responses of a range of nonlinear structures are computed, demonstrating phenomena such as bifurcations and branch switching. The application of the Lie group beam formulation for the computation of forced response curves and bifurcation analysis of geometrically nonlinear structures constitutes the novel contributions of this chapter.

- Chapter 7 presents initial results on the application of the $SE(3)$ formulation for modelling high aspect ratio wings and a box wing aircraft structure. This prospective chapter highlights the potential of the $SE(3)$ model in capturing complex nonlinear dynamic phenomena prevalent in these structures, and makes a compelling case for the suitability of the model in aeroelastic applications. The work in this chapter serves as a foundation, inviting further exploration and development in future research.

Finally, the conclusion chapter summarises the main results and offers perspectives on future research, providing a framework for studies that build upon the foundations laid by the work undertaken in this thesis.

Journal Publications

1. Bagheri, A.K., Sonneville, V., Renson, L. Nonlinear normal modes of highly flexible beam structures modelled under the $SE(3)$ Lie group framework. Nonlinear Dyn 112, 1641-1659 (2024). https://doi.org/10.1007/s11071-023-09106-1

Conference Publications

1. Bagheri, A.K., Sonneville, V., Renson, L. Computing Periodic Responses of Geometrically Nonlinear Structures Modelled Using Lie Group Formulations. In: Lacarbonara, W. (eds) Advances in Nonlinear Dynamics, Volume I. ICNDA 2023. NODYCON Conference Proceedings Series. Springer, Cham. (2024). https://doi.org/10.1007/978-3-031-50631-4_30

2. Bagheri, A.K., Sonneville, V., Renson, L. Computing Periodic Responses of Geometrically Nonlinear Structures Modelled Using Lie Group Formulations, Proceedings of ISMA 2022 - International Conference on Noise and Vibration Engineering and USD 2022 - International Conference on Uncertainty in Structural Dynamics 2550-2564, KU Leuven, Belgium (2022).

Journal Publications in Preparation

1. Bagheri, A.K., Sonneville, V., Renson, L. A Multiple Shooting Method for Computing Periodic Responses of Highly Flexible Beams Modelled under the $SE(3)$ Lie Group Framework.

2. Bagheri, A.K., Sonneville, V., Renson, L. Nonlinear Dynamics of Highly Flexible Aircraft Structures Modelled under the $SE(3)$ Lie Group Framework.

Chapter 2

Fundamentals and Literature Review

Abstract

This chapter provides a comprehensive review of the theoretical foundations relevant to nonlinear normal modes (NNMs) and their use in recent nonlinear dynamics literature. We outline the fundamental properties of NNMs and their significance in nonlinear dynamic analysis, followed by an exploration of key computational techniques, specifically the shooting and pseudo-arclength continuation methods, in the computation of NNMs. The discussion then shifts to a review of the literature surrounding geometrically exact beam models, highlighting various approaches to modelling geometric nonlinearity. We also discuss some benefits of the beam formulation based on the Special Euclidean group $SE(3)$, which will be formally introduced in the next chapter. Finally, we present the finite element formulation for a beam using von Kármán strains, setting the stage for subsequent comparisons with more advanced beam formulations based on the $SE(3)$ group in later chapters.

2.1 Introduction

The objective of this chapter is first to provide an overview of the theoretical concepts surrounding the topic of Nonlinear Normal Modes (NNMs), and to review the recent literature related to this subject. The fundamental properties of NNMs are discussed and some methods related to their calculation are briefly reviewed. The basic principles of shooting and pseudo-arclength continuation, which are used in subsequent chapters for the calculation of NNMs and forced responses, are detailed and discussed. This is followed by a review of literature surrounding geometrically exact beam formulations, with discussions related to the applicability and suitability of various beam models. Finally, the equations of motion of a finite element beam formulation with nonlinear von Kármán strains are developed, which is used as a reference model in Chapter 4 for comparison against the more accurate beam model based on the Special Euclidean Lie group, which is discussed in Chapter 3.

2.2 Nonlinear Normal Modes

The concept of normal modes in linear systems is well established and commonly used to analyse behaviour of dynamical systems. The two main properties of linear modes are their invariance, in that motion initiated on a specific mode remains on that mode, and modal superposition, such that free and forced vibrations can be expressed as linear combinations of individual modal vibrations. The motivation for developing the theory of nonlinear normal modes, is to provide a similar framework for the vibration analysis of nonlinear systems. As the counterpart to linear modal analysis, they can offer a rigorous method for interpreting a wide range of nonlinear dynamic phenomena, and are capable of characterising the behaviour of nonlinear systems.

There are two main definitions of NNMs in the literature, namely one by Rosenberg [187], and another by Shaw ane Pierre [198], [199], [200]. Rosenberg describes nonlinear modes as a straightforward extension of linear modes and defines them as periodic vibrations of a conservative system in unison, where all material points reach their extreme values and pass through zero simultaneously. This definition cannot account for internal resonances, however, it may be extended to define NNMs as non-necessarily synchronous periodic solutions of the conservative system, thereby encompassing internal resonances [116]. In case of non-conservative systems, the damped dynamics can often be interpreted based on the topological structure and bifurcations of the NNMs of the underlying undamped system [115]. This extended definition of NNMs is the one used in this thesis.

The Shaw and Pierre definition of an NNM is as a two-dimensional invariant manifold in phase space, which passes through a stable equilibrium point of the system, and is tangent to a plane which is an eigenspace of the system linearised about that equilibrium point [199]. This manifold is invariant under the flow, which extends the invariance property of LNMs to nonlinear systems [170]. Geometrically, LNMs are represented by planes in phase space, and NNMs are two-dimensional surfaces that are tangent to them at the equilibrium point [115].

Unlike Rosenberg's definition, Shaw and Pierre's definition is more general and is applicable to both conservative and non-conservative systems [182].

2.2.1 Properties of NNMs

NNMs have fundamental properties and characteristics which are unique to nonlinear systems, and do not have linear counterparts. The normal modes of a nonlinear system are not orthogonal to each other, and the principle of superposition does not hold, making the decoupling of the modes impossible [182]. In addition to this, NNMs also exhibit frequency-energy dependence, such that their modal curves in the configuration space, and their oscillation frequencies, change with increasing energies [115]. Mode localisation, where vibration energy gets confined to one particular area of the structure, is also a unique feature of NNMs [234], and is a result of the frequency-energy dependence of nonlinear systems. Even perfectly symmetric structures may experience localised vibrations due to the dependence of mode shapes on amplitude [72]. Such mode localisations may be utilised as a design strategy for vibration mitigation or vibration isolation objectives [13].

Another unique feature of nonlinear systems in that NNMs may interact during a general motion of the system, leading to internal resonances. This leads to an exchange of energy between the modes, where vibration in one mode can elicit a response in another mode. Internally resonance NNMs have no counterpart in linear systems, and are generated through bifurcations [115]. Such interactions could occur for modes with commensurate or near-commensurate natural frequencies [171], [184], due to the lining of the higher harmonics of lower modes with those of the higher modes. However, due to the frequency energy dependence of the NNMs, changes in the oscillation frequencies with the energy level could still result in interactions between modes with non-commensurate linear frequencies [86].

A third property of NNMs is the presence of mode bifurcations, which can lead to NNMs that bifurcate from other modes and thus have no linear counterpart [189]. An example of this is the classic symmetry-breaking bifurcation seen in the 2 degree of freedom oscillator with cubic nonlinearity, where unsymmetric NNMs emanate from the symmetric NNM branch [170]. As a result of the mode bifurcations, the number of NNMs in a nonlinear system can exceed the number of the system degrees of freedom, a property which has no analogy in linear systems [142]. The stability of NNMs is also a unique property, where unlike linear modes which are neutrally stable, NNMs could exchange stability and become unstable [157]. In the context of periodic motions, unstable NNMs are periodic solutions which are not sustainable under small perturbations applied to the initial conditions which generate the NNM motion.

2.2.2 Computation of NNMs

Considering NNMs as periodic solutions of the conservative system, they can be computed numerically using shooting techniques, in order to find initial conditions which result in a periodic motion, coupled with continuation methods to find families of such periodic solutions. Alternative methods such as the multiple scales method or the method of normal forms may

also be used [66], [142], [150], [228], [239]. The Harmonic Balance Method (HBM) is also a suitable alternative to the shooting method and can be combined with continuation tools to compute NNMs [62].

In this work, following the papers by Kerschen and Peeters et al. [115], [170], we use shooting and continuation to compute NNMs and forced responses of conservative and non-conservative systems, which is detailed in the following section. Numerical continuation methods have become quite advanced and sophisticated and have been applied to large-scale dissipative dynamical systems for the computation of equilibrium points, periodic orbits, and bifurcations [231]. For instance, Arquier et al. [8] combined a shooting method with the asymptotic numerical continuation method to identify the NNMs as closed periodic orbits of undamped unforced systems. The application of continuation methods in evaluating NNMs was shown for a full scale aircraft by Kerschen et al. [114], where the interaction of the modes with distinct linear frequencies was shown to generate additional nonlinear modes with no linear counterpart. Renson et al. [183] investigated the dynamics of a satellite structure with a strongly nonlinear component using continuation methods, and showed a wide variety of nonlinear phenomena such as jumps, energy transfers from local to global structural modes, and interactions between modes with incommensurable linear frequencies. Kuether and Allen [119] used the shooting method in conjunction with a continuation approach using a subset of the underlying linear modes of a geometrically nonlinear finite element model to compute the NNMs, which in turn greatly reduced the computational time. Sombroek et al. [207] further addressed the issue of computational time in calculating NNMs using the pseudo-arc length continuation method, by calculating NNMs from a reduced order model of a system constructed from linear modes and modal derivatives.

NNMs can also be identified experimentally using the method of force appropriation, where a multiharmonic force is applied such that each of its harmonics is in phase quadrature with the corresponding response harmonic. This approach causes the external input forces to counterbalance the internal damping forces exactly, aligning the system with the conservative underlying NNM motion [181]. Peeters et al. [169] also demonstrated that if the forced response across the structure is a monophase periodic motion in quadrature with the excitation, an NNM vibrates in isolation, and can therefore be identified. In case of internal resonances at low amplitudes, some phase quadrature may be observed in the response, especially if symmetry-breaking bifurcations occur, resulting in non-monophase modes [57], [87], [197]. Although the input force has to be multi-harmonic to correctly identify NNMs [181], [238], it has been shown that a single-point mono-harmonic forcing may also excite a single NNM motion, which is referred to as imperfect force appropriation [169]. This method, coupled with a pseudo-arclength continuation technique, has been shown to be able to compute NNMs up to moderate response amplitudes [120], although the computation of NNMs to higher energy levels and to regions of internal resonance would typically require additional harmonics in the forcing function.

2.2.3 Recent works on NNMs

More recent works on NNMs has seen the application of NNMs in reduced-order modelling of nonlinear systems [141]. Touzé et al. [229] reviewed recent developments on nonlinear methods for model reduction in structures with geometric nonlinearity based on the invariant manifold of the NNMs. Haller and Ponsioen [93] propose a unified framework for nonlinear modal analysis in dissipative systems, introducing Spectral Submanifolds (SSM) as an invariant manifold asymptotic to an NNM, and as the smoothest continuation of spectral subspaces in the linearised system, on which the reduced system dynamics may be approximated. Jain and Haller [104] developed methods for computing invariant manifolds and their reduced dynamics in very high-dimensional nonlinear systems, including finite element models of mechanical structures ranging from a simple beam to an aircraft wing with many degrees of freedom. Szalai et al. [221] developed a methodology to analytically compute both the shape of SSMs and their corresponding backbone curves from a data-assimilating model fitted to experimental vibration signals. Vizzaccaro et al. [237] developed ROMs of geometrically nonlinear structures based on the normal form theory, with a third-order approximation of the invariant manifolds (NNMs) of structures, which are able to approximate the reduced dynamics of nonlinear systems containing all possible third- and higher-order internal resonances. Lie and Wagg [131] developed a direct normal form decomposition to reduce the order of systems with both quadratic and cubic nonlinearities, and with 1:1 internal resonances. The use of normal forms has also been coupled with phase-locked-loop experimental continuation methods to identify the backbone curves of systems with distributed nonlinearities [60]. This follows from the concept of nonlinear phase resonance, which in [238] is used to predict nonlinear modes and oscillation frequencies at phase resonance, generalised to superharmonic and subharmonic resonances. A recent study on phase resonance testing and phase-locked-loop experimental continuation was conducted by Debeurre et al. [57], who experimentally identified backbone curves of a flexible vertical cantilever beam with base excitation, showing good agreement with numerical results based on the harmonic balance method.

2.2.4 Computation of NNMs with Shooting and Pseudo-arclength Continuation

As described in Section 2.2.2, in this thesis we compute families of periodic solutions along an NNM branch using shooting and pseudo-arclength continuation. In this work, we adopt the algorithm originally proposed by Keller [49], with some modifications to the correction procedure as introduced by Peeters et al. [170]. Let

$$\phi(\boldsymbol{X}(0), T),\ \phi : \mathbb{R}^{2N} \times \mathbb{R} \to \mathbb{R}^{2N}, \tag{2.1}$$

denote the result of the time integration of the equation of motion, over a time interval of length T, starting from the initial condition vector $\boldsymbol{X}(0)$. A periodic solution is one that satisfies the

periodicity condition given by

$$\boldsymbol{\psi}(\boldsymbol{X}(0), T) = \phi(\boldsymbol{X}(0), T) - \boldsymbol{X}(0) = \mathbf{0}. \tag{2.2}$$

This periodic solution is found using a shooting method, which is an iterative scheme for finding the roots of a smooth boundary value problem (BVP) using a sequence of initial value problems [113]. Finding the roots of the BVP reduces to finding the set of initial values, for which the boundary conditions are satisfied under time integration of the dynamic equations of the system.

The periodicity condition does not have a unique solution. Indeed, since the system is autonomous, any point on the periodic orbit can be used as an initial condition. An additional equation termed the phase condition, must be added to restrict the number of solutions to the shooting problem. Various choices for the phase condition exist, such as Poincaré [63] or integral phase conditions [194]. In this work, the initial velocities across all degrees of freedom of the system are set to zero as in [170]. The resulting phase condition equation is therefore given by

$$p(\boldsymbol{X}(0)) = \mathbf{B}\boldsymbol{X}(0) = \mathbf{0}, \tag{2.3}$$

where $\mathbf{B}$ is a $N \times 2N$ sparse Boolean matrix with ones corresponding to the velocities.

Starting from a converged periodic solution $\left(\boldsymbol{X}_j^\star(0),\, T_j^\star\right)$, a prediction for the next point on the NNM branch is made along the tangent vector at the current solution, $\boldsymbol{P}_j = \left[\boldsymbol{u}_j^T \;\; \lambda_j\right]^T$, which is found from solving the overdetermined linear system

$$\begin{bmatrix} \frac{\partial \boldsymbol{\psi}}{\partial \boldsymbol{X}_j^\star(0)} & \frac{\partial \boldsymbol{\psi}}{\partial T_j^\star} \\ \mathbf{B} & 0 \\ \boldsymbol{P}_{j-1}^T & \end{bmatrix} \begin{bmatrix} \boldsymbol{u}_j \\ \lambda_j \end{bmatrix} = \begin{bmatrix} \mathbf{0} \\ 1 \end{bmatrix}, \tag{2.4}$$

where the subscript j indicates the continuation index. $\boldsymbol{P}_{j-1}$ is the tangent at the previous continuation step; for the first continuation point where no previous tangent vector is available, this is replaced by $[\mathbf{0}_{2N} \;\; 1]$. It is noted that $\mathbf{B}$ is the derivative of the phase condition Eq. (2.3) with respect to $\boldsymbol{X}(0)$. The tangent vector found from solving Eq. (2.4) is then normalised to unit length. The prediction can therefore be written as

$$\begin{bmatrix} \boldsymbol{X}_{j+1}^0(0) \\ T_{j+1}^0 \end{bmatrix} = \begin{bmatrix} \boldsymbol{X}_j^\star(0) \\ T_j^\star \end{bmatrix} + z_j \begin{bmatrix} \boldsymbol{u}_j \\ \lambda_j \end{bmatrix}, \tag{2.5}$$

where the superscript 0 indicates that this is the first prediction point, and z_j is the continuation step size. The prediction point is generally not a periodic solution of the system. Corrections are therefore required to the prediction, which are found iteratively using a Newton-Raphson scheme. The corrections are forced to remain orthogonal to the tangent vector, thereby ensuring the adherence of the solution to turns in the NNM branch [170]. The corrections are found by

solving the following linear system

$$\begin{bmatrix} \frac{\partial \boldsymbol{\psi}}{\partial \boldsymbol{X}^k_{j+1}(0)} & \frac{\partial \boldsymbol{\psi}}{\partial T^k_{j+1}} \\ \mathbf{B} & 0 \\ \boldsymbol{u}_j^T & \lambda_j \end{bmatrix} \begin{bmatrix} \Delta \boldsymbol{X}^k_{j+1}(0) \\ \Delta T^k_{j+1} \end{bmatrix} = - \begin{bmatrix} \boldsymbol{\psi}(\boldsymbol{X}^k_{j+1}(0), T^k_{j+1}) \\ p(\boldsymbol{X}^k_{j+1}(0)) \\ 0 \end{bmatrix}. \tag{2.6}$$

where the superscript is now k and indicates the correction iteration index. The periodic solution is updated iteratively after the corrections are found by

$$\begin{aligned} \boldsymbol{X}^{k+1}_{j+1}(0) &= \boldsymbol{X}^k_{j+1}(0) + \Delta \boldsymbol{X}^k_{j+1}(0), \\ T^{k+1}_{j+1} &= T^k_{j+1} + \Delta T^k_{j+1}. \end{aligned} \tag{2.7}$$

This continues until desired convergence is met and a new periodic solution is found along the continuation branch as $\left(\boldsymbol{X}^\star_{j+1}(0),\ T^\star_{j+1}\right)$.

As seen in the Newton-Raphson scheme, derivatives of the periodicity equation are required with respect to the initial conditions at each iteration step. This can be evaluated using the Monodromy matrix

$$M = \frac{\partial \phi(\boldsymbol{X}(0), T)}{\partial \boldsymbol{X}(0)}, \tag{2.8}$$

which gives the variation in the solution of the system after time T with respect to the initial conditions [182]. This quantity is computed simultaneously with the time integration of the equation of motion of the mechanical system using sensitivity analysis [39].

As mentioned above, a converged starting solution needs to exist to begin the continuation process. In the calculation of NNMs of mechanical systems, this usually comes from the solution to the shooting problem, starting with an initial guess corresponding to a particular linear normal mode of the system [182]. The modal amplitude is scaled to ensure a linear-like response at very low energy. The corrections to this starting point are made to be orthogonal to the linear mode to ensure that the iterative process does not converge to the trivial zero solution.

It is noted that in Eq. (2.4), following the methodology proposed by Keller [49], the tangent is found by making it parallel to the normalised tangent from the previous continuation step. The last row of Eq. (2.4) can be written using the vector dot product and by taking ζ_j to be the angle between tangent vectors $\boldsymbol{P}_{j-1}$ and $\boldsymbol{P}_j$ as

$$\|\boldsymbol{P}_{j-1}\| \|\boldsymbol{P}_j\| \cos(\zeta_j) = 1. \tag{2.9}$$

Noting that $\|\boldsymbol{P}_{j-1}\| = 1$ as it has already been normalised, Eq. (2.9) implies that the angle between consecutive tangent vectors cannot exceed $\frac{\pi}{2}$ since the cosine must remain positive. This removes the necessity for computing the continuation step sign for following the NNM branch.

Adaptations are required to the shooting and pseudo-arclength methods described in this section to make them suitable for use with Lie group formulations. These adaptations are described in greater detail in Chapter 4, while the Lie group formulation of the beam equations

is detailed in Chapter 3.

2.3 Geometrically Exact Beam Formulations

Beam theory is dedicated to the modelling of large slender structures whose dimension in the length direction is much larger than the dimension in the transverse direction. As a simplification of 3D continuum mechanics, 1D beam theories typically allow to describe the motion and deformation of slender bodies in 3D space on the basis of proper kinematic, kinetic and constitutive resultant quantities [138]. The kinematics of beam models generally reduces to the displacement of the beam centreline, while maintaining the basic kinematic assumption of small strains and rigid cross sections. The term geometrically exact beam was initially coined by Simo [203], and refers to models where no simplifications are made to the geometric nonlinearities arising from large displacements and rotations, such that the model behaviour remains exact regardless of the magnitude of rotations. The pioneering work by Simo was based on earlier fundamental work by Reissner on 2D [179] and 3D [178] shear-deformable beams. Building on the work of Reissner, Simo [203] and Simo and Vu-Quoc [204], [205] laid the foundations of static and dynamic beam theory. Further significant contributions were made under the umbrella of geometrically exact formulations by Cardona and Geradin [44], Ibrahimbegović [102], and Betsch and Steinmann [27]. These contributions mainly differed by the type of rotation interpolation (e.g. interpolation of incremental, iterative or total rotational vectors), the choice of nodal rotation parametrisation (via rotation vectors, quaternions etc.), the type of iterative rotation updates (multiplicative or additive), or the time integration scheme applied to the rotational degrees of freedom (e.g. based on additive or multiplicative rotation increments) [139]. Many of these early contributions were plagued by the non-commutative nature of rotation matrices in their finite element implementations, leading to issues such as shear locking and non-objectivity of strains from the various parametrisations of rotations. The rotational configuration space is a Lie group, namely the Special Orthogonal group $SO(3)$[1], with elements that are non-additive and non-commutative, making their handling in 3D non-trivial. A significant breakthrough came with the later works of Crisfield and Jeleni [54], [107], who demonstrated that none of the rotation field discretisations in the beam formulations at the time preserved both properties of objectivity and path-independence. They further introduced a new orthogonal interpolation scheme that directly operates on the rotation manifold, rather than on its rotation vector parametrisations, and maintains objectivity and path-independence. This formulation marked the beginning of the development of various alternative rotation interpolation strategies for geometrically exact beams that preserve these properties. A significant contribution of Crisfield and Jeleni's work is that the rotation interpolation scheme they proposed is able to exactly represent the state of constant curvature as a geodesic on the rotation manifold. However, the main drawback of their method, and that of further contributions by other researchers that followed, is that that they are formulated on the $\mathbb{R}^3 \times SO(3)$ group, which assumes that the translations and rotations are uncoupled [23], [78], [122], [244]. This formu-

[1]Lie groups and in particular the $SO(3)$ group are introduced and discussed comprehensively in Chapter 3.

lation consists of two individual interpolations, one as a linear interpolation on the Euclidean vector space, and the other as a spherical interpolation on the $SO(3)$ group. This results in the direct product manifold of $\mathbb{R}^3 \times SO(3)$. As it will be discussed in Chapter 3, this kinematic description of the beam motion is inaccurate, as the rigid body motion of the bream cross sections is best and most accurately described using the Special Euclidean group $SE(3)$. The issues arising from this inaccurate kinematics, such as shear locking, are inherent in these beam models and cannot be resolved, including in the formulations by Crisfield and Jeleni. Notwithstanding, in what follows in this section, some of the more recent geometrically exact beam models on $\mathbb{R}^3 \times SO(3)$ are discussed and reviewed. The reader is also referred to the excellent review paper by Meier [139] for a detailed review of various geometrically exact beam models and their formulations.

A particular parametrisation of the rotation matrices is given by quaternions, which offers a singularity-free parametrisation with 4 parameters. Stuelpnagel [219] showed that it is topologically impossible to have a global 3D parametrisation without singular points for the rotation group and that quaternions offer the lowest dimensional parametrisation which is singularity-free. Among geometrically exact beam formulations with quaternion interpolation, we highlight the work of Gosh and Roy [84], who explored an isoparametric interpolation of total quaternion to achieve geometrically consistent, strain-objective, and path-independent finite element solutions for geometrically exact beams, while interpolating quaternions along a geodesic on the rotation manifold. Zupan et al. [253], [254] developed the Reissner-Simo beam formulations using the quaternion representation of rotations, formulating the governing equations consistently with quaternion algebra, and demonstrated the suitability of this formulation on a range of examples. The problem of shear locking persists in these formulations, which the authors have addressed using reduced integration. More recently, Cottanceau et al. [53] presented a finite element formulation of the geometrically exact beam model using rotational quaternions, leading to a polynomial formulation of the discrete equilibrium equations that they exploit through the use of the asymptotic numerical method. In general, although the quaternion-based formulations do not suffer from the singularity issues of other parametrisations of rotations, they still fail to account for the more appropriate description of the beam kinematics afforded by the $SE(3)$ model, and are prone to numerical issues such as shear locking.

Another class of geometrically exact beam formulations is the intrinsic beam theory developed by Hodges [96], [97]. In this formulation, the two vector states of linear and angular inertial velocities, and force and moment sectional resultants, are taken as the independent degrees of freedom, where both states are expressed in the local coordinate frame of the beam. The equations of motion are therefore written in terms of the velocities and the internal forces and moments. The intrinsic nature of the formulation means that displacements and rotations do not appear in the equations of motion, which therefore avoids the need for parametrisation of rotations. However, in case of configuration-dependent external forces, displacements and rotations will explicitly appear in the equations of motion [158]. An additional challenge of the intrinsic beam model is the application of boundary conditions, as displacement constraints

cannot be explicitly imposed [215]. Palacios [158] applied the intrinsic beam model to compute the NNMs of a cantilever beam and an anisotropic composite beam, describing the NNMs in the space of the intrinsic modal coordinates obtained by projecting the intrinsic beam equations using the linear modes of the model. The NNMs were defined as invariant manifolds that are tangent to the linear modes for infinitesimal amplitudes, and internal resonances were assumed to not take place. In other works, Artola, Wynn and Palacios [12] developed a nonlinear model predictive control strategy for flexible structures, where they used the aforementioned modal-based finite-dimensional approximation to intrinsic beam equations to model the geometrically nonlinear structures under consideration. They also extended this approach by incorporating a generalised Kelvin-Voigt damping model within the intrinsic framework, enabling the simulation of dissipative effects in the dynamics of very flexible structures. Regarding the study of highly flexible and high-aspect-ratio wings, Palacios et al. [161] applied the intrinsic beam model to simulate the flight dynamics of aircraft, where the model effectively captured the nonlinear couplings between structural deformations and vehicle dynamics. Patil and Hodges [167] and Cook et al. [52] also used the intrinsic beam model on high aspect ratio wings in aeroelastic applications.

Here, we also briefly discuss strain-based beam formulations, which represent another approach to avoiding the parametrisation of rotations. The underlying motivation is that by taking strains as the primary interpolated degrees of freedom, as opposed to rotations and displacements, the need to parametrise rotations is circumvented. Since strains, as derivatives, belong to a linear vector space, additive interpolation can be used without loss of objectivity. The resulting formulation is also locking-free [47]. However, the main drawback of the method is the difficulty of the integration of rotations from the given interpolated rotational strains, as they often cannot be performed analytically. Due to the complicated form of the kinematic equations, a numerical integration method is used to obtain the total rotations from the given rotational strains. Zupan and Saje [252] develop this numerical integration based on the Runge Kutta method, and apply it on the nonlinear rotation manifold, which they term as the non-additive update. In other works, Otsuka et al. [156] develop a multibody dynamic analysis framework based on the strain-based beam formulation, and Su and Cesnik [220] apply the strain-based beam formulation in aeroelastic analysis of very flexible aircraft. The strain-based beam model, though more accurate than the previously discussed formulations [252], is still founded on an inaccurate kinematic description of the beam, which can only be correctly described under the $SE(3)$ formulation.

Alternative formulations to the geometrically exact beam formulation also exist. Two notable examples which are briefly mentioned are the Absolute Nodal Coordinate Formulation (ANCF) and the corotational beam formulation. In ANCF [81], [155], [195], [196], the coordinates of the element are defined in an inertial frame and as such no coordinate transformation is required. Furthermore, since the formulation uses absolute nodal coordinates, no infinitesimal or finite rotations are used as nodal coordinates, and instead global slopes that are obtained as derivatives of the absolute displacements are used. The formulation leads to an exact modelling

of the rigid body motions, and inertia forces are simple due to a constant mass matrix. Despite these benefits, the ANCF model incorporates complex expressions of internal forces, and as shown by Bauchau et al. [18] and Romero [185], it suffers from accuracy issues and locking phenomena. In the corotational formulation [24], [26], [124], [224], the large nonlinear deformation of the beam is split into a mean rigid body motion followed by smaller local deformations which are expressed in the local frame, termed the corotational frame. Under large rotations and displacements, where the deformations remain small, linear strain and Cauchy stress are defined with respect to the corotated configuration so that geometrically linear elements can be used directly in the local formulation [134]. The internal forces are evaluated in the corotational frame and then projected onto the inertial frame.

As mentioned earlier, the beam formulation used in this work is based on the Special Euclidean group $SE(3)$, which is formally introduced in Chapter 3. A brief overview of the benefits of this formulation, especially in light of the other formulations discussed in this section, is now presented. Beam formulations based on the $SE(3)$ group circumvent issues associated with parametrisation of rotations by coupling the rotations and positions under a single group element and adopting a local frame approach [208]. The invariance of the strains under rigid body motion comes naturally from this formulation, as the local frame formulation allows the relative description of the nodal motions and velocities. Additionally, the local frame derivatives are at most quadratically nonlinear, which reduces the overall complexity of the numerical model. The global parametrisation of frames is avoided by the time integration method, which yields an efficient integration scheme that is guaranteed to be singularity-free [209]. Moreover, shear locking is avoided thanks to a nonlinear interpolation formula based on the exponential map that couples the rotation and position fields and governs the nonlinear configuration space. The geometrically exact formulation leads to the recovery of the exact displacements with no approximations in the curvature of the solution for pure bending [208]. The main benefits of the $SE(3)$ formulation are therefore numerical, leading to solutions which are more accurate with higher convergence rates, as demonstrated in Chapter 4. Aside from the numerical advantages, on a modelling level the $SE(3)$ formulation benefits from a correct and mathematically consistent kinematic description of rigid body motion, while fundamentally being subject to the assumptions of beam theory, much like other geometrically exact beam formulations which maintain objectivity. A discussion on the underlying PDEs of the $SE(3)$ beam prior to finite element discretisation, and the main differences compared to differential equations from other beam formulations, is given in Chapter 3.

The $SE(3)$ Lie group, owing to its consistent description of 3D rigid body motion, can also be leveraged in other beam formulations. For instance, Ma et al. [134] used the $SE(3)$ group to formulate the rigid body motion of their corotational beam formulation. A further example of other more recent beam models that leverage and build on the $SE(3)$ formulation include the total Lagrangian formulations with Petrov-Galerkin projection by Harsch et al. [94]. They show that, unlike the $SE(3)$ model, their beam formulation does not require involved expressions of the $SE(3)$ tangent operator and its derivative in the formulation. They further demonstrate

that the Petrov-Galerkin projection results in equations of motion that can be solved using standard numerical schemes without the need for specialised Lie group solvers.

2.4 3D Finite Element Beam Model with von Kármán Strains

In this section, we present the finite element equation of motion for a geometrically nonlinear beam using von Kármán strains. Formulations based on von Kármán strains have been widely adopted in the nonlinear dynamics community as a model for geometrically nonlinear structures, including beams, plates, and shells. Despite its popularity due to its simplicity, the von Kármán model offers only a limited and approximate description of the nonlinearities, being applicable primarily to beam deformations with small to moderate displacements and rotations. Due to its extensive use in the literature, we have chosen the von Kármán model for comparison with the Special Euclidean beam formulation, as provided in Chapter 4.

Notable examples in the literature on the use of the von Kármán formulation include the work by Thomas et al. [226], Apiwattanalunggarn et al. [6] and Jiang et al. [109] for modelling of nonlinear vibrations and NNMs of rotating cantilever beams. Bilbao et al. [30], Amabili [5], and Thomas and Bilbao [225] used the von Kármán formulation to model thin plates and shells vibrating at large amplitudes. Neukirch et al. [151] used the von Kármán model for modelling post-buckling vibrations of elastic beams. Raze et al. [176] used a von Kármán beam in tracking amplitude extrema of nonlinear frequency responses using the harmonic balance method. Many model reduction methods in the literature also consider the von Kármán formulation as the full-order basis for model reduction. Jain et al. [105] applied slow-fast decomposition and SSM reduction, to a von Kármán beam with geometric nonlinearities and viscoelastic damping. Li et al. [128] recently applied SSM to extract forced response curves in normal form coordinates for the reduced system, on beams with internal resonances. Jain et al. [106] described the use of a quadratic manifold based on modal derivatives for the model order reduction of plates with von Kármán kinematics. Most recently, Jain and Haller [104] developed methods for computing invariant manifolds and their reduced dynamics in very high-dimensional nonlinear systems, including a von Kármán beam. Other works on model order reduction of nonlinear beams based on the von Kármán model include that of Wu and Tiso [246], Givois et al. [86], and Vizzaccaro et al. [236]. Further contributions on model order reduction methods for geometrically nonlinear structures, including those modelled with the von Kármán formulation, are discussed in the recent review paper by Touzé et al. [229]. As previously mentioned, despite the extensive use of the von Kármán formulation, the model is predicated on approximate kinematics, which makes it unsuited for studying complex and highly nonlinear systems with large displacements. Therefore, reduced order models which are based on this formulation will suffer from the same inaccuracies of the full order model, and will not be able to adequately describe complex nonlinear dynamic phenomena of highly-flexible physical structures.

2.4.1 von Kármán Strains

Strain is a measure of a body's deformation under load. Linear strains are characterised by small deformations such that the body behaves linearly under loading; the sum of two infinitesimal deformation solutions is also a solution under their combined load. However, for larger deformations nonlinear terms will have to be included in the strain formulation. Green's strain expression is a second-order symmetric tensor with quadratic displacements. It is derived from computing the deformations at every point of the body with respect to a reference undeformed configuration, thus taking a Lagrangian point of view [79]. Physically, it is equal to the difference in the square of the lengths between two points on the body due to deformation. The strain tensor is given by the following formula, where Einstein's subscript notation is used, implying sums on repeated indices

$$\varepsilon_{ij} = \frac{1}{2}\left(\frac{\partial u_i}{\partial x_j} + \frac{\partial u_j}{\partial x_i} + \frac{\partial u_m}{\partial x_i}\frac{\partial u_m}{\partial x_j}\right) \tag{2.10}$$

The Cauchy or true stress tensor $\overline{\boldsymbol{\sigma}}$ of a body is the force in the deformed configuration that is measured per unit area of the deformed configuration. In other words, it is the current force per unit of deformed area [177]. The conjugate strain of the Cauchy stress tensor, that is, the strain increment whose product with the Cauchy stress tensor gives the strain energy per unit volume, is not widely used in large displacement structural analysis, since the shape of the body after deformation is not known a priori. Instead, the second Piola-Kirchhoff stress tensor $\boldsymbol{\sigma}$ and its associated conjugate strain tensor, which is the Green strain tensor introduced previously, are used. The second Piola-Kirchhoff stress tensor uses the transformed current force (pulled back to the reference configuration) per unit undeformed area. Note how this definition is in line with that of Green's strain tensor, where strains were also calculated with respect to the original undeformed configuration. The strain energy increment per unit volume is then given by [79]

$$\mathrm{d}W = \sigma_{ij}\ \mathrm{d}\varepsilon_{ij} \tag{2.11}$$

where the subscripts denote the components of the tensors. The strain energy density is thus defined by

$$W(\varepsilon_{ij}) = \int_0^{\varepsilon_{ij}} \sigma_{ij}\ \mathrm{d}\varepsilon_{ij} \tag{2.12}$$

The total strain energy is then computed as the volume integral of the strain energy density

$$V = \int_{V_0} W(\varepsilon_{ij})\ \mathrm{d}V \tag{2.13}$$

The strain energy, along with total kinetic energy, is used in Hamilton's principle to derive the equation of motion of a mechanical system. Using the equations above, the application of the variational operator on the strain energy can be written as follows.

$$\delta V = \int_{V_0} \frac{\partial W}{\partial \varepsilon_{ij}}\ \delta\varepsilon_{ij}\ \mathrm{d}V = \int_{V_0} \sigma_{ij}\ \delta\varepsilon_{ij}\ \mathrm{d}V \tag{2.14}$$

The expression for von Kármán strains arises from simplifying the Green strain measure by assuming that displacements and rotations are moderate, but the strains remain small. Strains derived using these assumptions are valid for slender bodies where (moderate) displacements do not cause large strains. Due to small strains, the linear constitutive law of stress and strain can be used. Starting from Green's strain equation in Eq. (2.10), the axial strain for a 3D beam can be written as

$$\varepsilon_{11} = \frac{\partial u_1}{\partial x_1} + \frac{1}{2}\left[\left(\frac{\partial u_1}{\partial x_1}\right)^2 + \left(\frac{\partial u_2}{\partial x_1}\right)^2 + \left(\frac{\partial u_3}{\partial x_1}\right)^2\right] \tag{2.15}$$

Assuming small axial component $(\partial u_1/\partial x_1)^2 \approx 0$, and retaining the quadratic terms, the von Kármán strain can be written as

$$\varepsilon_{11} = \frac{\partial u_1}{\partial x_1} + \frac{1}{2}\left[\left(\frac{\partial u_2}{\partial x_1}\right)^2 + \left(\frac{\partial u_3}{\partial x_1}\right)^2\right] \tag{2.16}$$

The quadratic terms in the above equations are the only source of nonlinearity in the von Kármán model. These so-called axial-bending or membrane-bending coupling terms [56] enable the von Kármán model to effectively model situations where bending displacements induce axial loads in the structure, such as beams with clamped boundary conditions. In these configurations, the rotations of the cross sections remain small to moderate; however, the boundary conditions result in axial strains under bending, which are adequately captured with the von Kármán model, allowing it to provide a reasonably accurate representation of the structural response under these specific conditions. In contrast, geometric nonlinearities arising from extremely large displacements and rotations of the cross section cannot be modelled accurately with the von Kármán model, as the truncation of the Green strain tensor omits higher-order terms that become significant under such conditions.

2.4.2 Finite Element Discretisation

The Finite Element (FE) discretisation of the von Kármán beam is now presented. The method is based on the FE formulation and developments by Géradin and Rixen [79]. More comprehensive reviews of the FE theory can be found in classical textbooks devoted to the subject (see Zienkiewicz & Taylor [250], Crisfield [33], Wriggers [244]).

The solution domain is first divided into a number of elements. Within each element, a finite number of interpolation functions are chosen as piecewise continuous polynomials, such that the generalised coordinates are equivalent to the local displacement values at the nodes of each element. Therefore, the solution in each element is approximated using the interpolation functions and based on their values at the nodes of the element. Boundary conditions are met as adjacent elements share mutual nodes. The displacements are expanded as a sum series of the products of the interpolation functions and the nodal displacements.

The interpolation functions, also known as the shape functions, need to satisfy the boundary conditions and be differentiable up to the order of the full continuous equations of motion when written in integral, or weak form. They are often written in terms of isoparametric coordinates,

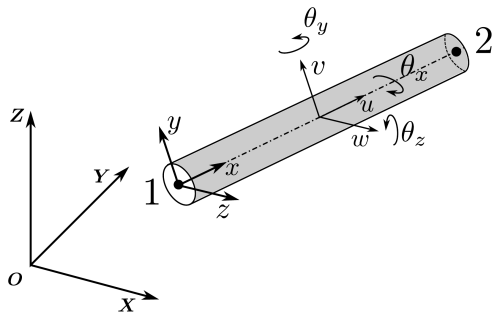


Figure 2.1: 3D beam element in global coordinate system

which are non-dimensionalised coordinates with respect to the length of each element. Hermite polynomials, which have the added benefit of being orthogonal, are often chosen for this purpose. For a beam under bending, the weak form of the equations includes second-order derivatives of the displacements. Therefore, to maintain differentiability, third-order Hermite polynomials are chosen as the shape functions such that the displacement boundary conditions at the nodes are satisfied. These functions are written for each element as

$$\mathbf{\Phi}_e^T(\xi) = \begin{bmatrix} 1 - 3\xi^2 + 2\xi^3 \\ l\xi(1-\xi)^2 \\ \xi^2(3-2\xi) \\ l\xi^2(\xi-1) \end{bmatrix} \tag{2.17}$$

where l is the element length, and $\xi \in [0, 1]$ is the isoparametric coordinate along the element, evaluated as

$$\xi = \frac{x - x_0}{l} \tag{2.18}$$

In the FE formulation that follows, the weak form of the equations are written for each element and the approximate displacements are substituted in the energy equations. The element mass and stiffness matrices are obtained from the kinetic and strain energy equations. The matrices from each element are then assembled into global matrices, which express the dynamic equilibrium of the entire system. This dynamic equation of motion is solved using the Newmark time integration method, and the nodal displacements are then obtained. Using the shape functions and the nodal displacement, the continuous displacement along each element can be computed.

Displacemets and Strain

Each node of the discretised beam has six degrees of freedom (3 axial and 3 rotational), which gives a total of 12 degrees of freedom for each element. A schematic of the beam element in the global coordinate system is shown in Figure 2.1 where the degrees of freedom of the beam can be seen. Euler beam assumptions of no shear stress and no planar deformation are imposed. The in-plane and out-plane rotation angles are equal to the derivative of the deflections in each direction. Finally, the beam is allowed to twist about its longitudinal axis under torque load,

but it is assumed that no warping takes place and that the rotary inertia of the beam is zero. With these assumptions, the displacement field can be written as

$$\begin{aligned} u_1 &= u(x) + z\theta_y - y\theta_z \\ u_2 &= v(x) \\ u_3 &= w(x) \\ u_4 &= \theta_x(x) \end{aligned} \tag{2.19}$$

where $\theta_y = -dw/dx$ and $\theta_z = du/dx$ indicate how the rotations are linearised and equal to the displacement derivatives. Substituting the displacement field into 2.16, the von Kármán axial strain can be written as

$$\begin{aligned} \varepsilon_{11} &= \frac{\partial u_1}{\partial x} + \frac{1}{2}\left(\frac{\partial u_2}{\partial x}\right)^2 + \frac{1}{2}\left(\frac{\partial u_3}{\partial x}\right)^2 + \frac{\partial u_4}{\partial x} \\ &= \frac{\mathrm{d}u}{\mathrm{d}x} - z\frac{\mathrm{d}^2 w}{\mathrm{d}x^2} - y\frac{\mathrm{d}^2 v}{\mathrm{d}x^2} + \frac{1}{2}\left(\frac{\mathrm{d}v}{\mathrm{d}x}\right)^2 + \frac{1}{2}\left(\frac{\mathrm{d}w}{\mathrm{d}x}\right)^2 + \frac{\mathrm{d}\theta_x}{\mathrm{d}x} \end{aligned} \tag{2.20}$$

which can be written in matrix form as

$$\varepsilon_{11} = \begin{Bmatrix} u_{1,1} + \frac{1}{2}u_{2,1}^2 + \frac{1}{2}u_{3,1}^2 \\ u_{2,11} \\ u_{3,11} \\ u_{4,1} \end{Bmatrix} \tag{2.21}$$

where $u_{i,1} = \mathrm{d}u_i/\,\mathrm{d}x$ and $u_{i,11} = \mathrm{d}^2(u_i)/\,\mathrm{d}x^2$. It is seen that the beam curvature is linearly related to the second derivative of the displacements, namely $u_{2,11} = \kappa_v$ and $u_{3,11} = \kappa_w$. Note that the coefficients $-y$ and $-z$ have been temporarily factored out of the strain equation and will be multiplied back in when evaluating the strain energy.

Finite Element Model

The FE model is formulated by choosing appropriate shape functions for approximating the displacements. The bending displacements are approximated using the Hermite polynomials introduced in Eq. (2.17), while the axial and twist displacements are approximated using a linear first order variation function. The displacement approximation equation for each element is written as

$$\boldsymbol{U}^e = \boldsymbol{\Phi}\boldsymbol{q}^e \tag{2.22}$$

where each term expanded is written as

$$\begin{aligned}
\boldsymbol{U}^e &= [u_1, u_2, u_3, u_4]^T \\
\boldsymbol{q}^e &= [u^1, v^1, w^1, \theta_x^1, \theta_y^1, \theta_z^1, u^2, v^2, w^2, \theta_x^2, \theta_y^2, \theta_z^2]^T \\
\boldsymbol{\Phi} &= \begin{bmatrix}
\phi_1 & 0 & 0 & 0 & 0 & 0 & \phi_2 & 0 & 0 & 0 & 0 & 0 \\
0 & \phi_3 & 0 & 0 & 0 & \phi_4 & 0 & \phi_5 & 0 & 0 & 0 & \phi_6 \\
0 & 0 & \phi_7 & 0 & -\phi_8 & 0 & 0 & 0 & \phi_9 & 0 & -\phi_{10} & 0 \\
0 & 0 & 0 & \phi_{11} & 0 & 0 & 0 & 0 & 0 & \phi_{12} & 0 & 0
\end{bmatrix}
\end{aligned} \tag{2.23}$$

where the shape functions, written in isoparametric terms, are

$$\begin{aligned}
\phi_1, \phi_{11} &= 1 - \xi & \phi_2, \phi_{12} &= \xi \\
\phi_3, \phi_7 &= 1 - 3\xi^2 + 2\xi^3 & \phi_5, \phi_9 &= \xi^2(3 - 2\xi) \\
\phi_4, \phi_8 &= l\xi(1 - \xi)^2 & \phi_6, \phi_{10} &= l\xi^2(\xi - 1)
\end{aligned}$$

and the superscripts 1 and 2 indicate the beginning and end nodes of each element, as shown in Figure 2.1. Substituting the displacement approximations into the strain equation in Eq. (2.21), and omitting the subscript $(\cdot)_{11}$ for clarity, we have

$$\varepsilon = \boldsymbol{B}_0 \boldsymbol{q}^e + \frac{1}{2}\boldsymbol{B}_1 \boldsymbol{q}^e + \frac{1}{2}\boldsymbol{B}_2 \boldsymbol{q}^e \tag{2.24}$$

where the matrices $\boldsymbol{B}_0$, $\boldsymbol{B}_1$, and $\boldsymbol{B}_2$ are defined as

$$\boldsymbol{B}_0 = \begin{bmatrix}
\phi_{1,1} & 0 & 0 & 0 & 0 & 0 & \phi_{2,1} & 0 & 0 & 0 & 0 & 0 \\
0 & \phi_{3,11} & 0 & 0 & 0 & \phi_{4,11} & 0 & \phi_{5,11} & 0 & 0 & 0 & \phi_{6,11} \\
0 & 0 & \phi_{7,11} & 0 & -\phi_{8,11} & 0 & 0 & 0 & \phi_{9,11} & 0 & -\phi_{10,11} & 0 \\
0 & 0 & 0 & \phi_{11,1} & 0 & 0 & 0 & 0 & 0 & \phi_{12,1} & 0 & 0
\end{bmatrix} \tag{2.25}$$

$$\boldsymbol{B}_1 = \boldsymbol{A}_1(\boldsymbol{u})\boldsymbol{G}_1 = \begin{bmatrix}
u_{2,1} & 0 & 0 & 0 \\
0 & 0 & 0 & 0 \\
0 & 0 & 0 & 0 \\
0 & 0 & 0 & 0
\end{bmatrix} \begin{bmatrix}
0 & \phi_{3,1} & 0 & 0 & 0 & \phi_{4,1} & 0 & \phi_{5,1} & 0 & 0 & 0 & \phi_{6,1} \\
0 & 0 & 0 & 0 & 0 & 0 & 0 & 0 & 0 & 0 & 0 & 0 \\
0 & 0 & 0 & 0 & 0 & 0 & 0 & 0 & 0 & 0 & 0 & 0 \\
0 & 0 & 0 & 0 & 0 & 0 & 0 & 0 & 0 & 0 & 0 & 0
\end{bmatrix} \tag{2.26}$$

$$\boldsymbol{B}_2 = \boldsymbol{A}_2(\boldsymbol{u})\boldsymbol{G}_2 = \begin{bmatrix}
u_{3,1} & 0 & 0 & 0 \\
0 & 0 & 0 & 0 \\
0 & 0 & 0 & 0 \\
0 & 0 & 0 & 0
\end{bmatrix} \begin{bmatrix}
0 & 0 & \phi_{7,1} & 0 & -\phi_{8,1} & 0 & 0 & 0 & \phi_{9,1} & 0 & -\phi_{10,1} & 0 \\
0 & 0 & 0 & 0 & 0 & 0 & 0 & 0 & 0 & 0 & 0 & 0 \\
0 & 0 & 0 & 0 & 0 & 0 & 0 & 0 & 0 & 0 & 0 & 0 \\
0 & 0 & 0 & 0 & 0 & 0 & 0 & 0 & 0 & 0 & 0 & 0
\end{bmatrix} \tag{2.27}$$

Finally, the increment of strain is evaluated as

$$\mathrm{d}\varepsilon = [\boldsymbol{B}_0 + \boldsymbol{B}_1 + \boldsymbol{B}_2]\,\mathrm{d}\boldsymbol{q}^e \tag{2.28}$$

Element Equation of Motion

As discussed previously, the material constitutive law can be taken as linear and equivalent to Hooke's law of elasticity. As such, the stress can be evaluated by multiplying the modulus of elasticity and the shear modulus by the strain terms. The equation of motion for each element can then be evaluated using Hamilton's principle. It is noted that, as the shape functions are written in isoparametric form, the chain rule is required when evaluating the equation of motion to transform the derivates and functions from x to ξ. This is done using the Jacobian, which using Eq. (2.18) can be written as

$$\begin{gathered} j_e = \frac{\mathrm{d}x}{\mathrm{d}\xi} = l \\ \frac{\mathrm{d}^n\phi_i}{\mathrm{d}x^n} = j_e^{-n}\frac{\mathrm{d}^n\phi_i}{\mathrm{d}\xi^n} \quad \& \quad \int_0^l \mathrm{d}x = \int_0^1 j_e \cdot \mathrm{d}\xi \end{gathered} \tag{2.29}$$

The integral equations are then evaluated from 0 to 1, and are computed numerically using Gauss-Legendre quadrature. The variation of strain energy is thus given by

$$\delta V = \int_V \boldsymbol{\sigma}\,\mathrm{d}\varepsilon\;\mathrm{d}V = \int_0^1\int_A \boldsymbol{\sigma}\,\mathrm{d}\varepsilon\;\mathrm{d}A\,j_e\cdot\mathrm{d}\xi = \int_0^1 \boldsymbol{D}\varepsilon\;\mathrm{d}\varepsilon\,j_e\cdot\mathrm{d}\xi \tag{2.30}$$

where

$$\boldsymbol{D} = \begin{bmatrix} EA & 0 & 0 & 0 \\ 0 & EI_{zz} & 0 & 0 \\ 0 & 0 & EI_{yy} & 0 \\ 0 & 0 & 0 & GJ \end{bmatrix}$$

is the rigidity matrix, and is found from the integration of the elasticity modulus with respect to area A, where the coefficients $-y$ and $-z$ factored out of Eq. (2.21) are re-introduced and integrated to give the second moment of area with respect to the z and y axes respectively.

The kinetic energy of the element can be written as

$$T = \frac{1}{2}\int_0^l m(\dot{u}^2 + \dot{v}^2 + \dot{w}^2) + mr_t^2\dot{\theta}_x^2\;\mathrm{d}x \tag{2.31}$$

where r_t is the radius of gyration about the longitudinal beam axis. The displacement approximations in Eq. (2.23) can be substituted into the kinetic energy equation and the terms can be gathered and written in matrix form. The variation of the kinetic energy can then be evaluated, which along with the variation of strain energy in Eq. (2.30) can be used in Hamilton's principle. After an integration by parts the full elemental equation of motion can be written as

$$\boldsymbol{M}^e\ddot{\boldsymbol{q}}^e + \boldsymbol{C}^e\dot{\boldsymbol{q}}^e + \boldsymbol{K}^e(\boldsymbol{q}^e)\boldsymbol{q}^e = \boldsymbol{P}^e(t) \tag{2.32}$$

where

$$\begin{aligned}
\boldsymbol{M}^e &= \int_0^1 \boldsymbol{\Phi}_{(1:3,:)}^T m \boldsymbol{\Phi}_{(1:3,:)}\, j_e \cdot \mathrm{d}\xi + \int_0^1 \boldsymbol{\Phi}_{(4,:)}^T m r^2 \boldsymbol{\Phi}_{(4,:)}\, j_e \cdot \mathrm{d}\xi \\
\boldsymbol{C}^e &= \alpha \boldsymbol{M}^e + \beta \boldsymbol{K}^e \\
\boldsymbol{K}^e(\boldsymbol{q}^e)\boldsymbol{q}^e &= \int_0^1 \boldsymbol{\sigma}\, \mathrm{d}\varepsilon\, j_e \cdot \mathrm{d}\xi = \left[\boldsymbol{K}_0^e + \boldsymbol{K}_1^e + \boldsymbol{K}_2^e\right] \boldsymbol{q}^e \\
\boldsymbol{P}^e(t) &= \int_0^1 \boldsymbol{\Phi}^T \boldsymbol{F}(x,t)\, j_e \cdot \mathrm{d}\xi
\end{aligned}$$

where $\boldsymbol{M}^e$ is the element mass matrix, $\boldsymbol{C}^e$ is the element damping matrix, which is taken to be proportional to the mass and stiffness matrices, $\boldsymbol{K}^e$ is the element stiffness matrix, and $\boldsymbol{P}^e$ is the applied external force. The element stiffness matrix is comprised of a linear part $\boldsymbol{K}_0^e$ which is fixed, and nonlinear parts $\boldsymbol{K}_1^e$ and $\boldsymbol{K}_2^e$ which are displacement-dependent and change with the degree of deformation. The terms of the stiffness matrix are written as

$$\begin{cases}
\boldsymbol{K}_0^e = \displaystyle\int_0^1 \boldsymbol{B}_0^T D \boldsymbol{B}_0\, j_e \cdot \mathrm{d}\xi \\
\boldsymbol{K}_1^e = \displaystyle\int_0^1 \left[\frac{1}{2}\boldsymbol{B}_0^T D \boldsymbol{B}_1 + \frac{1}{2}\boldsymbol{B}_0^T D \boldsymbol{B}_2 + \boldsymbol{B}_1^T D \boldsymbol{B}_0 + \boldsymbol{B}_2^T D \boldsymbol{B}_0\right] j_e \cdot \mathrm{d}\xi \\
\boldsymbol{K}_2^e = \dfrac{1}{2}\displaystyle\int_0^1 \left[\boldsymbol{B}_1^T D \boldsymbol{B}_1 + \boldsymbol{B}_1^T D \boldsymbol{B}_2 + \boldsymbol{B}_2^T D \boldsymbol{B}_1 + \boldsymbol{B}_2^T D \boldsymbol{B}_2\right] j_e \cdot \mathrm{d}\xi
\end{cases} \tag{2.33}$$

It is noted that the mass matrix remains constant as the beam deforms. Therefore, changes in inertia due to the change in the beam shape are not accounted for, and the nonlinearity related to inertia effects are ignored.

Coordinate Transformation

The element matrices need to be expressed in terms of the global coordinate system before they can be assembled to derive the full system matrices. As the beam orientation in 3D space can be arbitrary, these matrices therefore need to be transformed from their local coordinate system to the global coordinate system. The coordinate axes in the element's local frame are defined by $[\vec{e}_x, \vec{e}_y, \vec{e}_z]$ while the global reference frame is defined as $[\vec{e}_X, \vec{e}_Y, \vec{e}_Z]$. The local axes are defined a priori, where $\vec{e}_x$ lies along the length of the element, and forms an orthogonal set with $\vec{e}_y$ and $\vec{e}_z$, as seen in Figure 2.1. The rotation operator $\boldsymbol{R}_e$ describes the transformation between the frames, and is constructed from the dot product of the base vectors [79]

$$\begin{aligned}
\begin{bmatrix} x_i \\ y_i \\ z_i \end{bmatrix} &= \boldsymbol{R}^e \begin{bmatrix} X_i \\ Y_i \\ Z_i \end{bmatrix} \\
\boldsymbol{R}^e &= \begin{bmatrix}
\vec{e}_X \cdot \vec{e}_x & \vec{e}_Y \cdot \vec{e}_x & \vec{e}_Z \cdot \vec{e}_x \\
\vec{e}_X \cdot \vec{e}_y & \vec{e}_Y \cdot \vec{e}_y & \vec{e}_Z \cdot \vec{e}_y \\
\vec{e}_X \cdot \vec{e}_z & \vec{e}_Y \cdot \vec{e}_z & \vec{e}_Z \cdot \vec{e}_z
\end{bmatrix}
\end{aligned} \tag{2.34}$$

The transformation between the frames can be expressed for the element's 12 structural degrees of freedom using the following transformation matrix

$$\boldsymbol{T}^e = \begin{bmatrix} \boldsymbol{R}^e & 0 & 0 & 0 \\ 0 & \boldsymbol{R}^e & 0 & 0 \\ 0 & 0 & \boldsymbol{R}^e & 0 \\ 0 & 0 & 0 & \boldsymbol{R}^e \end{bmatrix} \tag{2.35}$$

and the stiffness and mass matrices can therefore be expressed in the global coordinate system as

$$\boldsymbol{K}_G^e = \boldsymbol{T}^{eT}\boldsymbol{K}^e\boldsymbol{T}^e \qquad \boldsymbol{M}_G^e = \boldsymbol{T}^{eT}\boldsymbol{M}^e\boldsymbol{T}^e \tag{2.36}$$

2.4.3 Numerical Time Integration: Newmark Method

The finite element method enables the nonlinear equation of motion of the system to be written in terms of a residual vector in the following standard discretised form

$$\boldsymbol{r}(\boldsymbol{q}) = \boldsymbol{M}\ddot{\boldsymbol{q}} + f_{nl}(\boldsymbol{q}, \dot{\boldsymbol{q}}) - \boldsymbol{p}(\boldsymbol{q}, t) = \boldsymbol{0} \tag{2.37}$$

where f_{nl} is the function which includes the system nonlinearities. This equation can be solved using time integration techniques to reveal the dynamic response of the system under external excitations. A highly popular method in the field of structural dynamics for this purpose is the Newmark method [79]. The Newmark equations are evaluated by a Taylor series expansion of the system velocity and displacements from a known solution to a solution at the next time step, ignoring terms higher than the system acceleration. Assuming linear variation of acceleration across each time step, and using numerical quadrature to evaluate the integrals, the Newmark equations can be written as the following implicit second order system

$$\begin{aligned} \dot{\boldsymbol{q}}_{n+1} &= \dot{\boldsymbol{q}}_n + (1-\gamma)h\ddot{\boldsymbol{q}}_n + \gamma h\ddot{\boldsymbol{q}}_{n+1} \\ \boldsymbol{q}_{n+1} &= \boldsymbol{q}_n + h\dot{\boldsymbol{q}}_n + h^2\left(\frac{1}{2} - \beta\right)\ddot{\boldsymbol{q}}_n + h^2\beta\ddot{\boldsymbol{q}}_{n+1} \end{aligned} \tag{2.38}$$

where h is the time step and γ and β are the quadrature parameters. The Newmark equation is substituted into Eq. (2.37) and the residual is expressed in terms of $\boldsymbol{q}_{n+1}$. The Newton-Raphson procedure is then implemented to iteratively solve the residual equation. The residual is expanded using Taylor series where only the linear term is retained

$$\boldsymbol{r}(\boldsymbol{q}_{n+1}^{k+1}) = \boldsymbol{r}(\boldsymbol{q}_{n+1}^{k}) + \boldsymbol{S}_T(\boldsymbol{q}_{n+1}^{k})(\boldsymbol{q}_{n+1}^{k+1} - \boldsymbol{q}_{n+1}^{k}) \tag{2.39}$$

where $\boldsymbol{S}_T$ is the system Jacobian matrix, and is written as

$$\begin{aligned}\boldsymbol{S}_T(\boldsymbol{q}) &= \left(\frac{\partial \boldsymbol{r}}{\partial \boldsymbol{q}}\right) \\ &= \frac{\partial f_{nl}}{\partial \boldsymbol{q}} + \frac{\partial f_{nl}}{\partial \dot{\boldsymbol{q}}}\frac{\partial \dot{\boldsymbol{q}}}{\partial \boldsymbol{q}} + \boldsymbol{M}\frac{\partial \ddot{\boldsymbol{q}}}{\partial \boldsymbol{q}} - \frac{\partial \boldsymbol{p}}{\partial \boldsymbol{q}} \\ &= \boldsymbol{K}_T + \boldsymbol{C}_T\frac{\gamma}{\beta h} + \boldsymbol{M}\frac{1}{\beta h^2}\end{aligned} \tag{2.40}$$

where the Newmark relationships are exploited to evaluate the time derivatives of the displacements $\boldsymbol{q}$. In the final expression of the Jacobian, $\boldsymbol{K}_T$ and $\boldsymbol{C}_T$ denote the tangent stiffness and damping matrices, respectively. The derivative of the force term is also omitted as it is unsymmetrical and does not affect the solution convergence. The Jacobian is inverted and Eq. (2.39) is used to evaluate the displacement corrections $\boldsymbol{\Delta q}$, which are used to find corrections to the velocity and acceleration. The Newton-Raphson iteration is continued until the residual falls below a desired error tolerance, and the final corrections to the velocity and acceleration are found, after which the Newmark time step is advanced, and a new Newton-Raphson iteration is started at the new time step. This process is continued until the time history of the system displacement, velocity, and acceleration is obtained.

Tangent Matrix

As pointed out in Section 2.4.3, the tangent stiffness and damping matrices are required to solve the dynamic equation of motion using Newmark's time integration scheme. Rewriting Eq. (2.32) in the same format as Eq. (2.37), the nonlinear forces can be written as

$$f_{nl} = \boldsymbol{C}^e\dot{\boldsymbol{q}}^e + \boldsymbol{K}^e(\boldsymbol{q}^e)\boldsymbol{q}^e \tag{2.41}$$

From the jacobian in Eq. (2.40), the element tangent stiffness and damping matrices can therefore be written as

$$\begin{aligned}\boldsymbol{K}_T &= \frac{\partial f_{nl}}{\partial \boldsymbol{q}} = \frac{\partial(\boldsymbol{K}^e(\boldsymbol{q}^e)\boldsymbol{q}^e)}{\partial \boldsymbol{q}^e} \\ \boldsymbol{C}_T &= \frac{\partial f_{nl}}{\partial \dot{\boldsymbol{q}}} = \frac{\partial(\boldsymbol{C}^e\dot{\boldsymbol{q}}^e)}{\partial \dot{\boldsymbol{q}}^e}\end{aligned} \tag{2.42}$$

The evaluation of the tangent damping matrix is straightforward since the damping is proportional to the mass and linear stiffness matrices and is therefore assumed to be fixed. We therefore have

$$\boldsymbol{C}_T = \boldsymbol{C}^e \tag{2.43}$$

The evaluation of the tangent stiffness matrix is done by differentiating the integral expression of stiffness with respect to the displacement vector, as follows

$$\begin{aligned}\boldsymbol{K}_T &= \int_V \frac{\partial\left(\left[\boldsymbol{B}_0+\boldsymbol{B}_1+\boldsymbol{B}_2\right]^T\boldsymbol{\sigma}\right)}{\partial \boldsymbol{q}^e}\,\mathrm{d}V \\ &= \int_V \frac{\partial\left[\boldsymbol{B}_0+\boldsymbol{B}_1+\boldsymbol{B}_2\right]^T}{\partial \boldsymbol{q}^e}\boldsymbol{\sigma}\,\mathrm{d}V + \int_V \left[\boldsymbol{B}_0+\boldsymbol{B}_1+\boldsymbol{B}_2\right]^T\frac{\partial\boldsymbol{\sigma}}{\partial\boldsymbol{q}^e}\,\mathrm{d}V\end{aligned} \tag{2.44}$$

where we have used

$$\delta V = \int_V \boldsymbol{\sigma}\,\mathrm{d}\varepsilon\,\mathrm{d}V = \boldsymbol{K}^e(\boldsymbol{q}^e)\boldsymbol{q}^e \tag{2.45}$$

Each term of the equation above is evaluated separately as

$$\int_V \left[\boldsymbol{B}_0+\boldsymbol{B}_1+\boldsymbol{B}_2\right]^T\frac{\partial\boldsymbol{\sigma}}{\partial\boldsymbol{q}^e}\,\mathrm{d}V = \int_V \left[\boldsymbol{B}_0+\boldsymbol{B}_1+\boldsymbol{B}_2\right]^T\boldsymbol{D}\left[\boldsymbol{B}_0+\boldsymbol{B}_1+\boldsymbol{B}_2\right]\mathrm{d}V \tag{2.46}$$

$$\begin{aligned}\int_V \frac{\partial\left[\boldsymbol{B}_0+\boldsymbol{B}_1+\boldsymbol{B}_2\right]^T}{\partial\boldsymbol{q}^e}\boldsymbol{\sigma}\,\mathrm{d}V &= \int_V\left(\frac{\partial\boldsymbol{B}_1^T}{\partial\boldsymbol{A}_1}\cdot\frac{\partial\boldsymbol{A}_1}{\partial u_{2,1}}\boldsymbol{\sigma}\cdot\frac{\partial u_{2,1}}{\partial\boldsymbol{q}^e}+\frac{\partial\boldsymbol{B}_2^T}{\partial\boldsymbol{A}_2}\cdot\frac{\partial\boldsymbol{A}_2}{\partial u_{3,1}}\boldsymbol{\sigma}\cdot\frac{\partial u_{3,1}}{\partial\boldsymbol{q}^e}\right)\mathrm{d}V \\ &= \int_V\left(\boldsymbol{G}_1^T\begin{bmatrix}1&0&0&0\\0&0&0&0\\0&0&0&0\\0&0&0&0\end{bmatrix}\boldsymbol{\sigma}\boldsymbol{G}_1+\boldsymbol{G}_2^T\begin{bmatrix}1&0&0&0\\0&0&0&0\\0&0&0&0\\0&0&0&0\end{bmatrix}\boldsymbol{\sigma}\boldsymbol{G}_2\right)\mathrm{d}V\end{aligned} \tag{2.47}$$

where the stress term can be written as

$$\begin{aligned}\begin{bmatrix}1&0&0&0\\0&0&0&0\\0&0&0&0\\0&0&0&0\end{bmatrix}\boldsymbol{\sigma} &= \begin{bmatrix}1&0&0&0\\0&0&0&0\\0&0&0&0\\0&0&0&0\end{bmatrix}\begin{bmatrix}EA&0&0&0\\0&EI_{zz}&0&0\\0&0&EI_{yy}&0\\0&0&0&GJ\end{bmatrix}\varepsilon \\ &= \begin{bmatrix}EA&0&0&0\\0&0&0&0\\0&0&0&0\\0&0&0&0\end{bmatrix}\begin{Bmatrix}u_{1,1}+\frac{1}{2}u_{2,1}^2+\frac{1}{2}u_{3,1}^2\\u_{2,11}\\u_{3,11}\\u_{4,1}\end{Bmatrix} = \begin{bmatrix}EA(u_{1,1}+\frac{1}{2}u_{2,1}^2+\frac{1}{2}u_{3,1}^2)&0&0&0\\0&0&0&0\\0&0&0&0\\0&0&0&0\end{bmatrix}\end{aligned} \tag{2.48}$$

The derivative of the displacement terms in Eq. (2.48) above are evaluated at the midpoint of each element for increased accuracy [177], and are found at every time step using the derivative of the shape function approximations to the displacements.

After evaluating the elemental stiffness, mass, and tangent matrices for each element, they are each transformed to the global coordinate system and are finally assembled to give the full system matrices in the equation of motion, which is then solved using Newmark's method to obtain the dynamic response of the beam to external excitations.

2.5 Conclusion

In this chapter, the fundamental theory of nonlinear normal modes and their properties was presented and discussed. A comprehensive review of the existing literature on NNMs was conducted, emphasising their significance in the analysis of nonlinear dynamics. The shooting and pseudo-arclength continuation methods for the computation of NNMs were presented, with a detailed discussion of their theoretical underpinnings. Additionally, the literature on geometrically exact beam formulations was reviewed, and various methods of modelling geometric nonlinearity were discussed. Finally, the three-dimensional finite element formulation of a beam incorporating von Kármán strains and solved using the Newmark time integration method was developed and presented.

As discussed in this chapter, the von Kármán model does not offer an accurate kinematic description of geometrically nonlinear beams and is not suitable for modelling structures with large displacements and rotations. Despite this, it is still a commonly used formulation in the modelling of beams and plates, and furthermore in constructing reduced order models of such structures. The more accurate nonlinear beam model based on the Special Euclidean group $SE(3)$ is formally introduced in Chapter 3, and a comparison between the $SE(3)$ formulation and the von Kármán formulation is presented in Chapter 4.

Chapter 3

Lie Groups

Abstract

This chapter presents a pedagogical introduction to the theory of Lie groups, specifically tailored for engineers and structural dynamicists. The objective is to present the theory in a clear and accessible manner, aiming to minimise the level of abstraction typically encountered in the literature. In doing so, we address the challenges often faced when encountering this topic for the first time, using examples aiming to overcome the initial barrier to entry into the theory of Lie groups.

Specifically, a two degree-of-freedom system is used to illustrate the formulation of the equation of motion of typical mechanical engineering systems using Lie group theory. This approach is intended to demystify the theory, providing a novel and accessible introduction that deliberately differs from traditional expositions of the subject. The structured presentation of the theory, combined with illustrative examples, and the detailed analysis of the two degree-of-freedom system, represents an original contribution of this chapter.

We then introduce the geometrically exact equations of motion for a three-dimensional beam model formulated on Lie groups. We highlight the advantages of this method over other geometrically exact formulations of beams introduced in Chapter 2.

3.1 Introduction to Lie Groups

The main theory of Lie groups is introduced in this section, and some of their principle mathematical properties are discussed. We will consider several key examples of Lie groups, including the group of rotations in three-dimensional space, namely the $SO(3)$ group, and the group of rigid body transformations in two-dimensional and three-dimensional space, namely the $SE(2)$ and the $SE(3)$ groups, respectively. We begin with a general introduction to Lie groups and will use the above groups as examples to illustrate the theory and offer a more practical overview of the topics.

3.1.1 Definition

A group $\mathcal{G}$ is a set with a composition operation $\circ$, and an identity element $\mathcal{E}$, with the following four basic properties [206]:

- Closure: $\forall \mathcal{X}_1, \mathcal{X}_2 \in \mathcal{G}, \quad \mathcal{X}_1 \circ \mathcal{X}_2 \in \mathcal{G}$
- Associativity: $\forall \mathcal{X}_1, \mathcal{X}_2, \mathcal{X}_3 \in \mathcal{G}, \quad \mathcal{X}_1 \circ (\mathcal{X}_2 \circ \mathcal{X}_3) = (\mathcal{X}_1 \circ \mathcal{X}_2) \circ \mathcal{X}_3$
- Identity: $\forall \mathcal{X} \in \mathcal{G}, \quad \mathcal{X} \circ \mathcal{E} = \mathcal{E} \circ \mathcal{X} = \mathcal{X}$
- Inverse: $\forall \mathcal{X} \in \mathcal{G}, \quad \mathcal{X} \circ \mathcal{X}^{-1} = \mathcal{X}^{-1} \circ \mathcal{X} = \mathcal{E}$

For groups whose members are matrices, namely, matrix groups, the composition operation is equivalent to the matrix product. It is noted that groups are generally not abelian[1], giving rise to the notion of left and right multiplication, since $\mathcal{X}_1\mathcal{X}_2$ and $\mathcal{X}_2\mathcal{X}_1$ are generally different. Lie groups, in addition to enjoying the properties above, are also differentiable manifolds, meaning that the composition and the inverse operations are smooth, and therefore a tangent space exists at every group element $\mathcal{X} \in G$, and is denoted by $T_{\mathcal{X}}\mathcal{G}$.

An example of a Lie group is the set of all three-dimensional rotation matrices. Rotation matrices fit the aforementioned axioms of a Lie group, and together with the operation of rotation concatenation (matrix multiplication), comprise the Special Orthogonal group of $\mathbb{R}^3$, denoted as $SO(3)$ [75]. The orthogonality of the group means that the transpose of a rotation matrix equals its inverse, while the term "special" means that the determinant of a rotation matrix equals one. The space of $SO(3)$ is defined as $SO(3) = \{\mathbf{R} \in \mathbb{R}^{3\times3} \mid \mathbf{R}^T\mathbf{R} = \mathbf{I}_3, \det(\mathbf{R}) = 1\}$ and constitutes a three-dimensional manifold in the Euclidean space $\mathbb{E}^3$ [75]. Additional concepts related to Lie groups will be introduced in the following sections, and examples will be drawn from the $SO(3)$ and $SE(3)$ groups, the latter being the group of rigid body motions, which will be formally defined in Section 3.3.

3.1.2 Group Action

Lie groups are capable of transforming elements of other sets, such as points and vectors, by means of their actions. Considering a matrix group $\mathcal{G}$ and a vector space V, the group acts

[1] An Abelian group is a commutative group, such that applying the group composition to two group elements does not depend on the order in which they are written. Examples include the group of integers under addition.

on this space by matrix multiplication [193]

$$a(\mathcal{G}, V): \quad \mathcal{G} \times V \mapsto V \;\; ; \;\; V \mapsto \mathcal{G}V \tag{3.1}$$

This implies that vector spaces can be transformed under the action of the group. An intuitive example would be the action of the $SO(3)$ group on vectors in $\mathbb{R}^3$, which transforms the vector by applying a rotation to it in 3D space. A group can also act on itself, by left or right multiplication of two group elements, giving another member of the group. Considering again the $SO(3)$ group, the multiplication of two rotation matrices results in a rotation matrix which belongs to the group.

3.1.3 Lie Algebra

An abstract notion of a Lie algebra can be defined as a finite-dimensional vector space $\mathfrak{g}$, together with a map $[\cdot, \cdot]$ from $\mathfrak{g} \times \mathfrak{g}$ into $\mathfrak{g}$, with the following properties [92]:

- $[\cdot, \cdot]$ is bilinear: $\forall X, Y, Z \in \mathfrak{g} \;\wedge\; a, b \in \mathbb{R}, \quad [aX + bY, Z] = a[X, Z] + b[Y, Z]$
- $[\cdot, \cdot]$ is skew-symmetric: $\forall X, Y \in \mathfrak{g}, \quad [X, Y] = -[Y, X]$
- The Jacobi identity holds: $\forall X, Y, Z \in \mathfrak{g}, \quad [[X, Y], Z] + [[Y, Z], X] + [[Z, X], Y] = 0$

This map is termed the Lie bracket, and for algebras associated with matrix Lie groups, it is given by:

$$[X, Y] = XY - YX \tag{3.2}$$

Geometrically, the Lie algebra is defined as the tangent space at the identity element $\mathcal{E}$ of the group ($\mathfrak{g} = T_{\mathcal{E}}\mathcal{G}$), and is a vector space whose elements can be identified[1] with vectors in $\mathbb{R}^m$, where m is the number of degrees of freedom of $\mathcal{G}$ [206]. This is illustrated in Figure 3.1. $\mathfrak{g}$ can be interpreted as a linearisation of $\mathcal{G}$ near $\mathcal{E}$, and the Lie bracket is a measure of the non-commutativity of the group operation [74]. A unique tangent space exists at each point on the group manifold, but they all have the same structure [206], such that vectors on different tangent spaces have the same dimension. The geometric significance of the tangent space at identity (the Lie algebra) is that we can move from this space to the tangent space at any other group element using the group composition [74] (see 3.1.4). Moreover, elements of the Lie algebra can be converted to the nonlinear group manifold by means of the exponential map [206], as discussed in the following sections.

As the Lie algebra is defined as a tangent space at the identity, the structure of the algebra for any group can be determined by differentiating the group constraint at the identity element [206]. Such algebra elements represent velocities, though other derivatives may also be taken for other physical quantities. For the $SO(3)$ group, the group constraint reads $\mathbf{R}^T\mathbf{R} = \mathbf{I}_3$. Taking the time derivative of this constraint gives

$$\mathbf{R}^T\dot{\mathbf{R}} + \dot{\mathbf{R}}^T\mathbf{R} = 0 \tag{3.3}$$

[1] We say the algebra is isomorphic to $\mathbb{R}^m$.

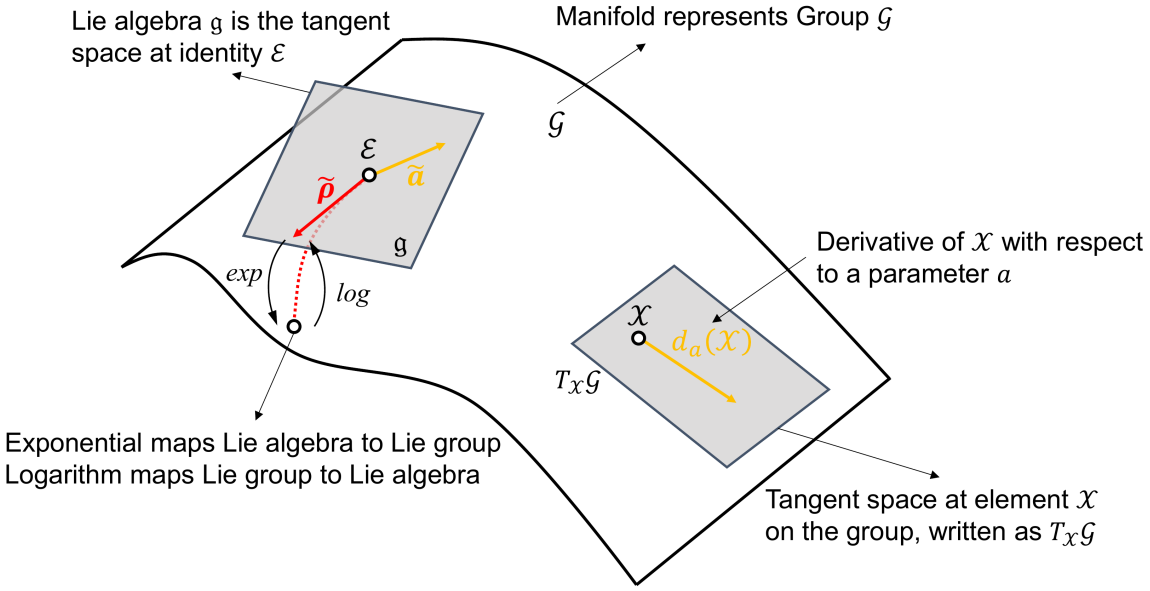


Figure 3.1: Illustration of a Lie group and its Lie algebra. $d_a(\mathcal{X}) \in T_{\mathcal{X}}\mathcal{G}$. Note that, using Eq. (3.33), we can write $d_a(\mathcal{X}) = \mathcal{X}\tilde{\mathbf{a}}$, where $\tilde{\mathbf{a}} \in \mathfrak{g}$. The geometric insight is that derivative vectors in other tangent spaces can be represented using vectors in the Lie algebra.

which can be rearranged as

$$\mathbf{R}^T\dot{\mathbf{R}} = -(\mathbf{R}^T\dot{\mathbf{R}})^T \tag{3.4}$$

which reveals that $\mathbf{R}^T\dot{\mathbf{R}}$ is a skew-symmetric matrix. We can express this skew-symmetric matrix as $[\boldsymbol{\omega}]_\times$ indicating rotational velocities, which takes the following form

$$[\boldsymbol{\omega}]_\times = \begin{bmatrix} 0 & -\omega_z & \omega_y \\ \omega_z & 0 & -\omega_x \\ -\omega_y & \omega_x & 0 \end{bmatrix}. \tag{3.5}$$

Therefore, Eq. (3.4) can now be written as

$$\mathbf{R}^T\dot{\mathbf{R}} = [\boldsymbol{\omega}]_\times \tag{3.6}$$

It is now evident that, at the identity element of $SO(3)$ where $\mathbf{R} = \mathbf{I}_3$, we will have

$$\dot{\mathbf{R}} = [\boldsymbol{\omega}]_\times \tag{3.7}$$

Therefore, the tangent space at the identity, which is the Lie algebra, will be equivalent to the space of all 3-dimensional skew-symmetric matrices. Two important observations can be made at this point. First, the dimension of the tangent space matches the dimension of the group manifold, which in the case of $SO(3)$, is equal to 3. Secondly, as the Lie algebra is a vector space, it is isomorphic to $\mathbb{R}^m$, where m denotes the dimension of the manifold. For $SO(3)$, $[\boldsymbol{\omega}]_\times$ is isomorphic to $\mathbb{R}^3$, which means that $\boldsymbol{\omega}$ can be written as a 3×1 vector that can be linearly mapped into a skew-symmetric matrix, representing an element of the algebra $\mathfrak{so}(3)$.

We generally consider this linear invertible map, or isomorphism, as a map from $\mathbb{R}^m$ to $\mathfrak{g}$, and we denote it using $\widetilde{(\bullet)}$ as:

$$\widetilde{(\bullet)} : \mathbb{R}^m \mapsto \mathfrak{g},\ \boldsymbol{x} \mapsto \widetilde{\boldsymbol{x}} \tag{3.8}$$

for $\boldsymbol{x} \in \mathbb{R}^m$ [208], [209]. In the case of $SO(3)$ we therefore have $\widetilde{\boldsymbol{\omega}} = [\boldsymbol{\omega}]_\times$ for $\boldsymbol{\omega} \in \mathbb{R}^3$. We can also construct an inverse map, denoted using $(\bullet)^\vee$, as a map from $\mathfrak{g}$ to $\mathbb{R}^m$, as follows

$$(\bullet)^\vee : \mathfrak{g} \mapsto \mathbb{R}^m,\ \widetilde{\boldsymbol{x}}^\vee \mapsto \boldsymbol{x} \tag{3.9}$$

3.1.4 Left and Right Invariant Vector Fields

As seen in Eq. (3.3), the time derivative of the group constraint reveals the structure of the algebra and leads to the expression of the Lie algebra velocities. For multiplicative matrix groups, such as $SO(3)$, the group constraint takes both forms:

$$\mathcal{X}^{-1}\mathcal{X} = \mathcal{E} \tag{3.10a}$$
$$\mathcal{X}\mathcal{X}^{-1} = \mathcal{E} \tag{3.10b}$$

We have already used Eq. (3.10a) with the $SO(3)$ group to obtain Eq. (3.6). The concept of left and right invariant vector fields emerges from the time derivation of each of the constraint terms in Eq. (3.10), which will lead to velocities that are left-multiplied or right-multiplied by the group element.

Time differentiating each of the constraint terms in Eq. (3.10) gives [75]:

$$\mathcal{X}^{-1}\dot{\mathcal{X}} = \widetilde{\mathbf{v}}_L \tag{3.11a}$$
$$\dot{\mathcal{X}}\mathcal{X}^{-1} = \widetilde{\mathbf{v}}_R \tag{3.11b}$$

where velocities are indicated with $\mathbf{v}$ and the left and right invariance is denoted using the subscripts. Each equation can in turn be re-arranged to give the equation for the time derivative of the group element using both vector fields as:

$$\dot{\mathcal{X}} = \mathcal{X}\widetilde{\mathbf{v}}_L \tag{3.12a}$$
$$\dot{\mathcal{X}} = \widetilde{\mathbf{v}}_R\mathcal{X} \tag{3.12b}$$

It is shown in subsequent sections that $\mathbf{v}_L$ corresponds to the velocities in the body frame, that is, the coordinate frame attached to the moving rigid body, and $\mathbf{v}_R$ corresponds to the velocities in the global frame, which is the inertial coordinate frame fixed in space. The left-invariant, local representation of the derivatives of the group gives rise to quantities that do not depend on the position or orientation of the body with respect to the fixed reference frame [209]. This invariance with respect to the fixed frame offers numerous computational benefits in deriving equations of motion of rigid bodies under the Lie group formulations, as discussed later. Many robotics authors also follow the same convention of using the left-invariant

derivatives to represent local quantities [206], motivated by the convention of transformation of local frames to global frames by left multiplication with a rotation matrix. The application of the left and right invariant vector fields in the $SO(3)$ group is further elaborated in Section 3.2.1.

Eq. (3.12) offers another geometric insight. It is clear that $\dot{\mathcal{X}}$ is a derivative of the group and therefore belongs to the tangent space at $\mathcal{X}$, (i.e., $\dot{\mathcal{X}} \in T_{\mathcal{X}}\mathcal{G}$). Furthermore, $\tilde{\mathbf{v}}$[1] belongs to the algebra, which is the tangent space at the identity element. Eq. (3.12) therefore shows that we can move from the tangent space at identity $\mathcal{E}$ to the tangent space at any other group element $\mathcal{X}$ by means of (left or right) multiplication with the group element.

3.1.5 Exponential and Logarithm Maps

The exponential map comes naturally from solving the differential equation in Eq. (3.12a). The analytic solution to this equation that passes through the identity element (i.e. initial conditions $\mathcal{X}(0) = \mathcal{E}$) is given by

$$\mathcal{X}(t) = \exp(\tilde{\mathbf{v}}_L t) \tag{3.13}$$

for all time values $t \in \mathbb{R}$. It is obvious per the definition that $\mathcal{X}(t)$ is a Lie group element, which implies that $\exp(\tilde{\mathbf{v}}_L t)$ must also be in the group. Noting that $\tilde{\mathbf{v}}_L t$ belongs to the algebra $\mathfrak{g}$, we can generalise the definition of the exponential by defining the increment [206] $\boldsymbol{\tau} = \mathbf{v}_L t \in \mathbb{R}^m$ such that we have $\tilde{\boldsymbol{\tau}} \in \mathfrak{g}$, and thus we can define the exponential map as

$$\exp: \quad \mathfrak{g} \mapsto \mathcal{G} \;\; ; \;\; \tilde{\boldsymbol{\tau}} \mapsto \mathcal{X} = \exp(\tilde{\boldsymbol{\tau}}) \tag{3.14}$$

The exponential therefore gives a mapping from the Lie algebra to the group. It allows the parametrisation of the Lie group elements using vector in the Lie algebra. The exponential is a surjective mapping for matrix Lie groups, and it is bijective near the identity. That is, there is a neighbourhood of 0 in the Lie algebra that maps bijectively to a neighbourhood of the identity in the group [193]. Therefore, an inverse mapping exists in the neighbourhood of the identity in the group, which maps back to the algebra. This map is commonly referred to as the logarithm map [206], and can be defined as

$$\log: \quad \mathcal{G} \mapsto \mathfrak{g} \;\; ; \;\; \mathcal{X} \mapsto \tilde{\boldsymbol{\tau}} = \log(\mathcal{X}) \tag{3.15}$$

The exponential map provides a means for defining the Lie algebra in a more methodical way as follows:

Definition: For a matrix Lie group $\mathcal{G}$, the Lie algebra of $\mathcal{G}$, denoted $\mathfrak{g}$, is the set of all matrices $\tilde{\boldsymbol{\tau}}$ such that $\exp(t\tilde{\boldsymbol{\tau}})$ is in $\mathcal{G}$ for all real numbers t [92].

It should be noted that from the above definition it naturally follows that if $\exp(\tilde{\boldsymbol{\tau}}) \in \mathcal{G}$, then we must have $\tilde{\boldsymbol{\tau}} \in \mathfrak{g}$.

Closed-form expressions of the exponential and logarithm maps can be derived for Lie groups of interest using the power series formulas for exp and log below, and using simplified expressions

[1] General velocity term, ignoring the left and right subscripts.

of successive powers of $\tilde{\boldsymbol{\tau}}$ and $\mathcal{X}$. These expressions are given in subsequent sections.

$$\exp(\tilde{\boldsymbol{\tau}}) = \sum_{p\geq 0} \frac{\tilde{\boldsymbol{\tau}}^p}{p!} \tag{3.16}$$

$$\log(\mathcal{X}) = \sum_{p\geq 1} \frac{(\mathcal{E}-\mathcal{X})^p}{p} \tag{3.17}$$

The exponential map has some key properties, which can be proved using the series expansion formulas. One property worth mentioning is the following [206]

$$\exp(\mathcal{X}\tilde{\boldsymbol{\tau}}\mathcal{X}^{-1}) = \mathcal{X}\exp(\tilde{\boldsymbol{\tau}})\mathcal{X}^{-1} \quad \forall \mathcal{X}\in\mathcal{G} \text{ and } \tilde{\boldsymbol{\tau}}\in\mathfrak{g} \tag{3.18}$$

It is generally possible to write any $\mathcal{X}\in\mathcal{G}$ as the composition of another group element $\mathcal{Y}\in\mathcal{G}$ with the exponential of an increment of the algebra $\mathfrak{g}$. Owing to the non-commutativity of the group, this can be done in two ways, by applying the group composition on the left or right hand side of the exponential as the following two forms

$$\mathcal{X} = \mathcal{Y}\circ\exp(\tilde{\boldsymbol{\sigma}}) \tag{3.19a}$$

$$\mathcal{X} = \exp(\tilde{\boldsymbol{\rho}})\circ\mathcal{Y} \tag{3.19b}$$

where both $\boldsymbol{\sigma}$ and $\boldsymbol{\rho}$ are vectors in the Lie algebra, and $\boldsymbol{\sigma}\neq\boldsymbol{\rho}$. The geometric interpretation of the above equations is illustrated in Figure 3.2. Two possible paths may be taken from the group identity $\mathcal{E}$ to $\mathcal{X}$. Either by composition of $\mathcal{Y}$ with an increment vector $\boldsymbol{\sigma}$ in the local tangent space at $\mathcal{Y}$ as in Eq. (3.19a), or by composition of an increment vector $\boldsymbol{\rho}$ at the tangent space at identity with $\mathcal{Y}$ as in Eq. (3.19b). As the structure of the tangent space is identical at each point on the group, the exponential can map both $\boldsymbol{\sigma}$ and $\boldsymbol{\rho}$ to the group, though they represent tangent vectors at two different points on the group. As $\boldsymbol{\sigma}$ is expressed locally at $\mathcal{Y}$, we say it represents a local increment vector, while $\boldsymbol{\rho}$ is thus a global increment vector as it is expressed at the identity (origin). It is noted that this is consistent with the left and right invariant velocities introduced in section 3.1.4, which respectively represent a local and global description of velocities. The vectors $\boldsymbol{\sigma}$ and $\boldsymbol{\rho}$ are related by the Adjoint transformation, as explained in the following section.

3.1.6 Adjoint Representation

Given a Lie group $\mathcal{G}$, for every $\mathcal{X}\in\mathcal{G}$ we can define a left translation as the map $L_{\mathcal{X}}:\mathcal{G}\mapsto\mathcal{G}$ such that $L_{\mathcal{X}}(\mathcal{Y}) = \mathcal{X}\mathcal{Y}$ for all $\mathcal{Y}\in\mathcal{G}$, and a right translation as the map $R_{\mathcal{X}}:\mathcal{G}\mapsto\mathcal{G}$ such that $R_{\mathcal{X}}(\mathcal{Y}) = \mathcal{Y}\mathcal{X}$ for all $\mathcal{Y}\in\mathcal{G}$ [74]. We can then define a conjugation as the following map from $\mathcal{G}$ to $\mathcal{G}$

$$h_{\mathcal{X}}(\mathcal{Y}): \quad \mathcal{G}\mapsto\mathcal{G} \;\; ; \;\; h_{\mathcal{X}}(\mathcal{Y}) = R_{\mathcal{X}^{-1}}L_{\mathcal{X}}(\mathcal{Y}) = \mathcal{X}\mathcal{Y}\mathcal{X}^{-1} \tag{3.20}$$

The conjugation operation reflects the departure of the group $\mathcal{G}$ from commutativity, as it can be shown that for an abelian group that commutes, one has $h_{\mathcal{X}}(\mathcal{Y}) = \mathcal{Y}$ for all $\mathcal{X},\mathcal{Y}\in\mathcal{G}$ [217].

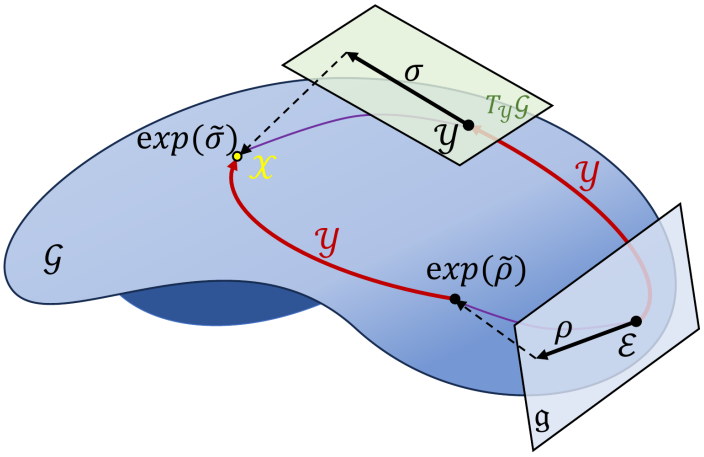


Figure 3.2: Composition with the exponential map on a Lie group.

An equivalent notation can be written in the algebra, by writing $\mathcal{Y}$ as the exponential of some $\tilde{\boldsymbol{\tau}} \in \mathfrak{g}$, as follows

$$h_{\mathcal{X}}(\mathcal{Y}) = \mathcal{X} \exp(\tilde{\boldsymbol{\tau}}) \mathcal{X}^{-1} \tag{3.21}$$

Using the property of the exponential map in Eq. (3.18), this can be written as

$$h_{\mathcal{X}}(\mathcal{Y}) = \exp(\mathcal{X} \tilde{\boldsymbol{\tau}} \mathcal{X}^{-1}) \tag{3.22}$$

which leads to the definition of the Adjoint action as:

$$\mathrm{Ad}_{\mathcal{X}}(\tilde{\boldsymbol{\tau}}) : \quad \mathfrak{g} \mapsto \mathfrak{g} \;\; ; \;\; \mathrm{Ad}_{\mathcal{X}}(\tilde{\boldsymbol{\tau}}) = \mathcal{X} \tilde{\boldsymbol{\tau}} \mathcal{X}^{-1} \tag{3.23}$$

The Adjoint is therefore a map from the Lie algebra onto the Lie algebra. It can also be given in vector form, as

$$\mathrm{Ad}_{\mathcal{X}}(\boldsymbol{\tau}) : \quad \mathbb{R}^m \mapsto \mathbb{R}^m \;\; ; \;\; \mathrm{Ad}_{\mathcal{X}}(\boldsymbol{\tau}) = \left(\mathcal{X} \tilde{\boldsymbol{\tau}} \mathcal{X}^{-1} \right)^{\vee} \tag{3.24}$$

Using the definition above, it can be shown that the tangent vectors $\boldsymbol{\sigma}$ and $\boldsymbol{\rho}$ in Eq. (3.19a) and Eq. (3.19b), depicted also in Figure 3.2, may be linearly related through the Adjoint as

$$\boldsymbol{\rho} = \mathrm{Ad}_{\mathcal{Y}}(\boldsymbol{\sigma}) \tag{3.25}$$

This provides a geometric interpretation of the action of the Adjoint, in that it transforms vectors from the tangent space at a group element to the tangent space at identity. A similar relationship can be written between the left and right invariant vector fields in Eq. (3.11), where the Adjoint maps the two velocity terms as

$$\mathbf{v}_R = \mathrm{Ad}_{\mathcal{X}}(\mathbf{v}_L) \tag{3.26}$$

The Adjoint can therefore be used to linearly map vectors expressed in the local frame at a group element, to those expressed in the global frame at the identity. Indeed, the left and right invariant velocities in Eq. (3.26) are representations in the local and global frames, respectively,

as discussed in Sections 3.2.1 and 3.3.1. The inverse transformation is also possible under the Adjoint, where tangent vectors in the algebra can be mapped onto the tangent space at a specific group element. In this sense, the Adjoint reveals how the group elements act upon the algebraic structure of $\mathfrak{g}$ (the tangent space at the identity, equipped with the Lie bracket). It is important to note that the mapping afforded by the Adjoint does not move vectors to a different vector space, as they are all embedded within the framework of the Lie algebra.

Example

An example involving the $SO(3)$ group is now given. We consider an element $\widetilde{\boldsymbol{\omega}} \in \mathfrak{so}(3)$ representing the instantaneous rotational velocity about the x axis as

$$\widetilde{\boldsymbol{\omega}} = \begin{bmatrix} 0 & 0 & 0 \\ 0 & 0 & -\omega \\ 0 & \omega & 0 \end{bmatrix} \in \mathfrak{so}(3) \tag{3.27}$$

We now consider a specific rotation in $SO(3)$ of 90 degrees about the z axis, given by g

$$g = \begin{bmatrix} 0 & -1 & 0 \\ 1 & 0 & 0 \\ 0 & 0 & 1 \end{bmatrix} \in SO(3) \tag{3.28}$$

The Adjoint action $\mathrm{Ad}_g(\widetilde{\boldsymbol{\omega}})$ then gives

$$\mathrm{Ad}_g(\widetilde{\boldsymbol{\omega}}) = g\widetilde{\boldsymbol{\omega}}g^T = \begin{bmatrix} 0 & 0 & \omega \\ 0 & 0 & 0 \\ -\omega & 0 & 0 \end{bmatrix} \in \mathfrak{so}(3) \tag{3.29}$$

which represents a rotation about the y axis. The intuitive explanation is that the Adjoint maps the initial rotation about the x axis, to a new rotation, which is still in the algebra, but results from the action of g on the rigid body. Therefore, it provides a mapping of the rotation under the action of the group element g. Indeed, the Adjoint action to map different algebraic entities offers a useful tool to transform velocities between two frames, such as body and inertial frames [148], [206]. This will be expanded in more detail in Section 3.2.1.

It can be shown that the Adjoint map is the derivative of the conjugation map at identity [74]. Similarly, we can differentiate the Adjoint map at the identity element, which in turn results in the Lie bracket [74], which is the commutator of two Lie algebra elements. This map is called the adjoint map (note lowercase), is denoted by ad and defined as

$$\mathrm{ad}_{\widetilde{\boldsymbol{\mu}}}(\widetilde{\boldsymbol{\nu}}) : \quad \mathfrak{g} \mapsto \mathfrak{g} \;\; ; \;\; \mathrm{ad}_{\widetilde{\boldsymbol{\mu}}}(\widetilde{\boldsymbol{\nu}}) = [\widetilde{\boldsymbol{\mu}}, \widetilde{\boldsymbol{\nu}}] = \widetilde{\boldsymbol{\mu}}\widetilde{\boldsymbol{\nu}} - \widetilde{\boldsymbol{\nu}}\widetilde{\boldsymbol{\mu}} \tag{3.30}$$

for $\widetilde{\boldsymbol{\mu}}, \widetilde{\boldsymbol{\nu}} \in \mathfrak{g}$. The ad map therefore captures the internal structure of the Lie algebra through the Lie bracket, which is a measure of the non-commutativity of the algebra. The physical interpretation of the adjoint is that it provides a measure of the commutativity of group elements

in the vector space of the algebra. Note that the adjoint can also be written in vector form, as

$$\mathrm{ad}_{\boldsymbol{\mu}}(\boldsymbol{\nu}): \quad \mathbb{R}^m \mapsto \mathbb{R}^m \;\; ; \;\; \mathrm{ad}_{\boldsymbol{\mu}}(\boldsymbol{\nu}) = \left([\widetilde{\boldsymbol{\mu}}, \widetilde{\boldsymbol{\nu}}]\right)^{\vee} \tag{3.31}$$

This vector form mapping allows us to interpret $\mathrm{ad}_{\boldsymbol{\mu}}(\boldsymbol{\nu})$ as the transformation of $\boldsymbol{\nu}$ by a certain matrix $\widehat{\boldsymbol{\mu}}$. Once the Lie bracket is computed and vectorised, the corresponding matrix $\widehat{\boldsymbol{\mu}}$ can be determined, which, when premultiplied by the vector $\boldsymbol{\nu}$, yields the same result. Therefore, the hat operator $\widehat{(\bullet)}$ serves as a linear operator that maps a vector in $\mathbb{R}^m$ to an $m \times m$ matrix. Eq. (3.31) can therefore be restated as

$$\mathrm{ad}_{\boldsymbol{\mu}}(\boldsymbol{\nu}) = \left([\widetilde{\boldsymbol{\mu}}, \widetilde{\boldsymbol{\nu}}]\right)^{\vee} = \widehat{\boldsymbol{\mu}}\boldsymbol{\nu} \tag{3.32}$$

3.1.7 Commutativity of Cross Derivatives

The cross derivative of a group element are commutative due to the symmetry of second-order derivatives, which leads to a compatibility equation between derivatives on the group [209]. For a group element $\mathcal{X}$ parametrised by two variables $a, b \in \mathbb{R}$, the left-invariant derivatives with respect to a and b are

$$\begin{aligned} d_a(\mathcal{X}) &= \mathcal{X}\widetilde{\mathbf{a}} \\ d_b(\mathcal{X}) &= \mathcal{X}\widetilde{\mathbf{b}} \end{aligned} \tag{3.33}$$

and the commutativity of the cross derivatives is expressed as

$$d_a(d_b(\mathcal{X})) = d_b(d_a(\mathcal{X})) \tag{3.34}$$

Using the left-invariant derivatives in Eq. (3.33) and applying the chain rule gives

$$\begin{aligned} d_a(\mathcal{X}\widetilde{\mathbf{b}}) &= d_b(\mathcal{X}\widetilde{\mathbf{a}}) \\ d_a(\mathcal{X})\widetilde{\mathbf{b}} + \mathcal{X}d_a(\widetilde{\mathbf{b}}) &= d_b(\mathcal{X})\widetilde{\mathbf{a}} + \mathcal{X}d_b(\widetilde{\mathbf{a}}) \\ \mathcal{X}(\widetilde{\mathbf{a}}\widetilde{\mathbf{b}} + d_a(\widetilde{\mathbf{b}})) &= \mathcal{X}(\widetilde{\mathbf{b}}\widetilde{\mathbf{a}} + d_b(\widetilde{\mathbf{a}})) \end{aligned} \tag{3.35}$$

Using the definition of the adjoint in Eq. (3.30), the last line above can be written as

$$d_b(\widetilde{\mathbf{a}}) - d_a(\widetilde{\mathbf{b}}) = \widetilde{\mathbf{a}}\widetilde{\mathbf{b}} - \widetilde{\mathbf{b}}\widetilde{\mathbf{a}} = [\widetilde{\mathbf{a}}, \widetilde{\mathbf{b}}] = \mathrm{ad}_{\widetilde{\mathbf{a}}}(\widetilde{\mathbf{b}}) \tag{3.36}$$

or equivalently in vector form as

$$d_b(\mathbf{a}) - d_a(\mathbf{b}) = \mathrm{ad}_{\mathbf{a}}(\mathbf{b}) \tag{3.37}$$

which is the compatibility equation which relates the derivatives of two Lie algebra elements through the adjoint. It is worth noting the derivatives of group elements, which are termed the Jacobians, can be related using the Ad map [206]. The relationship in Eq. (3.37) can therefore

be seen as the derivative of this Jacobian compatibility equation, given that ad is the derivative of Ad at the identity, as discussed. Eq. (3.37) shows that derivatives do not commute on the Algebra elements, though they do commute on the group elements, as expressed in Eq. (3.34).

3.1.8 Derivative of the Exponential and Tangent Operator

The derivative of the exponential plays a key role in the description of the composition of the group in the context of elements belonging to the algebra. In terms of matrix Lie groups, it confirms that all information about the product operation on the group is encoded in the Lie algebra [92]. That is to say, for every two group elements $\exp(\widetilde{\boldsymbol{\mu}})$ and $\exp(\widetilde{\boldsymbol{\nu}})$, their combined action, given by the product $\exp(\widetilde{\boldsymbol{\mu}})\exp(\widetilde{\boldsymbol{\nu}})$, has an analytic expression in terms of commutators in the algebra[1]. The derivative of the exponential map on any $\widetilde{\boldsymbol{\tau}} \in \mathfrak{g}$ is given by [74], [92]

$$D_{\exp}(\widetilde{\boldsymbol{\tau}}) = \exp(\widetilde{\boldsymbol{\tau}}) \left(\frac{\mathcal{E} - \exp(-ad_{\widetilde{\boldsymbol{\tau}}})}{ad_{\widetilde{\boldsymbol{\tau}}}} \right) \tag{3.38}$$

The derivative of the exponential also plays a role in the evaluation of what is known as the Tangent operator [209]. Consider an element $\mathcal{X}$ of the group $\mathcal{G}$. This can generally be represented as a function of some $\widetilde{\boldsymbol{\tau}} \in \mathfrak{g}$ as follows:

$$\mathcal{X} = \exp(\widetilde{\boldsymbol{\tau}}) \tag{3.39}$$

This can be differentiated with respect to any parameter $a \in \mathbb{R}$ to give

$$d_a(\mathcal{X}) = D_{\exp}(\widetilde{\boldsymbol{\tau}}) \cdot d_a(\widetilde{\boldsymbol{\tau}}) \tag{3.40}$$

where $D_{\exp}(\widetilde{\mathbf{x}}) \cdot \widetilde{\mathbf{y}}$ is the directional derivative of the exponential map in the direction of $\widetilde{\mathbf{y}}$. We also know from Eq. (3.12a) that $d_a(\mathcal{X})$ can be written in terms of a left-invariant vector field as

$$d_a(\mathcal{X}) = \mathcal{X}\widetilde{\mathbf{a}}_L \tag{3.41}$$

Equating Eq. (3.40) and Eq. (3.41) together, and using Eq. (3.39), we arrive at the following linear relationship

$$\begin{aligned} \widetilde{\mathbf{a}}_L &= \exp(\widetilde{\boldsymbol{\tau}})^{-1} D_{\exp}(\widetilde{\boldsymbol{\tau}}) \cdot d_a(\widetilde{\boldsymbol{\tau}}) \\ \Rightarrow \widetilde{\mathbf{a}}_L &= \widetilde{\mathbf{T}(\boldsymbol{\tau})d_a(\boldsymbol{\tau})} \end{aligned} \tag{3.42}$$

where $\mathbf{T}(\boldsymbol{\tau})$ is commonly known as the tangent operator [103], [208]. This is a map from the Lie algebra to itself $\mathfrak{g} \mapsto \mathfrak{g}$, which transforms a derivative of an algebra element to another algebra element. It effectively gives the geometric relation between parametrisations of the group element with respect to different elements in the algebra, here $\mathbf{a}_L$ and $\boldsymbol{\tau}$. Eq. (3.42) may also be written in vector form, using the isomorphisms of algebra elements with vectors in $\mathbb{R}^m$,

[1] Interested readers can refer to [92] for a description of the Baker-Campbell-Hausdorff formula.

as

$$\mathbf{a}_L = \mathbf{T}(\boldsymbol{\tau})\, d_a(\boldsymbol{\tau}) \tag{3.43}$$

The tangent map therefore gives a relationship between the left-invariant element $\mathbf{a}_L$ and the element $\boldsymbol{\tau}$ defined by the exponential map. Substituting Eq. (3.42) into Eq. (3.41) we have

$$d_a(\mathcal{X}) = \mathcal{X}(\widetilde{\mathbf{T}(\boldsymbol{\tau})d_a(\boldsymbol{\tau})}) \tag{3.44}$$

Therefore, the tangent operator can be used directly to differentiate group elements with respect to any parameter. A crucial observation can be made in Eq. (3.44): the derivative of a nonlinear group element can be expressed by the derivative of the corresponding linear algebra element, through transformation by the tangent map. A series expansion can be written for the tangent operator and closed-form expressions can be derived for Lie groups of interest [227].

The tangent operator is an invertible map and can therefore be inverted to give an equivalent expression for the derivative of the log map, as the log and the exp maps are inverses of one another. Expressing Eq. (3.39) in terms of $\widetilde{\boldsymbol{\tau}}$, we have

$$\widetilde{\boldsymbol{\tau}} = \log(\mathcal{X}) \tag{3.45}$$

which can be differentiated, leading to an equivalent expression to Eq. (3.43), such that

$$d_a(\boldsymbol{\tau}) = \mathbf{T}^{-1}(\boldsymbol{\tau})\mathbf{a}_L \tag{3.46}$$

This can directly be used in differentiating expressions involving logarithm maps, such as those related to the shooting function, as will be seen in Section 4.2. Note that $\mathbf{a}_L$ in Eq. (3.46) is the left-invariant vector field of the derivative of the term inside the log bracket (that is, $\mathcal{X}$), as given in Eq. (3.41).

3.2 Rotation Group $SO(3)$

The $SO(3)$ group has already been introduced in the previous sections. As discussed, it is the group of all 3D rotations in Euclidean space, represented by 3×3 orthogonal matrices $\mathbf{R} \in SO(3)$ with unit determinant. For a given rigid body that is free to rotate about a fixed frame, every configuration of the body can be represented by a unique $\mathbf{R} \in SO(3)$.

The inverse of a rotation matrix is given by its transpose. The group's Lie algebra $\mathfrak{so}(3)$ is the set of skew-symmetric 3×3 matrices $[\boldsymbol{\omega}]_\times$, which can be mapped from vectors in $\mathbb{R}^3$ to $\mathfrak{so}(3)$ using the $\widetilde{(\bullet)}$ operator. Therefore on $SO(3)$ we have

$$\widetilde{\boldsymbol{\omega}} = [\boldsymbol{\omega}]_\times \tag{3.47}$$

The cross product between two vectors in $\mathbb{R}^3$ may also be written using the $\widetilde{(\bullet)}$ operator as

$$\mathbf{a} \times \mathbf{b} = \widetilde{\mathbf{a}}\mathbf{b} \quad \forall \mathbf{a}, \mathbf{b} \in \mathbb{R}^3 \tag{3.48}$$

Normalising $\boldsymbol{\omega}$ and expressing it as $\boldsymbol{\omega} = \boldsymbol{u}\theta$, where θ is the magnitude of $\boldsymbol{\omega}$ ($\theta = \|\boldsymbol{\omega}\|$), and $\boldsymbol{u}$ is a unit vector, the exponential map from $\mathfrak{so}(3)$ to $SO(3)$ is given by Rodrigues's formula[1]

$$\exp_{SO(3)}(\boldsymbol{\omega}) = \mathbf{I}_{3\times 3} + \left(\frac{\sin(\theta)}{\theta}\right)[\boldsymbol{\omega}]_\times + \left(\frac{1-\cos(\theta)}{\theta^2}\right)[\boldsymbol{\omega}]_\times^2 \tag{3.49}$$

Geometrically, given a unit vector $\boldsymbol{u} \in \mathbb{R}^3$ and a scalar $\theta \in \mathbb{R}$, the exponential map $\exp_{SO(3)}(\boldsymbol{u}\theta)$ generates a rotation around the axis $\boldsymbol{u}$ by the angle θ. It can be shown that every rotation matrix can be represented as the exponential of some skew-symmetric matrix [148].

The inverse of the exponential, namely, the logarithm map, is given by

$$\log_{SO(3)}(\mathbf{R}) = \frac{\bar{\theta}}{2\sin(\bar{\theta})}\left(\mathbf{R} - \mathbf{R}^T\right) \quad \text{where} \quad \bar{\theta} = \arccos\left(\frac{\mathrm{tr}(\mathbf{R})-1}{2}\right) \tag{3.50}$$

The Adjoint map can be evaluated using Eq. (3.23) as follows

$$\mathrm{Ad}_{\mathbf{R}}(\widetilde{\boldsymbol{\omega}}) = \mathbf{R}\widetilde{\boldsymbol{\omega}}\mathbf{R}^T = \widetilde{\mathbf{R}\boldsymbol{\omega}} \tag{3.51}$$

where the right hand side can be verified by carrying out the matrix multiplication $\mathbf{R}\widetilde{\boldsymbol{\omega}}\mathbf{R}^T$. The above can be written in vector form and acting on vectors $\boldsymbol{\omega} \in \mathbb{R}^3$ as

$$\mathrm{Ad}_{\mathbf{R}}(\boldsymbol{\omega}) = \mathbf{R}\boldsymbol{\omega} \tag{3.52}$$

It is therefore seen that, on the $SO(3)$ group, the Adjoint action is the same as the group action. The hat operator $\widehat{(\bullet)}$ in Eq. (3.32) is equivalent to the tilde operator $\widetilde{(\bullet)}$ on $SO(3)$ in Eq. (3.47). In the case of $SO(3)$, we therefore have $\widehat{\boldsymbol{\omega}} = [\boldsymbol{\omega}]_\times$ for $\boldsymbol{\omega} \in \mathbb{R}^3$.

Finally, the tangent and inverse tangent operators are given by [208]

$$\mathbf{T}_{SO(3)}(\boldsymbol{\omega}) = \mathbf{I}_{3\times 3} - \left(\frac{1-\cos\theta}{\theta^2}\right)[\boldsymbol{\omega}]_\times + \left(\frac{\theta-\sin\theta}{\theta^3}\right)[\boldsymbol{\omega}]_\times^2 \tag{3.53}$$

$$\mathbf{T}^{-1}_{SO(3)}(\boldsymbol{\omega}) = \mathbf{I}_{3\times 3} + \frac{1}{2}[\boldsymbol{\omega}]_\times + \left(\frac{1}{\theta^2} - \frac{\sin\theta}{2\theta(1-\cos\theta)}\right)[\boldsymbol{\omega}]_\times^2 \tag{3.54}$$

3.2.1 Rigid Body Velocities on $SO(3)$

Considering a rigid body which is only free to rotate, we define coordinate frame A as the fixed spatial (inertial) frame, and coordinate frame B as the body frame attached to and moving with the rigid body. The position of a point q on the rigid body relative to frame A at any given time is denoted $q_A \in \mathbb{R}^3$, and can be written using the group action of the rotation matrix $\mathbf{R}(t) \in SO(3)$, which describes the orientation of the body relative to the fixed frame, as [148]

$$q_A(t) = \mathbf{R}(t)q_B \tag{3.55}$$

[1] Note we write the vector form of $\boldsymbol{\omega}$ as the argument to the exponential, as $[\boldsymbol{\omega}]_\times$ appears on the right hand side.

where $q_B \in \mathbb{R}^3$ is the position of the same point relative to the body frame. Generally speaking, rotation matrices serve as transformations which take coordinates of a point relative to one frame and map them to another[1]. The velocity of point q_A in the spatial frame can be written as

$$v_{q_A}(t) = \frac{d}{dt}(q_A(t)) = \dot{\mathbf{R}}(t)q_B \tag{3.56}$$

Using the right-invariant velocity representation in Eq. (3.12b), and introducing $\widetilde{\boldsymbol{\omega}}^s$ as the spatial angular velocity[2], we have $\dot{\mathbf{R}}(t) = \widetilde{\boldsymbol{\omega}}^s(t)\mathbf{R}(t)$. Substituting this into Eq. (3.56) above, and using Eq. (3.55), we have

$$v_{q_A}(t) = \widetilde{\boldsymbol{\omega}}^s(t)q_A(t) = \boldsymbol{\omega}^s(t) \times q_A(t) \tag{3.57}$$

where we have used Eq. (3.48) to also write the expression using the vector cross product. This gives the velocity relative to the spatial frame - of a point whose coordinates are also in the spatial frame - in terms of the angular velocity of the rigid body $\widetilde{\boldsymbol{\omega}}^s$. We therefore term this angular velocity as the spatial angular velocity. This therefore leads to the definition of the instantaneous spatial angular velocity of a rigid body, as the right invariant velocity vector, which can be computed from Eq. (3.11) as

$$\widetilde{\boldsymbol{\omega}}^s = \dot{\mathbf{R}}\mathbf{R}^{-1} \tag{3.58}$$

We will now derive a similar expression for the velocity relative to the body frame. Using the Adjoint relationship between the left and right invariant velocity fields in Eq. (3.26), we can write the following relationship with the left-invariant angular velocity, which we will denote as $\widetilde{\boldsymbol{\omega}}^b$

$$\widetilde{\boldsymbol{\omega}}^s = \mathrm{Ad}_{\mathbf{R}}(\widetilde{\boldsymbol{\omega}}^b) = \mathbf{R}\widetilde{\boldsymbol{\omega}}^b\mathbf{R}^{-1} \tag{3.59}$$

We also have the following relationship between the spatial and body velocities, using the group action of the rotation matrix similar to Eq. (3.55)

$$v_{q_A}(t) = \mathbf{R}(t)v_{q_B}(t) \tag{3.60}$$

Substituting Eq. (3.59) for $\widetilde{\boldsymbol{\omega}}^s$ in Eq. (3.57), and using the relationship between the spatial and body velocities in Eq. (3.60), we can write the velocity of point q in the body frame as

$$v_{q_B}(t) = \widetilde{\boldsymbol{\omega}}^b(t)q_B(t) = \boldsymbol{\omega}^b(t) \times q_B \tag{3.61}$$

where the instantaneous body angular velocity can be computed from Eq. (3.11) as

$$\widetilde{\boldsymbol{\omega}}^b = \mathbf{R}^{-1}\dot{\mathbf{R}} \tag{3.62}$$

[1] In fact, the "classical" frame transformation which maps local vectors $\mathbf{z}_l$ to global $\mathbf{z}_g$ is given by $\mathbf{z}_g = \mathbf{R}\mathbf{z}_l$.
[2] It will shortly be apparent why we have termed this spatial angular velocity.

As stated in Section 3.1.4, it is seen that the left-invariant angular velocity, $\tilde{\boldsymbol{\omega}}^b$, represents the rigid body velocity in the body frame, and is therefore independent of the orientation with respect to the fixed reference frame. This property of the left-invariant representation of the velocity is also present in case of the rigid body motion group $SE(3)$, as will be seen the the following section. It is noted that both velocities are elements of the same Lie algebra, which underscores the unified mathematical framework provided by Lie theory for dealing with different aspects of continuous motions. The distinction between body and spatial velocities is therefore not a matter of different algebraic entities, but rather different coordinate frames through which the same underlying algebraic structure can be viewed.

3.3 Rigid Body Motion Group $SE(3)$

A general rigid body motion comprises rotation and translation, and is defined as one that preserves the distance between points. A geometric description of such motion can be developed using the Special Euclidean Lie group $SE(3)$ in three-dimensional space. The advantage of such a framework is that it offers a global description of the motion without encountering singularities and gives a geometric description of rigid motion, which leads to a more compact and simplified analysis.

To formally introduce the $SE(3)$ group, we begin by considering a rigid body motion consisting of rotation and translation. This motion can be characterised using rigid body transformations to describe the position and orientation of a body coordinate frame in relation to an inertial frame. We denote the inertial frame as A, and the body frame as B, as depicted in Figure 3.3. Let $p_{AB} \in \mathbb{R}^3$ represent the position vector of frame B relative to frame A, and let $q_A \in \mathbb{R}^3$ and $q_B \in \mathbb{R}^3$ denote the coordinates of a point q relative to frames A and B, respectively. The relationship between q_A and q_B can then be expressed through an affine coordinate transformation as follows [148]:

$$q_A = p_{AB} + \mathbf{R}_{AB}\, q_B \tag{3.63}$$

where $\mathbf{R}_{AB} \in SO(3)$ expresses the orientation of frame B relative to A. A more concise ex-

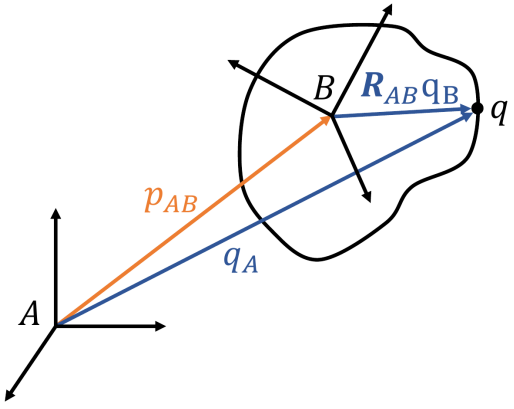


Figure 3.3: Rigid body motion frame.

pression of this relationship can be written using the homogeneous representation of vectors in $\mathbb{R}^4$, to encapsulate both rotation and translation as a single linear transformation matrix, as follows:

$$\begin{bmatrix} q_A \\ 1 \end{bmatrix} = \begin{bmatrix} \mathbf{R}_{AB} & p_{AB} \\ \mathbf{0} & 1 \end{bmatrix} \begin{bmatrix} q_B \\ 1 \end{bmatrix} \tag{3.64}$$

where the 4×4 matrix

$$\mathbf{H}_{AB} = \begin{bmatrix} \mathbf{R}_{AB} & p_{AB} \\ \mathbf{0} & 1 \end{bmatrix} \tag{3.65}$$

is a member of the Special Euclidean group $SE(3)$, which represents the combination of rotations and translations in three-dimensional space. We formally define this matrix group as the group of all transformations of vectors in $\mathbb{R}^3$ that can be expressed as a composition of a translation and an orthogonal linear transformation (rotation) [92]. The elements of $SE(3)$ take the form

$$\mathbf{H} = \begin{bmatrix} \mathbf{R} & \mathbf{x} \\ \mathbf{0}_{1\times 3} & 1 \end{bmatrix} \in SE(3) \tag{3.66}$$

where $\mathbf{R} \in SO(3)$ and $\mathbf{x} \in \mathbb{R}^3$, and with the matrix product as the group composition operation. The inverse of $\mathbf{H}$ is given by

$$\mathbf{H}^{-1} = \begin{bmatrix} \mathbf{R}^T & -\mathbf{R}^T\mathbf{x} \\ \mathbf{0}_{1\times 3} & 1 \end{bmatrix} \in SE(3) \tag{3.67}$$

and the composition of two group elements gives

$$\mathbf{H}_a\mathbf{H}_b = \begin{bmatrix} \mathbf{R}_a\mathbf{R}_b & \mathbf{x}_a + \mathbf{R}_a\mathbf{x}_b \\ \mathbf{0}_{1\times 3} & 1 \end{bmatrix} \in SE(3) \tag{3.68}$$

A distinction is drawn between the geometric description of the group action of $SO(3)$ and $SE(3)$ matrices. As explained in Section 3.2.1, the $SO(3)$ group serves as a transformation of points from one coordinate frame to another. For the $SE(3)$ group, however, the geometric interpretation of the group action is that it maps points from their initial coordinates to their final coordinates after the rigid body motion is applied and does so with respect to a single coordinate frame.

The Lie algebra element can be defined as

$$\mathfrak{se}(3) = \{(\mathbf{u}, \widetilde{\boldsymbol{\omega}}) \mid \mathbf{u} \in \mathbb{R}^3, \widetilde{\boldsymbol{\omega}} = [\boldsymbol{\omega}]_\times \in \mathfrak{so}(3)\} \tag{3.69}$$

which is written in homogeneous coordinates as

$$\widetilde{\boldsymbol{\xi}} = \begin{bmatrix} [\boldsymbol{\omega}]_\times & \mathbf{u} \\ \mathbf{0}_{1\times 3} & 0 \end{bmatrix} \in \mathfrak{se}(3) \tag{3.70}$$

An element of $\mathfrak{se}(3)$ is isomorphic to $\mathbb{R}^6$ as

$$\boldsymbol{\xi} = \begin{bmatrix} \mathbf{u} \\ \boldsymbol{\omega} \end{bmatrix} \in \mathbb{R}^6 \tag{3.71}$$

which are termed the twist coordinates [148]. Similarly to Eq. (3.49), we write $\boldsymbol{\omega} = \boldsymbol{u}\theta$, where $\boldsymbol{u}$ is a unit vector, and $\theta = \|\boldsymbol{\omega}\|$. The exponential map from $\mathfrak{se}(3)$ to $SE(3)$ is then given by

$$\exp_{SE(3)}(\boldsymbol{\xi}) = \begin{bmatrix} \exp_{SO(3)}(\boldsymbol{\omega}) & \mathbf{V}(\boldsymbol{\omega})\mathbf{u} \\ \mathbf{0}_{1\times 3} & 1 \end{bmatrix} \tag{3.72}$$

with

$$\mathbf{V}(\boldsymbol{\omega}) = \mathbf{I}_{3\times 3} + \left(\frac{1-\cos\theta}{\theta^2}\right)[\boldsymbol{\omega}]_\times + \left(\frac{\theta - \sin\theta}{\theta^3}\right)[\boldsymbol{\omega}]_\times^2 \tag{3.73}$$

It is noted that

$$\mathbf{V}(\boldsymbol{\omega}) = \mathbf{T}^T_{SO(3)}(\boldsymbol{\omega}) \tag{3.74}$$

It can be shown that every rigid body motion can be realised by a rotation about an axis combined with a translation parallel to that axis, and that every rigid body motion can be represented as the exponential of some twist, which gives the relative motion of a rigid body with respect to a single reference frame [148].

The logarithm map for the $SE(3)$ group is given by

$$\log_{SE(3)}(\mathbf{H}) = \begin{bmatrix} \widetilde{\boldsymbol{\omega}} & \mathbf{V}^{-1}(\boldsymbol{\omega})\mathbf{x} \\ \mathbf{0}_{1\times 3} & 0 \end{bmatrix} \tag{3.75}$$

where $\widetilde{\boldsymbol{\omega}} = \log_{SO(3)}(\mathbf{R})$.

The Adjoint map can be evaluated using Eq. (3.23) as follows

$$\mathrm{Ad}_{\mathbf{H}}(\widetilde{\boldsymbol{\xi}}) = \mathbf{H}\widetilde{\boldsymbol{\xi}}\mathbf{H}^T = \begin{bmatrix} [\mathbf{R}\boldsymbol{\omega}]_\times & [\mathbf{x}]_\times\mathbf{R}\boldsymbol{\omega} + \mathbf{R}\mathbf{u} \\ \mathbf{0} & \mathbf{0} \end{bmatrix} = \begin{bmatrix} \widetilde{[\mathbf{x}]_\times\mathbf{R}\boldsymbol{\omega} + \mathbf{R}\mathbf{u}} \\ \mathbf{R}\boldsymbol{\omega} \end{bmatrix} \tag{3.76}$$

which can be written in vector form, as acting on vectors $\boldsymbol{\xi} = [\mathbf{u}\ \boldsymbol{\omega}]^T \in \mathbb{R}^6$ as

$$\mathrm{Ad}_{\mathbf{H}}(\boldsymbol{\xi}) = \begin{bmatrix} [\mathbf{x}]_\times\mathbf{R}\boldsymbol{\omega} + \mathbf{R}\mathbf{u} \\ \mathbf{R}\boldsymbol{\omega} \end{bmatrix} = \begin{bmatrix} \mathbf{R} & [\mathbf{x}]_\times\mathbf{R} \\ \mathbf{0} & \mathbf{R} \end{bmatrix} \boldsymbol{\xi} \tag{3.77}$$

The hat operator $\widehat{(\bullet)}$ in Eq. (3.32) is given by

$$\widehat{\boldsymbol{\xi}} = \begin{bmatrix} \widetilde{\boldsymbol{\omega}} & \widetilde{\mathbf{u}} \\ \mathbf{0} & \widetilde{\boldsymbol{\omega}} \end{bmatrix} \tag{3.78}$$

The tangent operator is given by [208]

$$\mathbf{T}_{SE(3)}(\boldsymbol{\xi}) = \begin{bmatrix} \mathbf{T}_{SO(3)}(\boldsymbol{\omega}) & \mathbf{T}_{\mathbf{u}\boldsymbol{\omega}+}(\mathbf{u},\boldsymbol{\omega}) \\ \mathbf{0}_{3\times 3} & \mathbf{T}_{SO(3)}(\boldsymbol{\omega}) \end{bmatrix} \tag{3.79}$$

where

$$\mathbf{T}_{\mathbf{u}\boldsymbol{\omega}+}(\mathbf{u},\boldsymbol{\omega}) = \frac{-\beta}{2}\tilde{\mathbf{u}} + \frac{1-\alpha}{\theta^2}\lceil \mathbf{u},\boldsymbol{\omega}\rceil + \frac{\boldsymbol{\omega}^{\mathbf{T}}\mathbf{u}}{\theta^2}\left((\beta-\alpha)\tilde{\boldsymbol{\omega}} + \left(\frac{\beta}{2} - \frac{3(1-\alpha)}{\theta^2}\right)\tilde{\boldsymbol{\omega}}^2\right) \tag{3.80}$$

with $\theta = \|\boldsymbol{\omega}\|$, $\lceil \mathbf{u},\boldsymbol{\omega}\rceil = \tilde{\mathbf{u}}\tilde{\boldsymbol{\omega}} + \tilde{\boldsymbol{\omega}}\tilde{\mathbf{u}}$, and

$$\begin{aligned} \alpha &= \alpha(\boldsymbol{\omega}) = \frac{\sin\theta}{\theta} \\ \beta &= \beta(\boldsymbol{\omega}) = 2\frac{1-\cos\theta}{\theta^2} \end{aligned} \tag{3.81}$$

The inverse tangent operator is finally given by

$$\mathbf{T}^{-1}_{SE(3)}(\boldsymbol{\xi}) = \begin{bmatrix} \mathbf{T}^{-1}_{SO(3)}(\boldsymbol{\omega}) & \mathbf{T}_{\mathbf{u}\boldsymbol{\omega}-}(\mathbf{u},\boldsymbol{\omega}) \\ \mathbf{0}_{3\times 3} & \mathbf{T}^{-1}_{SO(3)}(\boldsymbol{\omega}) \end{bmatrix} \tag{3.82}$$

where

$$\mathbf{T}_{\mathbf{u}\boldsymbol{\omega}-}(\mathbf{u},\boldsymbol{\omega}) = \frac{1}{2}\tilde{\mathbf{u}} + \frac{\beta-\alpha}{\beta\theta^2}\lceil \mathbf{u},\boldsymbol{\omega}\rceil + \frac{1+\alpha-2\beta}{\beta\theta^4}(\boldsymbol{\omega}^{\mathbf{T}}\mathbf{u})\tilde{\boldsymbol{\omega}}^2 \tag{3.83}$$

Here we note that, instead of the axis-angle representation in $\boldsymbol{\omega} = \boldsymbol{u}\theta$ which has been used in Sections 3.2 and 3.3, the Euler-Rodrigues motion parametrisation may be adopted, which will greatly simplify the expressions for the exponential, logarithm, and tangent maps on $SO(3)$ and $SE(3)$, by removing all trigonometric terms from these equations. This will provide considerable computational advantages, both in terms of speed and ease of implementation, particularly in cases involving small angles. The details of this parametrisation are given in Appendix A.

3.3.1 Rigid Body Velocities on $SE(3)$

Starting from the description of the coordinates of a point on a rigid body in Eq. (3.64) and Eq. (3.65), these can be given over time as

$$\bar{q}_A(t) = \mathbf{H}_{AB}(t)\bar{q}_B \tag{3.84}$$

where here we have used $\bar{q}$ to indicate the 4×1 coordinate points in homogeneous form. Differentiating this to get velocities, we have

$$v_{\bar{q}_A}(t) = \dot{\mathbf{H}}_{AB}(t)\bar{q}_B = \dot{\mathbf{H}}_{AB}(t)\mathbf{H}^{-1}_{AB}(t)\bar{q}_A(t) \tag{3.85}$$

It is seen that, similar to the description of the $SO(3)$ velocities in Eq. (3.57), the term $\dot{\mathbf{H}}_{AB}(t)\mathbf{H}_{AB}^{-1}(t)$ has arisen, which indicates the right-invariant velocity vector in $SE(3)$. By analogy to the rotational velocity, we term this the spatial velocity in $\mathfrak{se}(3)$, which can be computed as [148]

$$\begin{aligned}\widetilde{\mathbf{v}}_{AB}^{s} = \dot{\mathbf{H}}_{AB}\mathbf{H}_{AB}^{-1} &= \begin{bmatrix}\dot{\mathbf{R}}_{AB} & \dot{p}_{AB}\\ \mathbf{0} & 0\end{bmatrix}\begin{bmatrix}\mathbf{R}_{AB}^{T} & -\mathbf{R}_{AB}^{T}p_{AB}\\ \mathbf{0} & 1\end{bmatrix}\\ &= \begin{bmatrix}\dot{\mathbf{R}}_{AB}\mathbf{R}_{AB}^{T} & -\dot{\mathbf{R}}_{AB}\mathbf{R}_{AB}^{T}p_{AB} + \dot{p}_{AB}\\ \mathbf{0} & 0\end{bmatrix}\end{aligned} \tag{3.86}$$

It is seen that $\widetilde{\mathbf{v}}_{AB}^{s}$ matches the homogeneous coordinates of an element in $\mathfrak{se}(3)$ given in Eq. (3.70), which can also be written in vector form as

$$\mathbf{v}_{AB}^{s} = (\widetilde{\mathbf{v}}_{AB}^{s})^{\vee} = \begin{bmatrix}-\dot{\mathbf{R}}_{AB}\mathbf{R}_{AB}^{T}p_{AB} + \dot{p}_{AB}\\ (\dot{\mathbf{R}}_{AB}\mathbf{R}_{AB}^{T})^{\vee}\end{bmatrix} = \begin{bmatrix}\mathbf{u}^{s}\\ \boldsymbol{\omega}^{s}\end{bmatrix} \tag{3.87}$$

The angular component of $\mathbf{v}_{AB}^{s}$, that is, $\boldsymbol{\omega}^{s}$, is the body angular velocity as viewed in the spatial frame. On the other hand, the linear component, $\mathbf{u}^{s}$, is interpreted as the velocity of a (possibly fictitious) point of the rigid body which is instantaneously located at the origin of the fixed reference frame in the current configuration [209]. A more intuitive description of the velocities can be obtained by considering the left-invariant velocity field in Eq. (3.11). Analogous to the rotational velocities, we define $\widetilde{\mathbf{v}}_{AB}^{b} \in \mathfrak{se}(3)$ as the body velocity, which we calculate as

$$\begin{aligned}\widetilde{\mathbf{v}}_{AB}^{b} = H_{AB}^{-1}\dot{H}_{AB} &= \begin{bmatrix}\mathbf{R}_{AB}^{T} & -\mathbf{R}_{AB}^{T}p_{AB}\\ \mathbf{0} & 1\end{bmatrix}\begin{bmatrix}\dot{\mathbf{R}}_{AB} & \dot{p}_{AB}\\ \mathbf{0} & 0\end{bmatrix}\\ &= \begin{bmatrix}\mathbf{R}_{AB}^{T}\dot{\mathbf{R}}_{AB} & \mathbf{R}^{T}\dot{p}_{AB}\\ \mathbf{0} & 0\end{bmatrix}\end{aligned} \tag{3.88}$$

Written in vector form, this yields

$$\mathbf{v}_{AB}^{b} = (\widetilde{\mathbf{v}}_{AB}^{b})^{\vee} = \begin{bmatrix}\mathbf{R}_{AB}^{T}\dot{p}_{AB}\\ (\mathbf{R}_{AB}^{T}\dot{\mathbf{R}}_{AB})^{\vee}\end{bmatrix} = \begin{bmatrix}\mathbf{u}^{b}\\ \boldsymbol{\omega}^{b}\end{bmatrix} \tag{3.89}$$

and Eq. (3.85) now becomes

$$v_{\bar{q}_B}(t) = \widetilde{\mathbf{v}}_{AB}^{b}(t)\bar{q}_B \tag{3.90}$$

The body velocity can be interpreted intuitively: $\mathbf{u}^{b}$ is the velocity of the body as viewed in the body frame, and relative to the spatial frame, and $\boldsymbol{\omega}^{b}$ is the body angular velocity as viewed in the body frame. It is interesting to note that the expression for $\boldsymbol{\omega}^{b}$ in Eq. (3.89) is identical to the body angular velocity for a motion under $SO(3)$ in Eq. (3.62). The rigid body velocity

can also be derived from the left-invariant derivative of the frame $\mathbf{H}_{AB}$ in Eq. (3.65), as

$$\dot{\mathbf{H}}_{AB} = \begin{bmatrix} \dot{\mathbf{R}}_{AB} & \dot{p}_{AB} \\ \mathbf{0} & 0 \end{bmatrix} = \mathbf{H}_{AB}\tilde{\mathbf{v}}_L = \begin{bmatrix} \mathbf{R}_{AB} & p_{AB} \\ \mathbf{0} & 1 \end{bmatrix} \begin{bmatrix} \tilde{\boldsymbol{\omega}}_L & \mathbf{u}_L \\ \mathbf{0} & 0 \end{bmatrix} \tag{3.91}$$

which when multiplied, gives

$$\begin{aligned} \dot{\mathbf{R}}_{AB} &= \mathbf{R}_{AB}\tilde{\boldsymbol{\omega}}_L \\ \dot{p}_{AB} &= \mathbf{R}_{AB}\mathbf{u}_L \end{aligned} \tag{3.92}$$

which is identical to Eq. (3.89), to give $\boldsymbol{\omega}_L = \boldsymbol{\omega}^b$ and $\mathbf{u}_L = \mathbf{u}^b$, and by extension, $\mathbf{v}_L = \mathbf{v}^b_{AB}$. It is therefore confirmed that the left-invariant description of the frame velocities leads to the rigid body velocities as expressed in the local body frame. Similar to the velocities on $SO(3)$, the velocities here are also connected through the action of the Adjoint, which maps the body velocity in the local frame to the spatial velocity in the global frame.

It can be shown that the left-invariant derivative of any $\mathbf{H} \in SE(3)$ is invariant under Euclidean transformations [208], [209]. That is to say, they do not depend on the position or orientation of the body with respect to the fixed inertial frame. This representation of the velocities, and other derivatives on the Lie group in a more general sense, therefore possesses analytical and computational advantages, and is thus the description adopted in this thesis. The left-invariant derivatives are also used in the derivation of the beam equations, as presented in Section 3.5. It should be noted that the expressions for body velocities presented in Eq. (3.89) are applicable to derivatives with respect to quantities other than time, with the notation suitably substituted and the expressions kept formally identical.

3.4 Equation of Motion of a Free Rigid Body

The equation of motion of a free rigid body is developed in this section, in order to showcase the application of Lie group theory in dynamic modelling of rigid bodies, and to provide an introduction to the beam equations formulated in subsequent sections. The methodology follows that of works done in the field of multibody dynamics [21], [36], [37], [209], [211]. Similar methodologies also exist in robotics literature, and can be consulted by the interested reader [133], [146], [148], [193], [247].

3.4.1 Problem Definition

The dynamic system in consideration comprises of an elastic pendulum with and axial and radial spring, and with no forcing or damping, as depicted in Figure 3.4. The equation of motion of the tip mass can be written in polar coordinates using the system Lagrangian. This is given as

$$\begin{aligned} m\ddot{r} - mr\dot{\theta}^2 + k_r(r - r_0) &= 0 \\ mr^2\ddot{\theta} + 2mr\dot{r}\dot{\theta} + J\ddot{\theta} + k_\theta(\theta - \theta_0) &= 0 \end{aligned} \tag{3.93}$$

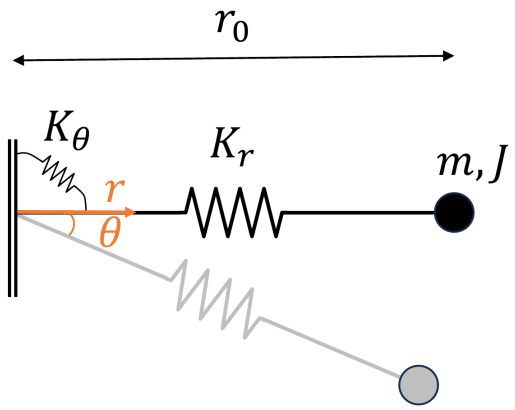


Figure 3.4: Unforced undamped elastic pendulum.

We will now derive the equation of motion of the system using Lie group theory. As the problem is two-dimensional and describes the rigid body motion of the tip mass, we need to formulate the equation of motion under the $SE(2)$ framework. This is the group of 2D rigid body motions, as introduced in Section 3.4.2, and is analogous to the $SE(3)$ group introduced in Section 3.3.

In formulating the equations of motion under $SE(2)$, we incorporate kinematic equations written under the Lie group setting, and use Hamilton's variational principle to derive the equation of motion. The rotational and translational movement of the tip mass is described using kinematic joints, which are geometrically specified using the notion of Lie subgroups, and are formulated as kinematic constraints with associated Lagrange multipliers in the equation of motion. The use of kinematic constraints is required to match the degrees of freedom of the system, when formulated using $SE(2)$ frames, with the physical degrees of freedom. This is detailed in Section 3.4.2. Finally, we note that any references made to the the $SE(3)$ relationships developed earlier in this chapter, and concerning the fundamental properties of that group, are also applicable to the $SE(2)$ group, bearing in mind that the expressions should be appropriately reduced to two dimensions, while remaining otherwise equivalent.

3.4.2 $SE(2)$ Lie group framework

The Lie group equations for the pendulum are developed using the 2-dimensional Special Euclidean $SE(2)$ group formulation. Analogous to $SE(3)$, this is the group of planar rigid body transformations. We denote an element of this group a frame, which is expressed in matrix form as

$$\mathbf{H} = \begin{bmatrix} \mathbf{R}_{2\times 2} & \mathbf{x}_{2\times 1} \\ \mathbf{0}_{1\times 2} & 1 \end{bmatrix}_{3\times 3} \in SE(2) \tag{3.94}$$

with a Lie algebra element given as

$$\boldsymbol{\chi} = \begin{bmatrix} \boldsymbol{\rho} \\ \theta \end{bmatrix} \in \mathbb{R}^3; \quad \tilde{\boldsymbol{\chi}} = \begin{bmatrix} [\theta]_\times & \boldsymbol{\rho} \\ \mathbf{0} & 0 \end{bmatrix} \in \mathfrak{se}(2) \tag{3.95}$$

The hat operator in Eq. (3.32) is given by

$$\mathrm{ad}_{\boldsymbol{\chi}}(\bullet) = \widehat{\boldsymbol{\chi}}(\bullet) = \begin{bmatrix} [\theta]_\times & [-1]_\times \boldsymbol{\rho} \\ \mathbf{0} & 0 \end{bmatrix} (\bullet) \tag{3.96}$$

Closed form expressions for the exponential, logarithm, and adjoint maps exist, and can be found in [206].

The Lie group formulation, in the context of multibody systems, aims to solve for the full configuration matrix of the system, which is comprised of the frames corresponding to N bodies and n joints. In this planar problem, the frame associated with the tip mass has 3 unknowns (the Lie algebra dimension is 3), and two joints are defined, each with 1 unknown. The joints describe the revolution and the translation motion of the tip. The total number of unknowns is therefore 5. Since the problem degrees of freedom equals 2, we therefore should have 3 constraints to be able to solve for the 2 degrees of freedom of the system. We begin by expressing the kinetic energy of the tip mass, and then describe the joints in the context of Lie subgroups.

3.4.3 Kinetic Energy

The kinetic energy of the system can be written using the velocity of the tip mass. We choose the left-invariant description of the velocity on $SE(2)$, which is expressed in the local coordinate frame attached to the mass. The advantage of this representation is that, due to the invariance of the velocity with respect to the position and orientation of the tip mass, the mass matrix used in the kinetic energy becomes constant, and it too will not depend on the position and orientation of the mass. The kinetic energy can be written as

$$\mathcal{K} = \frac{1}{2} \mathbf{v}^T \mathbf{M} \mathbf{v} \tag{3.97}$$

where $\mathbf{v} \equiv \mathbf{v}^b$ is the left-invariant body velocity developed in Eq. (3.89), and $\mathbf{M}$ is a constant 3×3 mass matrix in the form

$$\mathbf{M} = \begin{bmatrix} m\mathbf{I}_{2\times 2} & \mathbf{0} \\ \mathbf{0} & J \end{bmatrix} \tag{3.98}$$

where m is the mass of the tip, and J is its rotation inertia.

The variation of the kinetic energy is used in Hamilton's principle to derive the dynamic equation of motion of the body. This is written as

$$\delta \left(\int_{t_i}^{t_f} \mathcal{K} \, dt \right) \tag{3.99}$$

In order to develop the variation of the kinetic energy, we first write the time derivative and

variation of an element $\mathbf{H} \in SE(2)$ using Eq. (3.12) as

$$\begin{aligned} \dot{\mathbf{H}} &= \mathbf{H}\tilde{\mathbf{v}} \\ \delta(\mathbf{H}) &= \mathbf{H}\widetilde{\delta\mathbf{h}} \end{aligned} \tag{3.100}$$

where $\delta\mathbf{h}$ represents an infinitesimal motion in $\mathbb{R}^3$ that is mapped to the Lie algebra as $\widetilde{\delta\mathbf{h}}$. The compatibility relationship between derivatives in Eq. (3.37) can be used to relate $\mathbf{v}$ and $\delta\mathbf{h}$ in vector form as

$$\delta(\mathbf{v}) - (\dot{\delta\mathbf{h}}) = \mathrm{ad}_{\mathbf{v}}(\delta\mathbf{h}) = \hat{\mathbf{v}}\delta\mathbf{h} \tag{3.101}$$

where Eq. (3.32) has been used to write the above using the hat operator. Using the expression for kinetic energy and the left-invariant velocity in Eq. (3.97), and considering the variation of the velocity using Eq. (3.101), we can write Eq. (3.99) as

$$\delta\left(\int_{t_i}^{t_f} \mathcal{K}\, dt\right) = \int_{t_i}^{t_f} \left((\dot{\delta\mathbf{h}})^T + \delta\mathbf{h}^T\hat{\mathbf{v}}^T\right)\mathbf{M}\mathbf{v}\, dt \tag{3.102}$$

Expanding the above equation and integrating by parts yields

$$\delta\left(\int_{t_i}^{t_f} \mathcal{K}\, dt\right) = \left[\delta\mathbf{h}^T\mathbf{M}\mathbf{v}\right]_{t_i}^{t_f} - \int_{t_i}^{t_f} \delta\mathbf{h}^T(\mathbf{M}\dot{\mathbf{v}} - \hat{\mathbf{v}}^T\mathbf{M}\mathbf{v})\, dt \tag{3.103}$$

Since the variations are fixed at the initial and final times, the first term on the right hand side vanishes. We can therefore obtain the variation of the kinetic energy as

$$\delta\mathcal{K} = -\delta\mathbf{h}^T\mathbf{g}_{ine} \tag{3.104}$$

where the inertial forces are given by

$$\mathbf{g}_{ine} = \mathbf{M}\dot{\mathbf{v}} - \hat{\mathbf{v}}^T\mathbf{M}\mathbf{v} \tag{3.105}$$

In order to compute the inertial forces of the tip mass, the body velocity has to be calculated. This can be done using the 2D equivalent of the expressions in Eq. (3.89). We denote the body frame at the tip mass by $\mathbf{H}_M$ as

$$\mathbf{H}_M = \begin{bmatrix} \mathbf{R} & \mathbf{x} \\ \mathbf{0} & 1 \end{bmatrix} \tag{3.106}$$

with the unknowns

$$\mathbf{x} = \begin{bmatrix} x \\ y \end{bmatrix}, \quad \mathbf{R} = \begin{bmatrix} \cos\theta & -\sin\theta \\ \sin\theta & \cos\theta \end{bmatrix} \tag{3.107}$$

and we calculate the components of the body velocity at the tip mass $\mathbf{v}_M$ using Eq. (3.89) as

$$\mathbf{u}^b = \mathbf{R}^T\dot{\mathbf{x}} = \begin{bmatrix} \cos\theta & \sin\theta \\ -\sin\theta & \cos\theta \end{bmatrix}\begin{bmatrix} \dot{x} \\ \dot{y} \end{bmatrix} = \begin{bmatrix} \cos\theta\dot{x} + \sin\theta\dot{y} \\ -\sin\theta\dot{x} + \cos\theta\dot{y} \end{bmatrix} \tag{3.108}$$

and

$$\boldsymbol{\omega}^b = (\mathbf{R}^T\dot{\mathbf{R}})^\vee = \left(\begin{bmatrix} \cos\theta & \sin\theta \\ -\sin\theta & \cos\theta \end{bmatrix} \begin{bmatrix} -\dot{\theta}\sin\theta & -\dot{\theta}\cos\theta \\ \dot{\theta}\cos\theta & -\dot{\theta}\sin\theta \end{bmatrix} \right)^\vee = \dot{\theta} \tag{3.109}$$

We therefore have

$$\mathbf{v}_M = \begin{bmatrix} \cos\theta\dot{x} + \sin\theta\dot{y} \\ -\sin\theta\dot{x} + \cos\theta\dot{y} \\ \dot{\theta} \end{bmatrix} \tag{3.110}$$

With the expression for velocity, and using Eq. (3.96), the inertial forces in Eq. (3.105) can be written as

$$\begin{aligned} \mathbf{g}_{ine} &= \mathbf{M}\frac{d}{dt}\left(\begin{bmatrix} \cos\theta\dot{x} + \sin\theta\dot{y} \\ -\sin\theta\dot{x} + \cos\theta\dot{y} \\ \dot{\theta} \end{bmatrix} \right) - \begin{bmatrix} 0 & -\dot{\theta} & -\sin\theta\dot{x} + \cos\theta\dot{y} \\ \dot{\theta} & 0 & -\cos\theta\dot{x} - \sin\theta\dot{y} \\ 0 & 0 & 0 \end{bmatrix}^T \mathbf{M} \begin{bmatrix} \cos\theta\dot{x} + \sin\theta\dot{y} \\ -\sin\theta\dot{x} + \cos\theta\dot{y} \\ \dot{\theta} \end{bmatrix} \\ &= \begin{bmatrix} m(\ddot{x}\cos\theta + \ddot{y}\sin\theta) \\ m(-\ddot{x}\sin\theta + \ddot{y}\cos\theta) \\ J\ddot{\theta} \end{bmatrix} \end{aligned} \tag{3.111}$$

3.4.4 Kinematic Joints

In general multibody systems, bodies are interconnected by different types of joints, each allowing a certain type of relative movement between them. In the context of the elastic pendulum, we require these joints to provide a description of the extension and rotation of the pendulum which is consistent with the Lie group framework of the system. In the Lie group setting, the relative frame transformation between two connected bodies is used to formulate these kinematic joints. These relative motions can be described mathematically using subspaces of $SE(3)$, which leads to the theory of Lie subgroups [193], [209]. A Lie subgroup is a subset $\mathcal{H}$ of a Lie group $\mathcal{G}$ that is itself a Lie group under the same group operation inherited from $\mathcal{G}$. While specific mathematical criteria must be satisfied for $\mathcal{H}$ to qualify as a subgroup of $\mathcal{G}$, a more informal definition is that $\mathcal{H}$ offers a constrained perspective of $\mathcal{G}$, including a particular subset of $\mathcal{G}$'s operations. For instance, the $SO(3)$ group is a subgroup of $SE(3)$, signifying that it represents a specific subset of the general rigid body motions in $SE(3)$, this being only rotations without translations. For a list of subgroups of $SE(3)$ commonly used in multibody dynamics see [211].

Considering a Lie group $\mathcal{G}$ and its subgroup $\mathcal{H}$, and elements of their respective algebras $\widetilde{\mathbf{h}_J} \in \mathfrak{g}$ and $\widetilde{\mathbf{h}_j} \in \mathfrak{h}$, a linear mapping $\mathbf{A}$ exists between the algebras such that

$$\mathbf{A}: \quad \mathfrak{h} \mapsto \mathfrak{g} \;\; ; \;\; \widetilde{\mathbf{h}_j} \mapsto \widetilde{\mathbf{A}\mathbf{h}_j} = \widetilde{\mathbf{h}_J} \tag{3.112}$$

The matrix $\mathbf{A}$ is a $k \times l$ full rank matrix, where k and l are the dimensions of $\mathfrak{g}$ and $\mathfrak{h}$ respectively.

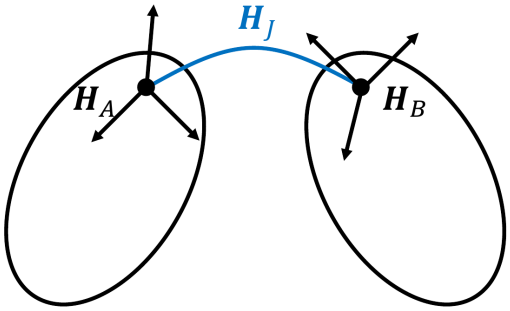


Figure 3.5: Relative transformation $\mathbf{H}_J$ from kinematic joint connecting two bodies.

The above relationship can also be stated in vector form as

$$\mathbf{h}_J = \mathbf{A}\mathbf{h}_j \tag{3.113}$$

In the $SE(3)$ formalism[1], the relationship between two body frames $\mathbf{H}_A$ and $\mathbf{H}_B$ which are connected by a kinematic joint J can be expressed as

$$\mathbf{H}_B = \mathbf{H}_A\mathbf{H}_J \tag{3.114}$$

where $\mathbf{H}_J$ is a transformation describing the relative motion between the two bodies due to the joint. This is shown schematically in Figure 3.5. This transformation belongs to a subgroup of $SE(3)$, and therefore has $l \leq 6$ motion variables. Depending on the type of joint, this can be described using a suitable $\mathbf{A}$ matrix which spans the subalgebra of allowed motions [211]. The variation and time derivative of $\mathbf{H}_J$ are given as

$$\delta(\mathbf{H}_J) = \mathbf{H}_J\widetilde{(\mathbf{A}\delta\mathbf{h}_j)} \quad \text{and} \quad (\dot{\mathbf{H}}_J) = \mathbf{H}_J\widetilde{(\mathbf{A}\mathbf{v}_j)} \tag{3.115}$$

where we have used Eq. (3.113) to substitute for the terms in the bracket[2]. Note that both vectors $\mathbf{A}\delta\mathbf{h}_j$ and $\mathbf{A}\mathbf{v}_j$ are expressed in the local frame, since they are left-multiplied by $\mathbf{H}_J$ in the above equation[3]. Returning to the elastic pendulum problem, the motion of the pendulum can be described by a revolute (hinge) joint $\mathbf{A}_R$, which allows rotation about a fixed axis, and a prismatic joint $\mathbf{A}_P$, which allows translation along a fixed axis. The $\mathbf{A}$ matrix for each joint is given by

$$\mathbf{A}_R = \begin{bmatrix} 0 \\ 0 \\ 1 \end{bmatrix} \quad \mathbf{A}_P = \begin{bmatrix} 1 \\ 0 \\ 0 \end{bmatrix} \tag{3.116}$$

It is noted that both matrices are 3×1, since the dimension of $\mathfrak{se}(2)$ is 3, and each joint only allows 1 relative motion. We therefore only have one motion variable for each joint. Eq. (3.113)

[1]Though our planar example is in $SE(2)$, all of what follows is applicable.
[2]The velocity term can also be written as Eq. (3.113) as $\mathbf{v}_J = \mathbf{A}\mathbf{v}_j$.
[3]Recall from Section 3.1.4 the left-invariant velocity field which was expressed in the local body frame.

can be written as

$$\begin{aligned} \mathbf{h}_{JR} &= \mathbf{A}_R \mathbf{h}_{jR} \\ \mathbf{h}_{JP} &= \mathbf{A}_P \mathbf{h}_{jP} \end{aligned} \tag{3.117}$$

where

$$\begin{aligned} \mathbf{h}_{jR} &\equiv \theta_j \\ \mathbf{h}_{jP} &\equiv r_j \end{aligned} \tag{3.118}$$

are the relative degrees of freedom (the motion variables) for each joint, which indicate the angle of the revolute joint, and the extension of the prismatic joint respectively. Given that the $\mathbf{A}$ matrices map these relative motions to $\mathbb{R}^3$ vectors in Eq. (3.117), the transformation frames corresponding to each joint $\mathbf{H}_{JR}, \mathbf{H}_{JP} \in SE(2)$ can be obtained from the group exponential map as follows:

$$\begin{aligned} \mathbf{H}_{JR} &= \exp_{SE(2)}(\widetilde{\mathbf{A}_R \mathbf{h}_{jR}}) = \exp_{SE(2)} \left(\begin{bmatrix} \widetilde{0} \\ 0 \\ \theta_j \end{bmatrix} \right) = \begin{bmatrix} \cos\theta_j & -\sin\theta_j & 0 \\ \sin\theta_j & \cos\theta_j & 0 \\ 0 & 0 & 1 \end{bmatrix} \\ \mathbf{H}_{JP} &= \exp_{SE(2)}(\widetilde{\mathbf{A}_P \mathbf{h}_{jP}}) = \exp_{SE(2)} \left(\begin{bmatrix} \widetilde{r_j} \\ 0 \\ 0 \end{bmatrix} \right) = \begin{bmatrix} 1 & 0 & r_j \\ 0 & 1 & 0 \\ 0 & 0 & 1 \end{bmatrix} \end{aligned} \tag{3.119}$$

With the above expressions, we can now describe the full state of the system using the following configuration matrix

$$\mathbf{H} = \mathrm{diag}(\mathbf{H}_M, \mathbf{H}_{JR}, \mathbf{H}_{JP}) \tag{3.120}$$

Similar to Eq. (3.115), infinitesimal motions and velocities can be written for the full configuration using the variation and the time derivative as

$$\delta(\mathbf{H}) = \mathbf{H}\widetilde{\delta\mathbf{h}^*} \tag{3.121}$$

and

$$(\dot{\mathbf{H}}) = \mathbf{H}\widetilde{\mathbf{v}^*} \tag{3.122}$$

with the following vectors

$$\delta\mathbf{h}^* = \begin{bmatrix} \delta\mathbf{h}_M & \delta\mathbf{h}_{JR} & \delta\mathbf{h}_{JP} \end{bmatrix}^T \tag{3.123}$$

and

$$\mathbf{v}^* = \begin{bmatrix} \mathbf{v}_M & \mathbf{v}_{JR} & \mathbf{v}_{JP} \end{bmatrix}^T \tag{3.124}$$

Both vectors can be written in terms of their respective subalgebra elements, as[1]

$$\delta\mathbf{h}^* = \mathbf{A}\delta\mathbf{h} \qquad \mathbf{v}^* = \mathbf{A}\mathbf{v} \tag{3.125}$$

where

$$\mathbf{A} = \text{diag}(\mathbf{I}, \mathbf{A}_R, \mathbf{A}_P) \tag{3.126}$$

and

$$\delta\mathbf{h} = \begin{bmatrix}\delta\mathbf{h}_M & \delta\mathbf{h}_{jR} & \delta\mathbf{h}_{jP}\end{bmatrix}^T \tag{3.127}$$

$$\mathbf{v} = \begin{bmatrix}\mathbf{v}_M & \mathbf{v}_{jR} & \mathbf{v}_{jP}\end{bmatrix}^T \tag{3.128}$$

3.4.5 Constraint Equation

For the planar pendulum under consideration, we consider a body frame located at the ground, $\mathbf{H}_G$, and write Eq. (3.114) using the joint frames, to relate $\mathbf{H}_M$ and $\mathbf{H}_G$ as

$$\mathbf{H}_M = \mathbf{H}_G\mathbf{H}_{JR}\mathbf{H}_{JP} \tag{3.129}$$

As the ground frame is fixed, $\mathbf{H}_G = \mathbf{I}$, and the above equation becomes

$$\mathbf{H}_M = \mathbf{H}_{JR}\mathbf{H}_{JP} \tag{3.130}$$

The tip mass frame can therefore be described solely by the combined action of the joints. Note that in general multibody problems, the full configuration matrix of the system will consist of the frames for N bodies and n joints. In this simple example, however, Eq. (3.130) contains the frames from the full system configuration in Eq. (3.120). It is also noted that, since each joint transformation is relative and expressed in the local frame, the pendulum's motion must be described by initially applying a rotation, followed by a translation. This sequence is crucial because the body frame at the tip mass will rotate with the application of the rotation, thereby aligning the local axis for subsequent translation, allowing all possible configurations of the pendulum in physical space to be accounted for.

Eq. (3.130) can be reformulated to give a constraint equation as

$$\mathbf{H}_\Phi = \mathbf{H}_M^{-1}\mathbf{H}_{JR}\mathbf{H}_{JP} = \mathbf{I}_{3\times3} \tag{3.131}$$

This constraint can be incorporated in the system's equation of motion by means of the Lagrange multiplier method in Hamilton's principle. To facilitate this, Eq. (3.131) must be written in vector form, which can be done using the logarithm map.

We use an alternative vectorial map, Φ, which is equivalent to the logarithm map near the identity element up to a second-order error term. This is used as it is computationally less expensive that the logarithm map, and the associated error can be assumed insignificant [209].

[1]For the revolute and prismatic joints, $\delta\mathbf{h}_{j\{R,P\}} = \delta(\mathbf{h}_{j\{R,P\}})$ and $\mathbf{v}_{j\{R,P\}} = (\dot{\mathbf{h}}_{j\{R,P\}})$. See Appendix B.

It is given as the following linear operator

$$\Phi: \quad SE(2) \mapsto \mathbb{R}^3 \;\mid\; \forall \mathbf{H} = \begin{bmatrix} \mathbf{R} & \mathbf{x} \\ \mathbf{0} & 1 \end{bmatrix} \in SE(2) : \Phi(\mathbf{H}) = \begin{bmatrix} \mathbf{x} \\ \frac{1}{2}(\mathbf{R} - \mathbf{R}^T)^\vee \end{bmatrix}_{3\times 1} \tag{3.132}$$

such that Eq. (3.131) can be written as

$$\Phi(\mathbf{H}_\Phi) = \Phi(\mathbf{I}_{3\times 3}) = \mathbf{0}_{3\times 3} \tag{3.133}$$

Computing the constraint equation using the tip mass and joint frames in Eq. (3.119) gives

$$\begin{aligned} \mathbf{H}_\Phi &= \begin{bmatrix} \cos\theta & -\sin\theta & 0 \\ \sin\theta & \cos\theta & 0 \\ 0 & 0 & 1 \end{bmatrix}^{-1} \begin{bmatrix} \cos\theta_j & -\sin\theta_j & 0 \\ \sin\theta_j & \cos\theta_j & 0 \\ 0 & 0 & 1 \end{bmatrix} \begin{bmatrix} 1 & 0 & r_j \\ 0 & 1 & 0 \\ 0 & 0 & 1 \end{bmatrix} \\ &= \begin{bmatrix} \cos(\theta_j - \theta) & -\sin(\theta_j - \theta) & r_j\cos(\theta_j - \theta) - x\cos\theta - y\sin\theta \\ \sin(\theta_j - \theta) & \cos(\theta_j - \theta) & r_j\sin(\theta_j - \theta) + x\sin\theta - y\cos\theta \\ 0 & 0 & 1 \end{bmatrix} \end{aligned} \tag{3.134}$$

which when vectorised using Φ yields the following constraint vector

$$\Phi(\mathbf{H}_\Phi) = \begin{bmatrix} r_j\cos(\theta_j - \theta) - x\cos\theta - y\sin\theta \\ r_j\sin(\theta_j - \theta) + x\sin\theta - y\cos\theta \\ \sin(\theta_j - \theta) \end{bmatrix} = \mathbf{0} \tag{3.135}$$

3.4.6 Constraint Gradient

The variation of the constraint vector is needed to formulate the equation of motion with Hamilton's principle and using a Lagrange multiplier method. The linearity of the vector map Φ ensures that it commutes with the variation, such that

$$\delta(\Phi(\mathbf{H}_\Phi)) = \Phi(\delta(\mathbf{H}_\Phi)) \tag{3.136}$$

Expanding the right hand side, we have

$$\begin{aligned} \Phi(\delta(\mathbf{H}_\Phi)) &= \Phi(\mathbf{H}_\Phi \widetilde{\delta\mathbf{h}_\Phi}) \\ &= \Phi(\widetilde{\delta\mathbf{h}_\Phi}) \\ &= \delta\mathbf{h}_\Phi \end{aligned} \tag{3.137}$$

where $\mathbf{H}_\Phi = \mathbf{I}$ drops from the expression, and the vector map Φ, by definition, reverses the $\widetilde{()}$ to produce a vector. In order to compute $\delta\mathbf{h}_\Phi$, the variation of $\mathbf{H}_\Phi$ in Eq. (3.131) can be

calculated as

$$\begin{aligned}\delta\mathbf{H}_\Phi &= \delta\mathbf{H}_M^{-1}\mathbf{H}_{JR}\mathbf{H}_{JP} + \mathbf{H}_M^{-1}\delta\mathbf{H}_{JR}\mathbf{H}_{JP} + \mathbf{H}_M^{-1}\mathbf{H}_{JR}\delta\mathbf{H}_{JP} \\ &= -\widetilde{\delta\mathbf{h}_M}\mathbf{H}_M^{-1}\mathbf{H}_{JR}\mathbf{H}_{JP} + \mathbf{H}_M^{-1}\mathbf{H}_{JR}\widetilde{\delta\mathbf{h}_{JR}}\mathbf{H}_{JP} + \mathbf{H}_M^{-1}\mathbf{H}_{JR}\mathbf{H}_{JP}\widetilde{\delta\mathbf{h}_{JP}}\end{aligned} \tag{3.138}$$

where we have used $\delta\mathbf{H}_M^{-1} = -\widetilde{\delta\mathbf{h}_M}\mathbf{H}_M^{-1}$. The variation of $\mathbf{H}_\Phi$ can also be computed as

$$\delta\mathbf{H}_\Phi = \mathbf{H}_\Phi\widetilde{\delta\mathbf{h}_\Phi} = \mathbf{H}_M^{-1}\mathbf{H}_{JR}\mathbf{H}_{JP}\widetilde{\delta\mathbf{h}_\Phi} \tag{3.139}$$

By equating Eq. (3.138) and Eq. (3.139), $\widetilde{\delta\mathbf{h}_\Phi}$ can be written as

$$\widetilde{\delta\mathbf{h}_\Phi} = -\widetilde{\delta\mathbf{h}_M} + \mathrm{Ad}_{\mathbf{H}_{JP}^{-1}}(\widetilde{\delta\mathbf{h}_{JR}}) + \widetilde{\delta\mathbf{h}_{JP}} \tag{3.140}$$

and in vector form, as

$$\delta\mathbf{h}_\Phi = -\delta\mathbf{h}_M + \mathrm{Ad}_{\mathbf{H}_{JP}^{-1}}(\delta\mathbf{h}_{JR}) + \delta\mathbf{h}_{JP} \tag{3.141}$$

Using the relationships in Eq. (3.117), this can be written as

$$\delta\mathbf{h}_\Phi = \begin{bmatrix}-\mathbf{I} & \mathrm{Ad}_{\mathbf{H}_{JP}^{-1}}\mathbf{A}_R & \mathbf{A}_P\end{bmatrix}\begin{bmatrix}\delta\mathbf{h}_M \\ \delta\mathbf{h}_{jR} \\ \delta\mathbf{h}_{jP}\end{bmatrix} \tag{3.142}$$

The right hand side of Eq. (3.136) has therefore been determined and is noted to be in vector form. Similarly, considering the left-hand side, which should also be expressed in vector form, the directional derivatives of the constraints can be written such that

$$\delta(\Phi(\mathbf{H}_\Phi)) = \mathrm{D}\Phi\,.\,\delta(\mathbf{H}_\Phi) = \mathrm{D}\Phi\,.\,\mathbf{H}_\Phi\widetilde{\mathbf{A}\delta\mathbf{h}} = \mathrm{D}\Phi\,.\,\widetilde{\mathbf{A}\delta\mathbf{h}} \tag{3.143}$$

Defining the constraint gradient Φ_q from the directional derivative, this can be written in vector form as

$$\mathrm{D}\Phi\,.\,\widetilde{\mathbf{A}\delta\mathbf{h}} = \Phi_q\mathbf{A}\delta\mathbf{h} \tag{3.144}$$

Finally, equating Eq. (3.142) and Eq. (3.144), the constraint gradient is given as

$$\Phi_q\mathbf{A} = \begin{bmatrix}-\mathbf{I} & \mathrm{Ad}_{\mathbf{H}_{JP}^{-1}}\mathbf{A}_R & \mathbf{A}_P\end{bmatrix} \tag{3.145}$$

This can be evaluated using the expressions for $\mathbf{A}_R$ and $\mathbf{A}_P$ in Eq. (3.116), and by computing the Adjoint of $\mathbf{H}_{JP}^{-1}$, to give the constrain gradient as

$$\Phi_q\mathbf{A} = \begin{bmatrix}-1 & 0 & 0 & 0 & 1 \\ 0 & -1 & 0 & r_j & 0 \\ 0 & 0 & -1 & 1 & 0\end{bmatrix} \tag{3.146}$$

3.4.7 Elastic Potential Energy

The potential energy of the joints can be accounted for by considering the stiffnesses related to the relative coordinates involved in each joint. The variation of the potential energy of each joint can be written as [211]

$$\delta(\mathcal{V}_{int}) = \delta\mathbf{h}_j^T \mathbf{g}_{int} \tag{3.147}$$

where the internal forces are found using the stiffness matrix $\mathbf{K}$, and is given by

$$\mathbf{g}_{int} = \mathbf{K}(\boldsymbol{\alpha} - \boldsymbol{\alpha}_0) \tag{3.148}$$

where $\boldsymbol{\alpha}$ defines the length parameter. For the planar pendulum, the internal forces for both joints can be written together as

$$\mathbf{g}_{int} = \begin{bmatrix} k_\theta & 0 \\ 0 & k_r \end{bmatrix} \begin{bmatrix} \theta_j - \theta_0 \\ r_j - r_0 \end{bmatrix} \tag{3.149}$$

3.4.8 Full Equation of Motion

The full equation of motion for the pendulum formulated on the $SE(2)$ group can now be derived. Hamilton's principle can be stated following a Lagrange multiplier method for the constraints as follows

$$\delta\left(\int_{t_i}^{t_f} \mathcal{K} - \mathcal{V}_{int} - \boldsymbol{\lambda}^T \Phi(\mathbf{H}_\Phi)\, dt\right) = 0 \tag{3.150}$$

where $\boldsymbol{\lambda}$ are the Lagrange multipliers associated with the kinematic constraints. Applying the variation to the different terms in the integral, and using the equations developed in previous sections, the equilibrium equations can be developed. Adding the kinematic equation for the full system configuration in Eq. (3.122), and the constraint equation in Eq. (3.135), the full equation of motion for the planar pendulum can be written as

$$\begin{aligned} \dot{\mathbf{H}} &= \mathbf{H}\widetilde{\mathbf{A}\mathbf{v}} \\ \mathbf{g}_{ine} + \mathbf{g}_{int} + \mathbf{A}^T \Phi_q^T \boldsymbol{\lambda} &= \mathbf{0} \\ \Phi(\mathbf{H}_\Phi) &= \mathbf{0} \end{aligned} \tag{3.151}$$

Depending on the system and the type of external forcing, the equations above may become uncoupled, such that the equilibrium equation can be solved first without having to solve for the position and orientation of the body, and the kinematic equation can then be used to obtain the configuration of the system. In the case of the unforced planar pendulum, these equations are indeed uncoupled and can be simplified further. Using the expressions for the inertial and internal forces developed in the previous sections, and considering the full system configuration,

the equilibrium equation may be written as

$$\begin{bmatrix} m & 0 & 0 & 0 & 0 \\ 0 & m & 0 & 0 & 0 \\ 0 & 0 & J & 0 & 0 \\ 0 & 0 & 0 & 0 & 0 \\ 0 & 0 & 0 & 0 & 0 \end{bmatrix} \begin{bmatrix} \ddot{x}\cos\theta + \ddot{y}\sin\theta \\ -\ddot{x}\sin\theta + \ddot{y}\cos\theta \\ \ddot{\theta} \\ 0 \\ 0 \end{bmatrix} + \begin{bmatrix} 0 & 0 & 0 & 0 & 0 \\ 0 & 0 & 0 & 0 & 0 \\ 0 & 0 & 0 & 0 & 0 \\ 0 & 0 & 0 & k_\theta & 0 \\ 0 & 0 & 0 & 0 & k_r \end{bmatrix} \begin{bmatrix} x \\ y \\ \theta \\ \theta_j - \theta_0 \\ r_j - r_0 \end{bmatrix} + \begin{bmatrix} -1 & 0 & 0 \\ 0 & -1 & 0 \\ 0 & 0 & -1 \\ 0 & r_j & 1 \\ 1 & 0 & 0 \end{bmatrix} \boldsymbol{\lambda} = \mathbf{0} \tag{3.152}$$

The inertial and internal forces are also uncoupled in the above equation. The Lagrange multipliers may therefore be written in terms of the inertial forces in the first three lines of the equation above as

$$\boldsymbol{\lambda} = \begin{bmatrix} m\cos\theta\ddot{x} + m\sin\theta\ddot{y} \\ m\cos\theta\ddot{y} - m\sin\theta\ddot{x} \\ J\ddot{\theta} \end{bmatrix} \tag{3.153}$$

These can now be substituted back into the last two equations of Eq. (3.152), and the internal forces can be evaluated, which gives

$$\begin{aligned} k_\theta(\theta_j - \theta_0) + r_j(m\cos\theta\ddot{y} - m\sin\theta\ddot{x}) + J\ddot{\theta} = 0 \\ k_r(r_j - r_0) + m\cos\theta\ddot{x} + m\sin\theta\ddot{y} = 0 \end{aligned} \tag{3.154}$$

Finally, the constraint equation in Eq. (3.135) can be solved, giving $\theta_j = \theta$, and can therefore be written as

$$\Phi(\mathbf{H}_\Phi) = \begin{bmatrix} r_j - x\cos\theta - y\sin\theta \\ x\sin\theta - y\cos\theta \\ 0 \end{bmatrix} = \mathbf{0} \tag{3.155}$$

which can be simplified further to give

$$\begin{aligned} x = r_j\cos\theta \\ y = r_j\sin\theta \end{aligned} \tag{3.156}$$

Putting these back into Eq. (3.154), as using $r_j \equiv r$ for simplicity, gives the final expression of the equation of motion as

$$\begin{aligned} k_\theta(\theta - \theta_0) + J\ddot{\theta} + m(r^2\ddot{\theta} + 2r\dot{r}\dot{\theta}) = 0 \\ k_r(r - r_0) + m(\ddot{r} - r\dot{\theta}^2) = 0 \end{aligned} \tag{3.157}$$

which is identical to the equation of motion in polar coordinates in Eq. (3.93).

3.5 Beam Equations Formulated on the $SE(3)$ Group

In this section, we present and illustrate the equations of motion and finite element discretisation of shear deformable geometrically exact beams formulated on the $SE(3)$ group, as developed by Sonneville [208].

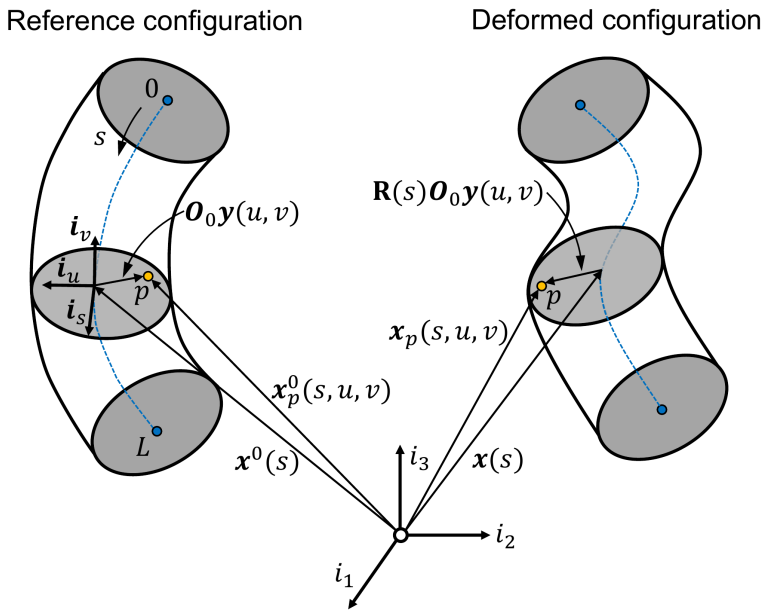


Figure 3.6: Description of beam kinematics.

We begin by considering a straight beam of length L with the value $s \in [0, L]$ defined as the longitudinal coordinate along its reference line, as depicted in Figure 3.6. The position of any point p on the reference beam at time $t = 0$ can be written in the inertial coordinate frame as [208]

$$\mathbf{x}_p^0(s,u,v) = \mathbf{x}^0(s) + \mathbf{O}_0\boldsymbol{y}(u,v) \tag{3.158}$$

where $\mathbf{x}(s)$ is the position vector along the neutral axis, $\mathbf{O}_0 = [\mathbf{i}_s \ \mathbf{i}_u \ \mathbf{i}_v]$ is a constant rotation matrix accounting for the beam's reference orientation relative to the inertial frame, and $\boldsymbol{y}(u,v) = [0 \ u \ v]^T$ contains the coordinates of the point along the cross section axes. We assume that the cross sections do not deform, and therefore the point coordinates along the cross section axes remain unchanged. Deformation of the beam will impose a translation and rotation of the cross sections relative to the fixed inertial frame. The position of the point p in the deformed configuration at time t, written in the inertial frame, will therefore be written as

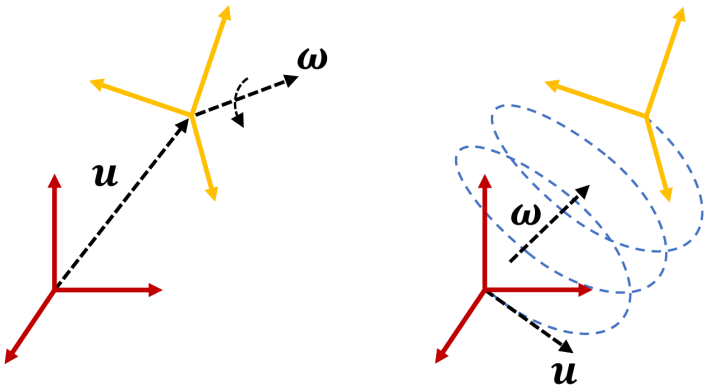
$$\mathbf{x}_p(s,u,v) = \mathbf{x}(s) + \mathbf{R}(s)\mathbf{O}_0\boldsymbol{y}(u,v) \tag{3.159}$$

where $\mathbf{R}(s) \in SO(3)$ is the rotation vector accounting for the rotation of the cross section, and which brings the vector $\mathbf{O}_0\boldsymbol{y}(u,v)$ from the local frame onto the global inertial frame. Similar to Eq. (3.64), this equation can be restated in homogenous form using a transformation matrix $\mathbf{H}(s) \in SE(3)$ pertaining to a rigid body motion, given by

$$\mathbf{H}(s) = \begin{bmatrix} \mathbf{R}(s) & \mathbf{x}(s) \\ \mathbf{0}_{1\times 3} & 1 \end{bmatrix} \tag{3.160}$$

such that

$$\begin{bmatrix} \mathbf{x}_p(s,u,v) \\ 1 \end{bmatrix} = \mathbf{H}(s) \begin{bmatrix} \mathbf{O}_0\boldsymbol{y}(u,v) \\ 1 \end{bmatrix} \tag{3.161}$$



(a) $\mathbb{R}^3 \times SO(3)$ (b) $SE(3)$

Figure 3.7: Description of rigid body motion. The $\mathbb{R}^3 \times SO(3)$ group defines a translation along the vector $\boldsymbol{u}$, followed by a rotation about the axis $\boldsymbol{\omega}$. The $SE(3)$ group defines rigid body motion as motion along a helix, where the vector $\boldsymbol{u}$ defines the direction and length of the helix trajectory, and $\boldsymbol{\omega}$ is the rotation axis. For $SE(3)$, $\boldsymbol{u}$ and $\boldsymbol{\omega}$ are the same as the twist parameters in Eq. (3.71).

We will term $\mathbf{H}(s)$ the material frame on the beam neutral axis, and adopt a local frame approach by attaching a frame to each material point of the beam. The beam deformation model then essentially reduces to the rigid body motion of its cross sections, which we assume do not deform themselves.

Remark:

With the $SE(3)$ group formally introduced and discussed in this chapter, a schematic comparison can now be made between the $SE(3)$ group, and the $\mathbb{R}^3 \times SO(3)$ group, which, as discussed in Section 2.3, is the group used by classical geometrically exact beam formulations. Defining the kinematic description of the beam deformation as the rigid body motion of its cross sections, this motion can be described in two ways. The $\mathbb{R}^3 \times SO(3)$ group defines rigid body motion in 3D space as independent translational and rotational motions, while the $SE(3)$ group defines rigid body motion as the coupled translational and rotational motion which results in a helical trajectory defined by the twist parameters in $\mathfrak{se}(3)$. This is illustrated in Figure 3.7.

3.5.1 Derivatives

The deformation of the beam is determined by taking the derivative of the position field. Differentiating Eq. (3.161) gives

$$\begin{bmatrix} \mathbf{x}_p'(s,u,v) \\ 0 \end{bmatrix} = \mathbf{H}'(s) \begin{bmatrix} \mathbf{O}_0\boldsymbol{y}(u,v) \\ 1 \end{bmatrix} \tag{3.162}$$

where $\mathbf{x}_p'(s,u,v) \equiv \frac{\partial \mathbf{x}_p(s,u,v)}{\partial s}$. From the left-invariant representation of derivatives on $SE(3)$ described in Section 3.1.4, the derivative of the frame may be written as

$$\frac{\mathrm{d}\mathbf{H}(s)}{\mathrm{d}s} = \mathbf{H}'(s) = \mathbf{H}(s)\widetilde{\mathbf{f}}(s) \tag{3.163}$$

where $\widetilde{\mathbf{f}}(s) \in \mathfrak{se}(3)$ is the deformation gradient, which is written in the local body frame, owing to the left-invariant representation. The deformation gradient can be written in terms of the twist parameters in vector form as

$$\mathbf{f}(s) = \begin{bmatrix} \mathbf{f}_U(s) \\ \mathbf{f}_\Omega(s) \end{bmatrix} \tag{3.164}$$

We may also write $\mathbf{H}'(s)$ by differentiating $\mathbf{R}(s)$ and $\mathbf{x}(s)$ in Eq. (3.160) directly, as

$$\mathbf{H}'(s) = \begin{bmatrix} \mathbf{R}'(s) & \mathbf{x}'(s) \\ \mathbf{0}_{1\times 3} & 0 \end{bmatrix} \tag{3.165}$$

By the equivalence of Eq. (3.163) and Eq. (3.165), and writing $\widetilde{\mathbf{f}}(s)$ using the parameters in Eq. (3.164) and using the definition in Eq. (3.70), we have

$$\begin{bmatrix} \mathbf{R}'(s) & \mathbf{x}'(s) \\ \mathbf{0}_{1\times 3} & 0 \end{bmatrix} = \mathbf{H}(s)\widetilde{\mathbf{f}}(s) = \begin{bmatrix} \mathbf{R}(s) & \mathbf{x}(s) \\ \mathbf{0}_{1\times 3} & 1 \end{bmatrix} \begin{bmatrix} \widetilde{\mathbf{f}}_\Omega(s) & \mathbf{f}_U(s) \\ \mathbf{0}_{1\times 3} & 0 \end{bmatrix} \tag{3.166}$$

which when multiplied gives

$$\begin{aligned} \mathbf{x}'(s) &= \mathbf{R}(s)\mathbf{f}_U(s) \\ \mathbf{R}'(s) &= \mathbf{R}(s)\widetilde{\mathbf{f}}_\Omega(s) \end{aligned} \tag{3.167}$$

which can be rearranged, such that the deformation gradients may be written as

$$\begin{aligned} \mathbf{f}_U(s) &= \mathbf{R}^T(s)\mathbf{x}'(s) \\ \mathbf{f}_\Omega(s) &= (\mathbf{R}^T(s)\mathbf{R}'(s))^\vee \end{aligned} \tag{3.168}$$

where we have used the inverse map in Eq. (3.9) to write the deformations in vector form.

The deformation gradient can now be split into those of the reference $\mathbf{f}^0$ and current $\boldsymbol{\epsilon}$ configurations, and classical notations of position $\boldsymbol{\gamma}$ and rotation $\boldsymbol{\kappa}$ deformations can be introduced as

$$\begin{aligned} \mathbf{f}(s) &= \begin{bmatrix} \mathbf{f}_U(s) \\ \mathbf{f}_\Omega(s) \end{bmatrix} = \mathbf{f}^0(s) + \boldsymbol{\epsilon}(s), \quad \text{with} \\ \boldsymbol{\epsilon}(s) &= \begin{bmatrix} \boldsymbol{\gamma}(s) \\ \boldsymbol{\kappa}(s) \end{bmatrix} \end{aligned} \tag{3.169}$$

Using Eq. (3.168), $\boldsymbol{\epsilon}(s)$ in Eq. (3.169) can therefore be written as

$$\begin{aligned} \boldsymbol{\gamma}(s) &= \mathbf{R}^T(s)\mathbf{x}'(s) - \mathbf{f}_U^0(s) \\ \boldsymbol{\kappa}(s) &= (\mathbf{R}^T(s)\mathbf{R}'(s))^\vee - \mathbf{f}_\Omega^0(s) \end{aligned} \tag{3.170}$$

which is equivalent to classical deformation measures of the neutral axis introduced in geometrically exact formulations, where $\boldsymbol{\gamma}$ represents the strains along the neutral axis and the

shear strains, and $\boldsymbol{\kappa}$ represents the torsion and the bending curvatures. These deformation measures are readily derived from the derivatives on the $SE(3)$ group. As per the local-frame representation of left-invariant derivatives on $SE(3)$ (see Section 3.3.1), these quantities are invariant under rigid body transformations, and are expressed in the local frame of the beam. This therefore leads to a beam formulation which maintains objectivity of the strain measures under rigid body motion.

Returning to Eq. (3.162), and using the expressions developed in Eq. (3.167) and Eq. (3.165), the partial derivative with respect to s at any point on the beam can be written as

$$\mathbf{x}'_p(s,u,v) = \mathbf{R}(s)(\mathbf{f}_U(s) + \widetilde{\mathbf{f}}_\Omega(s)\mathbf{O}_0\boldsymbol{y}(u,v)) = \mathbf{R}(s)\mathbf{N}(u,v)\mathbf{f}(s) \tag{3.171}$$

where

$$\mathbf{N} = \begin{bmatrix}\mathbf{I}_{3\times3} & -\widetilde{\mathbf{O}_0\boldsymbol{y}}(u,v)\end{bmatrix} \tag{3.172}$$

is used to make the expression more compact. Note the $\widetilde{(\bullet)}$ is moved from $\mathbf{f}_\Omega(s)$ to $\boldsymbol{y}(u,v)$ using the relationship $\widetilde{\mathbf{a}}\mathbf{b} = -\widetilde{\mathbf{a}\mathbf{b}}$.

The evaluation of the other partial derivatives of $\mathbf{x}_p(s,u,v)$ is more straightforward, as

$$\frac{\partial \mathbf{x}_p(s,u,v)}{\partial u} = \mathbf{R}(s)\mathbf{i}_u \qquad \frac{\partial \mathbf{x}_p(s,u,v)}{\partial v} = \mathbf{R}(s)\mathbf{i}_v \tag{3.173}$$

It is noted that due to the assumption that the cross-sections remain undeformed, both $\mathbf{i}_u$ and $\mathbf{i}_v$ are defined based on the reference configuration and do not depend on the beam's state of deformation.

The terms of the Green Lagrange strain tensor $\mathbf{GL}(s,u,v)$ can now be evaluated from

$$GL_{ij} = \frac{1}{2}\left(\frac{\partial \mathbf{x}_p^T}{\partial x_i}\frac{\partial \mathbf{x}_p}{\partial x_j} - \frac{\partial \mathbf{x}_p^{0T}}{\partial x_i}\frac{\partial \mathbf{x}_p^0}{\partial x_j}\right), \qquad x_i, x_j = s,u,v \tag{3.174}$$

which, from the derivatives, results in the following terms

$$\begin{aligned} GL_{ss} &= \mathbf{f}^{0T}\mathbf{N}^T\mathbf{N}\boldsymbol{\epsilon} + \frac{1}{2}\boldsymbol{\epsilon}^T\mathbf{N}^T\mathbf{N}\boldsymbol{\epsilon} \\ GL_{su} = GL_{us} &= \frac{1}{2}\mathbf{i}_u^T\mathbf{N}^T\boldsymbol{\epsilon} \\ GL_{sv} = GL_{vs} &= \frac{1}{2}\mathbf{i}_v^T\mathbf{N}^T\boldsymbol{\epsilon} \end{aligned} \tag{3.175}$$

Under the assumption of small deformations for $\boldsymbol{\gamma}$ and $\boldsymbol{\kappa}$, the second term in GL_{ss} vanishes. We can now introduce the following 3×1 vector

$$\mathbf{gl}(s,u,v) = \begin{bmatrix}GL_{ss} & 2GL_{su} & 2GL_{sv}\end{bmatrix}^T = \mathbf{D}(s,u,v)\boldsymbol{\epsilon}(s) \tag{3.176}$$

where

$$\mathbf{D}(s,u,v) = \begin{bmatrix} \mathbf{f}^{0T}\mathbf{N}^T\mathbf{N} \\ \mathbf{i}_u^T\mathbf{N} \\ \mathbf{i}_v^T\mathbf{N} \end{bmatrix} \tag{3.177}$$

is a 3×6 constant matrix.

Here we note that, if the derivatives are not expressed locally using the left-invariant vector fields, the terms in the resulting strain tensor would no longer be invariant under rigid body transformation, and would contain information about the large amplitude motions of the beam. As such, the second-order terms can no longer be neglected under the assumption of small deformations. It is further noted that, other geometrically exact beam formulations built on the $\mathbb{R}^3 \times SO(3)$ group (as reviewed in Section 2.3) still aim to work with the deformation measures $\boldsymbol{\gamma}$ and $\boldsymbol{\kappa}$ in Eq. (3.170). However, as these expressions cannot be immediately derived on the $\mathbb{R}^3 \times SO(3)$ group, additional manipulations become necessary to enable the deformations to be written in the local frame. However, these manipulations are not embedded in the Lie group structure of $\mathbb{R}^3 \times SO(3)$, and can therefore be seen as "fixes" rather than components supported by the group structure. The most consistent expression of the local strains can therefore only be obtained under the $SE(3)$ framework using the left-invariant representation of the derivates.

The conjugate stress to the Green Lagrange strain tensor, that is, the second Piola-Kirchhoff stress tensor can be formulated, and the strain energy can be written as

$$\mathcal{V}_{int} = \frac{1}{2}\int_V \mathbf{s}^T\mathbf{g}\mathbf{l}\, ds \tag{3.178}$$

where V is the volume of the beam in the reference configuration, and

$$\mathbf{s} = \begin{bmatrix} S^{ss} & S^{su} & S^{sv} \end{bmatrix}^T \tag{3.179}$$

are the terms of the second Piola-Kirchhoff stress tensor $\mathbf{S}(s,u,v)$. Using the Green Lagrange strain terms in (3.176), the strain energy can be written as

$$\mathcal{V}_{int} = \frac{1}{2}\int_0^L \boldsymbol{\epsilon}^T\mathbf{r}\, ds = \frac{1}{2}\int_0^L (\boldsymbol{\gamma}^T\mathbf{n} + \boldsymbol{\kappa}^T\mathbf{m}) \tag{3.180}$$

where $\mathbf{n}$ and $\mathbf{m}$ are the resulting force and moment vectors, integrated over the cross sections as

$$\mathbf{r}(s) = \begin{bmatrix} \mathbf{n}(s) \\ \mathbf{m}(s) \end{bmatrix} = \int_A \mathbf{D}^T\mathbf{s}\, ds \tag{3.181}$$

The cross section resultants can then be related to the strains through constitutive equations for a linear elastic material as

$$\begin{bmatrix} \mathbf{n}(s) \\ \mathbf{m}(s) \end{bmatrix} = \mathbf{K}\begin{bmatrix} \boldsymbol{\gamma}(s) \\ \boldsymbol{\kappa}(s) \end{bmatrix} \tag{3.182}$$

where $\mathbf{K}$ is the stiffness matrix. For initially undeformed beams whose neutral axis is aligned

with the reference frame, and whose cross sectional properties remain constant over its length, $\mathbf{K}$ becomes diagonal, and is given by

$$\mathbf{K} = \begin{bmatrix} \mathbf{K}_U & \mathbf{0}_{3\times3} \\ \mathbf{0}_{3\times3} & \mathbf{K}_\Omega \end{bmatrix} \tag{3.183}$$

with $\mathbf{K}_U = \text{diag}(EA, GA_u, GA_v)$ containing the axial and shear stiffness terms, and $\mathbf{K}_\Omega = \text{diag}(GJ, EI_u, EI_v)$ contains the torsional and bending stiffness terms. In general however, the stiffness matrix is not diagonal. With the stiffness matrix, the following expression for the strain energy can be written in quadratic form

$$\mathcal{V}_{int} = \frac{1}{2}\int_0^L \boldsymbol{\epsilon}^T(s)\mathbf{K}\boldsymbol{\epsilon}(s)\,ds \tag{3.184}$$

It is again noted that the exclusion of second-order strain terms is a significant advantage of representing the derivatives in the local frame using left-invariant vector fields. For other representations where these terms cannot be neglected, a quadratic form of the strain energy cannot be written in terms of these deformations.

The velocity field at any point of the beam can be obtained by the time derivative of the position field in Eq. (3.161) as

$$\begin{bmatrix} \dot{\mathbf{x}}_p(s,u,v) \\ 0 \end{bmatrix} = \dot{\mathbf{H}}(s) \begin{bmatrix} \mathbf{O}_0\boldsymbol{y}(u,v) \\ 1 \end{bmatrix} \tag{3.185}$$

where the time derivative of the material frame $\dot{\mathbf{H}}(s)$ can be expressed with left-invariant velocities $\tilde{\mathbf{v}}(s) \in \mathfrak{se}(3)$ expressed in the local frame as

$$\dot{\mathbf{H}}(s) = \mathbf{H}(s)\tilde{\mathbf{v}}(s) \tag{3.186}$$

Following the derivation of the rigid body velocities in Section 3.3.1, $\mathbf{v}(s)$ can be written as

$$\mathbf{v}(s) = \begin{bmatrix} \mathbf{v}_U(s) \\ \mathbf{v}_\Omega(s) \end{bmatrix} = \begin{bmatrix} \mathbf{R}^T(s)\dot{\mathbf{x}}(s) \\ (\mathbf{R}^T(s)\dot{\mathbf{R}}(s))^\vee \end{bmatrix} \tag{3.187}$$

or equivalently

$$\begin{aligned} \dot{\mathbf{x}}(s) &= \mathbf{R}(s)\mathbf{v}_U(s) \\ \dot{\mathbf{R}}(s) &= \mathbf{R}(s)\tilde{\mathbf{v}}_\Omega(s) \end{aligned} \tag{3.188}$$

Substituting the above into Eq. (3.185), the velocities at any point of the beam can thus be written as

$$\dot{\mathbf{x}}_p(s,u,v) = \mathbf{R}(s)(\mathbf{v}_U(s) + \tilde{\mathbf{v}}_\Omega(s)\mathbf{O}_0\boldsymbol{y}(u,v)) \tag{3.189}$$

The compatibility of the derivatives with respect to space and time also has to be satisfied

according to Eq. (3.37) which gives

$$\mathbf{v}' - \dot{\boldsymbol{\epsilon}} = \hat{\mathbf{v}}\boldsymbol{\epsilon} \tag{3.190}$$

With the expression for the velocity field, the kinetic energy of the beam can be computed as

$$\mathcal{K} = \frac{1}{2}\int_V \rho \dot{\mathbf{x}}_p^T \dot{\mathbf{x}}_p \, \mathrm{d}V = \frac{1}{2}\int_0^L \mathbf{v}^T(s)\mathbf{M}\mathbf{v}(s) \, \mathrm{d}s \tag{3.191}$$

where the mass matrix is calculated as

$$\mathbf{M} = \begin{bmatrix} \rho A \mathbf{I}_{3\times 3} & -\mathbf{O}_0 \mathbf{J}_I \mathbf{O}_0^T \\ -\mathbf{O}_0 \mathbf{J}_I^T \mathbf{O}_0^T & \mathbf{O}_0 \mathbf{J} \mathbf{O}_0^T \end{bmatrix} \tag{3.192}$$

where ρ is the element density and $\mathbf{J}_I$ and $\mathbf{J}$ are the first and second moments of inertia of the cross sections computed in the local frame. In most simple cases, $\mathbf{J}_I$ vanishes from the definition of the reference curve, and $\mathbf{M}$ becomes diagonal. Due to the assumption that the cross sections do not deform, $\mathbf{M}$ can be defined from the reference configuration, and does not depend on the motion or deformation of the beam.

3.5.2 Equations of Motion

To obtain the dynamic equilibrium equations, the variations of the energies are computed and used in Hamilton's principle given by

$$\int_{\tau_0}^{\tau_1} \delta(\mathcal{K}) - \delta(\mathcal{V}_{int}) + \delta(\mathcal{V}_{ext}) \, d\tau = 0. \tag{3.193}$$

The variations of the strain and kinetic energy are given by

$$\begin{aligned} \delta(\mathcal{V}_{int}) &= \int_0^L \delta(\boldsymbol{\epsilon})^T \mathbf{K}\boldsymbol{\epsilon} \, ds \\ \delta(\mathcal{K}) &= \int_0^L \delta(\mathbf{v})^T \mathbf{M}\mathbf{v} \, ds \end{aligned} \tag{3.194}$$

Necessary relationships are drawn between the derivatives according to Eq. (3.37), in order to relate the variations above to the variations of the configuration variables. This is done in terms of an infinitesimal motion $\delta\mathbf{h} \in \mathbb{R}^6$ defined from the variation of the frames $\mathbf{H}(s)$ as $\delta\mathbf{H}(s) = \mathbf{H}(s)\widetilde{\delta\mathbf{h}}$, which gives

$$\begin{aligned} \delta(\boldsymbol{\epsilon}) &= \delta(\mathbf{f}) = (\delta\mathbf{h})' + \hat{\mathbf{f}}\delta\mathbf{h} \\ \delta(\mathbf{v}) &= (\dot{\delta\mathbf{h}}) + \hat{\mathbf{v}}\delta\mathbf{h} \end{aligned} \tag{3.195}$$

Inserting the variations in Eq. (3.195) into Eq. (3.194) and integrating by parts yields

$$\delta(\mathcal{V}_{int}) = \left[\delta\mathbf{h}^T \mathbf{K}\boldsymbol{\epsilon}\right]_0^L - \int_0^L \delta\mathbf{h}^T \left((\mathbf{K}\boldsymbol{\epsilon})' - \hat{\mathbf{f}}^T \mathbf{K}\boldsymbol{\epsilon}\right) \, ds \tag{3.196}$$

and

$$\int_{\tau_0}^{\tau_1} \delta(\mathcal{K})\, d\tau = \left[\int_0^L \delta\mathbf{h}^T \mathbf{M}\mathbf{v}\, ds\right]_{\tau_0}^{\tau_1} - \int_{\tau_0}^{\tau_1}\int_0^L \delta\mathbf{h}^T(\mathbf{M}\dot{\mathbf{v}} - \hat{\mathbf{v}}^T\mathbf{M}\mathbf{v})\, ds\, d\tau \tag{3.197}$$

From the above, we obtain the internal forces as

$$\mathbf{g}_{int} = (\mathbf{K}\boldsymbol{\epsilon})' - \hat{\mathbf{f}}^T\mathbf{K}\boldsymbol{\epsilon} \tag{3.198}$$

and the inertial forces as

$$\mathbf{g}_{ine} = \mathbf{M}\dot{\mathbf{v}} - \hat{\mathbf{v}}^T\mathbf{M}\mathbf{v} \tag{3.199}$$

The variation of the external forces may then also be written in general form as

$$\delta(\mathcal{V}_{ext}) = \int_0^L \delta\mathbf{h}^T\mathbf{g}_{ext}\, ds \tag{3.200}$$

where $\mathbf{g}_{ext}$ contains the external forces and moments over the cross sections, and should be expressed in the local frame to be consistent with the rest of the formulation.

The first term on the right hand side of Eq. (3.196) is a boundary condition term. In addition, since the variations are fixed in the time integral, the first term on the right hand side of Eq. (3.197) vanishes. Substituting the variations of the energies inside the Hamilton equation in Eq. (3.193) gives the weak form of the dynamic equilibrium equations as

$$\left[\delta\mathbf{h}^T\mathbf{K}\boldsymbol{\epsilon}\right]_0^L - \int_0^L \delta\mathbf{h}^T(\mathbf{M}\dot{\mathbf{v}} - \hat{\mathbf{v}}^T\mathbf{M}\mathbf{v} + (\mathbf{K}\boldsymbol{\epsilon})' - \hat{\mathbf{f}}^T\mathbf{K}\boldsymbol{\epsilon} + \mathbf{g}_{ext})\, ds = 0, \tag{3.201}$$

from which the strong form of the dynamic equation is given by the following second-order non-linear PDE for the unknowns $\boldsymbol{\epsilon}$ and $\mathbf{v}$

$$\mathbf{M}\dot{\mathbf{v}} - \hat{\mathbf{v}}^T\mathbf{M}\mathbf{v} + (\mathbf{K}\boldsymbol{\epsilon})' - \hat{\mathbf{f}}^T\mathbf{K}\boldsymbol{\epsilon} + \mathbf{g}_{ext} = 0. \tag{3.202}$$

It is noted that this equation is intrinsic, as it was obtained without introducing any frame parametrisation and is solved for velocities $\mathbf{v}$ and deformations $\boldsymbol{\epsilon}$ only. The boundary conditions to be solved become

$$\delta\mathbf{h}^T(L)\mathbf{K}(L)\boldsymbol{\epsilon}(L) - \delta\mathbf{h}^T(0)\mathbf{K}(0)\boldsymbol{\epsilon}(0) = 0 \tag{3.203}$$

The compatibility equation in Eq. (3.190) must also be solved with the equations above, in addition to the kinematic equations in Eq. (3.163) and Eq. (3.186).

The PDEs governing the dynamic motion of the beam in Eq. (3.202) are, in principle, similar to PDEs from other beam formulations, such as the Reissner-Simo [204] or Cesnik [220] equations. A main difference however is that Eq. (3.202) is strictly a flow on the $SE(3)$ group manifold, and therefore the group structure on which the equations are evolving is different compared to other beam formulations. These equations therefore cannot be solved in a manner similar to that of Simo, as the underlying group structure needs to be preserved. Other beam formulations apply transformations which are not consistent with the group structure of rigid body motion in 3D space. Therefore, the PDEs in Eq. (3.202) are, strictly speaking, funda-

mentally different, as they are confined to evolve on the $SE(3)$ manifold. This can also be seen through the use of the $SE(3)$ adjoint map (the hat operator from Eq. (3.32)) on the velocity and strain terms in Eq. (3.202).

Finally, it should be noted that if external forces do not depend on the configuration of the beam, then the equilibrium equations in Eq. (3.202) and the compatibility equation in Eq. (3.190) would not depend on the position or orientation of the beam. They can therefore be solved for the velocities $\mathbf{v}$ and deformations $\boldsymbol{\epsilon}$, which are themselves expressed in the local frame, without having any knowledge of the configuration of the beam with respect to the fixed reference frame. This is a direct benefit of working with left-invariant derivatives on the $SE(3)$ framework. The configuration of the beam can then be recovered from the kinematic equations in either Eq. (3.163) or Eq. (3.186). In general however, external forces may depend on the beam configuration, in which case the equations above become coupled and therefore must be solved together.

3.5.3 Finite Element Discretisation

A finite element discretisation is introduced in order to solve the equations of motion. The discretisation along the neutral axis of the beam is achieved by means of an interpolation formula based on the $SE(3)$ exponential map. Given that the nodal frames are elements of the nonlinear and noncommutative $SE(3)$ space, the exponential map is essential for enabling the description of frames along an element based on interpolation of the nodal values. Indeed, in classical FE approaches, linear interpolation of shape functions at nodal values is adopted to describe the deformation field along a finite element. However, such linear interpolation is not valid in the $SE(3)$ formulation due to the nonlinear embedding of the configuration space.

Let $\mathbf{H}_A$ and $\mathbf{H}_B$ denote the material frames on two end nodes A and B of a single element of the FE mesh with length l. We calculate the frame at any point x along the element by the following interpolation

$$\mathbf{H}(x) = \mathbf{H}_A \exp_{SE(3)} \left(\frac{x}{l} \mathbf{d} \right) \tag{3.204}$$

where $x \in [0, l]$, and $\mathbf{d} = \begin{bmatrix} \mathbf{d}_U^T & \mathbf{d}_\Omega^T \end{bmatrix}^T$ is the relative configuration vector given by

$$\mathbf{d} = \log_{SE(3)}(\mathbf{H}_A^{-1} \mathbf{H_B}) \tag{3.205}$$

By the above definition, $\mathbf{d}$ is a Lie algebra element $\in \mathfrak{se}(3)$ representing a twist, and thus belongs to a linear vector space. The exponential map acts as a local parametrisation which maps the linear space to the nonlinear space of the nodal frames. This interpolation satisfies the frame invariance requirement, as for any rigid body motion defined by applying the same group composition to $\mathbf{H}_A$ and $\mathbf{H}_B$, $\mathbf{d}$ remains unchanged.

Coupling of Positions and Rotations

The nonlinear finite element interpolation formula in Eq. (3.204) offers an important geometric interpretation of the positions and rotations. Writing the frames as matrices on $SE(3)$ follow-

ing Eq. (3.66), and writing the exponential on $SE(3)$ in matrix form using Eq. (3.72), Eq. (3.204) can be written as

$$\begin{bmatrix} \mathbf{R}(x) & \mathbf{x}(x) \\ \mathbf{0}_{1\times 3} & 1 \end{bmatrix} = \begin{bmatrix} \mathbf{R}_A & \mathbf{x}_A \\ \mathbf{0}_{1\times 3} & 1 \end{bmatrix} \begin{bmatrix} \exp_{SO(3)}(\frac{x}{l}\mathbf{d}_\Omega) & \mathbf{T}^T_{SO(3)}(\frac{x}{l}\mathbf{d}_\Omega)\frac{x}{l}\mathbf{d}_U \\ \mathbf{0}_{1\times 3} & 1 \end{bmatrix} \tag{3.206}$$

Multiplying the above matrices, we get the following equations for the position and rotation of a point on the reference curve

$$\begin{aligned} \mathbf{x}(x) &= \mathbf{x}_A + \mathbf{R}_A \mathbf{T}^T_{SO(3)}(\frac{x}{l}\mathbf{d}_\Omega)\frac{x}{l}\mathbf{d}_U \\ \mathbf{R}(x) &= \mathbf{R}_A \exp_{SO(3)}(\frac{x}{l}\mathbf{d}_\Omega) \end{aligned} \tag{3.207}$$

These equations show a deep coupling between positions and rotations. The interpolation of both positions and rotations are nonlinear owing to the tangent and the exponential terms in the equations. This nonlinear coupling enables a geometrically exact representation of the beam curvature in pure bending with just a single element [208]. Furthermore, it is shown in [208] that this representation is inherently locking free, since the strain forces for a single element in pure bending does not include any spurious shear terms. An interpolation formula of the displacement field which does not depend on the rotations will not be able to represent constant curvature with exactly a single element, and would exhibit shear locking. This coupling is an important feature of the interpolation scheme on $SE(3)$, and is contrary to classical FE discretisation schemes, which treat rotations and positions as independent variables. It is also noted that the geometry of the interpolated position field is a helix, which allows to account consistently for an initially curved beam with a single element [209].

3.5.4 Derivatives

We can now find the derivatives and variations of the discretisation formulation. The discretised deformation field $\boldsymbol{\epsilon}(x)$ and arbitrary infinitesimal motion field $\delta\mathbf{h}(x)$ can be found in terms of the nodal variables. Taking the derivative of Eq. (3.204) with respect to x yields

$$\frac{\mathrm{d}\mathbf{H}(x)}{\mathrm{d}x} = \mathbf{H}(x)\left(\mathbf{T}_{SE(3)}(\frac{x}{l}\mathbf{d})\frac{\mathbf{d}}{l}\right)^{\sim} = \mathbf{H}(x)\frac{\widetilde{\mathbf{d}}}{l} \tag{3.208}$$

where we have used Eq. (3.44) to differentiate the exponential map, giving the tangent operator. The second equality may be obtained by considering the series expansion of the tangent operator [209]. Comparing this expression to the continuous equation in Eq. (3.163), we have

$$\mathbf{f} = \frac{\mathbf{d}}{l} \tag{3.209}$$

and from Eq. (3.169) we therefore have

$$\boldsymbol{\epsilon} = \frac{\mathbf{d} - \mathbf{d}^0}{l} \tag{3.210}$$

It is therefore seen that the deformations are constant over the element.

Next, we compute the variation of $\mathbf{d}$ by restating Eq. (3.205) as

$$\mathbf{H}_B = \mathbf{H}_A \exp_{SE(3)}(\mathbf{d}) \tag{3.211}$$

Introducing the infinitesimal motions vector $\delta\mathbf{h}_{AB} = [\delta\mathbf{h}_A^T \quad \delta\mathbf{h}_B^T]^T$ from the variation of the nodal frames as $\delta\mathbf{H}_A = \mathbf{H}_A\widetilde{\delta\mathbf{h}_A}$ and $\delta\mathbf{H}_B = \mathbf{H}_B\widetilde{\delta\mathbf{h}_B}$, we take the variation of Eq. (3.211) and use the product rule and the tangent operator from Eq. (3.44) as

$$\delta\mathbf{H}_B = \delta\mathbf{H}_A \exp_{SE(3)}(\mathbf{d}) + \mathbf{H}_A \exp_{SE(3)}(\mathbf{d}) \left(\mathbf{T}_{SE(3)}(\mathbf{d})\delta(\mathbf{d})\right)^{\sim} \tag{3.212}$$

writing the variations of the nodal frames using the infinitesimal motions, and making use of Eq. (3.211) again gives

$$\mathbf{H}_B\widetilde{\delta\mathbf{h}_B} = \mathbf{H}_A\widetilde{\delta\mathbf{h}_A} \exp_{SE(3)}(\mathbf{d}) + \mathbf{H}_B \left(\mathbf{T}_{SE(3)}(\mathbf{d})\delta(\mathbf{d})\right)^{\sim} \tag{3.213}$$

premultiplying both sides of the above by $\mathbf{H}_B^{-1}$ and noting from Eq. (3.211) that $\mathbf{H}_B^{-1}\mathbf{H}_A = \exp^{-1}_{SE(3)}(\mathbf{d}) = \exp_{SE(3)}(-\mathbf{d})$, we have

$$\widetilde{\delta\mathbf{h}_B} = \exp_{SE(3)}(-\mathbf{d})\widetilde{\delta\mathbf{h}_A} \exp_{SE(3)}(\mathbf{d}) + \left(\mathbf{T}_{SE(3)}(\mathbf{d})\delta(\mathbf{d})\right)^{\sim} \tag{3.214}$$

which using the Adjoint definition in Eq. (3.23) may be written as

$$\widetilde{\delta\mathbf{h}_B} = \mathrm{Ad}_{\exp_{SE(3)}(-\mathbf{d})}\widetilde{\delta\mathbf{h}_A} + \left(\mathbf{T}_{SE(3)}(\mathbf{d})\delta(\mathbf{d})\right)^{\sim} \tag{3.215}$$

The above can now be expressed in vector form as

$$\delta\mathbf{h}_B = \mathrm{Ad}_{\exp_{SE(3)}(-\mathbf{d})}\delta\mathbf{h}_A + \mathbf{T}_{SE(3)}(\mathbf{d})\delta(\mathbf{d}) \tag{3.216}$$

which gives $\delta(\mathbf{d})$ as

$$\delta(\mathbf{d}) = -\mathbf{T}^{-1}_{SE(3)}(\mathbf{d})\mathrm{Ad}_{\exp_{SE(3)}(-\mathbf{d})}\delta\mathbf{h}_A + \mathbf{T}^{-1}_{SE(3)}(\mathbf{d})\delta\mathbf{h}_B \tag{3.217}$$

Using the identity in Eq. (C.2), Eq. (3.217) may be written as

$$\delta(\mathbf{d}) = -\mathbf{T}^{-1}_{SE(3)}(-\mathbf{d})\delta\mathbf{h}_A + \mathbf{T}^{-1}_{SE(3)}(\mathbf{d})\delta\mathbf{h}_B \tag{3.218}$$

which may be written more compactly using the combined infinitesimal motions vector as

$$\delta(\mathbf{d}) = \mathbf{P}(\mathbf{d})\delta\mathbf{h}_{AB} \tag{3.219}$$

where

$$\mathbf{P}(\mathbf{d}) = \begin{bmatrix} -\mathbf{T}^{-1}_{SE(3)}(-\mathbf{d}) & \mathbf{T}^{-1}_{SE(3)}(\mathbf{d}) \end{bmatrix} \tag{3.220}$$

Secondly, we need to compute the variation of the interpolated field to obtain the infinitesimal motion field $\delta\mathbf{h}(x)$. Taking the variation of Eq. (3.204) and writing $\delta\mathbf{H}(x) = \mathbf{H}(x)\widetilde{\delta\mathbf{h}(x)}$ gives the following through the application of the product rule

$$\mathbf{H}(x)\widetilde{\delta\mathbf{h}(x)} = \delta\mathbf{H}_A \exp_{SE(3)}(\frac{x}{l}\mathbf{d}) + \mathbf{H}_A \exp_{SE(3)}(\frac{x}{l}\mathbf{d}) \left(\frac{x}{l}\mathbf{T}(\frac{x}{l}\mathbf{d})\delta(\mathbf{d})\right)^{\sim} \tag{3.221}$$

Following the same steps as before in evaluating $\delta(\mathbf{d})$, the above can be similarly simplified using the Adjoint and can subsequently be written in vector form. Using the identity in Eq. (C.2), and using Eq. (3.219), $\delta\mathbf{h}(x)$ can be written as

$$\delta\mathbf{h} = \mathbf{Q}(x, \mathbf{d})\delta\mathbf{h}_{AB} \tag{3.222}$$

where

$$\mathbf{Q}(x, \mathbf{d}) = \begin{bmatrix}\mathbf{I}_{6\times6} - \mathbf{T}^{\star}(x, \mathbf{d}) & \mathbf{T}^{\star}(x, \mathbf{d})\end{bmatrix} \tag{3.223}$$

and

$$\mathbf{T}^{\star}(x, \mathbf{d}) = \frac{x}{l}\mathbf{T}_{SE(3)}(\frac{x}{l}\mathbf{d})\mathbf{T}^{-1}_{SE(3)}(\mathbf{d}) \tag{3.224}$$

The final required derivative is the velocity field, whose computation follows the same steps as the computation of $\delta\mathbf{h}$, with the exception that derivatives are with respect to time. The velocity field can be computed as

$$\mathbf{v} = \mathbf{Q}(x, \mathbf{d})\mathbf{v}_{AB} \tag{3.225}$$

where $\mathbf{v}_{AB} = [\mathbf{v}_A^T \quad \mathbf{v}_B^T]^T$ contains the velocities of the the nodal frames as $\dot{\mathbf{H}}_A = \mathbf{H}_A\widetilde{\mathbf{v}_A}$ and $\dot{\mathbf{H}}_B = \mathbf{H}_B\widetilde{\mathbf{v}_B}$. It is noted that the discretised velocity also satisfy the compatibility equation in Eq. (3.190), which may be verified by inserting the discrete expressions for $\mathbf{v}$, $\mathbf{f}$, and $\boldsymbol{\epsilon}$ into the compatibility equation [209].

3.5.5 Discretised Equations of Motion

The variation of the deformations is required for the discretised equations of motion. This may be obtained by taking the variation of Eq. (3.210), and using Eq. (3.219) to get

$$\delta(\boldsymbol{\epsilon}) = \delta(\frac{\mathbf{d}}{l}) = \frac{1}{l}\mathbf{P}(\mathbf{d})\delta\mathbf{h}_{AB} \tag{3.226}$$

It is noted that $\delta(\boldsymbol{\epsilon})$ is constant over the element, owing to the deformations being constant as discussed previously. This may be substituted into the expression for the variation of strain energy in Eq. (3.194), to obtain the nodal internal forces $\mathbf{g}_{int_{AB}}$ as

$$\mathbf{g}_{int_{AB}} = \int_0^l \frac{1}{l}\mathbf{P}(\mathbf{d})^T\mathbf{K}\boldsymbol{\epsilon}\ \mathrm{d}x \tag{3.227}$$

defined such that $\delta(\mathcal{V}_{int}) = \delta\mathbf{h}_{AB}^T\mathbf{g}_{int_{AB}}$. The integration over the length of the element is trivial since all the terms are constant for a beam with constant cross sectional properties. The nodal

internal strain forces therefore only depend on nodal values $\mathbf{H}_A$ and $\mathbf{H}_B$, through the relative configuration between them which is represented by $\mathbf{d}$. Using Eq. (3.210), we can therefore write

$$\mathbf{g}_{int_{AB}} = \frac{1}{l}\mathbf{P}(\mathbf{d})^T\mathbf{K}^L\frac{\mathbf{d}-\mathbf{d}_0}{l} \tag{3.228}$$

where

$$\mathbf{K}^L = \int_0^l \mathbf{K}\ \mathrm{d}x \tag{3.229}$$

is the stiffness matrix of the element, resulting from the integration over the element length.

The external forces may also be treated similarly, using the discretised expression for $\delta\mathbf{h}$ in Eq. (3.222). With the definition of the variation of external forces from Eq. (3.200), we write the nodal external forces $\mathbf{g}_{ext_{AB}}$ as

$$\mathbf{g}_{ext_{AB}} = \int_0^l \mathbf{Q}(x,\mathbf{d})^T\mathbf{g}_{ext}\ \mathrm{d}x \tag{3.230}$$

defined such that $\delta(\mathcal{V}_{ext}) = \delta\mathbf{h}_{AB}^T\mathbf{g}_{ext_{AB}}$. As previously discussed, the external forces must be expressed in the local frame, such that for global force fields such as gravity, this implies the dependence of the forcing terms on the configuration of the beam nodes.

Tangent Stiffness Matrix

The evaluation of the tangent stiffness matrix is required for solving the equations iteratively. The contribution of the internal forces to the tangent stiffness matrix may be found by computing the variation of Eq. (3.228), which gives

$$\frac{1}{l}\delta(\mathbf{P}(\mathbf{d})^T\mathbf{K}^L\boldsymbol{\epsilon}) = \frac{1}{l}\mathbf{P}(\mathbf{d})^T\mathbf{K}^L\delta(\boldsymbol{\epsilon}) + \frac{1}{l}\delta(\mathbf{P}(\mathbf{d})^T)\mathbf{K}^L\boldsymbol{\epsilon} \tag{3.231}$$

The first term on the right hand side can be expanded using Eq. (3.226). To evaluate the second term, we must take the variation of $\mathbf{P}(\mathbf{d})^T$, using the expression for $\mathbf{P}(\mathbf{d})$ in Eq. (3.220). This may be evaluated as

$$\frac{1}{l}\delta(\mathbf{P}(\mathbf{d})^T)\mathbf{K}^L\boldsymbol{\epsilon} = \frac{1}{l}\begin{bmatrix}\mathrm{D}_{\mathbf{K}^L\boldsymbol{\epsilon}}\mathbf{T}_{SE(3)}^{-T}(-\mathbf{d})\delta(\mathbf{d}) \\ \mathrm{D}_{\mathbf{K}^L\boldsymbol{\epsilon}}\mathbf{T}_{SE(3)}^{-T}(\mathbf{d})\delta(\mathbf{d})\end{bmatrix} \tag{3.232}$$

Where the subscripts indicate the direction of the directional derivative of the tangent operator. The expressions for the derivatives of the tangent operator on $SE(3)$ may be found in [209]. Then, using Eq. (3.219), we can write the full expression for Eq. (3.231) as

$$\frac{1}{l}\delta(\mathbf{P}(\mathbf{d})^T\mathbf{K}^L\boldsymbol{\epsilon}) = \mathbf{K}_T\delta\mathbf{h}_{AB} = (\mathbf{K}_{Tm} + \mathbf{K}_{Tg})\delta\mathbf{h}_{AB} \tag{3.233}$$

where $\mathbf{K}_{Tm}$ and $\mathbf{K}_{Tm}$ are the material and geometric parts of the tangent stiffness matrix respectively, and are given by

$$\mathbf{K}_{Tm} = \frac{1}{l^2}\mathbf{P}(\mathbf{d})^T\mathbf{K}^L\mathbf{P}(\mathbf{d})^T \tag{3.234}$$

$$\mathbf{K}_{Tg} = \frac{1}{l}\begin{bmatrix} \mathrm{D}_{\mathbf{K}^L\boldsymbol{\epsilon}}\mathbf{T}^{-T}_{SE(3)}(-\mathbf{d})\mathbf{P}(\mathbf{d}) \\ \mathrm{D}_{\mathbf{K}^L\boldsymbol{\epsilon}}\mathbf{T}^{-T}_{SE(3)}(\mathbf{d})\mathbf{P}(\mathbf{d}) \end{bmatrix} \tag{3.235}$$

The dependence of the tangent stiffness matrix, $\mathbf{K}_T$, on $\mathbf{d}$ means that it is invariant under rigid body motion, and changes only with the relative motion of the nodes under deformation. In cases where this relative motion is small, the tangent stiffness matrix may be evaluated only once from the reference configuration, and kept constant for the whole simulation, offering potential computational savings. The external forces will also contribute to the tangent stiffness matrix if they depend on the orientation of the beam.

Carrying on with the derivation of the beam equations of motion, the inertia forces may be found by defining the nodal inertia forces $\mathbf{g}_{ine_{AB}}$ such that $\delta(\mathcal{K}) = \delta\mathbf{h}^T_{AB}\mathbf{g}_{ine_{AB}}$. Using the variation of inertial forces from Eq. (3.197) we have

$$\delta\mathbf{h}^T_{AB}\mathbf{g}_{ine_{AB}} = \int_0^l \delta\mathbf{h}^T(\mathbf{M}\dot{\mathbf{v}} - \hat{\mathbf{v}}^T\mathbf{M}\mathbf{v})\ \mathrm{d}x \tag{3.236}$$

Using the discretised expressions for $\delta\mathbf{h}$ in Eq. (3.222) and $\mathbf{v}$ in Eq. (3.225) gives the nodal inertia forces as

$$\mathbf{g}_{ine_{AB}} = \int_0^l \mathbf{Q}^T\left(\mathbf{M}\mathbf{Q}\dot{\mathbf{v}}_{AB} + \mathbf{M}\dot{\mathbf{Q}}\mathbf{v}_{AB} - \widehat{\mathbf{Q}\mathbf{v}_{AB}}^T\mathbf{M}\mathbf{Q}\mathbf{v}_{AB}\right)\ \mathrm{d}x \tag{3.237}$$

where $\mathbf{Q} = \mathbf{Q}(x, \mathbf{d})$. The time derivative of $\mathbf{Q}$ may be calculated analytically and can be found in [209].

The discretised mass matrix of an element can be written as

$$\mathbf{M}^L(\mathbf{d}) = \int_0^l \mathbf{Q}^T\mathbf{M}\mathbf{Q}\ \mathrm{d}x \tag{3.238}$$

which shows that it is only dependent on the relative configuration vector $\mathbf{d}$ and is thus invariant under rigid body transformations. This dependence also implies that the discretised mass matrix is not constant as the beam deforms, due to the relative motion of the nodes under deformation. This is of physical significance, since a deformed beam changes shape, and therefore inertia, which will be reflected in a changing mass matrix.

The element damping matrix can also be defined as

$$\mathbf{C}^L(\mathbf{d}, \mathbf{v}_{AB}) = \int_0^l \mathbf{Q}^T\left(\mathbf{M}\dot{\mathbf{Q}} - \widehat{\mathbf{Q}\mathbf{v}_{AB}}^T\mathbf{M}\mathbf{Q}\right)\ \mathrm{d}x \tag{3.239}$$

whose second term is related to gyroscopic effects. With these, the inertia forces may be written as

$$\mathbf{g}_{ine_{AB}} = \mathbf{M}^L(\mathbf{d})\dot{\mathbf{v}}_{AB} + \mathbf{C}^L(\mathbf{d}, \mathbf{v}_{AB})\mathbf{v}_{AB} \tag{3.240}$$

Tangent Mass and Damping Matrices

The tangent mass and damping matrices are also required for the iterative time integration of the equations of motion, as described in Section 3.6. The tangent mass matrix, $\mathbf{M}_T$ is the

same as $\mathbf{M}^L$. The tangent damping matrix may be evaluated as

$$\mathbf{C}_T = \mathbf{C}^L - \int_0^l (\widetilde{\mathbf{M}\mathbf{Q}\mathbf{v}_{AB}})^T \mathbf{Q} \, \mathrm{d}x \tag{3.241}$$

where $\check{(\bullet)}$ is defined as $\hat{\mathbf{h}}_1^T \mathbf{h}_2 = \check{\mathbf{h}}_2^T \mathbf{h}_1$, $\forall \mathbf{h}_1, \mathbf{h}_2 \in \mathbb{R}^3$. An additional contribution from $\dot{\mathbf{Q}}$ would also be present, but is considered negligible and is omitted. Furthermore, the element mass and damping matrices also contribute to the tangent stiffness matrix, but this is also considered negligible compared to the tangent stiffness matrix of the internal forces. It is noted that the terms in the tangent matrices are consistent with the rest of the formulation, in that they are also dependent on the nodal frames only through $\mathbf{d}$, and they are therefore invariant under rigid body motion.

Equations of Motion

Using the developed expressions, we have the discretised equations of motion which take the following form

$$\begin{aligned} \dot{\mathbf{H}}_A &= \mathbf{H}_A \tilde{\mathbf{v}}_A \\ \dot{\mathbf{H}}_B &= \mathbf{H}_B \tilde{\mathbf{v}}_B \\ \mathbf{g}_{ine_{AB}} + \mathbf{g}_{int_{AB}} - \mathbf{g}_{ext_{AB}} &= \mathbf{0}_{12\times 1} \end{aligned} \tag{3.242}$$

The compatibility equation in Eq. (3.190) is automatically satisfied, as proven mathematically in [209], thanks to the nonlinear interpolation of the deformation and velocity fields arising from Eq. (3.204). It therefore does not need to be solved with the equations of motion. It is emphasised that all the forces in the discretised equation of motion are naturally expressed in the local frame, such that the position and orientation of the nodes are involved only through the relative configuration vector $\mathbf{d}$, such that they are invariant under rigid body motion without deformation[1]. This is a direct benefit of the interpolation function based on the exponential map in Eq. (3.204) which preserves the local frame interpretation of the beam dynamics.

These equations are discretised in time and solved with a Lie group version of the generalised-α scheme, as briefly introduced in Section 3.6. In applications involving small relative motions in the elements, the tangent matrices may be calculated from the initial configuration and kept constant for the whole simulation. Application-specific strategies for improving computational time may be adopted; for instance, increasing the number of elements will reduce the relative motion at the nodes, which might mitigate the need to update the tangent matrices at each iteration step, but should be balanced against the increased computational time resulting from a greater number of elements.

[1] By which we technically mean superimposed Euclidean transformation, the explanation of which may be found in [209].

Assembly Process

In displacement-based finite element methods, the assembly of the equations of motion is based on the construction of the mass, stiffness, and damping matrices for the full structure. A similar approach may be employed here, using the following assembled matrices for m nodes,

$$\begin{aligned}\underline{\underline{\mathbf{M}}} &= \sum_{i=1}^{m} \mathbf{L}_i^T \mathbf{M}_i^L(\mathbf{d}_i)\mathbf{L}_i \\ \underline{\underline{\mathbf{C}}} &= \sum_{i=1}^{m} \mathbf{L}_i^T \mathbf{C}_i^L(\mathbf{d}_i, \mathbf{v}_i)\mathbf{L}_i \\ \underline{\underline{\mathbf{K}}} &= \sum_{i=1}^{m} \mathbf{L}_i^T \mathbf{K}_i^L \mathbf{L}_i\end{aligned} \tag{3.243}$$

where $\mathbf{L}_i$ are the localisation operators, which are boolean matrices which pick out nodal terms from the global system degrees of freedom. The combined nodal velocities and strains may also be written as

$$\underline{\underline{\mathbf{v}}} = \left[\mathbf{v}_1, \mathbf{v}_2, \cdots, \mathbf{v}_m\right] \tag{3.244}$$

and

$$\underline{\underline{\boldsymbol{\epsilon}}} = \left[l_1^{-1}(\mathbf{d}_1 - \mathbf{d}_{01}), l_2^{-1}(\mathbf{d}_2 - \mathbf{d}_{02}), \cdots, l_m^{-1}(\mathbf{d}_m - \mathbf{d}_{0m})\right] \tag{3.245}$$

where the subscripts indicate the element number. The equilibrium equation can then be written as

$$\underline{\underline{\mathbf{M}}}\ \underline{\dot{\mathbf{v}}} + \underline{\underline{\mathbf{C}}}\ \underline{\mathbf{v}} + \underline{\underline{\mathbf{P}}}^T\ \underline{\underline{\mathbf{K}}}\ \underline{\boldsymbol{\epsilon}} = \underline{\underline{\mathbf{g}_{ext}}} \tag{3.246}$$

where

$$\underline{\underline{\mathbf{P}}} = \operatorname{diag}\left(\frac{\mathbf{P}_1(\mathbf{d}_1)}{l_1}, \frac{\mathbf{P}_2(\mathbf{d}_2)}{l_2}, \cdots, \frac{\mathbf{P}_m(\mathbf{d}_m)}{l_m}\right) \tag{3.247}$$

and $\underline{\underline{\mathbf{g}_{ext}}}$ is the assembled external forces, integrated over the length of each element.

In practice, however, the above assembly process is not employed. Instead, the residual vector of the equations of motion is computed at the element level, and the full system residual is derived by assembling the element residuals. This approach is beneficial for nonlinear formulations as it leverages the modularity of finite element method and reduces computational burden from factorising large matrices resulting from the assembly process. Moreover, the dependence of the inertial forces on the relative configuration vector $\mathbf{d}$, through the terms in matrices $\mathbf{P}$ and $\mathbf{Q}$, and the dependence of the internal forces on the same, makes it more practical to compute these forces at the element level, ensuring local correctness rather than relying on proper handling during the global assembly process. This further highlights the robustness of computing the residual on the element level. Finally, the tangent matrices required for the iterative solver are also first evaluated on the element level, then assembled to evaluate the full Jacobian.

3.6 Time Integration

Classical iterative vector space solvers cannot be used to solve equations of motion formulated on nonlinear Lie groups, since the configuration space of these groups is not a vector

space. In order to use vector space solvers, rotations may be parametrised by expressing the motion in terms of a specific choice of coordinates with respect to the inertial frame. These parametrisations could be in terms of global minimal coordinates, such as Euler angles, or redundant global coordinates, such as quaternions, both of which facilitate the use of vector space solvers. The former parametrisation suffers from singularities and the introduction of complex nonlinear functions due to transformation dependencies, while the latter, though singularity free, suffers from an increased number of parameters and equations. Consequently, employing vector space solvers ultimately compromises the intrinsic properties of the original equations of motion. Iterative methods which preserve the Lie group structure of the equations of motion do not suffer from these drawbacks, and should be preferred as they maintain the mathematical integrity of the nonlinear configuration space. A review of geometric integrators and their closed form expressions may be found in [145].

The discretised dynamic equilibrium equations Eq. (3.242) are solved by a Lie group version of the generalised-α scheme, which preserves the Lie group structure of the problem [7], [37], [38]. The scheme is second-order accurate, and is general and applicable to both constrained multibody and flexible body dynamics with large rotations. Denoting the configuration state of the system by the frame q, velocity $\mathbf{v}$, and acceleration $\dot{\mathbf{v}}$, and the inertial, internal, and external forces respectively by $\mathbf{g}_{ine}$, $\mathbf{g}_{int}$, and $\mathbf{g}_{ext}$, the time integration relies on the discretised equations involving the exponential map as

$$\begin{aligned} q_{n+1} &= q_n \exp(\widetilde{\mathbf{x}}_{n+1}) \\ \mathbf{r} &\equiv \mathbf{g}_{ine}(\mathbf{v}_{n+1}, \dot{\mathbf{v}}_{n+1}) + \mathbf{g}_{int}(q_{n+1}) - \mathbf{g}_{ext} = \mathbf{0} \end{aligned} \tag{3.248}$$

and the time integration formulae

$$\begin{aligned} \mathbf{x}_{n+1} &= h\mathbf{v}_n + (0.5 - \beta)h^2\mathbf{a}_n + \beta h^2 \mathbf{a}_{n+1} \\ \mathbf{v}_{n+1} &= \mathbf{v}_n + (1-\gamma)h\mathbf{a}_n + \gamma h \mathbf{a}_{n+1}, \\ \mathbf{a}_{n+1} &= \frac{1}{(1-\alpha_m)}((1-\alpha_f)\dot{\mathbf{v}}_{n+1} + \alpha_f \dot{\mathbf{v}}_n - \alpha_m \mathbf{a}_n) \end{aligned} \tag{3.249}$$

where n is the time step and h refers to the time step size, and $\mathbf{r}$ is the residual denoting the entire force equation. The usual numerical parameters of the generalised-α scheme are α_m, α_f, γ, and β. Then, $\widetilde{\mathbf{x}}_{n+1}$ is interpreted as an average "frozen" velocity field spanning the interval from t_n and t_{n+1}. The exponential map in Eq. (3.248) provides a local parametrisation about $\mathbf{q}_n$. The use of the exponential is the particular adaptation which makes this scheme applicable to dynamic systems on Lie groups, as it projects algebraic corrections made on the Lie algebra's linear space to the group's nonlinear configuration space.

A time stepping scheme is used to advance the solution to the equations, whereby Eq. (3.248) and Eq. (3.249) are solved for all variables in step $n+1$ based on their value at step n. To this end, a Newton-Raphson algorithm is used, which relies on the linearisation of these equations. Denoting Δ as the derivative for the linearisation, applying the linearisation to the exponential

equation in Eq. (3.248) gives

$$\Delta(q_{n+1}) = q_{n+1}\widetilde{\Delta\mathbf{q}_{n+1}} \tag{3.250}$$

for $\widetilde{\Delta\mathbf{q}_{n+1}}$ in the Lie algebra. Using the definition of the tangent operator in Eq. (3.43), $\Delta\mathbf{q}_{n+1}$ can be written in vector form as

$$\Delta\mathbf{q}_{n+1} = \mathbf{T}(\mathbf{x}_{n+1})\Delta\mathbf{x}_{n+1} \tag{3.251}$$

The linearisation of the residual in Eq. (3.248) gives

$$\begin{aligned} D\mathbf{r}\cdot\Delta\mathbf{q}_{n+1} &= \mathbf{K}_T\Delta\mathbf{q}_{n+1} = \mathbf{K}_T\mathbf{T}(\mathbf{x}_{n+1})\Delta\mathbf{x}_{n+1} \\ D\mathbf{r}\cdot\Delta\mathbf{v}_{n+1} &= \mathbf{C}_T\Delta\mathbf{v}_{n+1} \\ D\mathbf{r}\cdot\Delta\dot{\mathbf{v}}_{n+1} &= \mathbf{M}_T\Delta\dot{\mathbf{v}}_{n+1} \end{aligned} \tag{3.252}$$

where $\mathbf{M}_T$, $\mathbf{C}_T$, and $\mathbf{K}_T$ are the tangent mass, damping, and stiffness matrices respectively, as introduced in Section 3.5.5. The linearisation can also be applied to the integration formulae in Eq. (3.249) to give

$$\begin{aligned} \Delta\dot{\mathbf{v}}_{n+1} &= \frac{1-\alpha_m}{\beta h^2(1-\alpha_f)}\Delta\mathbf{x}_{n+1} \\ \Delta\mathbf{v}_{n+1} &= \frac{\gamma}{\beta h}\Delta\mathbf{x}_{n+1} \end{aligned} \tag{3.253}$$

The finite variations of the configuration increments $\mathbf{x}_{n+1}$ are then calculated at each Newton step by solving

$$\left(\frac{1-\alpha_m}{\beta h^2(1-\alpha_f)}\mathbf{M}_T + \frac{\gamma}{\beta h}\mathbf{C}_T + \mathbf{K}_T\mathbf{T}(\mathbf{x}_{n+1})\right)\Delta\mathbf{x}_{n+1} = -\mathbf{r} \tag{3.254}$$

The term in the bracket is called the iteration matrix $\mathbf{S}_T$. It is noted that the incremental variable of the Newton solver is $\Delta\mathbf{x}_{n+1}$, which is indeed a Lie algebra element and thus belongs to a linear vector space. Once $\Delta\mathbf{x}_{n+1}$ is calculated, the finite variations of the velocities and accelerations are computed from Eq. (3.253) and are used to update the velocities and accelerations at the next time step. This is done in an additive manner since they all belong to the linear vector space. The system configuration is updated nonlinearly by correcting the term under the exponential in Eq. (3.248) by $\Delta\mathbf{x}_{n+1}$. It is noted that for multibody systems involving constraints, the derivatives of the constraint equation are also computed and stored in the iteration matrix, and the increments in the lagrange multipliers are found alongside the configuration increments [38], [211].

As discussed in Section 3.5.5 the tangent matrices are invariant under rigid body motion, and depend only on local relative motions between the finite element nodes. Therefore, they may be computed from the reference configuration in test cases involving small deformations. Consequently, the iteration matrix in Eq. (3.254) does not need to be updated to achieve convergence of the iterative solver. Of course, in cases involving external forces which depend

on the system configuration, or those involving large relative motion between nodes or in kinematic joints, the iteration matrix needs updating on every time step.

Other Lie group time integration schemes may also be developed from classical integration methods such as explicit Runge-Kutta, by suitable conversion of these methods using a local-global transition map on the Lie group to update absolute coordinates [99], [147], [230]. Implicit Lie group time integration using a Newmark scheme for multibody dynamics of robots has also been shown to be numerically efficient and robust [34].

3.7 Advantages of the $SE(3)$ Beam Model

The formulation of the beam equations on the $SE(3)$ group provides several numerical and mathematical advantages. Classical FE beam models formulated on the $\mathbb{R}^3 \times SO(3)$ group treat displacements and rotations and their increments as independent variables, and aim to work with deformation measures which incorporates both these motions [44], [54]. As a result, they require additional mathematical manipulations and transformations to provide a consistent kinematic description of the beam model. These transformations do not inherently belong to $\mathbb{R}^3 \times SO(3)$, and are introduced by necessity to enforce accurate kinematics. As a result, these beam models often face challenges with singularities and parametrisation of rotations, and also exhibit numerical challenges such as shear locking and non-objectivity of strains.

Beams formulated on $SE(3)$ however do not suffer from these challenges, since the coupling of rotations and translations is an inherent mathematical feature of the $SE(3)$ Lie group. The formulations therefore provides a consistent and mathematically accurate description of the beam kinematics, without having to resort to additional "fixes" such as transformations. As discussed, the deformation measures of the $SE(3)$ beam are expressed in the local material frame owing to the left-invariant derivative representation, and are thus invariant with respect to rigid body motions. Objectivity of strains is therefore achieved naturally with this formulation. Moreover, the equations of motion are naturally intrinsic, as they do not depend on the position and orientation of the beam. As discussed, the $SE(3)$ formulation leads to beam equations of motion which are compact and at most quadratic in nonlinearity, with the inherent nonlinearity of the model being embedded in the structure of the $SE(3)$ configuration space manifold.

The interpolation discussed in the finite element formulation, as outlined in Eq. (3.204), also offers important advantages. A natural nonlinear coupling between position and rotation arises from this interpolation, which allows for a perfect representation of the pure bending/torsion using a single element with constant curvature. In contrast, traditional linear interpolations commonly used in FE formulations offer linear elements which lack curvature, and therefore can only approximate a curve through multiple independent straight elements. This uncoupled finite element formulation leads to shear locking due to the geometric inconsistency of modelling shear-deformable beams with straight finite elements, a problem which is typically addressed by numerical fixes such as reduced integration. The $SE(3)$ formulation however is naturally locking free, owing to the nonlinear and coupled interpolation formula Eq. (3.207). Moreover, elements capable of capturing curvature provide the opportunity to model large deformations

with fewer finite elements, thus offering significant computational time savings.

Thanks to the interpolation method, the nodal strain forces depend only on the nodal values through the relative configuration vector, meaning that they are invariant under rigid body motions and that they only vary according to the relative motion of the nodes. Hence, no parametrisation of nodal values needs to be introduced [208]. The internal forces and tangent stiffness matrix can be integrated exactly over the length of the element, and as discussed, in cases involving small relative motion between the nodes, the tangent stiffness matrix may be kept constant, thereby offering savings on computational time. The proposed beam formulation is particularly suitable for modelling geometric nonlinearity of flexible beams where large-amplitude motions involving small deformations are observed [213]. Geometrically nonlinear problems can be solved in a reduced number of iterations and load steps compared to classical formulations [209].

3.8 Conclusion

In this chapter, we have introduced the theory of Lie groups, aiming to develop the theoretical content in a gradual and accessible manner. Through the use of mathematical examples, and by formulating the equation of motion of a two degree of freedom mechanical system using Lie groups, we have reduced the level of abstraction surrounding the topic that is commonly found in literature, offering a clearer path to understanding the theory.

Additionally, we have introduced the formulation of a geometrically exact beam modelled on the group of rigid body motions, namely the $SE(3)$ group, aiming to make the theoretical development of the formulation clear and understandable for structural dynamicists. Throughout stages of the development of the equations of motion, we have highlighted and discussed the advantages of the $SE(3)$ model over classical geometrically exact beam formulations. The $SE(3)$ beam introduced in this chapter serves as the main formulation for the analysis of geometrically nonlinear structures conducted in subsequent chapters of this thesis.

Chapter 4

Nonlinear Dynamics of 2D Beams Formulated on the $SE(2)$ Group

Abstract

This chapter presents results on the computation of periodic responses of geometrically nonlinear 2D beams modelled under the $SE(2)$ Lie group formulation. This is done by a combination of shooting and pseudo-arclength continuation. Special adaptations are made to the shooting and continuation methods to ensure compatibility with the Lie group framework. NNMs of various 2D structures including a doubly-clamped beam, a shallow arch, and a cantilever beam are computed. Results are compared with a reference displacement-based FE model with von Kármán strains, as introduced in Chapter 2. Significant difference is observed in the dynamic response of the two models in test cases involving large degrees of beam displacements and rotation. Differences in the contribution of higher-order modes substantially affect the frequency-energy dependence and the nonlinear modal interactions observed between the models. It is shown that the $SE(2)$ model, owing to its exact representation of the beam kinematics, is better suited at adequately capturing complex nonlinear dynamics compared to the von Kármán model.

The adaptations made to the shooting and pseudo-arclength continuation methods enable their use within the Lie group framework. This represents the novel and significant contribution of this chapter. Results in this chapter have been published in the Journal of Nonlinear Dynamics [14].

4.1 Introduction

The shooting and pseudo-arclength continuation methods developed in Chapter 2 are applicable to dynamical systems formulated under a Euclidean embedding. In order to be used with Lie group systems, they need to be appropriately modified to preserve the underlying group structure of the system. These adaptations are developed and discussed in this chapter, and the modified shooting and continuation methods are applied to a range of 2D structures modelled under the $SE(2)$ formulation.

The methods developed in this chapter are general, and can be used with any dynamical system formulated on Lie groups, provided that the appropriate choice of the exponential, logarithm, and tangent maps are made for the specific Lie group under study. Some existing studies on Lie group shooting methods in the literature can be found in [1], [130]. In these works, the shooting method is used to solve nonlinear BVPs formulated on the Minkowski space[1], for a range of low-dimensional academic examples. Their method is based on transforming the original BVP into a set of algebraic equations by embedding the problem into an augmented system that respects the Lie group structure. However, this transformation cannot be simply extended to large multi-dimensional problems such as those encountered in finite element analysis. Furthermore, the root finding of the shooting problem is achieved using the half-interval method, and not using Newton iterations, as is done in this chapter. The generality of the shooting and continuation methods developed in this chapter therefore underscores the versatility of the techniques presented here, making them not only powerful tools for the analysis of finite element model, but also applicable to a wide range of problems across different fields where Lie group formulations are relevant.

In what follows in this chapter, the modifications to the shooting and continuation methods are first presented, followed by their application to find period solutions (NNMs) of 2D structures formulated on the $SE(2)$ group. The results are compared to those obtained using the finite element beam formulation with von Kármán strains. The limitations of the von Kármán model in capturing geometric nonlinearities arising from large displacements and rotations are highlighted and discussed.

4.2 Shooting Adaptation to Lie Group Formulation

Following from the presentation of the shooting and pseudo-arclength continuation methods in Chapter 2, we discuss some modifications which are required to enable the use of these methods on a system whose dynamic equations are formulated on the $SE(3)$ group. We discuss these adaptations here in the context of the $SE(3)$ group for general 3D beams, while the same can be applied to 2D beams modelled on $SE(2)$.

The first adaptation concerns the periodicity equation, which should be modified to a form suitable for computing the periodicity on the nonlinear configuration space of the SE group.

[1]Minkowski space is a mathematical description of spacetime in special relativity, within which certain Lie group transformations are defined.

As discussed in Chapter 2, the periodicity equation is typically formulated as the difference between the system states at times 0 and T as in Eq. (2.2), with a zero result signifying a periodic system. For a system formulated on $SE(3)$ however, owing to the nonlinearity of the group configuration space, the initial and final beam configurations over a shooting period cannot be simply subtracted. Computing a simple difference between the configurations relies on the assumption of working under a Euclidean embedding, which is not the case considering the nonlinear manifold of the group. This would therefore not offer a meaningful comparison between the body frames of the discretised beam, and would not offer a measure of how close the system is to periodicity. The periodicity equation in Eq. (2.2) should therefore be modified to account for the nonlinearity of the group.

The beam configuration at time T, that is $\mathbf{H}(T)$, may be written as the group composition of the beam configuration at time 0, $\mathbf{H}(0)$, with the exponential of an increment vector belonging to the tangent space at $\mathbf{H}(0)$. This may be written in the form given by Eq. (3.19a) as

$$\mathbf{H}(T) = \mathbf{H}(0)\exp_{SE(3)}(\widetilde{\psi_{\mathbf{H}}}) \tag{4.1}$$

As discussed in Chapter 3, the vector $\psi_{\mathbf{H}}$ represents a local increment vector at $\mathbf{H}(0)$, which leads to a local periodicity condition as explained below. A global view of the periodicity condition may also be adopted, and is explained in Chapter 5.

From Eq. (4.1), the difference between the beam configurations can therefore be measured by the relative increment vector between them, which may be computed using the logarithm map by rearranging Eq. (4.1), resulting in the following modified periodicity equation in vector form

$$\boldsymbol{\psi}(\boldsymbol{X}(0), T) = \begin{bmatrix} \psi_{\mathbf{H}} \\ \psi_{\mathbf{v}} \end{bmatrix} = \begin{bmatrix} \log_{SE(3)}(\mathbf{H}^{-1}(0)\mathbf{H}(T))^{\vee} \\ \mathbf{v}(T) - \mathbf{v}(0) \end{bmatrix} = \mathbf{0}_{12\times 1} \tag{4.2}$$

where $\mathbf{H} \in SE(3)$ is the frame on a material point along the beam, and $\mathbf{v} \in \mathfrak{se}(3)$ is the point's local body velocity. This zero function is computed for all FE nodes along the discretised beam. Note the use of the logarithm map to find the difference between the initial and final frames. In contrast, the local velocities belong to the linear vector space of the Lie algebra $\mathfrak{se}(3)$, and can thus be readily subtracted.

Since the velocities of the system are expressed in the body frame, the periodicity function in Eq. (4.2) misinterprets cases where the dynamics of the beam configuration is not periodic, but the body velocities are periodic or constant. To illustrate this point, consider a simple circular motion with constant angular velocity, as depicted in Figure 4.1. While two points $p(t_1)$ and $p(t_2)$ on the circle will have the same local body velocity $\mathbf{v}_b$ at different times, their positions and orientations will differ. The periodicity function in Eq. (4.2) will incorrectly assess the constant velocities as periodic, while the configuration of the system is not periodic between those points. To overcome this ambiguity, the periodicity function in Eq. (4.2) may be modified further by using a formulation without directly subtracting velocities. Instead, the logarithm map in Eq. (4.2) can be differentiated with respect to time, yielding a term which may be used to assess periodicity for velocities. The advantage of this approach is that it prevents

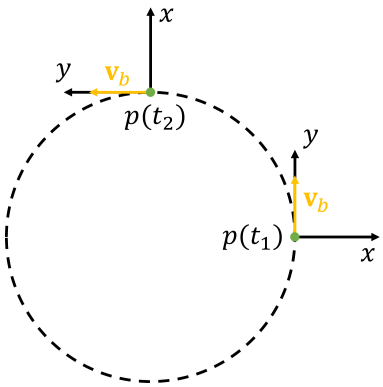


Figure 4.1: Motion around a circle, depicting constant body velocity $\mathbf{v}_b$ as seen in the body frame.

misinterpreting cases where the velocities might be periodic, but the beam configuration is not.

Using the inverse tangent operator for the derivative of the logarithm in Eq. (3.46), the derivative of the frame periodicity in Eq. (4.2) with respect to time can be written as[1]

$$\frac{\mathrm{d}}{\mathrm{d}t}(\psi_{\mathbf{H}}) = \frac{\mathrm{d}}{\mathrm{d}t}(\log_{SE(3)}(\mathbf{H}^{-1}(0)\mathbf{H}(T))) = \mathbf{T}^{-1}_{SE(3)}(\psi_{\mathbf{H}})\boldsymbol{\nu} \tag{4.3}$$

where $\boldsymbol{\nu}$ is the left-invariant vector field of $\mathbf{H}^{-1}(0)\mathbf{H}(T)$ such that

$$\frac{\mathrm{d}}{\mathrm{d}t}(\mathbf{H}^{-1}(0)\mathbf{H}(T)) = \mathbf{H}^{-1}(0)\mathbf{H}(T)\tilde{\boldsymbol{\nu}} \tag{4.4}$$

In order to find the expression for $\boldsymbol{\nu}$, we expand the above using the product rule as

$$\frac{\mathrm{d}}{\mathrm{d}t}(\mathbf{H}^{-1}(0))\mathbf{H}(T) + \mathbf{H}^{-1}(0)\frac{\mathrm{d}}{\mathrm{d}t}(\mathbf{H}(T)) = \mathbf{H}^{-1}(0)\mathbf{H}(T)\tilde{\boldsymbol{\nu}} \tag{4.5}$$

Writing the time derivative of each frame using its left-invariant velocity field we have

$$-\tilde{\mathbf{v}}(0)\mathbf{H}^{-1}(0)\mathbf{H}(T) + \mathbf{H}^{-1}(0)\mathbf{H}(T)\tilde{\mathbf{v}}(T) = \mathbf{H}^{-1}(0)\mathbf{H}(T)\tilde{\boldsymbol{\nu}} \tag{4.6}$$

Which may be written in terms of $\tilde{\boldsymbol{\nu}}$ as

$$\tilde{\boldsymbol{\nu}} = -\left(\mathbf{H}^{-1}(0)\mathbf{H}(T)\right)^{-1}\tilde{\mathbf{v}}(0)\mathbf{H}^{-1}(0)\mathbf{H}(T) + \tilde{\mathbf{v}}(T) \tag{4.7}$$

Noting from Eq. (4.1) that $\mathbf{H}^{-1}(0)\mathbf{H}(T) = \exp_{SE(3)}(\widetilde{\psi_{\mathbf{H}}})$, we have

$$\tilde{\boldsymbol{\nu}} = -\exp^{-1}_{SE(3)}(\widetilde{\psi_{\mathbf{H}}})\tilde{\mathbf{v}}(0)\exp_{SE(3)}(\widetilde{\psi_{\mathbf{H}}}) + \tilde{\mathbf{v}}(T) \tag{4.8}$$

Which may be simplified using the Adjoint in Eq. (3.23), to give

$$\tilde{\boldsymbol{\nu}} = -\mathrm{Ad}_{\exp_{SE(3)}(-\widetilde{\psi_{\mathbf{H}}})}\tilde{\mathbf{v}}(0) + \tilde{\mathbf{v}}(T) \tag{4.9}$$

[1]Note we have dropped the $^\vee$ notation from Eq. (4.3) for clarity of presentation. The vector form of the equations is reinstated in Eq. (4.10).

The above can now be written in vector form, and substituted into Eq. (4.3) to give

$$\frac{\mathrm{d}}{\mathrm{d}t}(\psi_{\mathbf{H}}) = \mathbf{T}^{-1}_{SE(3)}(\psi_{\mathbf{H}}) \left(-\mathrm{Ad}_{\exp_{SE(3)}(-\widetilde{\psi_{\mathbf{H}}})} \mathbf{v}(0) + \mathbf{v}(T) \right) \tag{4.10}$$

The tangent operator is then multiplied into the bracket and simplified using Eq. (C.2) to give

$$\frac{\mathrm{d}}{\mathrm{d}t}(\psi_{\mathbf{H}}) = -\mathbf{T}^{-1}_{SE(3)}(-\psi_{\mathbf{H}})\mathbf{v}(0) + \mathbf{T}^{-1}_{SE(3)}(\psi_{\mathbf{H}})\mathbf{v}(T) \tag{4.11}$$

This expression may replace $\psi_{\mathbf{v}}$ in Eq. (4.2) for a modified periodicity function given by

$$\boldsymbol{\psi}(\boldsymbol{X}(0), T) = \begin{bmatrix} \psi_{\mathbf{H}} \\ \psi_{\mathbf{v}} \end{bmatrix} = \begin{bmatrix} \log_{SE(3)}(\mathbf{H}^{-1}(0)\mathbf{H}(T))^{\vee} \\ -\mathbf{T}^{-1}_{SE(3)}(-\psi_{\mathbf{H}})\mathbf{v}(0) + \mathbf{T}^{-1}_{SE(3)}(\psi_{\mathbf{H}})\mathbf{v}(T) \end{bmatrix} = \mathbf{0}_{12\times 1} \tag{4.12}$$

Note that as $\psi_{\mathbf{H}} \to 0$ during the Newton corrections, Eq. (4.12) tends to Eq. (4.2), as the inverse tangent maps will both tend to identity. Returning to Figure 4.1, it is seen from Eq. (4.12) that when the body velocities are constant, the velocity component of the modified periodicity equation will not be zero when the configurations at times 0 and T are not equal, as the tangent maps will be non-zero, and $\mathbf{T}^{-1}_{SE(3)}(\psi_{\mathbf{H}}) \neq \mathbf{T}^{-1}_{SE(3)}(-\psi_{\mathbf{H}})$.

With the modified periodicity condition, the shooting method is fully adapted to be used under the Lie group framework for the computation of periodicity of the nonlinear system. The methods developed here are generally applicable to differential equations formulated on Lie groups, and are not limited to the Special Euclidean group. With the appropriate use of group-specific expressions for the exponential and logarithm maps, the periodicity equation may be used in shooting methods for initial value problems on any Lie group of interest.

4.3 Continuation Adaptation to Lie Group Formulation

The general predictor-corrector method of the pseudo-arclength continuation routine, as detailed in Chapter 2, is applicable to problems formulated on the Lie group framework. The underlying mechanics of the continuation algorithm do not require fundamental modifications when applied in this context. The main adaptation is related to the correct choice of the initial conditions vector, which should be based on increments in the Lie algebra. Additional adaptations may also be made from an implementation perspective, to better leverage the mathematical tools provided by the Lie group framework, enhancing the overall efficiency and robustness of the continuation process.

4.3.1 Prediction Step and Relative Increments

The initial conditions vector $\boldsymbol{X}(0)$, which is formed during the prediction stage of the continuation process, is typically comprised of the initial state variables of the system. For systems not formulated on Lie groups, these may be initial displacements and velocities. For Lie group dynamical systems, the positional state of the system is uniquely specified by the twist vectors

in the Lie algebra, which can be transformed to group elements through the exponential map, as described in Section 3.1.5. On the other hand, the velocity variables are already in the linear vector space of the Lie algebra, and therefore may be used in the initial conditions vector without modification. Therefore, for the beam model formulated on $SE(3)$, $\boldsymbol{X}(0)$ comprises the N initial state increments and velocities for the entire discretised beam as

$$\boldsymbol{X}_{2N\times 1}(0) = \left[\mathbf{h}_{N\times 1}^T(0) \;\; \mathbf{v}_{N\times 1}^T(0)\right]^T \tag{4.13}$$

where $\mathbf{h}(0)$ represents the twist increments for each FE node, which map the reference beam configuration $\mathbf{H}_0$ to the deformed configuration for the shooting initial conditions $\mathbf{H}(0)$ as

$$\mathbf{H}(0) = \mathbf{H}_0 \exp_{SE(3)}(\mathbf{h}(0)) \tag{4.14}$$

A further adaptation to the prediction point may be made to take full advantage of the Lie group framework of the model, by defining relative increments which are generated with reference to the previous continuation step. After a converged periodic solution is found at step j, the deformed beam configuration $\mathbf{H}_j^\star(0)$ containing the beam initial position and orientation is stored. The initial conditions vector $\boldsymbol{X}^{j+1}(0)$ for the next continuation step is then reimplemented relative to $\mathbf{H}_j^\star(0)$, such that it will contain the increment with respect to $\mathbf{H}_j^\star(0)$, instead of the increment with respect to the undeformed beam configuration $\mathbf{H}_0$. Denoting this increment by $\bar{\mathbf{h}}_j(0)$, $\mathbf{H}_{j+1}(0)$ can then be found using the exponential map as

$$\mathbf{H}_{j+1}(0) = \mathbf{H}_j^\star(0) \exp_{SE(3)}(\widetilde{\bar{\mathbf{h}}_j(0)}) \tag{4.15}$$

and the initial conditions vector is therefore modified as

$$\boldsymbol{X}_{2N\times 1}(0) = \left[\bar{\mathbf{h}}_{N\times 1}^T(0) \;\; \mathbf{v}_{N\times 1}^T(0)\right]^T \tag{4.16}$$

The initial reference beam configuration remains unchanged, and the absolute deformed state in $\mathbf{H}_{j+1}(0)$ is still an absolute deformation with respect to the reference configuration, maintaining the geometric nonlinearity of the system which arises from large deformations. However, as the state of a converged continuation solution is used as the basis of the increment vector for the next prediction point, this relative increment vector will therefore be smaller in magnitude. As the increment is used in the exponential map to find the new beam state in Eq. (4.15), the smaller magnitude of this vector results in reduced nonlinearity from the exponential map, which considerably reduces the number of iterations required in the continuation correction process.

4.3.2 Correction Step and Orthogonality Condition

The significance of forming the initial conditions vector based on increments in the Lie algebra is that the correction step of the continuation method may be applied without any

modifications. As shown in Eq. (4.13), the vector $\boldsymbol{X}(0)$ includes the nodal increments and velocities, both of which belong to the linear space of the Lie algebra $\mathfrak{se}(3)$. As such, Newton corrections can be directly applied to the increments during the continuation process by simple addition in Euclidean space. Furthermore, the orthogonality condition in Eq. (2.6) remains valid, and does not require modifications to be used with the Lie group model. This is due to both the tangent vector and the corrections existing in a linear vector space, thus making it possible for the orthogonality condition to force corrections to remain orthogonal to the tangent vector.

Orthogonality between the corrections and the tangent vector is a common approach used in the pseudo-arclength continuation algorithm to enforce convergence towards the desired solution path, as detailed in Chapter 2. In contrast, Keller [49] proposes an alternative condition which ensures the next continuation solution lies on the hyperplane orthogonal to the tangent vector, and at a distance away from the previous converged solution equal to the continuation step. The key distinction in Keller's method is that, instead of enforcing orthogonality on the corrections, it requires the full solution (prediction plus corrections) to lie on this orthogonal hyperplane. This can be expressed as follows for dynamical systems not formulated on Lie groups:

$$\boldsymbol{u}_j^T(\boldsymbol{X}_{j+1}^k(0) - \boldsymbol{X}_j(0)) + \lambda_j(T_{j+1}^k - T_j) = z_j \tag{4.17}$$

where j is the continuation step, and k indicates the correction iteration. For systems not formulated on Lie groups, calculating the difference between initial condition vectors results in a vector which effectively points from the solution at continuation step j to that at step $j+1$. However, for Lie group systems, as the initial condition vectors contain the increments from the reference configuration[1], taking their difference would not yield the difference between the configurations at consecutive continuation steps, and would therefore not generate the directional vector between them. Since we require the corrections to the increments to be such that the solution at step $j+1$ lies on the hyperplane, it is important that the correct difference between the configurations at consecutive continuation steps are computed. The correct way to compute the difference vector required in Eq. (4.17) is to determine the relative configuration vector between the frame at steps j and $j+1$. This would require an adaptation of Eq. (4.17) to include the logarithm map to find the relative difference between the frames for every correction iteration k, as follows

$$\boldsymbol{u}_j^T \begin{bmatrix} \log_{SE(3)}(\mathbf{H}_j^\star(0)^{-1}\mathbf{H}_{j+1}^k(0))^\vee \\ \mathbf{v}_{j+1}^k(0) - \mathbf{v}_j^\star(0) \end{bmatrix} + \lambda_j(T_{j+1}^k - T_j) = z_j \tag{4.18}$$

where it is seen that the velocities can be simply subtracted following Eq. (4.17).It is noted that, if the continuation is performed using relative increments for the prediction points, as described in Section 4.3.1, then the relative increment vector serves as the correct difference between the solutions at step j and $j+1$, and may be used directly in the orthogonality condition.

[1]Here we are referring to the case where relative increments are not computed, and increments at each step are measured from the reference configuration.

The orthogonality condition can be incorporated into the continuation correction step by computing its derivative and augmenting the Jacobian in the Newton iterations. With the adapted formulation in Eq. (4.18), this would require derivatives on the Lie group, which would lead to a more difficult implementation. This orthogonality condition is therefore not employed in this thesis, although it could be further investigated as it could result in a more robust correction algorithm [49].

4.4 Sensitivities

As discussed in Chapter 2, the sensitivity of the periodicity function with respect to the initial conditions and the period is required in the Newton-Raphson correction step in Eq. (2.6). To this end, the derivative of the periodicity equation in Eq. (4.12) should be computed. The gradient of $\psi_{\mathbf{H}}$ can be written using the inverse tangent operator as

$$\mathrm{d}\psi_{\mathbf{H}} = -\mathbf{T}^{-1}_{SE(3)}(-\psi_{\mathbf{H}})\,\mathrm{d}\mathbf{h}(0) + \mathbf{T}^{-1}_{SE(3)}(\psi_{\mathbf{H}})\,\mathrm{d}\mathbf{h}(T) \tag{4.19}$$

Using this equation, we can find the sensitivity of $\psi_{\mathbf{H}}$ with respect to the initial conditions as

$$\frac{\partial \psi_{\mathbf{H}}}{\partial \mathbf{X}(0)} = -\mathbf{T}^{-1}_{SE(3)}(-\psi_{\mathbf{H}})\frac{\partial \mathbf{h}(0)}{\partial \mathbf{X}(0)} + \mathbf{T}^{-1}_{SE(3)}(\psi_{\mathbf{H}})\frac{\partial \mathbf{h}(T)}{\partial \mathbf{X}(0)} \tag{4.20}$$

We now consider the monodromy matrix, that is the derivatives of the system's final states with respect to the initial conditions (increments and velocities), as $M_{2N\times 2N} = [\underline{w}_{N\times 2N} \quad \underline{v}_{N\times 2N}]^T$, where $\underline{w}$ and $\underline{v}$ represent the rows of the monodromy corresponding to the spatial and velocity derivatives respectively. The partial derivative in the second term in Eq. (4.20) is identical to the spatial derivatives included in the monodromy[1], which may be used to simplify the sensitivity as

$$\frac{\partial \psi_{\mathbf{H}}}{\partial \mathbf{X}(0)}_{N\times 2N} = -\mathbf{T}^{-1}_{SE(3)}(-\psi_{\mathbf{H}})\begin{bmatrix}\mathbf{I} & \mathbf{0}\end{bmatrix}_{N\times 2N} + \mathbf{T}^{-1}_{SE(3)}(\psi_{\mathbf{H}})\underline{w} \tag{4.21}$$

which is computed for each node of the finite element model. It is noted that the first term in the above equation is nonzero only on the diagonal of the first N columns, and therefore adds only to the first N columns of the second term. It is further noted that, as $\psi_{\mathbf{H}} \to 0$ during the Newton corrections, $\dfrac{\partial \psi_{\mathbf{H}}}{\partial \mathbf{X}(0)} \to \underline{w} - \begin{bmatrix}\mathbf{I} & \mathbf{0}\end{bmatrix}$, which is the typical periodicity function sensitivity for dynamic systems not formulated on Lie groups.

The gradient of $\psi_{\mathbf{v}}$ can also be evaluated and is written as follows,

$$\begin{aligned}\mathrm{d}\psi_{\mathbf{v}} = &-\mathbf{T}^{-1}_{SE(3)}(-\psi_{\mathbf{H}})\,\mathrm{d}\mathbf{v}(0) + \mathbf{T}^{-1}_{SE(3)}(\psi_{\mathbf{H}})\,\mathrm{d}\mathbf{v}(T)\\ &-\mathrm{D}_{\mathbf{v}(0)}\mathbf{T}^{-1}_{SE(3)}(-\psi_{\mathbf{H}})(-\,\mathrm{d}\psi_{\mathbf{H}}) + \mathrm{D}_{\mathbf{v}(T)}\mathbf{T}^{-1}_{SE(3)}(\psi_{\mathbf{H}})(\mathrm{d}\psi_{\mathbf{H}})\end{aligned} \tag{4.22}$$

The derivatives of the inverse tangent operators above are interpreted as directional derivatives

[1] Recall from Eq. (4.13) that $\mathbf{h}$ represents the state increments which are the Lie algebra twist elements for each beam node. Therefore, the derivative of $\mathbf{h}(T)$ with respect to $\mathbf{X}(0)$ is precisely the first N rows of the monodromy matrix.

along the velocity vectors indicated by the subscripts of the derivative operator. Sonneville [209] represents these directional velocity vectors as a second argument to $\mathbf{T}^{-1}_{SE(3)}$ and has developed closed-form expressions for these derivatives. Equivalent expressions for these based on the Euler-Rodrigues motion parametrisation are provided in Appendix A. The sensitivities may now be written as below

$$\begin{aligned}\frac{\partial \psi_{\mathbf{v}}}{\partial \mathbf{X}(0)} =& -\mathbf{T}^{-1}_{SE(3)}(-\psi_{\mathbf{H}})\frac{\partial \mathbf{v}(0)}{\partial \mathbf{X}(0)} + \mathbf{T}^{-1}_{SE(3)}(\psi_{\mathbf{H}})\frac{\partial \mathbf{v}(T)}{\partial \mathbf{X}(0)} \\ &- \mathrm{D}_{\mathbf{v}(0)}\mathbf{T}^{-1}_{SE(3)}(-\psi_{\mathbf{H}})(-\frac{\partial \psi_{\mathbf{H}}}{\partial \mathbf{X}(0)}) + \mathrm{D}_{\mathbf{v}(T)}\mathbf{T}^{-1}_{SE(3)}(\psi_{\mathbf{H}})(\frac{\partial \psi_{\mathbf{H}}}{\partial \mathbf{X}(0)})\end{aligned} \tag{4.23}$$

Similar to Eq. (4.21), the monodromy can be substituted into the equations and the terms can be simplified to give

$$\begin{aligned}\frac{\partial \psi_{\mathbf{v}}}{\partial \mathbf{X}(0)}_{N\times 2N} =& -\mathbf{T}^{-1}_{SE(3)}(-\psi_{\mathbf{H}})\begin{bmatrix}\mathbf{0} & \mathbf{I}\end{bmatrix}_{N\times 2N} + \mathbf{T}^{-1}_{SE(3)}(\psi_{\mathbf{H}})\underline{v} \\ &- \mathrm{D}_{\mathbf{v}(0)}\mathbf{T}^{-1}_{SE(3)}(-\psi_{\mathbf{H}})(-\frac{\partial \psi_{\mathbf{H}}}{\partial \mathbf{X}(0)}) + \mathrm{D}_{\mathbf{v}(T)}\mathbf{T}^{-1}_{SE(3)}(\psi_{\mathbf{H}})(\frac{\partial \psi_{\mathbf{H}}}{\partial \mathbf{X}(0)})\end{aligned} \tag{4.24}$$

It is noted that the first term in the above equation is nonzero only on the diagonal of the second N columns, and therefore adds only to the second N columns of the remaining terms. The sensitivities of $\psi_{\mathbf{H}}$ also appear in the equations, which have already been found in Eq. (4.21) and can be substituted in.

It is noted that, as periodicity is achieved and $\psi_{\mathbf{H}} \to 0$, the terms involving derivatives of the inverse tangent operator generally do not disappear, as they represent how the derivative is influenced by the direction vector. However, with a phase condition of velocities on all degrees of freedom equal to zero (see Section 4.5), the direction vectors $\mathbf{v}(0)$ and $\mathbf{v}(T)$ will both be zero for a periodic solution, and thus we have $\frac{\partial \psi_{\mathbf{v}}}{\partial \mathbf{X}(0)} \to \underline{v} - \begin{bmatrix}\mathbf{0} & \mathbf{I}\end{bmatrix}$. This is a special case, and for other phase conditions, the derivatives of the tangent operator will generally be non-vanishing. An alternative periodicity condition based on a global view of the increments between the frames is formulated in Section 5.7, which leads to expressions of the tangent operator in the sensitivity equations which do vanish with periodicity.

The sensitivity of the periodicity function with respect to the shooting period T is computed in a similar way. Taking the sensitivity of the final states of the system with respect to period as $\underline{t}_{2N\times 1} = [\underline{tw}_{N\times 1} \quad \underline{tv}_{N\times 1}]^T$ we can then follow a similar procedure and use Eq. (4.21) to compute the spatial derivatives $\frac{\partial \psi_{\mathbf{H}}}{\partial T}_{N\times 1}$, and Eq. (4.24) to compute the velocity derivatives $\frac{\partial \psi_{\mathbf{v}}}{\partial T}_{N\times 1}$. These are therefore given as

$$\frac{\partial \psi_{\mathbf{H}}}{\partial T}_{N\times 1} = \mathbf{T}^{-1}_{SE(3)}(\psi_{\mathbf{H}})\underline{tw} \tag{4.25}$$

and

$$\frac{\partial \psi_{\mathbf{v}}}{\partial T}_{N\times 1} = \mathbf{T}^{-1}_{SE(3)}(\psi_{\mathbf{H}})\underline{tv} - \mathrm{D}_{\mathbf{v}(0)}\mathbf{T}^{-1}_{SE(3)}(-\psi_{\mathbf{H}})(-\frac{\partial \psi_{\mathbf{H}}}{\partial T}) + \mathrm{D}_{\mathbf{v}(T)}\mathbf{T}^{-1}_{SE(3)}(\psi_{\mathbf{H}})(\frac{\partial \psi_{\mathbf{H}}}{\partial T}) \tag{4.26}$$

4.4.1 Computation of the Monodromy

The monodromy itself can be calculated using sensitivity analysis through a direct differentiation method wherein the equations of motion are directly differentiated with respect to the parameters. Two direct differentiation methods can be developed, either by integration of the differentiated equations of motion, or the differentiation of the time-discretised equations of motion [212]. In the first approach, the equations of motion and the initial conditions are differentiated, and the sensitivities are solved by integration using the generalised-α method with the same numerical parameters as the nominal problem. The compact formulation of the equations of motion within the Lie group framework is advantageous in this regard. The Lie bracket operator appears throughout the equations due to the nonlinearity of the Lie group. In the second approach, rather than differentiating the equations of motion, the time integration method on these equations is differentiated, leading to a linear differential equation to be solved alongside the nominal problem. The exponential operator and its derivative appear in these equations due to the Lie group structure. Crucially, in this second approach, unlike the first, the iteration matrix in solving the sensitivity equation is the same as the nominal problem, simplifying implementation in simulation codes. In both approaches, sensitivities may be computed on the fly and simultaneously with the mechanical system. The second approach is used in this work to compute sensitivities. Starting from the time integration equation introduced in Eq. (3.248)

$$q_{n+1} = q_n \exp(\widetilde{\mathbf{x}}_{n+1}) \tag{4.27}$$

and denoting $\bullet'$ as the derivative with respect to a parameter p, the derivative of the above may be written as

$$q'_{n+1} = q'_n \exp(\widetilde{\mathbf{x}}_{n+1}) + q_n \exp'(\widetilde{\mathbf{x}}_{n+1}) \tag{4.28}$$

Writing the derivative of q using the Lie algebra element $\widetilde{\mathbf{w}}$ as

$$q' = q\widetilde{\mathbf{w}} \tag{4.29}$$

Eq. (4.28) can be written as

$$\widetilde{\mathbf{w}}_{n+1} = \exp^{-1}(\widetilde{\mathbf{x}}_{n+1})\widetilde{\mathbf{w}} \exp(\widetilde{\mathbf{x}}_{n+1}) + \exp^{-1}(\widetilde{\mathbf{x}}_{n+1}) D_{\exp}(\widetilde{\mathbf{x}}_{n+1}) \cdot \widetilde{\mathbf{x}}'_{n+1} \tag{4.30}$$

Using the tangent operator in Eq. (3.43) the following linear relationship can be written in vector form

$$\mathbf{w}_{n+1} = \mathbf{D}\left(\exp(\widetilde{\mathbf{x}}_{n+1})\right) \mathbf{w}_n + \mathbf{T}(\mathbf{x}_{n+1})\mathbf{x}'_{n+1} \tag{4.31}$$

where $\mathbf{D}(q)$ is a matrix satisfying $\widetilde{\mathbf{D}(q)\mathbf{w}} = q^{-1}\widetilde{\mathbf{w}}q$. The differentiation is also applied to the residual vector in the equation of motion in Eq. (3.248), leading to the update scheme

$$\mathbf{M}_T \dot{\mathbf{v}}'_{n+1} + \mathbf{C}_T \mathbf{v}'_{n+1} + \mathbf{K}_T \mathbf{w}_{n+1} = -\mathbf{r} \tag{4.32}$$

to be solved alongside Eq. (4.31). The complete sensitivity analysis algorithm is obtained by combining the above equations with the differentiated form of the time integration formulas in Eq. (3.249) as

$$\begin{aligned}
\mathbf{x}'_{n+1} &= h\mathbf{v}'_n + (0.5-\beta)h^2\mathbf{a}'_n + \beta h^2\mathbf{a}'_{n+1} \\
\mathbf{v}'_{n+1} &= \mathbf{v}'_n + (1-\gamma)h\mathbf{a}'_n + \gamma h\mathbf{a}'_{n+1}, \\
\mathbf{a}'_{n+1} &= \frac{1}{(1-\alpha_m)}((1-\alpha_f)\dot{\mathbf{v}}'_{n+1} + \alpha_f\dot{\mathbf{v}}'_n - \alpha_m\mathbf{a}'_n)
\end{aligned} \tag{4.33}$$

It is seen that the iteration matrix is exactly the same as the nominal problem in Eq. (3.254), which simplifies implementation of the algorithm.

It is noted that, the discrete adjoint method may also be used for sensitivity analysis, which is more efficient for problems involving numerous design parameters. Callejo et al. [43] have developed a Lie group compatible discrete adjoint solver based on the generalised-α time integration scheme, which does not rely on backward time integration to solve the adjoint equations.

4.5 Phase Condition

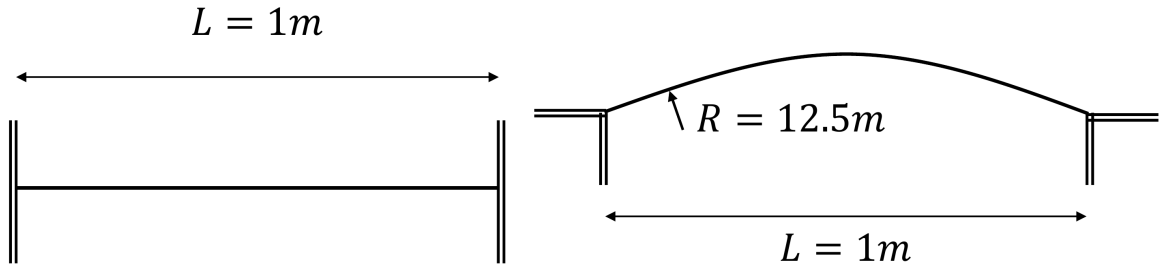
As discussed in Chapter 2, a phase condition is required to ensure a unique periodic solution is found by the shooting algorithm. As the system trajectory must be periodic, the velocities must change sign and therefore cross zero. A suitable phase condition would therefore be to set the velocity to zero for only one degree of freedom with a single constraint equation [76]. In the context of a Lie group formulation, special care must be taken when enforcing a velocity phase condition to correctly account for the group's nonlinearity. A phase condition on velocities is essentially a non-holonomic constraint, since velocities are expressed in the local frame and are therefore configuration dependent. A phase condition may only be enforced on the inertial frame, which serves as a fixed holonomic basis. However, setting only one velocity to zero in the inertial frame requires special attention, as velocities are expressed locally, and non-zero local velocities may combine to give zero velocities in the inertial frame. Consequently, the approach in Eq. (2.3) cannot be used to set only one velocity to zero, as velocities should be transformed to the inertial frame first, through a configuration-dependent rotation matrix which itself evolves with the system's equation of motion. In addition, the gradient of such a phase constraint should also be calculated as it is needed in the Newton corrections.

To minimise computational complexity, the analysis done in this chapter utilises the phase condition of setting all initial velocities to zero, as it can be used with the Lie group formulation without extra modifications. No special consideration is required for such a condition as it will hold true irrespective of the choice of local or inertial frame. The equation for this phase condition and its derivative are given in Eq. (2.3). Such a phase condition is practical and has been employed in both shooting [170] and harmonic balance methods [86]. However, this phase condition is unsuitable for computing asymmetric NNMs or NNMs represented by a closed-loop configuration space, or when the degrees of freedom do not cross zero synchronously [170].

Additionally, the resulting Jacobian matrix in the Newton iterations of the continuation correction step is non-square due to an overdetermined system, and the problem must therefore be solved in a least-squares sense. Other phase conditions, such as the Poincaré or integral phase condition, may also be used. However, they also need to be modified for use within the Lie group formulation.

4.6 Comparison of SE & von Kármán Beams on 2D Cases

Three 2D test cases were chosen to compare NNMs found using the SE FE model and those from the von Kármán model. These are a straight clamped-clamped beam, a shallow arch, and a cantilever beam. In all cases, the beam is discretised with 30 elements, and its geometric and material properties are given as [207]: $E = 210\,GPa$, $\rho = 7850\,kg/m^3$, $L = 1\,m$, $A = 10^{-4}\,m^2$. The geometry for the straight beam and the arch is illustrated in Figure 4.2. As the cases are 2D, the beam formulation is made under the $SE(2)$ framework. The NNMs are calculated using shooting and pseudo-arclength continuation, as discussed previously. Since the periodic solutions are for a conservative system, the numerical damping for the generalised-α integrator is not used. The generalised-α defaults thus to the Newmark scheme.

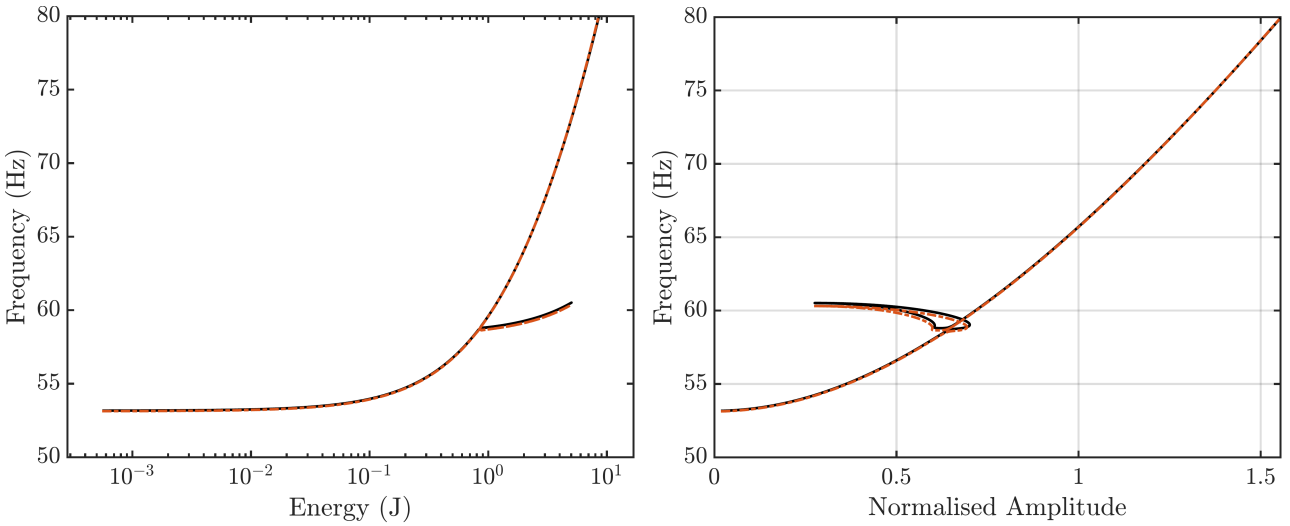


(a) Clamped-clamped beam. (b) Shallow arch.

Figure 4.2: Geometry of 2D test cases. Cantilever beam is identical to the clamped-clamped beam geometry.

4.6.1 Straight Clamped-Clamped Beam: NNM1

The frequency-energy plot (FEP) for the first NNM of the clamped-clamped beam is shown in Figure 4.3a, where the effects of nonlinearity can be observed in the increase of frequency with energy. The figure shows the occurrence of a thin loop, termed an internal resonance tongue, comprising periodic solutions that indicate a 5:1 interaction between NNM1 and NNM3. The $SE(2)$ and the von Kármán model agree well on this example, as the beam is not experiencing large displacements and rotations, and the von Kármán model can therefore adequately predict the system dynamics. As discussed in Chapter 2, the coupling between the axial and the bending displacements, also known as membrane-bending coupling, can be modelled under the von Kármán framework with sufficient accuracy. For the doubly clamped beam, this coupling



(a) Frequency Energy plot.

(b) Max normalised amplitude at $x/L = 0.5$.

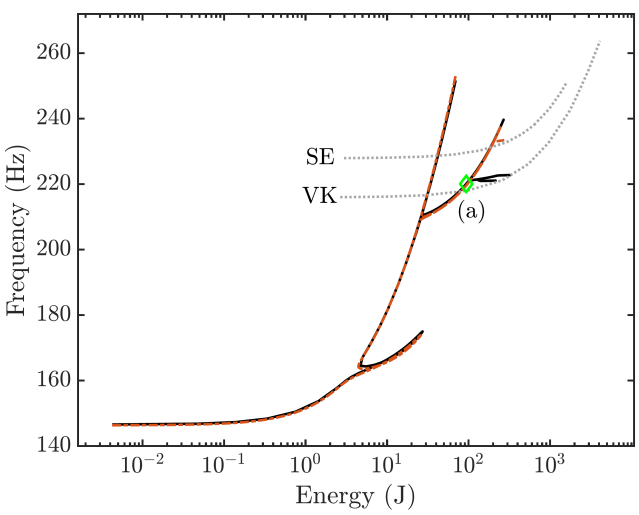
Figure 4.3: First NNM of clamped-clamped beam. Comparison between von Kármán (black) and $SE(2)$ (orange). Amplitude normalised with respect to beam thickness $b = 10^{-2}\,m$.

constitutes the main source of nonlinearity, as the beam cannot undergo large displacements and rotations due to the constrained boundaries.

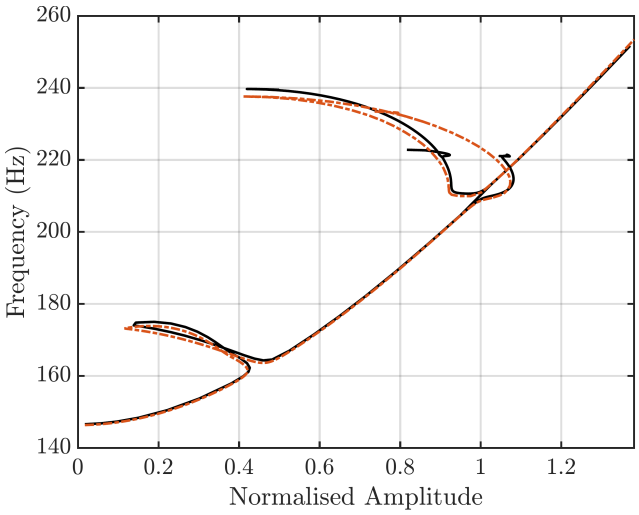
Figure 4.3b shows the maximum absolute in-plane displacement of the beam midpoint normalised with respect to the beam thickness, over the range of frequencies observed in the FEP. The maximum is taken as the largest displacement during the full period of the shooting solution. The backbone and tongue are observed, and again good agreement is noted between the models which continues through to larger amplitude displacements.

4.6.2 Straight Clamped-Clamped Beam: NNM2

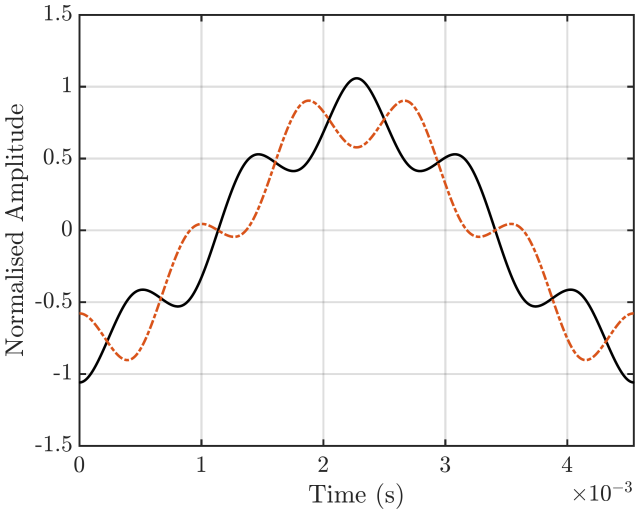
The frequency energy plot corresponding to the second NNM is seen in Figure 4.4a. Two resonance tongues appear on the solution curve, the first starting at approximately 160 Hz and corresponding to a 3:1 interaction with NNM4, and the second starting at approximately 207 Hz and corresponding to a 5:1 interaction with NNM6. Additional smaller secondary branches can be seen on the higher tongue, namely at approx. 221 Hz for the von Kármán model and at approx. 233 Hz for the $SE(2)$ model. These correspond to higher order harmonic interactions with NNM13 at a 17:1 ratio for both models. The backbones of NNM13 are included in Figure 4.4a in grey for both models, where the frequency has been divided by the harmonic ratio of 17. It is seen that the backbones cross the curve near the regions where the secondary tongues are located. The linear natural frequencies for mode 13 for the von Kármán and the $SE(2)$ model are 3672 Hz and 3928 Hz respectively. This difference in the frequencies of the higher modes leads to the separation of the backbone curves, and thus to the difference in the frequency at which the 17:1 interactions on the FEP occur. In general, the frequency-energy dependence is also greater for higher modes, resulting in greater difference between the linear natural frequencies and the trend of the backbone curves. The differences in the higher modes could therefore have a significant effect on the location and shape of the interaction tongues.



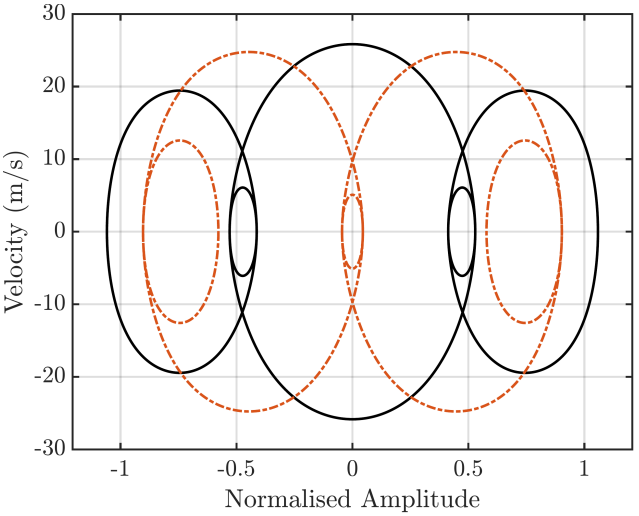
(a) Frequency Energy plot.



(b) Max normalised amplitude at $x/L = 0.3$.



(c) Time history of point (a).



(d) Phase space.

Figure 4.4: Second NNM of clamped-clamped beam. Comparison between von Kármán (black) and $SE(2)$ (orange). Dotted grey lines indicate NNM13 for both models with frequency divided by 17. Time history of displacement of point (a) depicted, showing normalised vertical amplitude at $x/L = 0.3$. A 5:1 interaction between modes 2 and 6 is observed, and a $\pi/2$ phase difference exists between the 5th harmonics of the two solutions. Amplitude normalised with respect to beam thickness $b = 10^{-2}\,m$.

The difference between the NNMs can also be observed in the amplitude plots in Figure 4.4b, which shows the maximum absolute in-plane displacement at the $x/L = 0.3$ point along the beam, normalised with respect to the beam thickness. The time evolution of the vertical displacement at the $x/L = 0.3$ point for the periodic solution (a) indicated in Figure 4.4a can be seen in Figure 4.4c. The 5:1 frequency ratio can clearly be seen, and a difference is observed between the solutions from the two models. This is also highlighted in Figure 4.4d which shows the solutions in phase space. The difference in the solutions is due to a $\pi/2$ phase shift in the 5th harmonic of the responses from the two models. It is known that through an interaction tongue, the phase of the periodic solution changes by $\pi/2$ [115], [207]. As the modal interactions are occurring at different energy levels for the two models, the phase shift in the 5th harmonic

could be attributable to a difference in the energy level at which the solution passes through the tongue and the phase changes for the two models. It is noted that a direct comparison of solutions from points selected on the frequency-energy plot is extremely challenging, as the graph is a 2D projection of a high-dimensional state space. Selected points are here chosen based on their qualitative similarity (for instance, turning points on the FEP), bearing in mind that solutions may not be strictly identical.

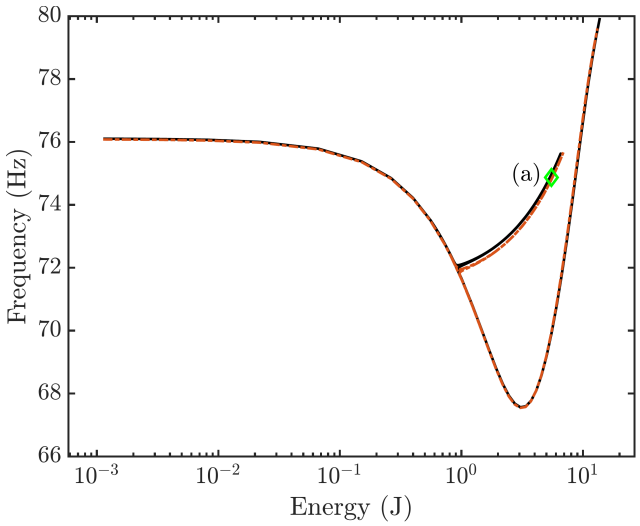
4.6.3 Shallow Arch: NNM1

A shallow arch is created by curving the doubly clamped beam such that the midpoint is displaced vertically by $10mm$, thus creating a curvature of radius $R = 12.5m$. The material properties of the beam are unchanged. The effects of curvature are manifested as the existence of both vertical and lateral displacements in the linear mode shapes of the model [207].

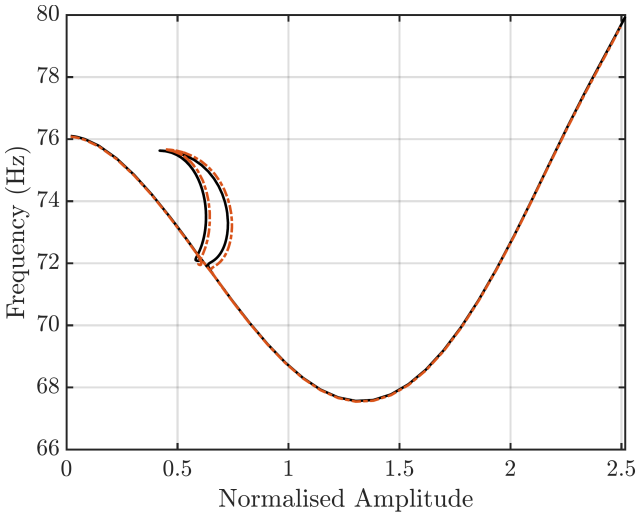
The FEP of the first NNM is shown in Figure 4.5a. A softening-hardening behaviour is observed, which is characteristic of structures with initial curved geometries [207], and an internal resonance tongue is seen within the softening region. The tongue indicates a 4:1 resonance between NNM1 and NNM3. This is in contrast with the 5:1 resonance seen between these modes for the first NNM of the straight beam, which is due to the asymmetry of initial curvature promoting the occurrence of even interaction ratios [207]. The normalised absolute maximum vertical displacement of the beam midpoint is depicted in Figure 4.5b. Despite displacement amplitudes larger than twice the beam thickness, the von Kármán model is able to make a correct prediction of the periodic solutions. Similar to the clamped-clamped beam, the shallow arch also exhibits axial-bending coupling due to the clamped boundaries, which the von Kármán formulation can model sufficiently accurately with the quadratic bending terms in the axial strains (see Eq. (2.20)). The time history of the vertical displacement of the arch mid-point from the periodic solution at point (a) from Figure 4.5a is presented in Figure 4.5c, which shows the 4:1 frequency ratio between the harmonics. Similar to the clamped-clamped beam, a $\pi/2$ phase shift exists between the 4th harmonic of the responses, causing a difference in the time history of the two models.

4.6.4 Shallow Arch: NNM2

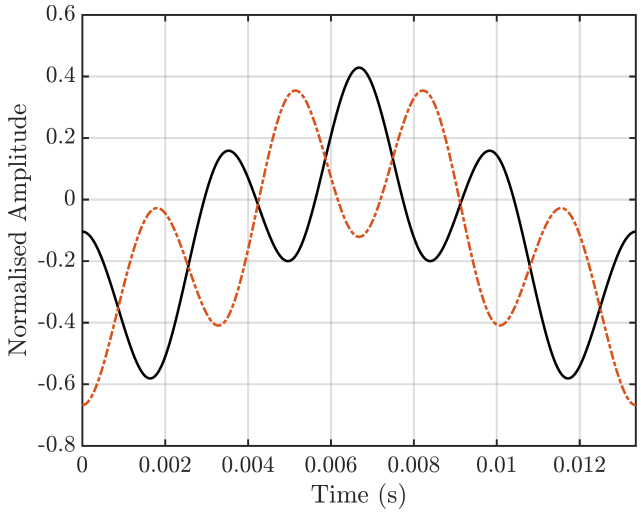
The FEP for the second NNM is presented in Figure 4.6a. Increasingly complex dynamics can be seen, with multiple interactions between various modes of the system. The main tongue spans a large frequency range between 160 and 180 Hz, and corresponds to a 3:1 interaction between NNM2 and NNM4. Higher-order interactions are seen as secondary tongues which branch away from the main curve. The secondary tongue between 168-170 Hz (terminating at point (a) on the FEP) is captured by both models and indicates the presence of NNM7 at an 8:1 ratio with NNM2, along with static contributions from NNMs 1 and 3. Similar static contributions from additional modes were also reported by Sombroek et al. [207] for the arch. Figure 4.6b shows the time history of the periodic solution at point (a) depicting the normalised vertical displacement at the beam point $x/L = 0.36$. It is seen that for this point



(a) Frequency Energy plot.



(b) Max normalised amplitude at x/L = 0.5.

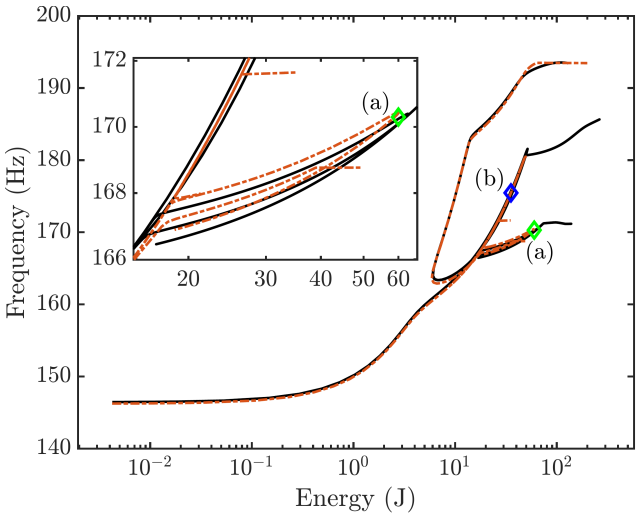


(c) Time history of point (a).

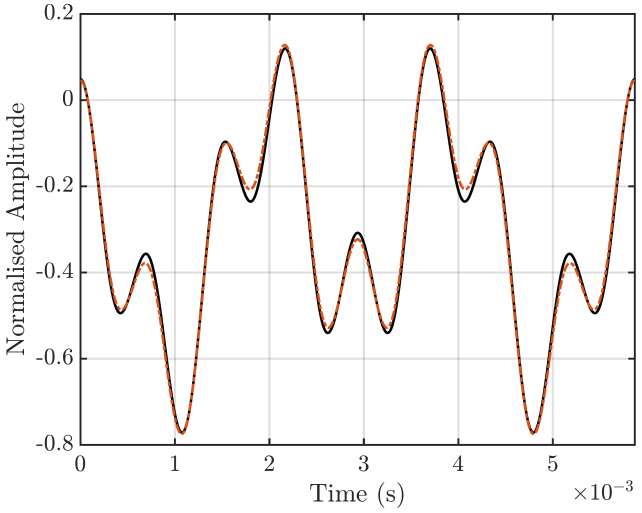
Figure 4.5: First NNM of shallow arch. Comparison between von Kármán (black) and $SE(2)$ (orange). Time history of displacement of point (a) depicted, showing normalised vertical amplitude at $x/L = 0.5$.A 4:1 interaction between modes 1 and 3 is observed, and a $\pi/2$ phase difference exists between the 4th harmonics of the two solutions. Amplitude normalised with respect to beam thickness $b = 10^{-2}\,m$.

the models predict the same periodic solution corresponding to the same point on the FEP. The von Kármán and $SE(2)$ solutions start to differ at higher frequency ranges above this point. A smaller secondary tongue which emanates at approx. 172 Hz on the $SE(2)$ curve indicates higher-order dynamic interaction through the 24th harmonic which is not captured by the von Kármán model. An additional interaction occurring at approx. 180 Hz on the main tongue is with NNM9 through the 12th harmonic, and is found only by the von Kármán model. As seen previously with the doubly clamped beam, the differences in the higher modes between the models can lead to high-order interactions appearing at different frequencies, which is why these interactions are not captured by both models at the same locations on the FEP.

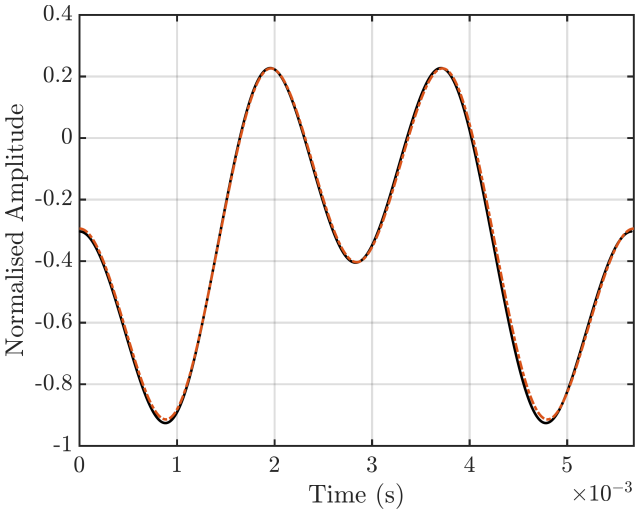
The periodic solution at point (b) in Figure 4.6a is presented in Figure 4.6c, which shows the



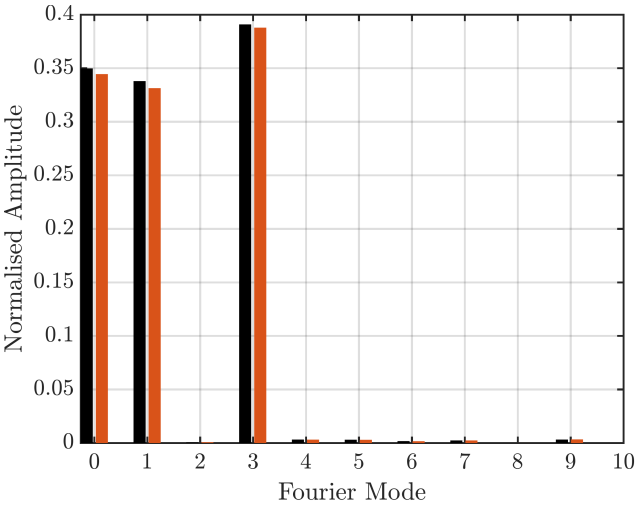
(a) Frequency Energy plot.



(b) Time history of point (a).



(c) Time history of point (b).



(d) Frequency content of point (b).

Figure 4.6: Second NNM of shallow arch, comparison between von Kármán (black) and $SE(2)$ (orange). Time history of displacement of points (a) and (b) depicted, showing normalised vertical amplitude at $x/L = 0.36$. NNM7 present at 8:1 ratio with NNM2 at point (a). Amplitude normalised with respect to beam thickness $b = 10^{-2}\,m$.

time series of the vertical displacement at the $x/L = 0.36$ point, and its frequency spectrum, respectively. The 3:1 interaction between NNM2 and NNM4 is observed, where some static contribution is also present from NNM 1. There is good agreement between the time histories for both models, which is to be expected as higher-order dynamics are not manifested on the periodic solution at point (b).

4.6.5 Straight Cantilever Beam: NNM1

As a final test case, the straight beam was made free on one end to create a straight cantilever beam. The material properties of the beam remain unchanged.

The FEP of the first NNM is shown in Figure 4.7. It is seen that the responses from the beam models are characteristically different, with the $SE(2)$ model showing hardening

behaviour in contrast to the softening behaviour of the von Kármán model. The hardening effect for the $SE(2)$ model is in agreement with the results obtained using an intrinsic beam model by Palacios [158] and a geometrically exact model by Debeurre et al. [58]. This supports the conclusion that the softening behaviour observed from the von Kármán model is incorrect. This softening behaviour is not observed if the von Kármán model is solved with full integration, as the effect of full integration is seen in an overall stiffening of the structure. This serves as a strong motivation to not use the von Kármán formulation to model large displacements and rotations, as full integration can lead to shear locking [177], and reduced integration, as observed here, can lead to incorrect results.

The $SE(2)$ model is able to trace the backbone of NNM1 to higher energy levels, compared to the lower levels found by the von Kármán model. The highest energy point on the backbone is indicated by a green marker on the FEP for both models. The deformed shape of the beam corresponding to this point is given in Figure 4.8. It is clearly seen that the $SE(2)$ model is able to capture periodic responses with significantly larger displacements and rotations compared to the von Kármán model. Despite significant efforts, the continuation algorithm was not able to trace the von Kármán curve beyond the point already found in Figure 4.7. The geometric nonlinearity arising from extremely large displacements and rotations of the cantilever at high energy levels cannot be modelled with the von Kármán formulation due to the linearisation of the rotations, as discussed in Chapter 2. At higher energies, solutions on the $SE(2)$ backbone start showing contributions from NNM8, which is the first axial mode of the beam, due to the large deformations leading to axial motion. The frequency content of the solutions also shows vibrations at the third harmonic of the fundamental frequency of NNM1. As the contribution of NNM8 grows along the backbone, higher-order interaction tongues begin to appear. These correspond to mixed interactions with higher axial modes such as 14, 19, and 22, primarily at the 15th, 17th, and 19th harmonic. The presence of the axial modes in the response, which is characterised by large cross sectional rotations and displacements, further motivates the use of the $SE(2)$ model to ensure the axial deformations and their effect on the periodic solution is captured correctly. An additional source of nonlinearity is due to the inertia forces which become nonlinear under large rotations and displacement. As described in Chapter 2, these are not taken into account in the von Kármán formulation. The $SE(2)$ model however accounts for the change in inertia following a change in the beam shape due to deformation, as detailed in Chapter 3.

It was further found that the von Kármán model required a smaller time step by an order of magnitude in the shooting time integration for tracing the NNM curve compared to the $SE(2)$ model, resulting in slower convergence of the continuation process. Though not systematically quantified here, it was observed that the $SE(2)$ model can accurately produce the correct NNM solutions with fewer FE elements - an observation that is supported by other observations already made in the literature [208]. This indicates a further usable possibility for reducing the overall computational time. The cantilever therefore presents a case where there are starker differences between the NNMs obtained by the $SE(2)$ and von Kármán models. A strong

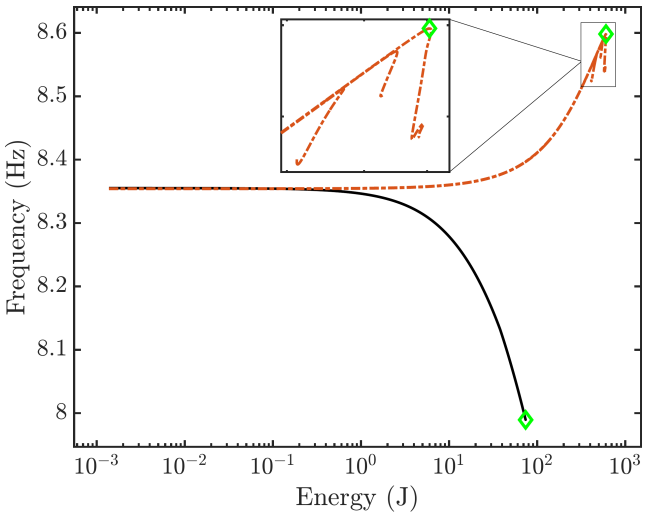
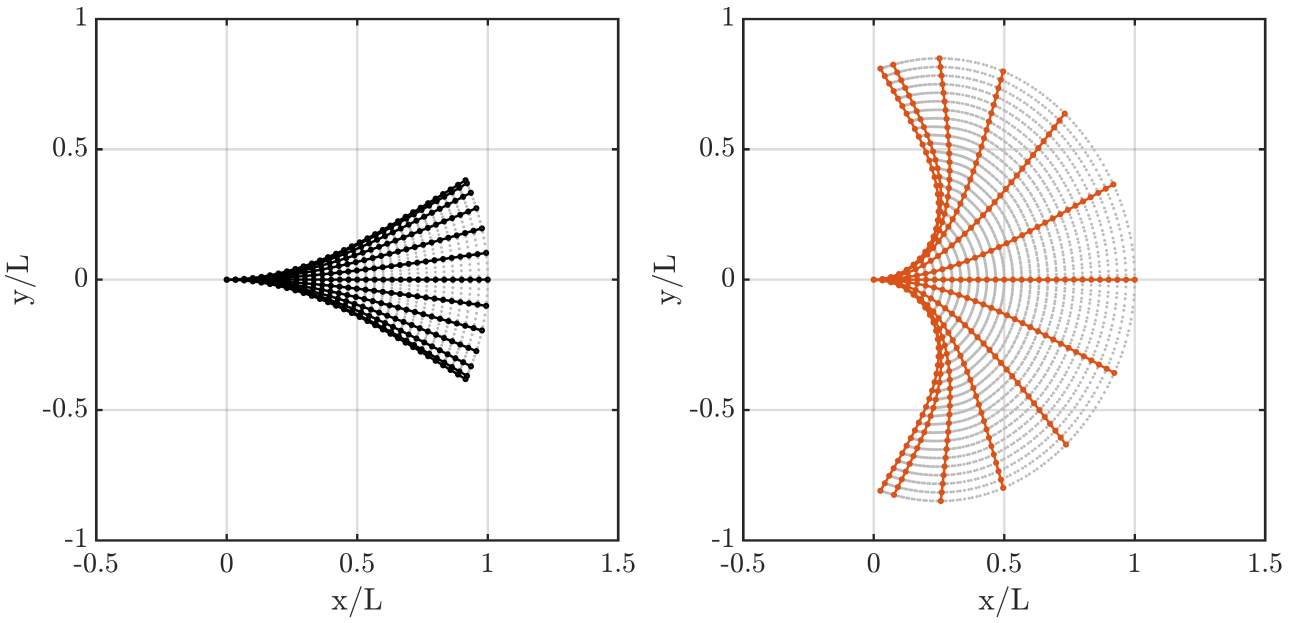


Figure 4.7: FEP of first NNM of straight cantilever. Comparison between von Kármán (black) and $SE(2)$ (orange). Point shown indicates highest energy point captured on the backbone for each model.



(a) von Kármán. (b) $SE(2)$.

Figure 4.8: Deformed beam shape of first NNM of cantilever beam, at points indicated by green marker in Figure 4.7.

argument can therefore be made for using the $SE(2)$ model over the von Kármán for modelling beams with large rotations and deformations such as the cantilever.

4.6.6 Straight Cantilever Beam: NNM2

The FEP of the second NNM is shown in Figure 4.9. Here, the backbones are in agreement, while various interaction tongues are observed on the $SE(2)$ curve. A prominent tongue appears at around 51 Hz, which corresponds to a 41:1 interaction with NNM11. Smaller tongues corresponding to high order harmonics also appear further along the backbone. The deformed beam shape at the lowest frequency point on the backbone (approx. 44.8 Hz) for both models is

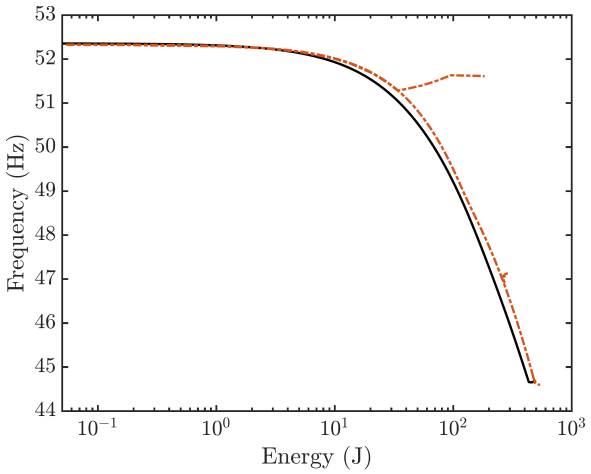


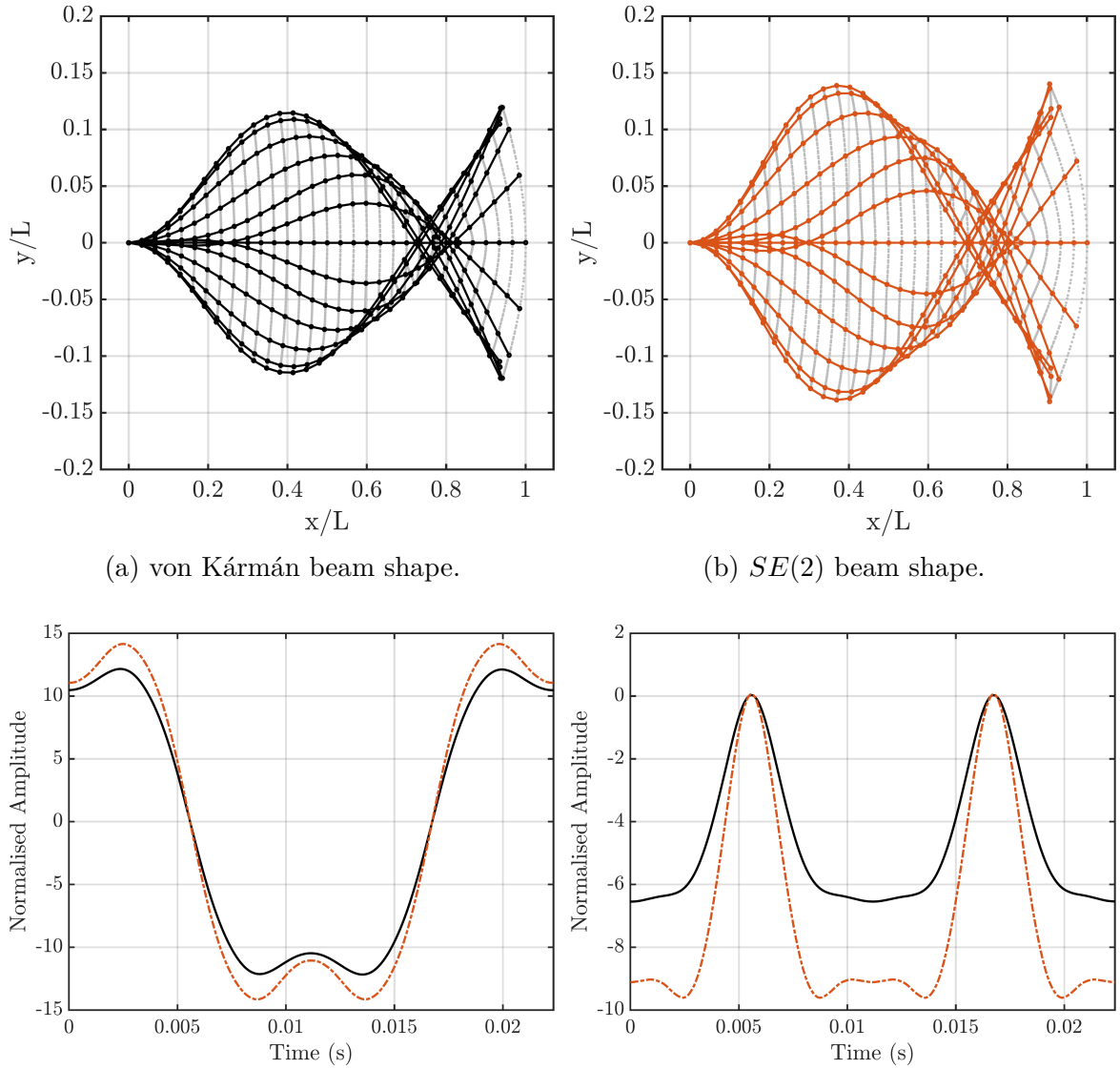
Figure 4.9: FEP of second NNM of straight cantilever. Comparison between von Kármán (black) and $SE(2)$ (orange).

shown in Figure 4.10. There is good agreement between the models and the von Kármán beam shape does not show significant deviation from that of the reference $SE(2)$ model. Owing to the smaller cross-sectional rotations and displacements of the cantilever in the second bending mode, compared to the first mode, the von Kármán model is able to capture the dynamics more effectively in this case. The presence of axial deformation is clearly seen in the beam shapes owing to contributions from axial modes in the response: mainly NNM 8, along with NNMs 14, 19, 22, and 24. The normalised vertical and axial displacements of the beam tip are also depicted in Figure 4.10. The presence of the third harmonic is seen in the vertical tip displacement, which manifests as double the frequency in the axial displacement. NNM3 begins to contribute to the response by means of excitation through the third harmonic of NNM2. The deformed beam shape in Figure 4.10 also reveals the presence of the beam's third mode shape, more prominently on the $SE(2)$ beam where it is relatively stronger. Though the vertical tip displacements are in relatively close agreement between the two models, there is greater difference in the displacement in the axial direction. The importance of using a more accurate beam model is therefore highlighted once more, as the significant contribution from higher order axial modes needs to be modelled correctly for the full dynamics to be captured.

4.7 Convergence Analysis

The analysis of the convergence rate of the $SE(2)$ and the von Kármán models is depicted in Figure 4.11 for the cantilever and the clamped-clamped beams studied in this chapter. For each case, an $SE(2)$ beam with 1000 finite elements is chosen as the reference beam model. This choice of the reference model is supported by the verification of the SE beam against known reference solutions, as provided in the literature [17], [94], and is similar in process to the convergence study of the $SE(2)$ beam performed by Sonneville et al. [208].

The von Kármán model utilises full integration in case of the cantilever beam, as reduced integration yields incorrect softening behaviour as observed in Section 4.6.5. The steady response of the beam under a tip load of 400 N is computed and compared to the reference solution. For



(a) von Kármán beam shape.

(b) $SE(2)$ beam shape.

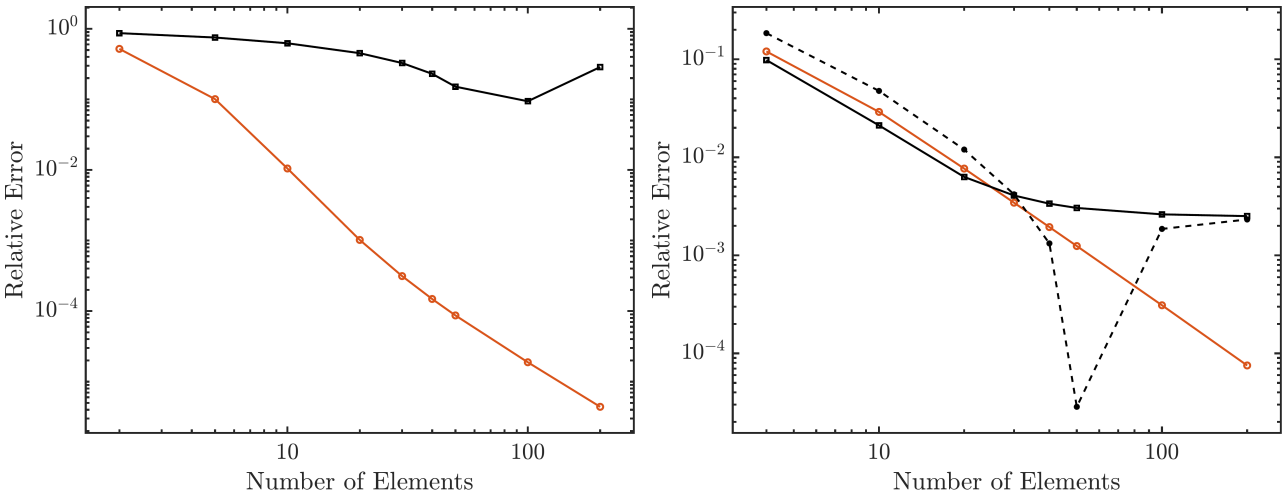
(c) Vertical direction.

(d) Axial direction.

Figure 4.10: Time history corresponding to solution at lowest frequency point on the backbone in Figure 4.9 (approx. 44.8 Hz). Deformed beam shapes, and normalised amplitude vs time at beam tip depicted. Comparison between von Kármán (black) and $SE(2)$ (orange). Amplitude normalised with respect to beam thickness $b = 10^{-2}\,m$.

the clamped-clamped beam, results for both reduced and full integration of the von Kármán beam are given, where the steady response of the beam is computed under a point load of 10000 N applied at the beam mid point.

It is seen in Figure 4.11 that the $SE(2)$ model offers second-order spatial convergence for increased number of finite elements for both test cases. In case of the cantilever beam, the von Kármán model does not give the same convergence rate, and generally fails to reduce the relative error in the beam response for increased number of elements along the beam. This is expected, as the von Kármán model is more suited to modelling beams undergoing coupled axial and bending motion, as discussed in Chapter 2 and in Section 4.6.5. In case of the clamped-clamped beam, the von Kármán model with full integration performs sufficiently well in terms of convergence in comparison to the $SE(2)$ model for lower number of elements. As



(a) Cantilever. (b) Clamped-clamped.

Figure 4.11: Convergence analysis of beam models. Comparison between $SE(2)$ (orange), von Kármán with full integration (solid black), and von Kármán with reduced integration (dashed black). Relative error measured against reference model of $SE(2)$ beam with 1000 finite elements, emphasising error in vertical displacement of beam tip in (a), and vertical displacement of beam mid-point in (b).

the number of elements along the beam is increased, the relative error of the von Kármán model reaches a plateau as the model fails to converge to lower error values. The trend is similar for the von Kármán beam with reduced integration, with the exception of single solution point corresponding to 50 elements along the beam length, which has a relative error of less than 10^{-4}.

The overall behaviour of the von Kármán model with full integration is that the beam is initially stiff due to shear locking, resulting in smaller displacements, and progressively becomes less stiff as the number of elements increases, leading to increased displacements and convergence from below towards the final value. In contrast, the von Kármán model with reduced integration initially exhibits lower stiffness, resulting in larger displacements, and progressively becomes stiffer as the number of elements, and accuracy of the model, increases. Consequently, the model converges from above towards the final solution. Somewhere along this general trend, the reduced integration model's solution computed with 50 elements fortuitously aligns with the reference $SE(2)$ solution, which therefore gives a low relative error. This behaviour is depicted in Figure 4.12. This is the reason for the low relative error of the reduced integration von Kármán solution point corresponding to 50 elements, as seen in Figure 4.11. As the error subsequently grows beyond this point, and reaches a plateau similar to the case with full integration, is it concluded that this particular point is an outlier.

This further demonstrates an additional drawback of the von Kármán model, stemming from the uncertainty over whether the model should be employed with full or reduced integration, as the convergence rate offers inconclusive evidence regarding the objective suitability of a spatial integration order. It can therefore be concluded that the $SE(2)$ model offers higher convergence rates and more robust convergence behaviour compared to the von Kármán model.

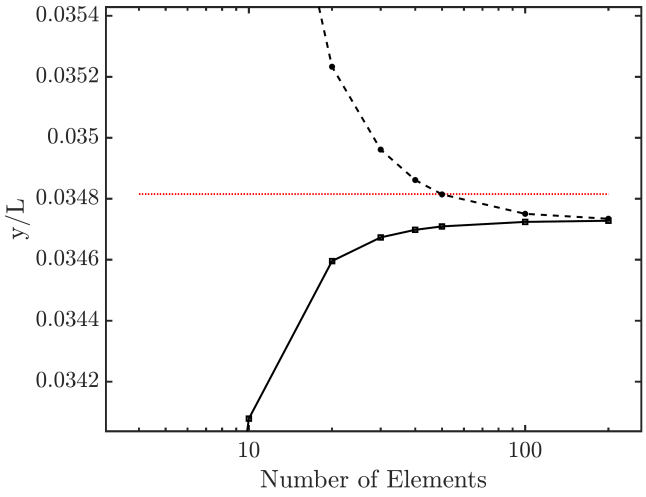


Figure 4.12: Convergence of the von Kármán beam with full integration (solid black), and reduced integration (dashed black), showing steady state vertical displacement of clamped-clamped beam mid-point. Reference $SE(2)$ solution also shown (red dotted line). The reduced integration model intersects the reference solution line at 50 elements, resulting in lower relative error of corresponding point in Figure 4.11.

4.8 Conclusion

This chapter presented a novel method for computing periodic responses of geometrically nonlinear structures modelled with the $SE(2)$ Lie group formulation. The modelling of geometrically nonlinear structures currently relies on approaches that have approximate kinematic assumptions, require approximations when implemented, or are difficult to generalise to more complex (3D) examples. In this chapter, these issues were addressed by using beam models formulated on $SE(2)$. A doubly clamped straight beam, a shallow arch, and a cantilever beam were modelled using this formulation. To analyse the nonlinear dynamics of these structures, their nonlinear normal modes were computed using the shooting and pseudo-arclength continuation methods. The use of the underlying Lie group model required modifications to both methods to account for the non-Euclidean nature of the configuration space, which is a novel contribution of this chapter.

Comparison with the results obtained using the popular von Kármán model highlighted several important observations, as listed below.

- The approximate kinematics of the von Kármán model can lead to erroneous qualitative predictions (see Section 4.6.5). As anticipated, the geometrically exact nature of the $SE(2)$ model captures the correct frequency-energy dependence of the NNMs. For large vibrations of the cantilever beam, the responses along the backbone of the NNM exhibit a relatively strong higher-harmonic content and the contribution of several high-frequency linear modes with significant axial components, which is not captured by the von Kármán model.

- Differences in the kinematic assumptions between the two models lead to differences in the natural frequencies of the higher modes, and can also affect their overall frequency-

energy dependence. As such, mode interactions were seen to differ in location and shape between the two models. In principle, this could also affect the order of the interactions observed between the two models.

- In cases with large rotations and displacements, such as the first bending mode of the cantilever, the von Kármán model is not able to adequately capture the geometric nonlinearities, owing to its simplified assumptions and truncation of nonlinear rotation terms. Nonlinear inertial effects are also not captured with the von Kármán model. Though the von Kármán model can be effective in modelling cases with axial-bending coupling, such as the doubly clamped beam configurations, higher order modal interactions and internal resonances may still not be modelled correctly.

- Finding periodic solutions is computationally less expensive with the $SE(2)$ model, which generally requires fewer time steps during shooting. The number of finite elements in the $SE(2)$ model can also be reduced compared to the von Kármán model, while preserving the accuracy of the results.

Very high-order modal interactions were observed to some extent in all the test cases modelled with the $SE(2)$ formulation. These interactions are captured by shooting and continuation, but might not exist in practice due to their sensitivity to damping. Unfortunately, it is very difficult to avoid capturing these high-order interactions with the shooting method. Other methods such as the harmonic balance method could be used in order to filter these internal resonances.

Differences between the von Kármán and Lie group formulations are expected to be even more important when considering 3D structures with larger rotations and displacements. Owing to the correct underlying kinematics of the Lie group model, and thanks to its local frame formulation, problems such as shear locking and rigid body strain are completely avoided. The higher efficiency of the Lie group model also results in the need for fewer finite elements, which has a significant computational advantage in modelling 3D structures. The Lie group model considered, and the new shooting and continuation methods developed here, are thus expected to significantly benefit the modelling and analysis of vibrations of complex and highly flexible structures, such as those being increasingly developed by industry.

Chapter 5

Multiple Shooting on the $SE(3)$ Group with Application to 3D Beams

Abstract

This chapter presents a multiple shooting method for computing periodic responses of 3D structures modelled under the $SE(3)$ framework. This is motivated by the advantages of the multiple shooting method over standard shooting, such as robustness in computing unstable periodic orbits. A 3D right-angled beam is chosen for this purpose, as it can undergo large displacements and rotations, which are amplified by the inertia forces of the structure. The multiple shooting algorithm is used alongside the pseudo-arclength continuation method presented in earlier chapters. Adaptations of the multiple shooting method to Lie group formulations are presented, and the challenges of the algorithm are discussed. Comparisons are also made with the standard (single) shooting method presented earlier, and the suitability of the $SE(3)$ formulation in modelling geometrically nonlinear beams in 3D with large displacements and rotations is shown.

A significant contribution of this chapter is the adaptation of the multiple shooting method to enable its application to beam models formulated within the Lie group framework. We also address the inherent challenges of the methodology, and provide suggestions to enhance the robustness of the method, as a further contribution. To the best of our knowledge, the multiple shooting method has not previously been applied to Lie group beam models, thereby underscoring the novelty of the work in this chapter. The results of this chapter were presented at the 11th European Nonlinear Dynamics Conference ENOC 2024 in Delft, Netherlands.

5.1 Introduction

The single shooting method discussed in previous sections has numerous advantages when used to find solutions to boundary value problems. A notable advantage is its simplicity, and ease of implementation alongside existing simulation code. Furthermore, as it relies on the computation of sensitives, it gives rise to the monodromy matrix which may be used in stability computations. However, it also suffers from some drawbacks which can limit its use in some applications [132]. The method has a very limited domain of attraction for unstable orbits, and integration of unstable orbits over a long time interval can lead to cumulative growth of error terms present during the initial time steps. Finding Unstable Periodic Orbits (UPOs) is also difficult due to the high sensitivity of these solutions to initial conditions of the system [123]. Furthermore, in cases where solution branches exist in close neighbourhoods of each other, the single shooting method could lead to branch jumps and the computation of unintended branches.

The multiple shooting method for boundary value problems, as originally developed by Keller [113], aims to alleviate these issues. The periodic orbit is discretised into a number of partitions, and time simulations are carried out on each partition separately. As a result of this discretisation, the domain of attraction increases and the likelihood of branch jumps reduces. Crucially, UPOs can be found with greater accuracy, since reducing the length of time intervals over which the equations are integrated minimises error propagation and reduces the chance of system divergence. Increasing the number of partitions will further reduce the length of the time intervals, and can thus be used as a strategy for handling rapidly diverging systems. Finally, this method is well-suited for parallel implementation, as each partition can be integrated independently, offering significant computational time savings. This is particularly advantageous when dealing with multi-degree-of-freedom large FE models, such as those studied in this thesis, where using a single shooting method would result in prohibitively long runtimes.

The multiple shooting method has garnered significant attention in the literature. Early pioneering work by Cebeci and Keller [46] laid the foundational principles for this approach to reduce the sensitivity of the system to the initial condition of the single shooting method, thereby improving the stability and accuracy of the solutions. Later, Bock and Plitt [31] applied the multiple shooting method for obtaining the numerical solution of parametrised optimal control problems. Al-Mdallal et al. [137] present an approach for solving fractional boundary value problems by combining the collocation method with piecewise polynomials, with the multiple shooting method, showing the efficiency of the method on a number of numerical examples. Gonzales and James [88] use multiple shooting to compute stable and unstable invariant manifolds attached to periodic orbits of discrete-time dynamic systems, showing that the dynamics of the manifold may be recovered and fold bifurcations can be followed correctly, while significant savings in computational time may also be achieved by the multiple shooting method. In control, Artola et al. [10] demonstrated that multiple shooting helps in the convergence of highly nonlinear problems in the optimal control of very flexible structures, and can be further accelerated through parallelisation. Schäfer et al. [191] used a variation of the multiple shooting

method for nonlinear model predictive control showing significant gains in computational time.

5.2 Multiple Shooting Formulation

The formulation of the multiple shooting problem as applied to a general dynamic system not formulated by Lie groups is given in this section, and the Lie group specific adaptations are followed subsequently. Different flavours of the linear matrix equation in the Newton update scheme have been given in the literature, and the interested reader may refer to [32], [126], [132], [188] to consult those methods. The formulation given in this section follows that of Lust [132].

Following the notation adopted in Chapter 2, we denote the result of the time integration of the system's equations of motion, over an interval of length T and from an initial condition vector $\boldsymbol{x}_0$ as

$$\phi(\boldsymbol{x}_0, T),\ \phi : \mathbb{R}^M \times \mathbb{R} \to \mathbb{R}^M, \tag{5.1}$$

We now consider s as a partition of the unit interval such that

$$0 = s_0 < s_1 < \cdots < s_{m-1} < s_m = 1 \tag{5.2}$$

with

$$\Delta s_i = s_i - s_{i-1} \tag{5.3}$$

Note that if the unit interval is split into equal partitions, we have $\Delta s = \frac{1}{m}$ for all values of i. Multiple shooting then solves the following nonlinear system of m equations for finding a periodic orbit

$$\begin{cases} \boldsymbol{\psi}_0 = \phi(\boldsymbol{x}_0, \Delta s_1 T) - \boldsymbol{x}_1 = 0, \\ \boldsymbol{\psi}_1 = \phi(\boldsymbol{x}_1, \Delta s_2 T) - \boldsymbol{x}_2 = 0, \\ \vdots \\ \boldsymbol{\psi}_{m-2} = \phi(\boldsymbol{x}_{m-2}, \Delta s_{m-1} T) - \boldsymbol{x}_{m-1} = 0, \\ \boldsymbol{\psi}_{m-1} = \phi(\boldsymbol{x}_{m-1}, \Delta s_m T) - \boldsymbol{x}_0 = 0 \end{cases} \tag{5.4}$$

This is shown schematically in Figure 5.1, which depicts a periodic orbit split into m partitions over the period. For the orbit to be periodic, the time integration from the starting point of each partition and over the length of the partition should bring the system to the starting point of the next partition, within the tolerance specified. For the final partition, the time integration should bring the system back to the first partition in order to close the orbit.

To find a periodic solution, the sensitivities of the periodicity equations with respect to the initial conditions are computed and stored in the Jacobian matrix in Eq. (5.5). Following the pseudo-arclength continuation method, the phase condition and orthogonality condition are also added, resulting in the following linear system of equations which is solved iteratively in

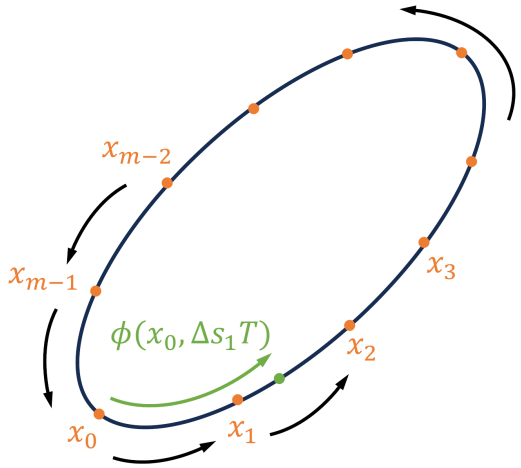


Figure 5.1: Schematic illustration of the multiple shooting method.

the Newton scheme to obtain corrections to the initial conditions

$$\begin{bmatrix} \mathbf{M}_0 & -\mathbf{I} & & & & \mathbf{b}_0 \\ & \mathbf{M}_1 & -\mathbf{I} & & & \mathbf{b}_1 \\ & & \mathbf{M}_2 & -\mathbf{I} & & \mathbf{b}_2 \\ & & & \ddots & & \vdots \\ -\mathbf{I} & & & & \mathbf{M}_{m-1} & \mathbf{b}_{m-1} \\ \mathbf{B}_0 & \mathbf{B}_1 & \mathbf{B}_2 & \cdots & \mathbf{B}_{m-1} & \mathbf{0} \\ \mathbf{u}_0 & \mathbf{u}_1 & \mathbf{u}_2 & \cdots & \mathbf{u}_{m-1} & \lambda \end{bmatrix} \begin{bmatrix} \Delta \boldsymbol{x}_0 \\ \Delta \boldsymbol{x}_1 \\ \Delta \boldsymbol{x}_2 \\ \vdots \\ \Delta \boldsymbol{x}_{m-1} \\ \Delta T \end{bmatrix} = - \begin{bmatrix} \boldsymbol{\psi}_0 \\ \boldsymbol{\psi}_1 \\ \boldsymbol{\psi}_2 \\ \vdots \\ \boldsymbol{\psi}_{m-1} \\ p(\boldsymbol{X}(0)) \\ 0 \end{bmatrix} \tag{5.5}$$

In Eq. (5.5), $\mathbf{M}_i$ is the i-th monodromy matrix resulting from the derivative of each $\boldsymbol{\psi}_i$ function with respect to $\boldsymbol{x}_i$, and is given by

$$\mathbf{M}_i = \frac{\partial \phi(\boldsymbol{x}_i, \Delta s_i T)}{\partial \boldsymbol{x}_i} \tag{5.6}$$

For a periodic solution, the monodromy of the system computed with respect to $\boldsymbol{x}_0$ over the full orbit may be recovered by the product of the $\mathbf{M}_i$ terms as

$$\mathbf{M} = \frac{\partial \phi(\boldsymbol{x}_0, \Delta T)}{\partial \boldsymbol{x}_0} = \mathbf{M}_{m-1}\mathbf{M}_{m-2}\ldots\mathbf{M}_1\mathbf{M}_0 \tag{5.7}$$

The $-\mathbf{I}$ identity matrices result from the derivative of each $\boldsymbol{\psi}_i$ function with respect to $\boldsymbol{x}_{i+1}$. The $\mathbf{b}_i$ terms indicate the derivatives with respect to the period, as

$$\mathbf{b}_i = \frac{\partial \phi(\boldsymbol{x}_i, \Delta s_i T)}{\partial T} = \frac{\partial \phi(\boldsymbol{x}_i, \Delta s_i T)}{\partial \Delta s_i T} \times \Delta s_i \tag{5.8}$$

where it is noted that the system state sensitivities with respect to simulation time on each partition may be scaled by Δs_i to give the sensitivities with respect to the full period T. The matrices $\mathbf{B}_i$ are the boolean matrices corresponding to the velocity phase condition as given by Eq. (2.3), and $p(\boldsymbol{X}(0))$ is the phase condition of zero velocity for the degrees of freedom

indicated by the $\mathbf{B}_i$ matrices. We denote $\boldsymbol{X}(0) = [\boldsymbol{x}_0\ \boldsymbol{x}_1 \dots \boldsymbol{x}_{m-1}]^T$ as the vector of all initial conditions across all partitions. Following the phase condition of zero initial velocities on all degrees of freedom, as introduced and discussed in Chapter 4, we adopt the same condition here, noting that only the initial velocities on the first partition must be prescribed as zero, as the remaining partitions will have non-zero velocities. This leads to the $\mathbf{B}_i$ terms corresponding to the partitions other than the first partition to be zero.

$$\mathbf{B}_1 = \mathbf{B}_2 = \cdots = \mathbf{B}_{m-1} = \mathbf{0} \tag{5.9}$$

Finally, the last row in the Jacobian matrix in Eq. (5.5) is the orthogonality condition and corresponds to the tangent vector $\mathbf{P} = \left[\mathbf{u}_1^T\ \mathbf{u}_2^T \dots \mathbf{u}_{m-1}^T\ \lambda\right]^T$, with $\mathbf{u}_i$ as the components on each partition, and λ as the period component of the tangent vector. The tangent vector is computed similarly to the method explained in Chapter 2 and shown in Eq. (2.4), by finding the vector orthogonal to the Jacobian by solving the following overdetermined linear system

$$\begin{bmatrix} \mathbf{M}_0 & -\mathbf{I} & & & & \mathbf{b}_0 \\ & \mathbf{M}_1 & -\mathbf{I} & & & \mathbf{b}_1 \\ & & \mathbf{M}_2 & -\mathbf{I} & & \mathbf{b}_2 \\ & & & \ddots & & \vdots \\ -\mathbf{I} & & & & \mathbf{M}_{m-1} & \mathbf{b}_{m-1} \\ \mathbf{B}_0 & \mathbf{B}_1 & \mathbf{B}_2 & \cdots & \mathbf{B}_{m-1} & \mathbf{0} \\ & & & \mathbf{P}_{j-1}^T & & \end{bmatrix} \mathbf{P}_j = \begin{bmatrix} \mathbf{0} \\ 1 \end{bmatrix} \tag{5.10}$$

where $\boldsymbol{P}_{j-1}$ is the tangent at the previous continuation step. Similar to Eq. (2.4), for the first continuation point where no previous tangent vector is available, this is replaced by $[\mathbf{0}\ \ 1]$, with $\mathbf{0}$ corresponding to all the $\mathbf{u}_i$ terms.

5.2.1 Alternative Multiple Shooting Equations

A few variations of the multiple shooting equation exist in the literature, potentially offering improved performance, though this has not been investigated within the scope of this thesis. Lee et al. [126] introduce an extra unknown $\mathbf{x}_m$ to the equations, and solve for periodicity by ensuring this new term equals to x_0. The multiple shooting periodicity equation in Eq. (5.4) therefore is modified to the following

$$\begin{cases} \boldsymbol{\psi}_0 = \phi(\boldsymbol{x}_0, \Delta s_1 T) - \boldsymbol{x}_1 = 0, \\ \boldsymbol{\psi}_1 = \phi(\boldsymbol{x}_1, \Delta s_2 T) - \boldsymbol{x}_2 = 0, \\ \vdots \\ \boldsymbol{\psi}_{m-2} = \phi(\boldsymbol{x}_{m-2}, \Delta s_{m-1} T) - \boldsymbol{x}_{m-1} = 0, \\ \boldsymbol{\psi}_{m-1} = \phi(\boldsymbol{x}_{m-1}, \Delta s_m T) - \boldsymbol{x}_m = 0 \\ \boldsymbol{x}_m - \boldsymbol{x}_0 = 0 \end{cases} \tag{5.11}$$

resulting in a modified expression for the linear equation in Eq. (5.5) and Eq. (5.10). Separating periodic boundary conditions on the last partition from the other equations may be advantageous when developing codes for bifurcation point computation [132].

Sánchez et al. [188] also propose an alternative variation to the multiple shooting equation in Eq. (5.5) by swapping the order of the subtraction in the periodicity function in Eq. (5.4), and writing the closure equation on the final partition, $\boldsymbol{\psi}_{m-1}$, on the first row of the Jacobian matrix, resulting in the following Jacobian

$$\begin{bmatrix} \mathbf{I} & & & & -\mathbf{M}_{m-1} & -\mathbf{b}_{m-1} \\ -\mathbf{M}_0 & \mathbf{I} & & & & -\mathbf{b}_0 \\ & -\mathbf{M}_1 & \mathbf{I} & & & -\mathbf{b}_1 \\ & & & \ddots & & \vdots \\ & & & -\mathbf{M}_{m-2} & \mathbf{I} & -\mathbf{b}_{m-2} \\ \mathbf{B}_0 & \mathbf{B}_1 & \mathbf{B}_2 & \cdots & \mathbf{B}_{m-1} & \mathbf{0} \\ \mathbf{u}_0 & \mathbf{u}_1 & \mathbf{u}_2 & \cdots & \mathbf{u}_{m-1} & \lambda \end{bmatrix} \tag{5.12}$$

This particular form of the Jacobian has the following format

$$\begin{bmatrix} \mathbf{I} - D_X \boldsymbol{\psi} & -D_T \boldsymbol{\psi} \\ [\mathbf{B}\ \mathbf{u}]^T & [\mathbf{0}\ \lambda]^T \end{bmatrix} \tag{5.13}$$

where the block comprising the monodromy matrices has a block cyclic structure. This structure of the Jacobian is advantageous for computing preconditioners based on its leading invariant subspaces, which can accelerate the convergence of the linear solver. Sánchez et al. [188] present a method for computing a preconditioner based on the partial periodic Schur decomposition of the block cyclic monodromy. They demonstrate speedups for the multiple shooting algorithm with the preconditioner applied. The preconditioner does not need updating on every step, and can be prepared for updating in the background while the continuation is proceeding, before being incorporated as the updated preconditioner. However, they also note that the choice of the block cyclic matrix to compute the preconditioner provides better performance in case of sequential parameter continuation. For the pseudo-arclength continuation whose full Jacobian in Eq. (5.13) has a bordered structure, additional spreading of the eigenvalues is not captured with the preconditioner based on the block cyclic matrix alone. A preconditioner based on the full bordered Jacobian is required, which could be solved with the Block Elimination Mixed (BEM) algorithm in a stable way [89].

5.2.2 Initial Periodic Orbit

In order to begin the continuation process, an initial guess is required for the first periodic solution. This could be taken as the eigenvector corresponding to the NNM of interest, scaled to ensure small displacements of the system that remain within the linear regime. A single shooting method may be employed here, with corrections applied to achieve periodicity. Once

a periodic orbit is found, it can be partitioned to create the sections required for multiple shooting. The partition locations along the orbit are kept fixed throughout the continuation process, although they may be changed adaptively if required.

As an additional strategy to increase robustness, the number of partitions may be increased along sections of the solution branch corresponding to highly unstable periodic orbits. If a phase condition of setting all initial velocities to zero is imposed, it is important to ensure that the first partition remains fixed, while other partitions may be added or moved, so that the phase condition may be applied correctly on the initial velocities.

5.3 Application to a Two Degree of Freedom Oscillator

In order to validate our multiple shooting formulation and methodology, we apply the algorithm to compute NNMs of the two degree of freedom system with cubic stiffness as studied by Peeters et al. [170]. The system is depicted in Figure 5.2, and its equation of motion is

$$\begin{aligned} \ddot{x}_1 + (2x_1 - x_2) + 0.5x_1^3 &= 0 \\ \ddot{x}_2 + (2x_2 - x_1) &= 0 \end{aligned} \tag{5.14}$$

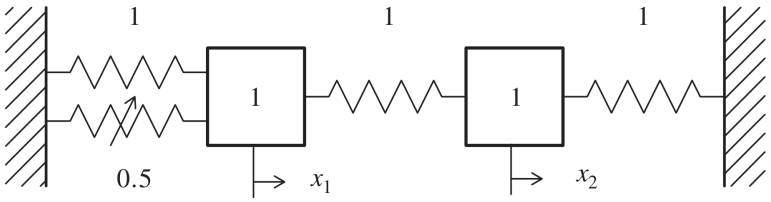


Figure 5.2: Schematic illustration of the 2 DoF system [170].

The system above exhibits two NNMs, representing in-phase and out-of-phase motions. The symmetric periodic motion, referred to as $S11+$ in [170], denotes the in-phase motion, and reveals internal resonance branches at higher energy levels. The resonance tongues emanate from the $S11+$ branch and coalesce into the out-of-phase solution branch, demonstrating high-frequency ratio multiples (2:1, 3:1, 4:1, etc.) between the motions.

The FEP for the in-phase branch was computed using the multiple shooting method described, and is shown in Figure 5.3. Three partitions were chosen, and kept fixed through the continuation process. Zero initial velocity was enforced on both degrees of freedom as the phase condition, and therefore the symmetric NNMs were targeted and captured[1]. Excellent agreement is observed between the multiple shooting and single shooting results through a range of modal interactions, thus validating the formulation of the multiple shooting problem.

The time history of the periodic solution at the point on the $S31$ tongue on the multiple shooting branch (indicated by the green marker in Figure 5.3) is shown in Figure 5.4. The 3:1 interaction between the degrees of freedom is clearly seen. The periodicity of the multiple

[1]These are referred to as "open curve" solutions in the configuration space [170].

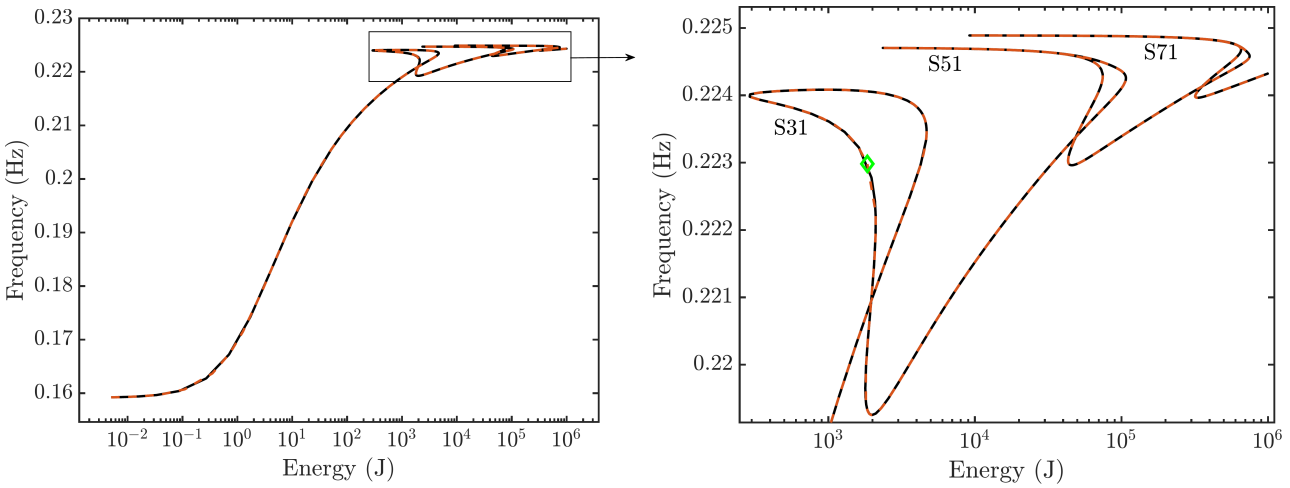


Figure 5.3: First NNM of cubic spring. Comparison between single shooting (solid black) and multiple shooting (dashed orange). Symmetric internal resonances with 3:1, 5:1, and 7:1 frequency ratios captured and labelled. Green marker indicates chosen solution for time series plots in Figures 5.4 and 5.5.

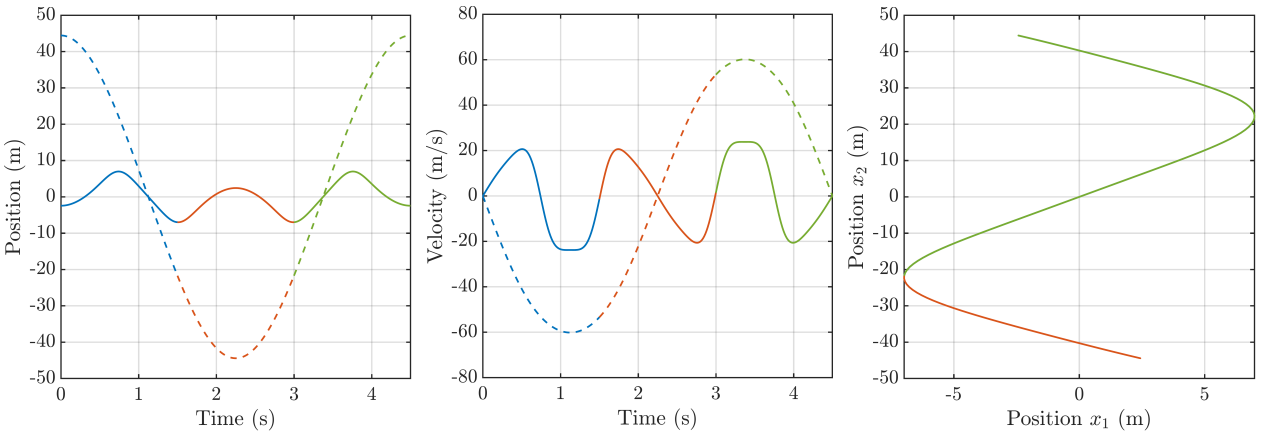


Figure 5.4: Time series of multiple shooting periodic solution on the $S31$ tongue. Partitions differentiated by colour. Solid line shows x_1 and dashed line shows x_2 solution. Rightmost figure shows open curve on configuration space, characteristic of symmetric internal resonance.

shooting equation is achieved, evident by the closure of the partitions and the periodicity of the full orbit.

Figure 5.5 shows the velocity of x_1 against the position of x_2 for the same time series as shown in Figure 5.4. The figure depicts how the orbit segments between the partitions close and periodicity is achieved as the corrections are applied during the Newton iterations of the multiple shooting solver. The periodicity error drops for 10^{-1} to 10^{-5} over 4 correction steps. This therefore validates the formulation of the multiple shooting algorithm and verifies its integration with the pseudo-arclength continuation process, as formulated in this chapter.

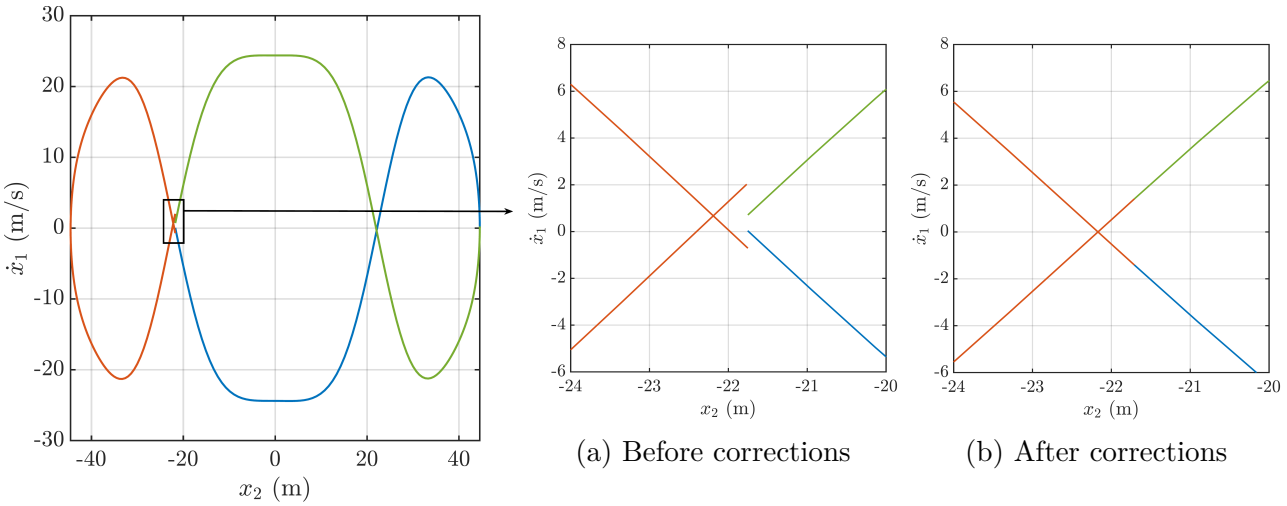


Figure 5.5: Closure of partitions on periodic orbit from corrections applied during the multiple shooting iteration. Plot corresponds to same solution as depicted in Figure 5.4. Partitions differentiated by colour. (a) shows orbit close-up before corrections are applied, and (b) shows fully closed orbit with periodicity error of 10^{-5} after the application of corrections.

5.4 Adaptation of the Multiple Shooting Method to Lie Group Formulations

Before the multiple shooting method can be applied to beams modelled on $SE(3)$, it has to be adapted to fit the underlying Lie group framework of the structural model. This is similar to the modifications made to the single shooting algorithm in Chapter 4, and is motivated by the same principles.

5.4.1 Periodicity Equation

We begin by modifying the periodicity condition in Eq. (5.4) to a form similar to Eq. (4.12). This is due to the nonlinearity of the configuration space of the Lie group manifold, which requires the use of the logarithm map on $SE(3)$ to compute the relative difference between beam configurations. In contrast to the single shooting approach detailed in Chapter 4, here we need to apply this periodicity condition across all partitions of the multiple shooting method. This results in a Lie group-specific multiple shooting periodicity condition, where the beam frames and velocities are compared at the boundaries of each partition to compute the periodicity error. Following the notation introduced in Eq. (4.12), and the discussions in Section 4.2, the

multiple shooting periodicity function is written as

$$\begin{cases} \boldsymbol{\psi}_0 = \begin{bmatrix} \psi_{\mathbf{H}_0} \\ \psi_{\mathbf{v}_0} \end{bmatrix} = \begin{bmatrix} \log_{SE(3)}(\mathbf{H}_1^{-1}(0)\mathbf{H}_0(\Delta s_1 T))^\vee \\ -\mathbf{T}^{-1}_{SE(3)}(-\psi_{\mathbf{H}_0})\mathbf{v}_1(0) + \mathbf{T}^{-1}_{SE(3)}(\psi_{\mathbf{H}_0})\mathbf{v}_0(\Delta s_1 T) \end{bmatrix}, \\ \boldsymbol{\psi}_1 = \begin{bmatrix} \psi_{\mathbf{H}_1} \\ \psi_{\mathbf{v}_1} \end{bmatrix} = \begin{bmatrix} \log_{SE(3)}(\mathbf{H}_2^{-1}(0)\mathbf{H}_1(\Delta s_2 T))^\vee \\ -\mathbf{T}^{-1}_{SE(3)}(-\psi_{\mathbf{H}_1})\mathbf{v}_2(0) + \mathbf{T}^{-1}_{SE(3)}(\psi_{\mathbf{H}_1})\mathbf{v}_1(\Delta s_2 T) \end{bmatrix}, \\ \vdots \\ \boldsymbol{\psi}_{m-2} = \begin{bmatrix} \psi_{\mathbf{H}_{m-2}} \\ \psi_{\mathbf{v}_{m-2}} \end{bmatrix} = \begin{bmatrix} \log_{SE(3)}(\mathbf{H}_{m-1}^{-1}(0)\mathbf{H}_{m-2}(\Delta s_{m-1} T))^\vee \\ -\mathbf{T}^{-1}_{SE(3)}(-\psi_{\mathbf{H}_{m-2}})\mathbf{v}_{m-1}(0) + \mathbf{T}^{-1}_{SE(3)}(\psi_{\mathbf{H}_{m-2}})\mathbf{v}_{m-2}(\Delta s_{m-1} T) \end{bmatrix}, \\ \boldsymbol{\psi}_{m-1} = \begin{bmatrix} \psi_{\mathbf{H}_{m-1}} \\ \psi_{\mathbf{v}_{m-1}} \end{bmatrix} = \begin{bmatrix} \log_{SE(3)}(\mathbf{H}_0^{-1}(0)\mathbf{H}_{m-1}(\Delta s_m T))^\vee \\ -\mathbf{T}^{-1}_{SE(3)}(-\psi_{\mathbf{H}_{m-1}})\mathbf{v}_0(0) + \mathbf{T}^{-1}_{SE(3)}(\psi_{\mathbf{H}_{m-1}})\mathbf{v}_{m-1}(\Delta s_m T) \end{bmatrix} \end{cases} \tag{5.15}$$

where $\mathbf{H}_i(0) \in SE(3)$ and $\mathbf{v}_i(0) \in \mathfrak{se}(3)$ are, respectively, the initial frames and velocities for each partition. The final frames and velocities at the end of the time integration along each partition, are denoted by $\mathbf{H}_i(\Delta s_i T)$ and $\mathbf{v}_i(\Delta s_i T)$ respectively. The $2N \times 1$ vector of initial conditions for each partition will now consist of the N initial increments and N initial velocities, that is $\boldsymbol{x}_i = [\mathbf{h}_i(0) \;\; \mathbf{v}_i(0)]^T$, where the increments give the initial beam configuration through the application of the exponential map, as given by Eq. (4.14), and N is the number of degrees of freedom of the model.

The Logarithm map on $SE(3)$ finds the relative difference between the final frames at the end of each partition and the initial frames at the start of the next partition. The velocity component of the periodicity equation is then taken as the time derivative of the frame component, and involves the use of the Tangent operator on $SE(3)$, as discussed in Section 4.2. It is noted here that this offers a local view of the periodicity condition, as the relative increments belong to the tangent space local to the initial frames $\mathbf{H}_i(0)$. An alternative formulation, offering a global view of the periodicity, may be adopted. This is discussed in detail in Section 5.7.

The second adaptation discussed in Section 4.2 concerned the initial conditions vector $\mathbf{X}(0)$, which consists of increments relative to the converged frames at the previous continuation step. The same adaptation is applied to the multiple shooting algorithm. Specifically, the initial conditions across all partitions are taken relative to the converged beam configuration at the previous continuation step. This method preserves the partitioning of the periodic orbit, meaning that the initial conditions for partition i are taken relative to the converged frame for partition i at the previous continuation step. The implications of this adaptation, including potential impacts on robustness of the continuation method, are explored further in Section 5.6.

5.4.2 Sensitivities

The sensitivities of the multiple shooting periodicity equation in Eq. (5.15) with respect to the initial conditions and the period are required in the Jacobian matrix in Eq. (5.5) to calculate the Newton corrections. These sensitivities can be found in the same way as those

described in Section 4.4. Considering the periodicity equation for partition i, given by

$$\boldsymbol{\psi}_i = \begin{bmatrix} \psi_{\mathbf{H}_i} \\ \psi_{\mathbf{v}_i} \end{bmatrix} = \begin{bmatrix} \log_{SE(3)}(\mathbf{H}_{i+1}^{-1}(0)\mathbf{H}_i(\Delta s_{i+1}T))^{\vee} \\ -\mathbf{T}_{SE(3)}^{-1}(-\psi_{\mathbf{H}_i})\mathbf{v}_{i+1}(0) + \mathbf{T}_{SE(3)}^{-1}(\psi_{\mathbf{H}_i})\mathbf{v}_i(\Delta s_{i+1}T) \end{bmatrix} \tag{5.16}$$

the gradients of the periodicity equation are given by

$$\mathrm{d}\psi_{\mathbf{H}_i} = -\mathbf{T}_{SE(3)}^{-1}(-\psi_{\mathbf{H}_i})\,\mathrm{d}\mathbf{h}_{i+1}(0) + \mathbf{T}_{SE(3)}^{-1}(\psi_{\mathbf{H}_i})\,\mathrm{d}\mathbf{h}_i(\Delta s_{i+1}T) \tag{5.17}$$

and

$$\begin{aligned} \mathrm{d}\psi_{\mathbf{v}_i} =& -\mathbf{T}_{SE(3)}^{-1}(-\psi_{\mathbf{H}_i})\,\mathrm{d}\mathbf{v}_{i+1}(0) + \mathbf{T}_{SE(3)}^{-1}(\psi_{\mathbf{H}_i})\,\mathrm{d}\mathbf{v}_i(\Delta s_{i+1}T) \\ & - \mathrm{D}_{\mathbf{v}_{i+1}(0)}\mathbf{T}_{SE(3)}^{-1}(-\psi_{\mathbf{H}_i})(-\,\mathrm{d}\psi_{\mathbf{H}_i}) + \mathrm{D}_{\mathbf{v}_i(\Delta s_{i+1}T)}\mathbf{T}_{SE(3)}^{-1}(\psi_{\mathbf{H}_i})(\mathrm{d}\psi_{\mathbf{H}_i}) \end{aligned} \tag{5.18}$$

We now consider the monodromy matrix for partition i as $M_i = [\underline{w}_i \quad \underline{v}_i]^T$, where $\underline{w}_i$ and $\underline{v}_i$ indicate the rows of the monodromy corresponding to the spatial and velocity derivatives respectively. Similar to the development of Eq. (4.21) and Eq. (4.24), we substitute the monodromy into the gradient equations, and separate the terms for the derivatives of each partition, to obtain the sensitivities of the periodicity equations with respect to the initial conditions of partitions i and $i+1$ as

$$\begin{aligned} \frac{\partial \psi_{\mathbf{H}_i}}{\partial \mathbf{X}_i(0)} &= \mathbf{T}_{SE(3)}^{-1}(\psi_{\mathbf{H}_i})\underline{w}_i \\ \frac{\partial \psi_{\mathbf{H}_i}}{\partial \mathbf{X}_{i+1}(0)} &= -\mathbf{T}_{SE(3)}^{-1}(-\psi_{\mathbf{H}_i})\begin{bmatrix}\mathbf{I} & \mathbf{0}\end{bmatrix}_{N\times 2N} \end{aligned} \tag{5.19}$$

and

$$\begin{aligned} \frac{\partial \psi_{\mathbf{v}_i}}{\partial \mathbf{X}_i(0)} =& \mathbf{T}_{SE(3)}^{-1}(\psi_{\mathbf{H}_i})\underline{v}_i - \mathrm{D}_{\mathbf{v}_{i+1}(0)}\mathbf{T}_{SE(3)}^{-1}(-\psi_{\mathbf{H}_i})(-\frac{\partial \psi_{\mathbf{H}_i}}{\partial \mathbf{X}_i(0)}) \\ & + \mathrm{D}_{\mathbf{v}_i(\Delta s_{i+1}T)}\mathbf{T}_{SE(3)}^{-1}(\psi_{\mathbf{H}_i})(\frac{\partial \psi_{\mathbf{H}_i}}{\partial \mathbf{X}_i(0)}) \\ \frac{\partial \psi_{\mathbf{v}_i}}{\partial \mathbf{X}_{i+1}(0)} =& -\mathbf{T}_{SE(3)}^{-1}(-\psi_{\mathbf{H}_i})\begin{bmatrix}\mathbf{0} & \mathbf{I}\end{bmatrix}_{N\times 2N} - \mathrm{D}_{\mathbf{v}_{i+1}(0)}\mathbf{T}_{SE(3)}^{-1}(-\psi_{\mathbf{H}_i})(-\frac{\partial \psi_{\mathbf{H}_i}}{\partial \mathbf{X}_{i+1}(0)}) \\ & + \mathrm{D}_{\mathbf{v}_i(\Delta s_{i+1}T)}\mathbf{T}_{SE(3)}^{-1}(\psi_{\mathbf{H}_i})(\frac{\partial \psi_{\mathbf{H}_i}}{\partial \mathbf{X}_{i+1}(0)}) \end{aligned} \tag{5.20}$$

These derivatives are then put back together to give the derivative of the full periodicity equation in Eq. (5.16) as

$$\frac{\partial \boldsymbol{\psi}_i}{\partial \mathbf{X}_i(0)} = \begin{bmatrix} \frac{\partial \psi_{\mathbf{H}_i}}{\partial \mathbf{X}_i(0)} \\ \frac{\partial \psi_{\mathbf{v}_i}}{\partial \mathbf{X}_i(0)} \end{bmatrix} \qquad \frac{\partial \boldsymbol{\psi}_i}{\partial \mathbf{X}_{i+1}(0)} = \begin{bmatrix} \frac{\partial \psi_{\mathbf{H}_i}}{\partial \mathbf{X}_{i+1}(0)} \\ \frac{\partial \psi_{\mathbf{v}_i}}{\partial \mathbf{X}_{i+1}(0)} \end{bmatrix} \tag{5.21}$$

These sensitivities therefore replace the $\mathbf{M}_i$ and $\mathbf{I}$ terms in the Jacobian matrix in Eq. (5.5), giving the following Jacobian matrix for the multiple shooting equations formulated on Lie

groups

$$\begin{bmatrix} \frac{\partial \boldsymbol{\psi}_0}{\partial \mathbf{x}_0(0)} & \frac{\partial \boldsymbol{\psi}_0}{\partial \mathbf{x}_1(0)} & & & & \mathbf{b}_0 \\ & \frac{\partial \boldsymbol{\psi}_1}{\partial \mathbf{x}_1(0)} & \frac{\partial \boldsymbol{\psi}_1}{\partial \mathbf{x}_2(0)} & & & \mathbf{b}_1 \\ & & \frac{\partial \boldsymbol{\psi}_2}{\partial \mathbf{x}_2(0)} & \frac{\partial \boldsymbol{\psi}_2}{\partial \mathbf{x}_3(0)} & & \mathbf{b}_2 \\ & & & \ddots & & \vdots \\ \frac{\partial \boldsymbol{\psi}_{m-1}}{\partial \mathbf{x}_0(0)} & & & & \frac{\partial \boldsymbol{\psi}_{m-1}}{\partial \mathbf{x}_{m-1}(0)} & \mathbf{b}_{m-1} \\ \mathbf{B}_0 & \mathbf{B}_1 & \mathbf{B}_2 & \cdots & \mathbf{B}_{m-1} & \mathbf{0} \\ \mathbf{u}_0 & \mathbf{u}_1 & \mathbf{u}_2 & \cdots & \mathbf{u}_{m-1} & \lambda \end{bmatrix} \tag{5.22}$$

5.5 Right-Angled Beam: NNM1

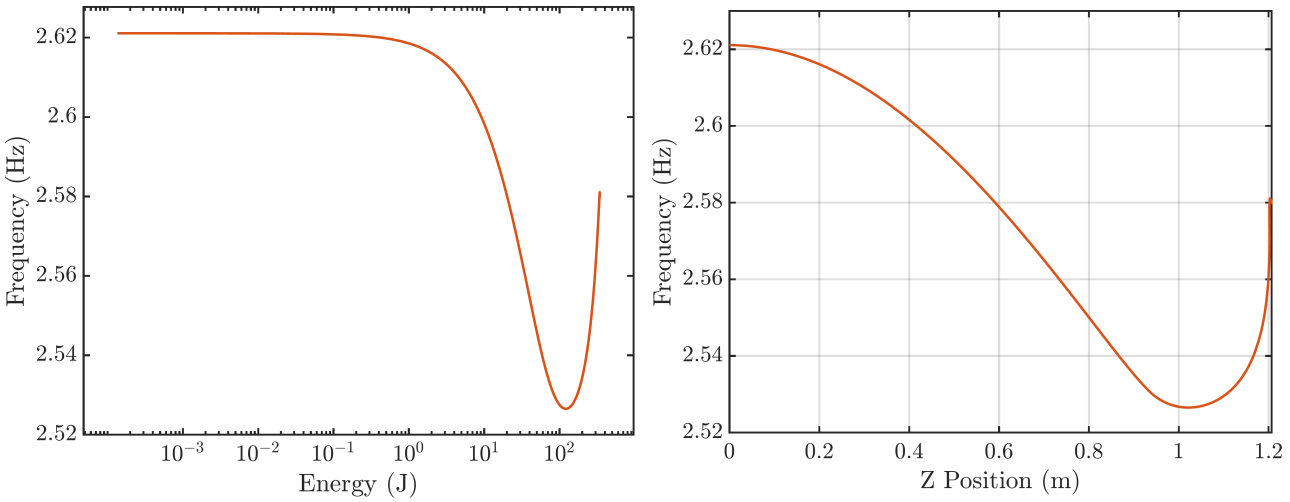
A right-angled cantilever beam, modelled using the $SE(3)$ formulation as presented in Chapter 3, was chosen as the test case to compute periodic solutions with the multiple shooting algorithm. The model was created by joining two beams at right angles, each having the following material and geometric properties: $E = 210\,GPa$, $\rho = 7850\,kg/m^3$, $L = 1\,m$, $b = 10^{-2}\,m$, $h = 10^{-2}\,m$, and each discretised with 21 finite elements. This model of the right-angled beam was inspired by the L beam proposed by Simo [205] and studied by Lens and Cardona [127], with some variations of the geometry and material properties as listed above.

5.5.1 Single shooting

NNM1 of the right-angled beam was first computed using the single shooting method described in Chapter 4. The frequency energy plot for this mode is depicted in Figure 5.6a. Initial softening behaviour which is commonly seen in cantilever type beams is observed, followed by hardening at higher energy levels. The maximum absolute vertical position of the beam tip during the periodic motion is shown in Figure 5.6b, where it is seen that the motion exceeds the length of the beam at higher energy levels. These large degrees of displacement can only be modelled correctly with the geometrically exact $SE(3)$ beam model.

The initial beam shape for the final solution on the NNM branch, corresponding to the maximum energy point, is shown in Figure 5.7, with planar views shown in Figure 5.8. The beam tip velocities for the same solution are shown in Figure 5.9. Recall from Chapter 3 that, due to the $SE(3)$ formulation, these velocities are expressed in the local body frame which moves with the beam during its motion. The velocity figures reveal higher harmonic oscillations which are present in the response.

The periodic solutions on the backbone curve can be characterised further by modal and frequency analysis. Considering the initial deformed beam position corresponding to the maximum energy solution point on the FEP, the relative increment vector between the reference undeformed beam and the deformed beam may be found using the nodal frames and using logarithm map on $SE(3)$. The increment vector can then be projected onto the linear modes of the system to evaluate the amplitude of the linear modal coordinates of the periodic response. The amplitudes from the projection onto the basis of the first five linear eigenmodes of the



(a) Frequency Energy plot.

(b) Maximum absolute amplitude at beam tip.

Figure 5.6: First NNM of right-angled beam computed with single shooting. Full beam discretised with 42 elements.

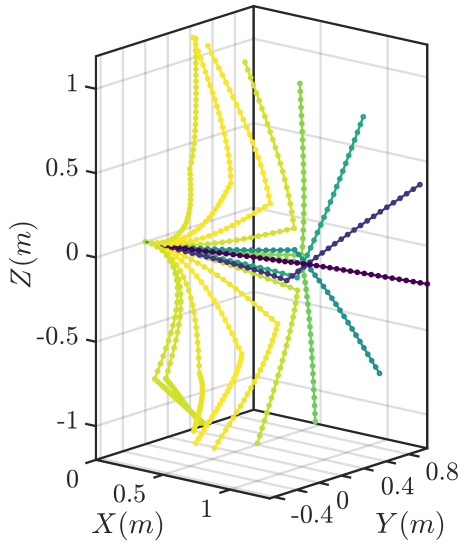


Figure 5.7: Deformed beam shape for highest energy point solution on the NNM curve in Figure 5.6.

system are shown in Figure 5.10a. The projection is done for all solutions on the NNM branch, and the amplitude vectors at each solution are normalised to unity. It is seen that, as the continuation step increases along the backbone curve, the contribution of mode 1 to the periodic solution drops slightly, and modes 2 to 4 start to contribute more. As the projection quantifies the magnitude of each linear mode's presence in the response, the increase in the amplitudes of modes 2 and 4 is indicative of some planar motion at higher energy levels. This is also seen in the deformed beam shapes in Figure 5.8, which shows the largest amplitude motion for the solution at the end of the NNM curve. It is noted that the basis of the linear modes can be used to interpret the physics of the NNM responses, as it reveals which linear modes contribute most significantly to the NNM motion. By tracking the modal amplitudes resulting from the projection over a range of frequencies on the NNM curve, the emergence or disappearance of internal resonances may be revealed. Furthermore, the projection can also offer useful qualitative

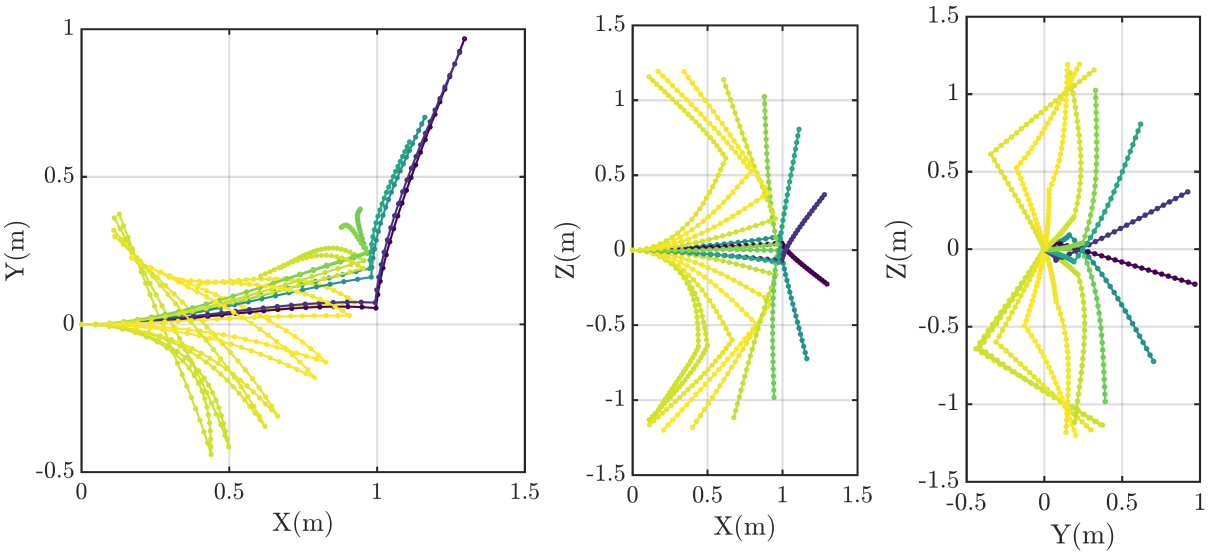


Figure 5.8: Planar views of Figure 5.7.

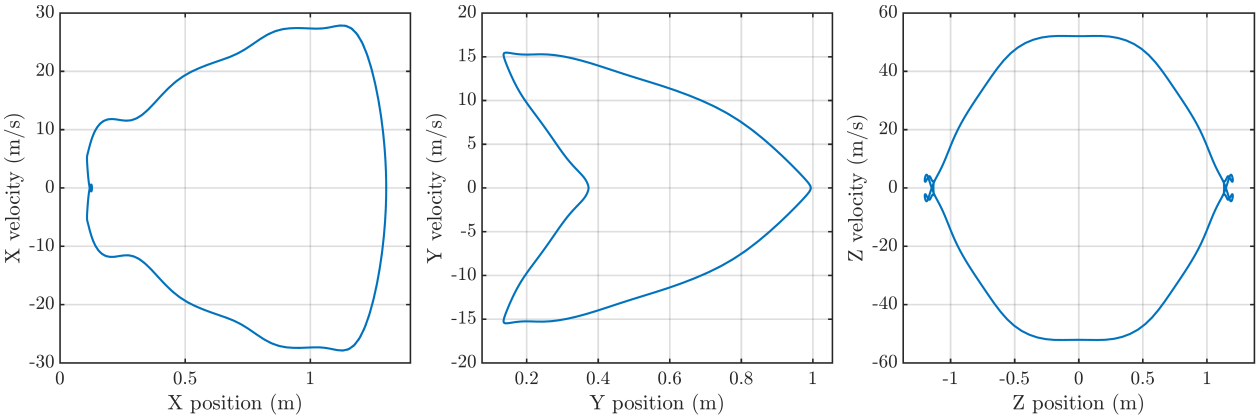
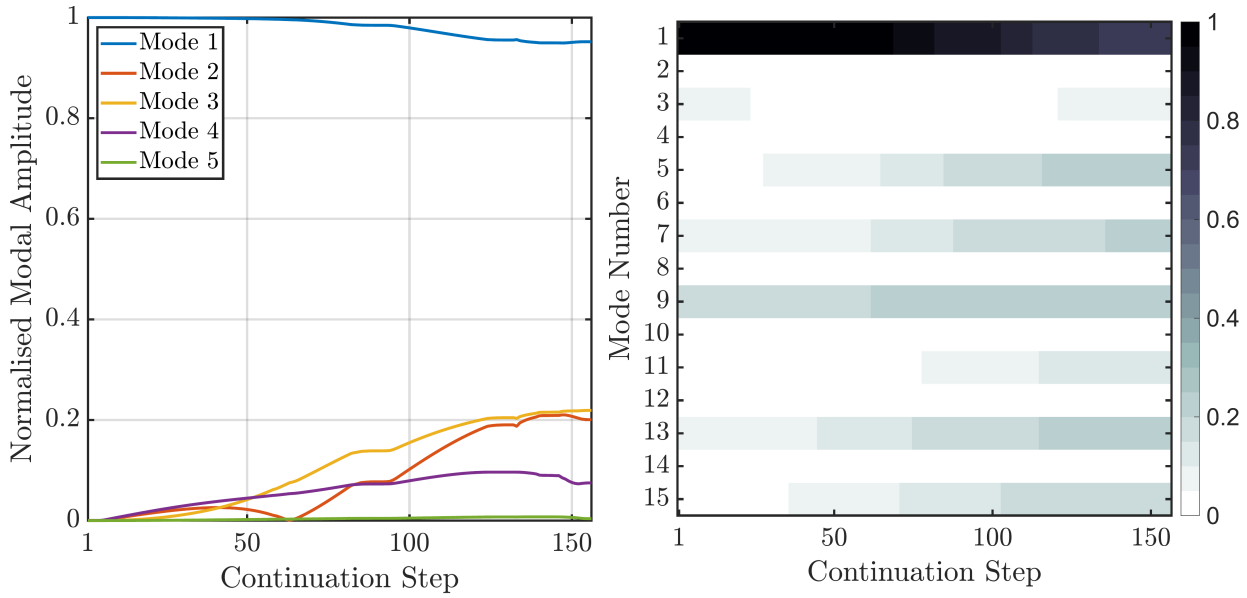


Figure 5.9: Beam tip local velocities for highest energy point solution on the NNM curve in Figure 5.6.

information, especially when comparing different NNMs; if two NNMs project onto different linear modes, they will likely involve distinct modal interactions and exhibit different nonlinear behaviours.

Another quantity which could be used to analyse the modal content of the periodic solution is the Modal Assurance Criterion (MAC). The MAC is a statistical measure of the geometric correlation between two sets of vectors [164]. When used to compare the NNM initial conditions with the linear eigenmodes, it quantifies the similarity between the shapes of the two modes. It therefore could be used to track the evolution of modal characteristics along the NNM branch, identifying which modes are excited or contribute significantly as the NNM curve develops into the higher energy regime. Figure 5.10b shows the MAC matrix using the first 15 linear modes of the system, and depicts how the shapes of the NNM solutions progress along the solution branch. It is seen that the deformed shape is dominated by mode 1, with gradual presence of odd modes at higher energy levels. Though the NNM solution incorporates planar motion at higher energies, as confirmed by the increased modal amplitudes seen in Figure 5.10a, the in-plane modes do not have large MAC values as the first mode dominates the response and



(a) Modal participation factor.

(b) Modal Assurance Criterion (MAC).

Figure 5.10: Modal coordinates and MAC plot of first NNM of right-angled beam, computed over whole range of periodic solutions in Figure 5.6, and showing contributions from the linear modes of the system.

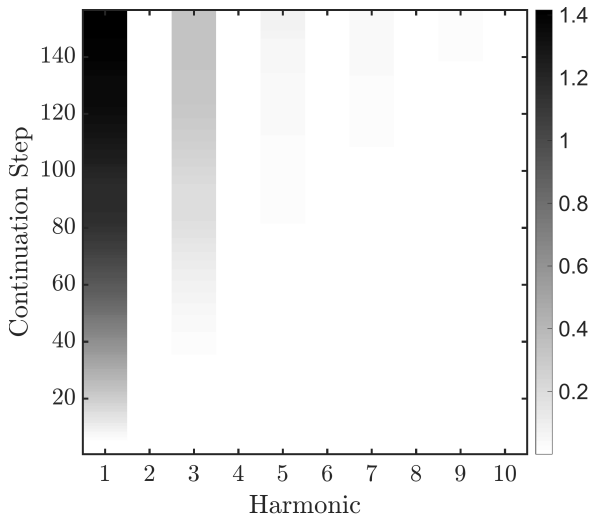


Figure 5.11: Frequency spectrum of first NNM of right-angled beam, computed over whole range of periodic solutions in Figure 5.6.

planar displacements arise from the large bending of the beam in the first mode.

The frequency content of the periodic solutions is computed using Fourier transforms of the full periodic orbit. The absolute vertical position of the beam tip is used and the frequency content is found using the Fast Fourier Transform (FFT). The frequencies are normalised with respect to the period of the full orbit in order to find the harmonics. Figure 5.11 shows the amplitude of the first 10 harmonics in the response. It is seen that the amplitude of the fundamental harmonic increases at higher energy levels of the NNM curve. In addition, the response also exhibits minor contributions in the 3^{rd} and 5^{th} harmonic of the fundamental response, which increase in amplitude with increasing energy levels along the NNM branch.

5.5.2 Multiple shooting

The frequency energy plot of the first NNM of the right-angled beam computed using the multiple shooting method with 3 partitions is shown in Figure 5.12. Unfortunately, the multiple shooting method could not trace the full curve due to convergence issues in the continuation method. The current challenges of the multiple shooting implementation are discussed in the following section, to be addressed in future research efforts on this problem.

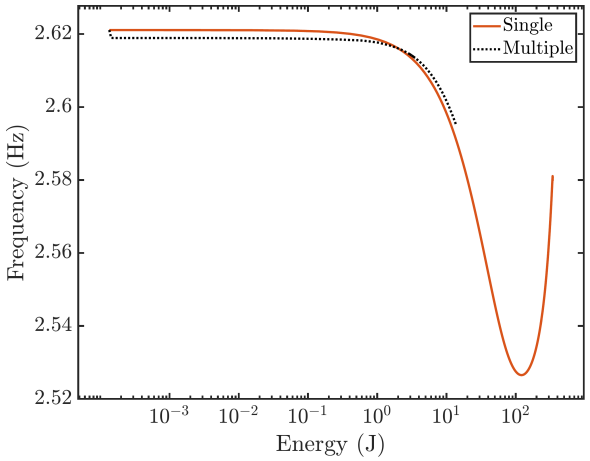


Figure 5.12: First NNM of right-angled beam computed with single shooting, and multiple shooting with 3 partitions.

5.6 Challenges and Suggestions

The convergence of the multiple shooting algorithm for the right-angled beam presented several challenges, which are discussed in this section. We highlight some of our findings, and offer suggestions which might enhance the method's robustness. It is hoped that these insights will prove beneficial to future researchers in their work.

5.6.1 Large Dimensionality

An inherent challenge of the multiple shooting method is that it increases the dimension of the problem. Each partition has its own vector of initial conditions which needs to be corrected in the Newton solver to achieve periodicity and closure of the full orbit. This results in a very large and sparse Jacobian with $8N^2p$ elements, where N indicates the model degrees of freedom and p is the number of partitions. The resulting linear equation for the corrections, as given in Eq. (5.5), can become very large, and the condition number of the Jacobian may increase, leading to difficulties in solving the equation. As discussed, preconditioners could be used on the Jacobian matrix in an iterative solver, or specific methods for solving large sparse linear matrix equations could be employed[1], but they have not been investigated in this thesis. Here, we have used a direct solver to solve the overdetermined system in the continuation equation.

[1]Examples include the Generalised Minimal Residual (GMRES) and the Bi-Conjugate Gradient Stabilised (BiCGSTAB) method.

5.6.2 Continuation Step Size

The increased dimensionality of the problem also results in a larger tangent vector composed of the vectors corresponding to each partition. This larger tangent vector will also have a bigger magnitude, and as the tangent should be normalised in the pseudo-arclength continuation method, this would cause the components of the normalised tangent vector to become smaller. As a result, the prediction for the next continuation step will be placed closer to the current step than it would be with single shooting. Therefore, to maintain an effective stepping scheme, the continuation step size has to be increased to compensate for the smaller tangent. This makes it challenging to maintain consistency with the step size used in a single shooting simulation. Moreover, increasing the number of partitions can exacerbate the issue, requiring even larger step sizes to compensate for the smaller tangent. Determining the correct step size can thus be challenging and may require some trial and error. To address this, one could normalise the tangent with respect to the infinity norm instead of the 2-norm, or instead scale the tangent such that the period component of the tangent is always fixed at the value of 1. However, we did not achieve robust behaviour with these methods, and found that there were still challenges in selecting the appropriate continuation step for the full NNM curve.

5.6.3 Continuation Orthogonality Condition

A further implementation strategy that was explored for aiding the convergence of the multiple shooting algorithm was to impose the orthogonality condition only on the first partition. The working assumption is that the continuity conditions at the partition boundaries, which ensure closure of the orbit, inherently propagate any corrections made in the first partition through the rest of the trajectory, and imposing orthogonality on the first partition can therefore influence subsequent partitions due to the coupling of the partitions at their boundaries. By imposing orthogonality only on the first partition, the overall equations will be less constrained, and therefore might converge more rapidly. This was tested for the right-angled beam, and some improvements were made to the continuation robustness. However, these improvements were not universally applicable, and in some instances, the equations converged better with orthogonality on all partitions. It can therefore be argued that for highly nonlinear and highly sensitive systems, the interaction between partitions could be more complex, and the imposed corrections in the first partition may not adequately influence or control the dynamics in later partitions. Imposing orthogonality across all partitions ensures that the corrections applied at each partition maintain the overall direction and stability of the entire solution curve, rather than adjusting each partition independently without regard to the overall path. Imposing orthogonality on all partitions ensures that the solution space is explored comprehensively. Nevertheless, a hybrid and adaptive strategy could be employed, where the imposition of the orthogonality condition can be dynamically adjusted based on the observed performance of the continuation process.

5.6.4 Relative Increments

Another strategy for improving the convergence could be to modify the initial conditions vector across all partitions. As discussed in Section 5.4.1, the initial condition vector is constructed with increments relative to the converged frames at the previous continuation point, with the increment in each partition calculated relative to the converged frame of the same partition. An alternative implementation, which still leverages the Lie group formulation of the model, would be to compute the relative increments with respect to the converged frame at only the first partition of the previous continuation step. This would result in partitions further away from the starting partition having a greater initial increment vector. Given that the initial velocities for these partitions are also nonzero and potentially large, this would produce an initial conditions vector with more consistent magnitudes across all partitions. Consequently, the corrections needed would be of similar sizes, and could therefore lead to a more robust formulation, though this has not been numerically verified in this work.

5.6.5 Initial Accelerations

A final remark is made about initial accelerations. The multiple shooting periodicity equation only enforces closure on the positions and velocities across the partitions. The accelerations are therefore omitted from the periodicity condition. It is important that the time integration method of the system's equations of motion is able to calculate the initial accelerations, given the initial positions and velocities. If the initial accelerations are initiated as zero, though from a mechanical point of view the equations of motion can be solved, the accelerations are crucially a numerical state of the time integration scheme, and numerical consistency should be enforced. The value of the accelerations at the initial conditions will affect the rest of the system trajectory under time iteration. It is therefore crucial that the solver is able to initialise them correctly before time integration, otherwise the accelerations will not match at the partition boundaries, which could cause numerical issues in the multiple shooting algorithm.

5.7 A Global Periodicity Condition

The Lie group periodicity equations used for both the single and multiple shooting formulations are based on a local view of the relative increment between the frames. In both Eq. (4.12) and Eq. (5.16), the increment vector $\psi_{\mathbf{H}}$ computed by the logarithm map lies in the tangent space of the frame whose inverse appears in the equations, that is $\mathbf{H}(0)$, and is local to that frame. A global periodicity equation can be formulated which results in increment vectors which lie on the tangent space at the Lie algebra, that is, the identity of the $SE(3)$ group. The different views of the tangent spaces on the group were illustrated in Figure 3.2. The global periodicity condition offers some advantages, as explained in this section, and could offer further improvements to the multiple shooting algorithm in terms of stability and robustness.

The local periodicity equation was formulated based on Eq. (3.19a). That is, periodicity was measured as the relative increment on the tangent space at $\mathbf{H}(0)$ which takes $\mathbf{H}(0)$ to $\mathbf{H}(T)$,

as follows

$$\mathbf{H}(T) = \mathbf{H}(0) \circ \exp(\widetilde{\psi_{\mathbf{H}}}) \tag{5.23}$$

To formulate the global periodicity condition, we instead use Eq. (3.19b), as this relies on vectors which are expressed at the Lie algebra, as discussed in Section 3.1.5. In this formulation, periodicity is measured as the increment in the Lie algebra which takes $\mathbf{H}(0)$ to $\mathbf{H}(T)$, as follows

$$\mathbf{H}(T) = \exp(\widetilde{\varphi_{\mathbf{H}}}) \circ \mathbf{H}(0) \tag{5.24}$$

The spatial component of the global periodicity vector is therefore written as

$$\varphi_{\mathbf{H}} = \log_{SE(3)}(\mathbf{H}(T)\mathbf{H}^{-1}(0))^{\vee} \tag{5.25}$$

where we have changed the notation from $\psi_{\mathbf{H}}$ to $\varphi_{\mathbf{H}}$, reserving the former for the local periodicity condition. It is noted that this is the single shooting variant of the periodicity, however, the multiple shooting equations follow in an identical manner. The velocity component of the periodicity equation can then be obtained by time differentiating Eq. (5.25). This is done similarly to Eq. (4.11), and follows the derivative of the logarithm map in Eq. (3.46). The time derivative of Eq. (5.25) is therefore written as

$$\frac{\mathrm{d}\varphi_{\mathbf{H}}}{\mathrm{d}t} = \mathbf{T}^{-1}_{SE(3)}(\varphi_{\mathbf{H}})\mathbf{u} \tag{5.26}$$

where $\mathbf{u}$ is the left-invariant vector field of the derivative of the term inside the log bracket. To find $\mathbf{u}$, we write

$$\frac{\mathrm{d}\left(\mathbf{H}(T)\mathbf{H}^{-1}(0)\right)}{\mathrm{d}t} = \mathbf{H}(T)\mathbf{H}^{-1}(0)\tilde{\mathbf{u}} \tag{5.27}$$

and expand the left hand side using the product rule, as

$$\frac{\mathrm{d}\mathbf{H}(T)}{\mathrm{d}t}\mathbf{H}^{-1}(0) + \mathbf{H}(T)\frac{\mathrm{d}\mathbf{H}^{-1}(0)}{\mathrm{d}t} = \mathbf{H}(T)\mathbf{H}^{-1}(0)\tilde{\mathbf{u}} \tag{5.28}$$

Each derivative above can be written using its respective left-invariant vector field as

$$\mathbf{H}(T)\tilde{\mathbf{v}}(T)\mathbf{H}^{-1}(0) - \mathbf{H}(T)\tilde{\mathbf{v}}(0)\mathbf{H}^{-1}(0) = \mathbf{H}(T)\mathbf{H}^{-1}(0)\tilde{\mathbf{u}} \tag{5.29}$$

where we have used $\mathrm{d}\mathbf{H}^{-1} = -\widetilde{\delta\mathbf{v}}\mathbf{H}^{-1}$. Multiplying the inverse of the terms on the right into the left hand side of the equation gives an expression for $\mathbf{u}$ as

$$\tilde{\mathbf{u}} = \mathbf{H}(0)\left(\tilde{\mathbf{v}}(T) - \tilde{\mathbf{v}}(0)\right)\mathbf{H}^{-1}(0) \tag{5.30}$$

which can be written in vector form and using the Adjoint map as

$$\mathbf{u} = \mathrm{Ad}_{\mathbf{H}(0)}(\mathbf{v}(T) - \mathbf{v}(0)) \tag{5.31}$$

Substituting this into Eq. (5.26) therefore gives the velocity component of the periodicity equation as

$$\varphi_{\mathbf{v}} = \mathbf{T}^{-1}_{SE(3)}(\varphi_{\mathbf{H}})\mathrm{Ad}_{\mathbf{H}(0)}(\mathbf{v}(T) - \mathbf{v}(0)) \tag{5.32}$$

Therefore, the full periodicity equation expressed in the global frame is given by

$$\boldsymbol{\varphi}(\boldsymbol{X}(0), T) = \begin{bmatrix} \varphi_{\mathbf{H}} \\ \varphi_{\mathbf{v}} \end{bmatrix} = \begin{bmatrix} \log_{SE(3)}(\mathbf{H}(T)\mathbf{H}^{-1}(0))^{\vee} \\ \mathbf{T}^{-1}_{SE(3)}(\varphi_{\mathbf{H}})\mathrm{Ad}_{\mathbf{H}(0)}(\mathbf{v}(T) - \mathbf{v}(0)) \end{bmatrix} = \mathbf{0}_{12\times 1} \tag{5.33}$$

and contrasts with the periodicity equation expressed in the local frame in Eq. (4.12).

It is noted that, for a periodic solution, the tangent term in Eq. (5.32) tends to identity. As a result, $\varphi_{\mathbf{v}}$ would equal the difference between the velocities in the local frame[1], which are mapped to the global frame through the action of the Adjoint. Recall from 3.1.6 that the Adjoint linearly maps vectors expressed in the local frame at a group element to a vector expressed in the global frame at the identity. This is also true for the spatial component of the periodicity equation, and it can be shown that the Adjoint maps the local $\psi_{\mathbf{H}}$ to the global $\varphi_{\mathbf{H}}$ as

$$\varphi_{\mathbf{H}} = \mathrm{Ad}_{\mathbf{H}(0)}\psi_{\mathbf{H}} \tag{5.34}$$

An expression for $\varphi_{\mathbf{v}}$ may also be found by time differentiating Eq. (5.34), which can be shown to lead to an identical relationship to that given in Eq. (5.32).

5.7.1 Sensitivities of the Global Periodicity Condition

The sensitivities of the global periodicity condition with respect to the shooting initial conditions can be calculated similar to those found for the local periodicity conditions in 4.4. Starting with $\varphi_{\mathbf{H}}$, its gradient can be expressed as

$$\mathrm{d}\varphi_{\mathbf{H}} = \mathbf{T}^{-1}_{SE(3)}(\varphi_{\mathbf{H}})\mathrm{Ad}_{\mathbf{H}(0)}(\mathrm{d}\mathbf{h}(T) - \mathrm{d}\mathbf{h}(0)) \tag{5.35}$$

which, similar to the previous sensitivity formulations, can be written using the monodromy matrix $M_{2N\times 2N} = [\underline{w}_{N\times 2N} \quad \underline{v}_{N\times 2N}]^T$, giving the sensitivity of $\varphi_{\mathbf{H}}$ with respect to the initial conditions vector as

$$\frac{\partial \varphi_{\mathbf{H}}}{\partial \mathbf{X}(0)}_{N\times 2N} = \mathbf{T}^{-1}_{SE(3)}(\varphi_{\mathbf{H}})\mathrm{Ad}_{\mathbf{H}(0)}\left(\underline{w} - \begin{bmatrix}\mathbf{I} & \mathbf{0}\end{bmatrix}_{N\times 2N}\right) \tag{5.36}$$

The sensitivity of the velocity component of the periodicity equation can be found by first taking the derivative of $\varphi_{\mathbf{v}}$ which can be written as

$$\mathrm{d}\varphi_{\mathbf{v}} = \mathrm{d}\left(\mathbf{T}^{-1}_{SE(3)}(\varphi_{\mathbf{H}})\mathrm{Ad}_{\mathbf{H}(0)}(\mathbf{v}(T) - \mathbf{v}(0))\right) \tag{5.37}$$

[1]Note $\mathbf{v}(0)$ and $\mathbf{v}(T)$ are local velocities, as they represent the left-invariant derivatives in Eq. (5.29).

which can be expanded by applying the derivative into the bracket to give

$$\mathrm{d}\varphi_{\mathbf{v}} = \mathrm{D}_{\mathbf{V}^\star}\mathbf{T}^{-1}_{SE(3)}(\varphi_{\mathbf{H}})(\mathrm{d}\varphi_{\mathbf{H}}) + \mathbf{T}^{-1}_{SE(3)}(\varphi_{\mathbf{H}})\,\mathrm{d}\left(\mathrm{Ad}_{\mathbf{H}(0)}(\mathbf{v}(T)-\mathbf{v}(0))\right) \tag{5.38}$$

where $\mathbf{V}^\star = \mathrm{Ad}_{\mathbf{H}(0)}(\mathbf{v}(T)-\mathbf{v}(0))$ indicates the direction vector of the directional derivative of the tangent operator. Applying the derivative in the second term into the bracket yields the final form of the gradient as

$$\begin{aligned}\mathrm{d}\varphi_{\mathbf{v}} &= \mathrm{D}_{\mathbf{V}^\star}\mathbf{T}^{-1}_{SE(3)}(\varphi_{\mathbf{H}})(\mathrm{d}\varphi_{\mathbf{H}}) \\ &\quad + \mathbf{T}^{-1}_{SE(3)}(\varphi_{\mathbf{H}})\mathrm{Ad}_{\mathbf{H}(0)}\left(\mathrm{d}\mathbf{v}(T) - \mathrm{d}\mathbf{v}(0) + \widehat{\mathrm{d}\mathbf{h}(0)}(\mathbf{v}(T)-\mathbf{v}(0))\right)\end{aligned} \tag{5.39}$$

where the hat operator $\widehat{(\bullet)}$ is used as an equivalent expression for the adjoint map in vector form as given by Eq. (3.32). As discussed in Section 3.1.6, the adjoint (ad) is the derivative of the Adjoint (Ad) at the identity element, and thus it appears when differentiating the Adjoint in Eq. (5.38). The steps required in differentiating the Adjoint and the mathematical development of the derivate are given in Appendix C.4. Using the expression of the gradient in Eq. (5.39), along with the monodromy, the sensitivity of $\varphi_{\mathbf{v}}$ with respect to the initial conditions vector is written as

$$\begin{aligned}\frac{\partial \varphi_{\mathbf{v}}}{\partial \mathbf{X}(0)}_{N\times 2N} &= \mathrm{D}_{\mathbf{V}^\star}\mathbf{T}^{-1}_{SE(3)}(\varphi_{\mathbf{H}})\left(\frac{\partial \varphi_{\mathbf{H}}}{\partial \mathbf{X}(0)}\right) \\ &\quad + \mathbf{T}^{-1}_{SE(3)}(\varphi_{\mathbf{H}})\mathrm{Ad}_{\mathbf{H}(0)}\left(\underline{v} - \begin{bmatrix}\mathbf{0} & \mathbf{I}\end{bmatrix}_{N\times 2N} - (\widehat{\mathbf{v}(T)-\mathbf{v}}(0))\begin{bmatrix}\mathbf{I} & \mathbf{0}\end{bmatrix}_{N\times 2N}\right)\end{aligned} \tag{5.40}$$

The final term in the bracket above comes from expanding $\widehat{\mathrm{d}\mathbf{h}(0)}(\mathbf{v}(T)-\mathbf{v}(0))$ using the definition of $\widehat{(\bullet)}$ on $SE(3)$ in Eq. (3.78), and computing the derivative of the resulting term with respect to $\mathbf{X}(0)$.

5.7.2 Advantages of the Global Periodicity Condition

The global periodicity condition offers a more consistent formulation compared to the local condition, as it always expressed relative to a fixed frame. More importantly, it also offers a numerical advantage, as the terms containing the tangent operator in the sensitivity equations, which are unique to the Lie group framework, vanish for a periodic solution. Recall from Section 4.4 that these terms do not vanish from the sensitivity equations for the local periodicity condition. In contrast, considering Eq. (5.36) and Eq. (5.40), it is seen that for a periodic solution[1], we have

$$\frac{\partial}{\partial \mathbf{X}(0)}\begin{bmatrix}\varphi_{\mathbf{H}} \\ \varphi_{\mathbf{v}}\end{bmatrix} = \mathrm{Ad}_{\mathbf{H}(0)}\,(M-\mathbf{I}) \tag{5.41}$$

[1]For a periodic solution, we have $\varphi_{\mathbf{H}} = 0$, $\mathbf{T}^{-1}_{SE(3)}(\varphi_{\mathbf{H}}) = \mathbf{I}$, $\mathbf{v}(T)-\mathbf{v}(0) = 0$, $\mathbf{V}^\star = 0$, and $\mathrm{D}_{\mathbf{V}^\star}\mathbf{T}^{-1}_{SE(3)}(\varphi_{\mathbf{H}}) = 0$.

Recall from Chapter 3 that the local frame approach is adopted in the formulation of the finite element beam equations. As such, the monodromy matrix of the system itself is calculated based on variables which are defined locally on the underlying $SE(3)$ framework of the model. The Adjoint in Eq. (5.41) can therefore be interpreted as a mapping which brings $(M - \mathbf{I})$ to the global frame. The consistency of this periodicity condition and the simplification of the Lie-group-specific terms in the sensitivities suggest that the global periodicity equation is a better choice for the single and multiple shooting algorithms adapted on Lie groups.

5.8 Computational Savings and Parallel Implementation

As convergence of the multiple shooting method has not yet been achieved for the beam, no quantification of computational savings can be made. However, the following discussions remain valid.

As discussed, the multiple shooting method offers a viable opportunity for leveraging parallel computation for increased time efficiency. Since the time integrations along each partition are independent of one another, each integration can be performed on a separate CPU, significantly reducing overall wall-clock time. This is highlighted by Sánchez [188] who also suggests that parallelisation is only beneficial if increasing the number of partitions allows for a reduction in the number of time steps per partition. Finding the optimal balance between the number of partitions and the number of time steps per partition requires careful consideration.

Other strategies for parallelising the entire continuation process have also been proposed. For instance, Wang et al. [241] use a variable-step parallel continuation algorithm, where they propose that once a periodic solution point is found, multiple predictions of the next point are made by selecting points with varying step sizes along the tangent. The correction step can then be performed in parallel, where each point is corrected simultaneously to fall back on the solution curve. This could be coupled with a parallel adaptation of the multiple shooting method, where each shooting partition is parallelised, to maximise potential computation time savings. However, this has to be balanced against the computational overhead of implementing such a system, and a numerical analysis must be conducted to optimise the number of cores and parallel threads.

5.9 Conclusion

In this chapter, we have developed the multiple shooting equations for computing periodic responses (NNMs) of nonlinear finite element models. The equations are first derived for systems not formulated on Lie groups, and are applied to a two degree of freedom oscillator with cubic nonlinearity. The adaptations required to the multiple shooting method in order to facilitate its use with models formulated on Lie groups are then developed and presented, and the sensitivities of the multiple shooting equations are derived. The benefits of the multiple shooting method compared to the standard single shooting method are also explored and discussed.

A right-angled cantilever beam modelled under the $SE(3)$ framework was chosen to compute

its periodic responses using the multiple shooting method. The first NNM of the system was computed by single shooting, where extremely large displacements and rotations of the beam cross sections were observed for periodic solutions at large energy levels. However, the multiple shooting method could not converge to the same solution branch as the single shooting on this test case. The challenges of the multiple shooting method are discussed, and some solutions are presented which could resolve the current implementation issues of the multiple shooting algorithm, which is the focus of ongoing research efforts.

Finally, a global periodicity equation is derived that is applicable to both the single shooting and multiple shooting methods for computing periodic solutions of nonlinear systems formulated on Lie groups. The advantages of the global periodicity equation are highlighted and discussed. A comprehensive numerical comparison between the global periodicity equation and the local approach would be a valuable contribution and remains an open area for future research.

Chapter 6

Forced Continuation of Periodic Solutions of Beams on $SE(2)$ and $SE(3)$

Abstract

This chapter presents a novel study on the forced responses of geometrically nonlinear beams modelled under the $SE(2)$ and $SE(3)$ formulations, employing shooting and pseudo-arclength continuation methods not previously applied to such models. We incorporate geometrically exact damping based on the strain rate to maintain strain objectivity of the Lie group beam models and ensure invariance under Euclidean transformation. The $SE(2)$ model effectively captures complex dynamics and large displacements and rotations in a 2D cantilever beam under resonance conditions, surpassing vibration levels reported in existing literature. Sine sweeps on a 2D vertical cantilever beam under gravity reveal multi-modal dynamics and complex subharmonic responses. Finally, the $SE(3)$ model successfully captures large-scale 3D rotations and displacements of a 3D cantilever beam in 1:1 internal resonance, identifying pitchfork bifurcations and tracing secondary resonance branches. The novelty of this chapter lies in the use of the Lie group beam formulations along with the adapted shooting and continuation methods to compute forced responses of geometrically nonlinear beams.

6.1 Introduction

The numerical continuation algorithm discussed in Chapter 2, along with the single shooting method in Chapter 4, can be used to compute the forced response of a system to harmonic excitation at different forcing amplitudes. The forced response curve (FRC) gives the amplitude of the periodic response as a function of the excitation frequency [128]. To compute the FRC with numerical continuation, the forcing period is used as a continuation parameter, and initial conditions are sought that result in a periodic solution of the system. The shooting and pseudo-arclength continuation method can be used for this purpose, as they allow the periodic solutions to be followed over varying parameters such as forcing period or amplitude. As an extension of the methodology used to compute NNMs of FE beams in previous chapters of this thesis, in this chapter, we also use shooting and pseudo-arclength continuation to determine the forced response of various geometrically nonlinear systems. Other methods for computing periodic solutions, such as the harmonic balance method [62] may also be used, and its application in forced responses and bifurcation tracking in nonlinear systems has been studied extensively in the literature (see, for instance, [72], [86], [226]). The application of continuation methods in computing the forced response of geometrically nonlinear beams can be found in [25], [29], [83], [101], [190].

Unlike the computation of NNMs on conservative systems with no damping, forced periodic solutions of the system are computed with the addition of physical damping on the model. The forced response of a nonlinear system is distributed in the neighbourhood of the undamped NNMs of system [115], [182]. Therefore, the underlying NNM curve (also known as the backbone curve) represents the skeleton of the dynamics, in that it connects the forced responses at their resonance point [86], under appropriate excitation. As the forcing amplitude is varied, the topology of FRCs also changes, and stable and unstable branches appear and disappear. This is due to the inherent nonlinearity of the system and the invalidity of the superposition principle between the nonlinear modes [2]. As the FRC of a harmonically excited system sits in the vicinity of the underlying NNM, the forced response may also be used for computing the NNMs of the system. This is the principle of the force appropriation method, which is based on enforcing a quadrature condition such that the phases of the external forces and the phases of the displacements of the structure are at a difference of 90 degrees. In such a condition, the external forces exactly counterbalance the internal damping forces and hence the system responds as the underlying conservative system, giving rise to the NNM of the conservative system [181], [245]. It is clarified that the force appropriation method is not used in this chapter, as here we compute forced responses alone and without a quadrature condition.

6.2 Continuation Procedure

The pseudo-arclength continuation method described in Chapter 2 forms the basis of the numerical algorithm to find the forced response of the system. The primary objective of the shooting procedure remains the same, in that we solve for an initial condition vector $\mathbf{X}(0)$

and a period T such that the system's response is periodic. A key difference, however, is the presence of additional forcing terms. The external force in the dynamic equations of the beam formulated on the Special Euclidean group and given by Eq. (3.200) takes the following form

$$\mathbf{g}_{ext} = \mathbf{F}\sin(\Omega t) \tag{6.1}$$

where $\mathbf{F}$ is the vector of the applied forcing amplitude, and the external forces are integrated over the beam length and assembled. The forcing frequency is set to $\Omega = 2\pi/T$, and the system's equations of motion are integrated over the time interval 0 to T. Therefore, the period of the external force and the simulation time of the system are equal. The periodicity equation, which is formulated on the Special Euclidean group as given in Eq. (4.12) remains the same. The continuation parameter is set as the period T, and the continuation of the periodic solutions is carried out for a constant forcing amplitude. The orthogonality condition remains the same, with corrections to the initial conditions forced to remain orthogonal to the tangent vector of the previous continuation step. The phase condition is no longer applicable and is not required in the continuation algorithm, as the forced periodic orbit is uniquely determined by the phase of the forcing [216]. With the removal of the phase condition, the linear equations for the computation of the tangent vector in Eq. (2.4) and the continuation corrections in Eq. (2.6) become square problems, allowing them to be solved using direct methods without the need for pseudo-inverse or least squares techniques.

6.2.1 Sensitivity to Period

As discussed in Chapter 2, the sensitivity of the periodicity function with respect to the initial conditions and the period of the system is required during the Newton iteration. These sensitivities were derived for the conservative single shooting periodicity equations formulated on Lie groups in Chapter 3. The sensitivities with respect to the initial condition vector remain the same for the forced problem. However, due to the dependence of the external harmonic forcing on the period, the sensitivity of the periodicity function with respect to the period will have additional terms. The full sensitivity with respect to period may be written as [216]

$$\frac{\partial \boldsymbol{\psi}}{\partial T} = \frac{\partial \boldsymbol{\psi}}{\partial t}\bigg|_{t=T} + \frac{\partial \boldsymbol{\psi}}{\partial T}\bigg|_{t=T} \tag{6.2}$$

where $\boldsymbol{\psi} \equiv \boldsymbol{\psi}(\boldsymbol{X}(0), t = T, T)$ is the periodicity function given in Eq. (4.12). The first term in the equation above represents the change in the shooting function with respect to time at the end of the period, and is the same as the unforced time sensitivity computed for the conservative system in Section 4.4. The second term however appears due to the explicit dependence of the external force on the period T. This is calculated using sensitivity analysis by a direct differentiation method, similar to the computation of the monodromy matrix as explained in Section 4.4.1, by accounting for the explicit derivate of the forcing term with respect to the period.

6.3 Geometrically Exact Damping

The existence of damping plays a critical role in balancing the input energy from the external forcing with the energy dissipated by the system, and is necessary to achieve a periodic response under forced conditions [95]. In fact, energy balancing has been demonstrated as a useful mechanism for predicting forced resonances from NNM solutions [100]. In the context geometrically exact beam models, it is important that the damping model is also geometrically exact, and is suitable for modelling large displacements and rotations. The local-frame description of the beam motion under the $SE(3)$ formulation, as discussed in Chapter 3, ensures invariance under Euclidean transformations. It is therefore of fundamental importance to preserve this property through a suitable choice of the damping model.

6.3.1 Damping Based on Strain Rate

Linear viscous damping models, such as Rayleigh damping, function by forming a damping matrix as a linear combination of the mass and stiffness matrices, which is then used to compute damping forces which are made proportional to nodal velocities. Such models are not applicable to geometrically exact formulations as they do not account for the geometric nonlinearity arising from large deflections and rotations, and fail to accurately model the dissipative effects of the structure's complex dynamic behaviour. Furthermore, they cannot adapt to the nonlinear strain measures of geometrically exact formulations. Consequently, the strain objectivity of the model would not be maintained with linear damping. Moreover, as the damping force is made proportional to velocities in such models, energy dissipation will occur in rigid body motion, which causes erroneous damping in free body motions without deformations, and over-damps the relative rigid body motions between the nodal frames of the structure during deformation.

For geometrically exact beam formulations, a damping model based on the strain rate would be more suitable than one based on nodal velocities, as it preserves the strain objectivity of the formulation and provides a more accurate representation of the energy dissipation in the material. The Kelvin-Voigt model, which relies on a first-order constitutive relationship between the stresses and the strain rate, is appropriate for this purpose. This damping model has been used by Gupta et al. [91] on a 3D geometrically exact beam model, where they employ a variational asymptotic method to split the problem into a 2-D cross-sectional analysis and a 1-D beam analysis. They demonstrate how the constitutive equations are modified to consider 3D damping behaviour of the beam. Artola et al. [11] extend the application of the Kelvin-Voigt model to the intrinsic beam model of Hodges [97], where they show that the solutions to the damped intrinsic beam model remain invariant with rigid body displacement. They further show that, when modifying the constitutive relationship between forces and strains, additional nonlinear terms appear in the damping due to cross product couplings between forces and velocities. A linearisation of the damping provides simpler equations, however, leads to increased dissipation, especially when rigid body motion is present.

6.3.2 Kelvin-Voigt Damping

We offer a brief overview of the geometrically exact Kelvin-Voigt damping model, as developed by Linn et al. [129] for Cosserat rods, and employed by Bauchau and Nemani [20] for flexible joints and beams. This offers a frame-indifferent viscoelastic constitutive model which preserves the framework of the $SE(3)$ beam and leads to a damped formulation which is invariant under superimposed Euclidean transformations. This damping model is based on a few basic assumptions. First, it is assumed that the strains remain small and that strain rates vary slowly relative to the internal relaxation processes within the material. Second, it is assumed that the beam is lightly damped, and that oscillation frequencies of the beam's dynamic motion have associated wave lengths which are much longer than the dimensions of the cross section [20]. As explained by Bauchau and Nemani [20], as excitation frequencies increase, local inertial forces such as warping forces become prominent and can no longer be predicted by sectional stress resultants. This is an inherent limit of beam theory, even in the absence of viscoelastic materials, and a truly three-dimensional structural model would be required to model cross-sectional deformations.

The formulation of the damped beam model requires a change in the sectional constitutive laws to incorporate the strain rate. The calculation of the strain energy for the undamped beam, as explained in Chapter 3, uses the Green-Lagrange strain and the second Piola-Kirchhoff stress tensors, and formulates the stress resultants over the cross sections using the local-frame strains and stiffness parameters arising from the elasticity tensor. The local-frame expression of the strains leads to a local expression of the stresses as well, as they are energetically conjugated with the deformations. In the context of the damped beam, the constitutive model of the Kelvin-Voigt formulation is different, additionally incorporating the strain rates into the formula. The stress resultants integrated over the cross sections are given by

$$\begin{aligned} \mathbf{n}(s) &= \mathbf{K}_U \boldsymbol{\gamma}(s) + \hat{V}_F \dot{\boldsymbol{\gamma}}(s) \\ \mathbf{m}(s) &= \mathbf{K}_\Omega \boldsymbol{\kappa}(s) + \hat{V}_M \dot{\boldsymbol{\kappa}}(s) \end{aligned} \tag{6.3}$$

where $\mathbf{n}$ and $\mathbf{m}$ are the resulting force and moment vectors, with components along the beam reference curve, parametrised by s, and shear components along the cross section axes (See (3.181)). The strains along the reference curve and the cross-sectional shear strains are given by $\boldsymbol{\gamma}$, while $\boldsymbol{\kappa}$ represents the torsion and bending curvatures, as given in Eq. (3.169). $\mathbf{K}_U = \text{diag}(EA, GA_1, GA_2)$ and $\mathbf{K}_\Omega = \text{diag}(GJ, EI_1, EI_2)$ are the effective stiffness parameters of the cross-sectional dimensions, containing the axial and shear stiffness terms, and the torsional and bending stiffness terms, respectively, as given by Eq. (3.183). Recall that the stiffness terms come from integration over the cross section and would only be diagonal in the case of an initially straight beam whose neutral axis and reference curve are chosen to be the same. The matrices $\hat{V}_F$ and $\hat{V}_M$ contain the effective viscosity parameters, representing the integrated cross-sectional viscous damping behaviour also associated with the axial, shear, torsional, and bending modes, given by $\hat{V}_F = \text{diag}(\gamma_A, \gamma_{S1}, \gamma_{S2})$ and $\hat{V}_M = \text{diag}(\gamma_T, \gamma_{B1}, \gamma_{B2})$.

These terms multiply into the strain rates in Eq. (6.3), which come from the time derivative of the Green-Lagrange strain tensor. The total strain energy is then computed with the viscoelastic constitutive relationship above and the local-frame expression of the strains. Bauchau and Nemani [20] develop a similar formulation to the one described here, writing the sectional constitutive laws based on a generalised Maxwell model and in the form of a convolution integral with a relaxation function. The discretisation of the finite element beam with the viscoelastic stresses does not change and is achieved with the interpolation formula based on the $SE(3)$ exponential map, as discussed in Section 3.5.3.

Considering a homogeneous and isotropic material, the viscosity parameters may be related to the material and geometric properties of the beam. Taking ζ and η as the bulk and shear viscosities of a viscoelastic Kelvin-Voigt solid, and introducing the following shear, bending, and extension relaxation time constants τ_S, τ_B, and τ_E, given by

$$\begin{aligned} \tau_S &= \frac{\eta}{G} \\ \tau_B &= \zeta \left(\frac{E}{3(1-2\nu)} \right)^{-1} \\ \tau_E &= \frac{1}{3} \left((1-2\nu)\tau_B + 2(1+\nu)\tau_S \right) \end{aligned} \tag{6.4}$$

where ν is the Poisson ratio, it is shown that the viscous parameters may be written as [129]

$$\begin{aligned} \frac{\gamma_{S1/2}}{GA} &= \frac{\gamma_T}{GJ} = \tau_S \\ \frac{\gamma_A}{EA} &= \frac{\gamma_{B1/2}}{EI_{1/2}} = \tau_E \end{aligned} \tag{6.5}$$

The Kelvin-Voigt damping model has been tested and validated on a range of examples of geometrically exact beams. Linn et al. [129] show results of the damping model with a cantilever beam. In their numerical setup, they used identical values for all relaxation time constants and performed calculations on the beam using three distinct values of this constant. Their results show an expected exponential envelope of the free beam response and further reveal that the damping effect becomes weaker in the nonlinear range of the beam's motion with large displacements and rotations. The logarithmic decrement between successive peaks of the response shows the damping ratio approaching constant values as the beam response decays and enters the linear regime. Artola et al. [11] also validate the damping model on a number of test cases. Bauchau and Nemani [20] use a generalised Maxwell damping model, of which the Kelvin-Voigt model is a particular case, on a range of cantilever beams. They suggest that the Maxwell model is better suited than the Kelvin-Voigt model, as the latter leads to energy dissipations which rise rapidly as the excitation frequency increases. They show the onset of the rapid increase in the loss modulus of the Kelvin-Voigt model to begin at a nondimensionalised frequency of 10, defined as the forcing frequency times the relaxation time constant. It is noted that this attribute of the Kelvin-Voigt model could result in increased damping of the higher modes, and could therefore damp out the higher modal interactions in the forced response.

Finally, the Kelvin-Voigt damping model has also been used in flexible multibody dynamics and soft robotics, such as by Renda et al. in the modelling of underwater soft robots [180].

In this thesis, we use a modified viscous damping model which is proportional to the strain rate, and is closely aligned with the Kelvin-Voigt model. A damping matrix is created on the element level, proportional to the constant cross-sectional stiffness matrix by some constant τ. This damping matrix is multiplied by the element strain rate, and added to the stress, which is then integrated along the length of the beam. What results is a stiffness-proportional damping model which is proportional to the strain rates, and therefore maintains strain objectivity and geometric exactness. This is easier to implement than the full Kelvin-Voigt model, and due to the similar formulation it shares with the Kelvin-Voigt model, it behaves in a qualitatively similar manner, with increased damping for higher frequencies. As the Kelvin-Voigt model has been shown to provide a low frequency approximation of second-order accuracy to the generalised Maxwell model [129], it is a suitable choice for the forced responses in low frequency ranges studied in this chapter.

Alternative Derivation from Dissipation Function

Linn et al. [129] consider the development of the viscoelastic beam model from stress resultants to be an alternative to their main proposed method, which relies on a dissipation function to represent the dissipation of energy due to viscoelastic effects. Writing the Green-Lagrange strain tensor and the viscosity tensor as $\hat{\mathbf{GL}}$ and $\mathbf{V}$ respectively, the dissipation function is given as a quadratic form of the strain rate by

$$D_{KV} = \int_0^L \mathrm{d}s \, \frac{1}{2} \left\langle \partial_t \hat{\mathbf{GL}} : \mathbf{V} : \partial_t \hat{\mathbf{GL}} \right\rangle_{\mathcal{A}} \tag{6.6}$$

The integration of the dissipation density function over the cross sections yields the dissipation function of the beam with damping coefficient matrices given by $\hat{V}_F$ and $\hat{V}_M$, and damping parameters given by Eq. (6.5). They argue that direct computation of the forces and moments as resultant cross section integrals with the viscous constitutive equations fails to account for the in-plane strain rates, associated with lateral contractions induced by axial strains through Poisson's effects. However, these terms are accounted for through the cross sectional resultant integrals on the $SE(3)$ beam formulation, as demonstrated by Bauchau and Nemani [20] and by Bauchau, Lao, and Linn [19]. Furthermore, the dissipation function formulation relies on ad-hoc corrections made to the damping and stiffness parameters, using shear correction factors depending on sectional geometry, and therefore limits its applications to complex geometries and material properties [19].

Figure 6.1 depicts a beam differential element with the semi-discretised nodal displacements $\underline{u}(s)$ at a cross section along the beam. As detailed in [20], the components of the strain tensor, including the out-of-plane and in-plane elements, can be evaluated based on the semi-discretisation, which enables the displacement field to be written using the axial variable s along the beam's neutral axis. This in turn can be used to evaluate the strain rates within the beam, which are then used in a convolution integral incorporating the relaxation matrix to

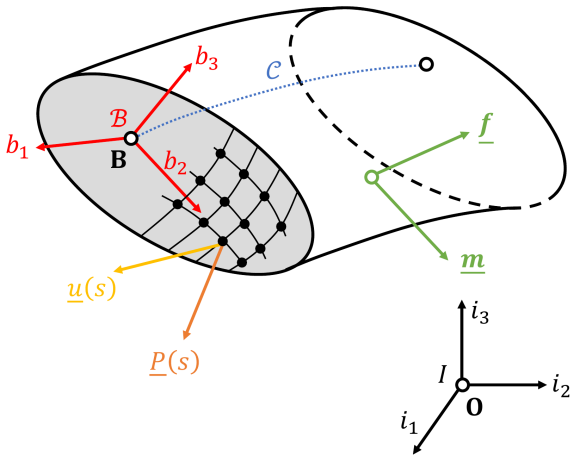


Figure 6.1: Beam differential element, adapted from [20]. $\mathcal{C}$ indicates the reference line of the beam neutral axis, $\mathcal{B}$ is the local body frame at point **B** on the cross section, I is the global frame at the origin **O**, $\underline{\boldsymbol{f}}$ and $\underline{\boldsymbol{m}}$ are the external forces and moments, and $\underline{u}(s)$ and $\underline{P}(s)$ are the nodal displacement field and the internal forces and moments respectively.

compute the time-dependent viscous stresses.

6.4 Bifurcations and Stability of Periodic Orbits

The stability of the periodic solution is determined by the Floquet multipliers, which are the eigenvalues of the monodromy matrix. As the monodromy is computed during the continuation procedure, the Floquet multipliers are also obtained as a by-product. Floquet theory assesses stability in dynamical systems by evaluating how small perturbations to the periodic solution evolve over time. As the monodromy matrix is defined as the sensitivity of the system's final states to the initial conditions, eigenvalues of the monodromy matrix with a magnitude greater than one cause perturbations to initial conditions to grow over time. Therefore, for a periodic solution to be stable, all Floquet multipliers must lie inside the unit complex circle. For periodic solutions, also known as cycles, there will always be a trivial multiplier at $+1$ [28] due to periodicity. It is noted that, other definitions of stability, such as the Lyapunov and Poincaré definitions, do not provide any scheme for determining the stability of dynamic periodic solutions, and are only applicable to equilibrium solutions [218].

A bifurcation occurs when a periodic solution loses hyperbolicity, that is, it transitions from being stable to being unstable [28]. At the bifurcation point, there will exist at least one non-trivial Floquet multiplier of unit modulus. In case of periodic solutions for discrete-time systems, a stable periodic solution could lose stability in one of three ways. These are referred to as codimension-1 or one-parameter bifurcations of [28], [121], as they appear through the variation of a single parameter[1].

The three bifurcations types are [194]:

- Fold (limit point, turning point, or saddle node): A single multiplier leaves the unit circle

[1]In both NNM and forced continuation, we vary a single continuation parameter, namely the period T of the periodic solution.

through +1. At this point, a stable and an unstable periodic orbit come together and annihilate each other, which is reflected as a turning point on the FRC.

- Flip (period doubling): A single multiplier leaves the unit circle through -1. A new periodic orbit will emerge with a period which is twice that of the original orbit. The new period-doubled orbit may be stable or unstable. This bifurcation is often the first step in the route to chaos.

- Neimark-Sacker (torus): A pair of nonreal complex conjugate multipliers leave the unit circle. The stable periodic orbit becomes unstable and gives rise to a quasi-periodic trajectory, characterised by oscillations with two frequencies, which lies on a torus. These frequencies are generally incommensurate, although in special cases they can be rational. The new orbit on the torus may be stable or unstable. This bifurcation is also called the Hopf bifurcation of periodic orbits, as it closely resembles the dynamics of a Hopf bifurcation of equilibrium points.

In order to detect the occurrence of the above bifurcation during continuation of periodic solutions, bifurcation functions (also known as test functions) can be used. These are scalar smooth functions that have regular zeros at the bifurcation point. A bifurcation may therefore be detected between two successive continuation points on the curve, if the value of the test function has opposite signs at those points. Verily, more accurate analysis could be adopted to exactly compute the bifurcation point, such as by applying a Newton-like method to locate the solution of the bifurcation function iteratively.

Let $\mu_1, \mu_2, \ldots, \mu_{n-1}$ be the non-trivial eigenvalues of the monodromy matrix (the Floquet multipliers) at a given periodic solution along the continuation curve[1], the following test functions locate fold, flip, and Neimark-Sacker bifurcations respectively [28], [121]

$$\psi_f = \prod_{i=1}^{n-1} (\mu_i - 1) \tag{6.7a}$$

$$\psi_{fl} = \prod_{i=1}^{n-1} (\mu_i + 1) \tag{6.7b}$$

$$\psi_{NS} = \prod_{i>j} (\mu_i \mu_j - 1) \tag{6.7c}$$

To ensure the Neimark-Sacker bifurcation is detected correctly, we must check the test function is zero due to non-real multipliers only. As the product of the eigenvalues of a matrix equals its determinant, we may write the above bifurcation function using the determinant of the monodromy, M, which is more computationally efficient than computing the eigenvalues. The

[1]Recall the existence of the trivial multiplier $\mu_n = 1$ for periodic solutions.

test functions become

$$\psi_f = \det(M - I_{2N}) \tag{6.8a}$$

$$\psi_{fl} = \det(M + I_{2N}) \tag{6.8b}$$

$$\psi_{NS} = \det(M \odot M - I_m) \tag{6.8c}$$

where $m = \frac{1}{2}N(N-1)$, and $\odot$ denotes the bialternate product.

6.4.1 Branch Switching and Symmetry Breaking Bifurcation

Upon the detection of a bifurcation point on the main continuation branch of an NNM or FRC, a computational strategy could be employed to find and trace the emanating bifurcated branch from the bifurcation point. An initial point on the emanating branch may be found, which would serve as the starting point for continuation along the entire bifurcating branch. A simple branching technique is to make a prediction of a point near the bifurcating branch, and subsequently use Newton corrections to bring the point onto the branch. Beyn et al. [28] and Seydel [194] discuss various methods for approximating the initial prediction point near the bifurcating branch. The first method is to find the tangent to the emanating branch at the bifurcation point, and make a prediction along this tangent. This offers a systematic way for finding the bifurcating branch. However, it requires the solution a linear equation with second order derivatives, in addition to requiring the bifurcation point to be calculated accurately. It is therefore computationally expensive. An alternative approach is to make a prediction along the vector orthogonal to the tangent of the main branch, which is readily available from the pseudo-arclength continuation method. Corrections can then be made orthogonal to this new vector, to arrive at the bifurcating branch. This method, though computationally cheaper, requires extra care to ensure the solution is not taken back to the original known branch.

This branch switching strategy falls under the general umbrella of perturbation techniques for computing bifurcation branches. A typical bifurcation associated with branch switching in symmetric systems is the symmetry-breaking bifurcation. This bifurcation causes a branch shift, such that the periodic solution loses its original symmetry, and unsymmetric periodic solutions emerge. An example of this bifurcation occurs for the 2 DoF system studied in Section 5.3. Though not shown in this thesis, Peeters et al. [170] show the emergence of unsymmetric tongues with even frequency ratios on the frequency-energy plot of this system. These branches may be traced by restarting the continuation at the bifurcation point, while applying a small perturbation to the initial conditions in the direction of the eigenvector associated with the bifurcating Floquet multiplier, encouraging the continuation procedure to trace the curve off the original branch and onto the new symmetry-breaking branch. Stoykov and Margenov [218] also employ a similar method for tracking secondary branches on the FRC of a 3D doubly clamped beam. After detecting a bifurcation point on the main branch of the FRC, the continuation is restarted with a new prediction, which consists of the periodic solution where the stability is lost plus the eigenvector corresponding to the unstable Floquet multiplier. The eigenvector

allows the method to converge to the solution from the secondary branch. They show that the solutions of the main branch present vibrations of the beam in the plane of the applied external force, while the solutions from the secondary branch, present vibrations in space. For a comprehensive study on the computation of periodic solutions for forced mechanical systems and a detailed discussion on the types of stability changes of periodic solutions, see Guillot et al. [90].

6.5 2D Cantilever Beam

A two-dimensional cantilever beam was chosen as the first test case for simulation of the forced response of geometrically nonlinear structures. The cantilever beam was chosen due to the large degree of displacement and rotation which manifest in the dynamic response of the model. This test case was initially investigated by Debeurre et al. [58] who computed the forced response of the beam using a geometrically exact FE model based on the Timoshenko beam with linear shape functions [71]. The primary objective of choosing this test case is to validate the methodology developed in this thesis for computing forced responses. Given that this is a 2D model, the differences between the Timoshenko beam and the $SE(2)$ beam are less prominent, as the parametrisation of 2D rotations in the Timoshenko formulation is relatively effective due to its two-dimensional nature. While the $SE(2)$ model offers superior kinematic accuracy, the Timoshenko model is sufficiently accurate for a 2D problem, and can therefore serve as an appropriate test case for validating our method.

The forced response for the first two nonlinear modes of the cantilever is computed using a uniformly distributed load on the full length of the beam. For geometrically nonlinear structures, where strong couplings between the modes could exist, the external force should excite all modes of the system to ensure such couplings can be captured. A single-point load will only excite modes which have a significant displacement at the point of application of the load, while a uniform load distribution ensures higher modes are also excited and can contribute to the final beam response. Equally, however, a uniform load will not excite modes with out of phase motions. An alternative approach to uniform loading is to apply base excitation at the fixed end of the cantilever, which equally excites higher modes of the system [69], [72]. It is noted that a single point load could be appropriate for some test cases, such as a doubly clamped beam, where due to symmetry, an off-centre point load could still result in a response with contribution from all higher modes [86].

The beam was discretised with 21 elements of equal length for computing the primary forced response around mode one, and 24 elements for computing the secondary response around mode two. The material properties of the beam are: Young's modulus $E = 210$ GPa, and density $\rho = 7800$ kg/m^3, and the geometric properties are: length $L = 1$ m, width $b = 0.05$ m, and height $h = 0.001$ m. The configuration of the undeformed beam is shown in Figure 6.2. The natural frequencies of the first two linear modes of the system are $\omega_1 = 42$ Hz and $\omega_2 = 259$ Hz respectively. The proportional damping model described in Section 6.3, which is proportional to the stiffness matrix and strain rates, was used, with coefficient values of $\tau_1 = 3.8 \times 10^{-5}$

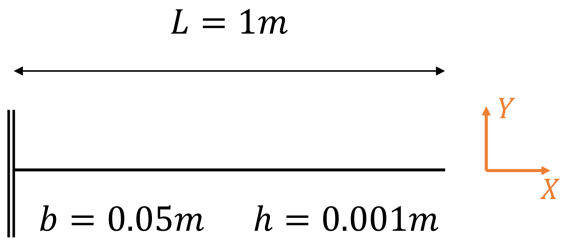


Figure 6.2: Configuration diagram of undeformed 2D cantilever beam.

and $\tau_2 = 6.1 \times 10^{-6}$ for modes 1 and 2 respectively. These values were chosen such that the free response of the beam, initiated from its deformed mode shape corresponding to each mode, gives a damping ratio of 0.5 percent as determined by the logarithmic decrements of the successive maxima in the response. It is noted that Debeurre et al. [58] employ simple mass proportional damping in their numerical model to avoid damping higher modes of the system, and formulate the damping force as proportional to nodal velocities. However, as discussed in section 6.3, this damping model is not geometrically exact, and does not account for nonlinear strains.

6.5.1 Primary Resonance Frequency Response

The first nonlinear mode of the beam is depicted in Figure 6.3. The FRCs illustrated include the maximum absolute values of the axial position at the beam tip, x_p, the transverse position at the beam tip, y_p, and the rotation of the cross section at the beam tip, θ, over one period of oscillation. The positions are normalised with respect to beam length, and the frequency is normalised with respect to the natural frequency of the first mode. A range of increasing forcing amplitudes were considered, and the frequency response for each amplitude was computed. The total amplitude of the integrated uniform force along the length of the beam for each excitation level is provided in the figure caption. The underlying NNM backbone curves, which were computed using the methodology presented in Chapter 4, are also shown. As a distributed load does not excite the system exactly on the mode shape, at higher forcing amplitudes the resonance peak of the FRCs slowly drifts away from the underlying NNM backbone curve. Hardening behaviour is observed as the resonant peaks of the FRCs shift to the right, and increase with increasing vibration amplitude.

Two small resonance tongues can be seen on the NNM curves, one at a lower frequency and the other at a higher frequency level. These indicate modal interactions with higher nonlinear modes. Additional modal interactions occurring at different frequency levels were also reported in [58]. Although these interactions were not explored further in this work, the shooting and continuation methods used are capable of identifying and investigating such areas. However, an inherent limitation of the shooting method is the lack of an effective mechanism for filtering higher-order interactions, other than modifying the number of time steps per periodic orbit. As such, it is difficult to target specific interactions for comparison with other computational results. This is in contrast with the harmonic balance method, which was employed by Debeurre

et al. [58], which allows the selection of a specific number of harmonics, thus enabling more effective filtering of higher order interactions, and as a result more effective targeting of specific resonance tongues [182].

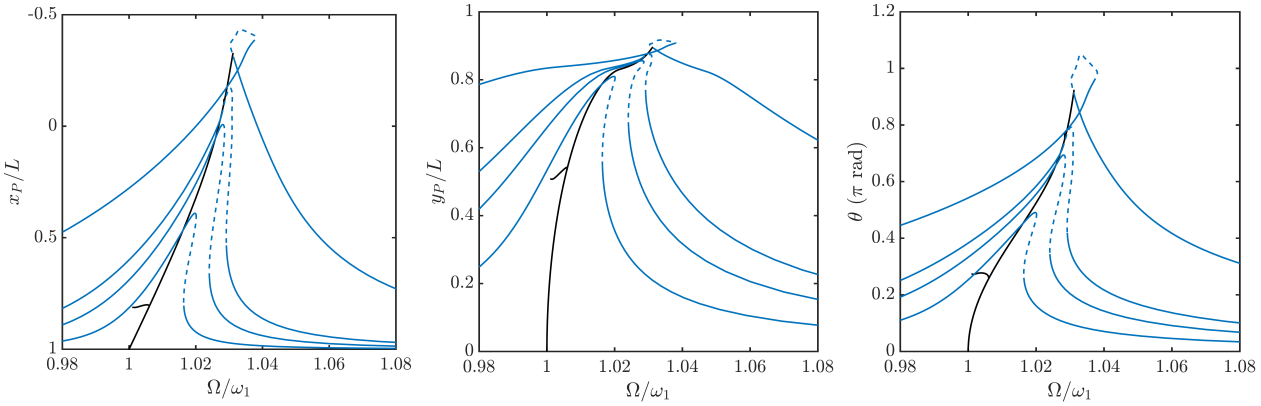


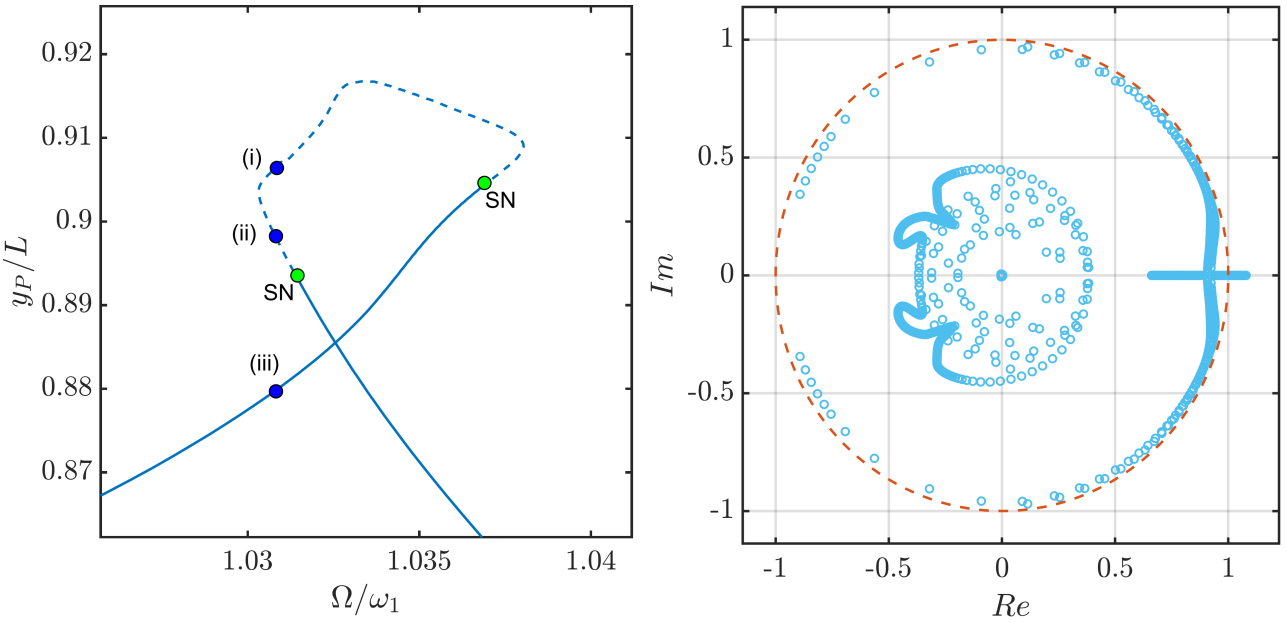
Figure 6.3: Frequency amplitude plots of cantilever beam in primary resonance, showing beam tip maximum absolute axial position, transverse position, and cross section angle respectively. Positions normalised with respect to beam length. NNM backbone curves shown in black, and FRCs shown in blue. Dashed lines indicate unstable periodic solutions. Total forcing amplitude over the full length of the beam equals 200, 400, 600, and 2000 N from low to high amplitude. Beam is discretised with 21 finite elements.

The stability of the forced responses in Figure 6.3 was determined by investigating the Floquet multipliers associated with each periodic solution. Unstable solutions, characterised by multipliers outside the unit circle, were identified and are shown with dashed lines in the figure. A close-up of the highest amplitude FRC in Figure 6.3, along with the locus of the Floquet multipliers in the complex plane along the curve, is shown in Figure 6.4. It is seen that a single multiplier leaves the unit circle through +1, which indicates the occurrence of a fold bifurcation.

It is seen in Figure 6.4a that the change of stability does not occur at the geometric fold points on the FRC. In order to investigate this, time simulations were carried out from initial conditions corresponding to the unstable solution points indicated by the labels (i) and (ii) in Figure 6.4a, which are located on either side of the turning point of the curve. The time history for these simulations can be seen in Figure 6.5, which shows the normalised beam tip transverse position over time. It is seen that both points are indeed unstable, as predicted by the Floquet multipliers. It is further observed that both unstable trajectories eventually converge to the same lower amplitude point on the FRC, which is indicated by the label (iii) in Figure 6.4a. It is therefore confirmed that the saddle node bifurcations indeed do not occur on the geometric turning points on the curve.

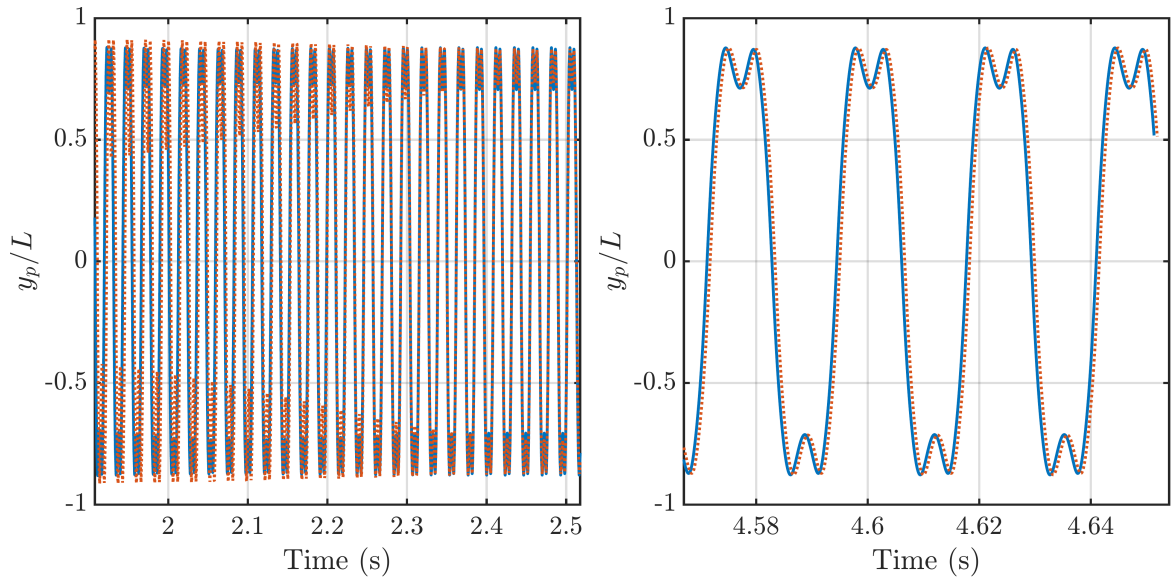
The deformed beam shape associated with the resonant peak of the FRC in Figure 6.4a is shown in Figure 6.6a. Extremely large amplitude motion of the beam over a single period of the forced response is seen, where the beam has bent backwards with a tip cross section rotation close to 180 degrees. The $SE(2)$ model is therefore capable of predicting these large displacements and rotations effectively.

An interesting feature of the frequency response curve associated with the largest forcing



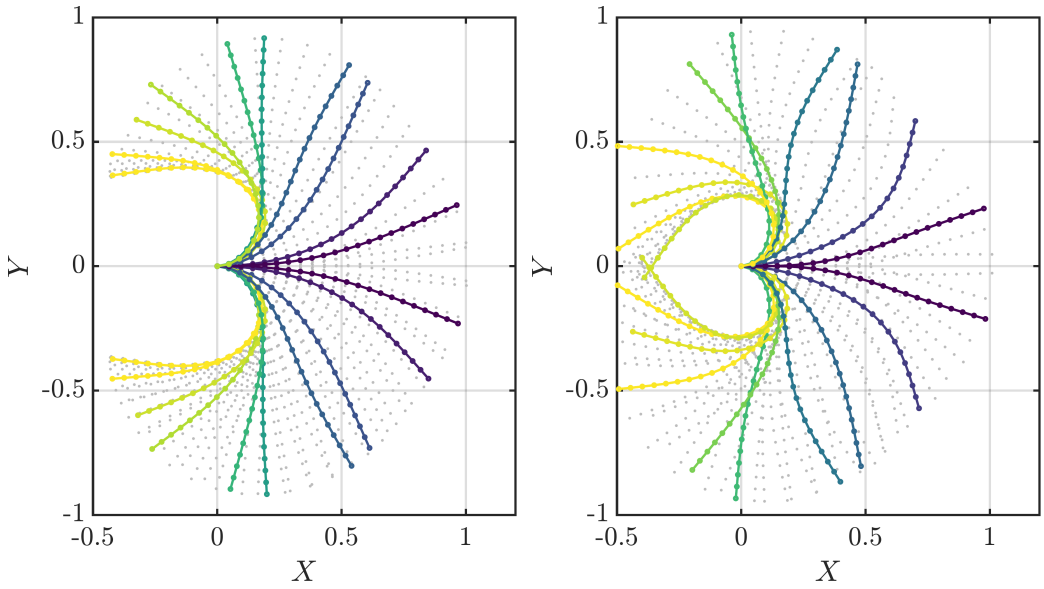
(a) FRC. (b) Floquet Multipliers.

Figure 6.4: (a) Close up of highest amplitude FRC in Figure 6.3 with forcing amplitude of 2000N, showing beam tip maximum absolute transverse position, normalised with beam length. (b) Locus of Floquet multipliers along the FRC. Saddle Node (SN) or fold bifurcations identified. Time history of points labelled (i) and (ii) can be found in Figure 6.5.



(a) Transition to lower branch point (iii). (b) Steady state response.

Figure 6.5: Time simulation of solution points labelled by (i) and (ii) in Figure 6.4a, showing transverse tip position. Blue curve corresponds to solution point (i), and orange to solution point (ii). Unstable response indicated by transients. Steady state response converges to solution indicated by label (iii) in Figure 6.4a for both curves.



(a) $F = 2000$ N (b) $F = 8000$ N

Figure 6.6: Nonlinear deformed shape of the cantilever beam at over a period of forced motion for (a) resonant peak corresponding to FRC with forcing magnitude of 2000N in Figure 6.3, and (b) resonant peak corresponding to FRC with forcing magnitude of 8000N in Figure 6.7.

amplitude in Figure 6.3 and Figure 6.4a is the occurrence of a loop around the resonance peak. Such large amplitude responses were not computed in [58], and could be an indication of the existence of Isolated Response Curves (IRCs), or isolas. These are defined as solution branches which form close curves in the parameters space, and are not connected to the main branch computed in the continuation process. Similar loops on FRCs were observed by Detroux et al. [62] on a nonlinear satellite structure, and by Kuether et al. [118] on a cantilever beam with nonlinear spring at the tip. In both these studies, isola branches were shown to exist, which would eventually merge into the main forced response curve at higher forcing amplitudes. Wiser and Golubitsky [243] also demonstrated the emergence of isolas in the vicinity of loops in forced frequency response curves through the interaction of secondary Hopf bifurcations and homoclinic connections. It is therefore speculated that the occurrence of the loops in the forced responses of the cantilever may be an indication of the presence of isolas, although, proper bifurcation tracking and branch switching techniques are required to verify this phenomena.

Figure 6.7 shows additional frequency response curves for the cantilever with larger forcing amplitudes, depicting the cross sectional rotation of the beam tip on the vertical axis. It is seen that the largest FRC corresponds to a beam tip rotation of 237 degrees at the peak of the curve, as depicted in Figure 6.6b. A likely location for the presence of IRC's is the region above the FRCs for low forcing amplitudes, suggesting that the loops could be a result of the merging of the isolas with the main branch. Compared to the forced response curves computed by Debbuere et al. [58], the results here show an increase by a factor of 2 in the rotation angle of the beam tip for the largest load case. In comparison to the backbone curves found in [58], which extend to higher beam displacement levels, the results here show an increase by a factor of 1.2 in the rotation angle of the beam tip for the largest load case (note that FRC

and backbone curves from [58] are not depicted here). The looping behaviour of the FRCs at higher forcing amplitudes is also not recorded in [58].

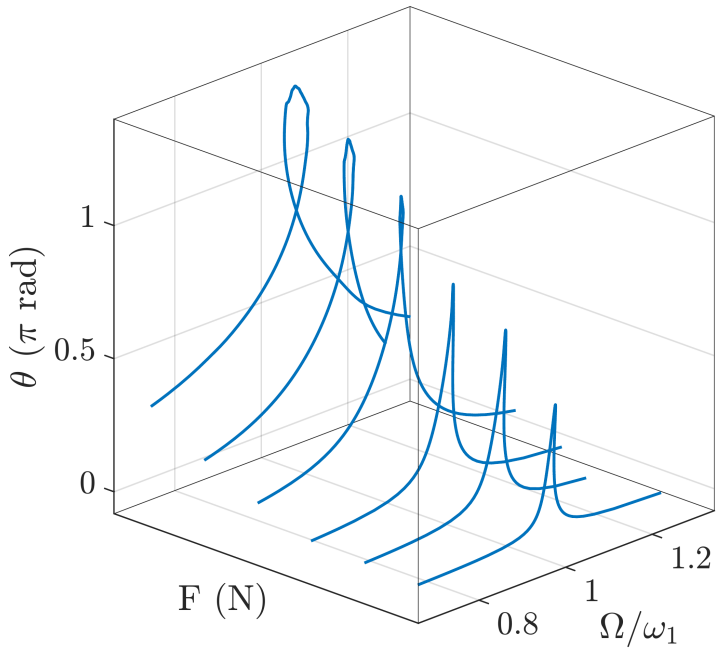


Figure 6.7: Frequency response curves of first nonlinear mode of cantilever beam for increasing forcing amplitudes of 200, 400, 600, 2000, 4000, and 8000 N over the full length of the beam. Vertical axis shows beam tip maximum absolute cross section rotation angle.

The most common method for finding and tracing the isola curves is bifurcation tracking, which consists of following the location of a bifurcation point in a codimension-2 parameters space [140]. The location of fold bifurcations could be traced with respect to the forcing frequency and the forcing amplitude to reveal a fold curve. As isolas generally exhibit two fold bifurcations due to their closed curve, the fold branch would have multiple solutions on the isola for a given value of the continuation parameter. The significance of computing IRCs is highlighted by their associated periodic solutions, which can exhibit much larger displacements and deformations compared to the main branch. When they merge with the main branch, they could lead to a dramatic change in resonant frequency, and could therefore significantly alter the system's dynamic behaviour. The interested reader may refer to Vadcard et al. [232] for a method for detecting isolas and discontinuous evolutions of forced responses, Raze et al. [176] for a method for tracking amplitude extrema of nonlinear forced responses, Detroux et al. [61] for experimental study of isolas and modal interactions, and Mélot et al. [140] for control and optimisation of isolas.

6.5.2 Secondary Resonance Frequency Response

The second nonlinear mode of the beam and the FRCs are depicted in Figure 6.8. The beam shows a softening behaviour for this mode, with the resonant peaks of the FRC occurring at lower frequencies with increased forcing amplitude. The range of transverse displacements and cross sectional rotations seen here are larger than those illustrated by Debeurre et al. [58].

Similar to the first mode, the forced solutions exchange stability through a fold bifurcation, with the unstable solutions indicated by a dashed line in the figure.

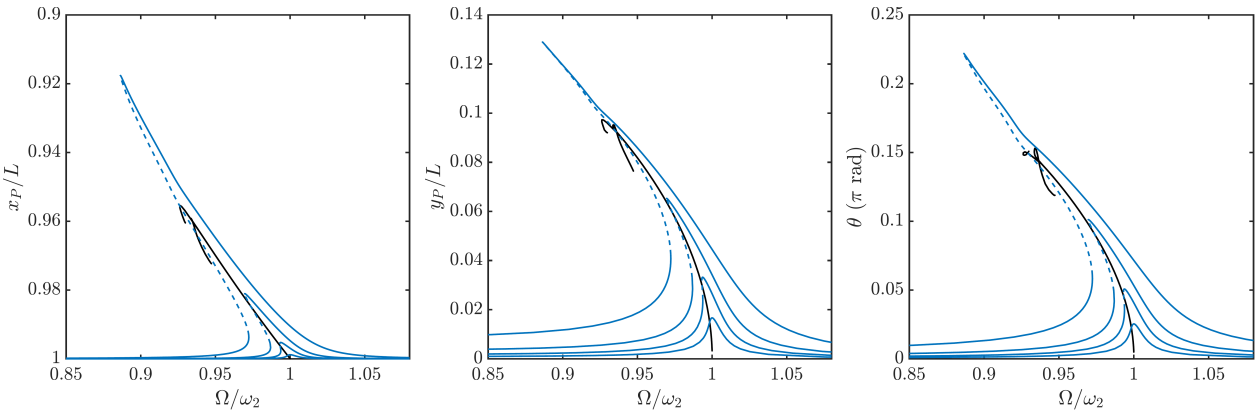
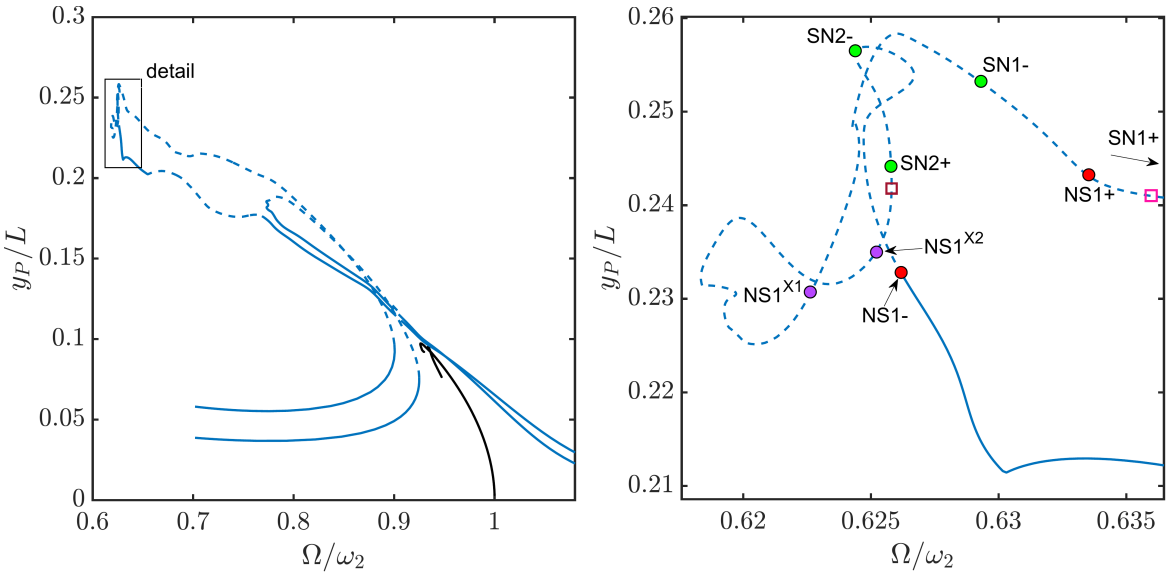


Figure 6.8: Frequency amplitude plots of cantilever beam in secondary resonance, showing beam tip maximum absolute axial position, transverse position, and cross section angle respectively. Positions normalised with respect to beam length. NNM backbone curves shown in black, and FRCs shown in blue. Dashed lines indicate unstable periodic solutions. Total forcing amplitude over the full length of the beam equals 200, 400, 800, and 2000 N from low to high amplitude. Beam is discretised with 24 finite elements.

Additional FRCs were computed with increased excitation amplitudes in order to drive the beam to more extreme displacements and reveal interesting dynamic phenomena. These correspond to a total forcing amplitude along the beam length of 8000 N and 12000 N, and are shown in Figure 6.9. It is seen that, similar to Figure 6.3, the peak of the FRCs begins to form a loop, and the higher amplitude curve shows extremely large displacements of the beam. The thinning of the higher amplitude forced response curve near a frequency ratio of 0.7 in Figure 6.9a, followed by a separation between the upper and lower segments of the curve towards lower frequencies, is qualitatively similar[1] to the FRC obtained from the merging of an isola with the resonance peak, as shown by Detroux et al. [61]. It is therefore suspected that a merging of an isola with a main frequency response branch has taken place. As discussed, isolas need to be computed with bifurcation tracking, and continuation of periodic solutions in the basic sense can only produce the main FRC and cannot identify the isola. However, if the isola has merged with the main forced branch, it becomes possible to identify and trace this curve using continuation on the main branch. Alternatively, continuation could be restarted from a solution point on the merged isola, and the beam could be forced using a lower excitation amplitude. This could lead to the convergence on a detached isola at a lower forcing amplitude level.

Figure 6.9b shows the bifurcations that occur along the higher amplitude FRC. Moving along the unstable branch at the top right of Figure 6.9b, an earlier fold bifurcation denoted by SN1+ has led to a Floquet multiplier outside the unit circle. We then encounter a Neimark-Sacker bifurcation NS1+ as a pair of complex eigenvalues also leaves the unit circle. This is followed by the point SN1-, which indicates the return of the unstable real eigenvalue from

[1]Note that the thinning of the FRC is also a function of the damping level.



(a) FRC. (b) Bifurcation detail.

Figure 6.9: Frequency amplitude plot of cantilever beam in second resonance, showing beam tip maximum absolute transverse position normalised with respect to beam length. Total forcing amplitude over the full length of the beam equals 8000 and 12000 N. (a) depicts full FRC, (b) depicts detail of the FRC. Saddle Node (SN) and Neimark-Sacker (NS) bifurcations shown, + indicates the corresponding eigenvalue leaving the unit circle, and − indicates the same eigenvalue returning inside the unit circle. Beam shape corresponding to solution indicated by the square brown marker is depicted in Figure 6.11. Time simulation of solution indicated by brown and pink square markers depicted in Figure 6.12.

the fold bifurcation to inside of the circle, while the pair of unstable complex eigenvalues remain outside. Following along the branch, the pair of complex eigenvalues collide at the the point indicated by the purple marker, NS1^{X1}. The collision occurs on the real axis, and the eigenvalues both become purely real. This indicates a transition from quasi-periodic dynamics to real instability, described by the overall change in the system's behaviour as the eigenvalues move from a quasi-periodic solution to indicating an exponentially unstable solution. The pair of eigenvalues remain on the real axis, and drift away from the circle as we move along the FRC, with one eigenvalue moving away from the circle as a comparatively faster rate than the other. The faster eigenvalue reaches a magnitude of 2 on the real axis. After a turn in the branch, the eigenvalues get closer again, and at the point NS1^{X2}, they become complex once more and leave the real axis, forming a complex conjugate pair and indicating a return to quasi-periodic dynamics. Further along the curve, at point SN2+, a real eigenvalue leaves the unit circle through +1, indicating a fold, and returns back to the unit circle at point SN2-. Eventually, at point NS1-, the unstable complex eigenvalues return to the unit circle, and the periodic solution regains stability. The Neimark-Sacker bifurcations detected in Figure 6.9 indicate the emergence of quasi-periodic branches that bifurcate out of the main branch, and which can be traced with suitable branch switching strategies and algorithms for solving the quasi-periodicity.

To the best of our knowledge, these complex dynamics on the geometrically nonlinear can-

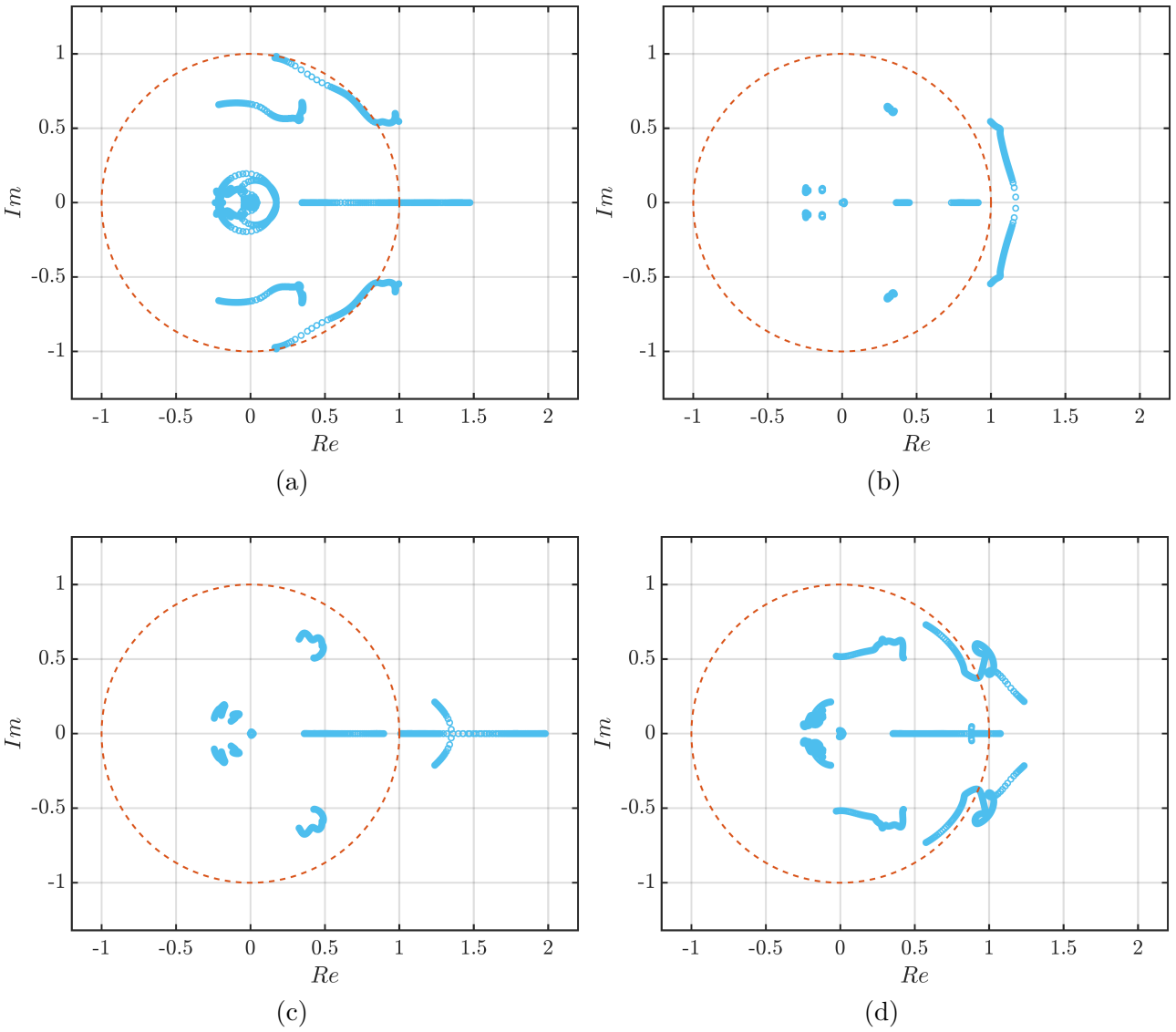
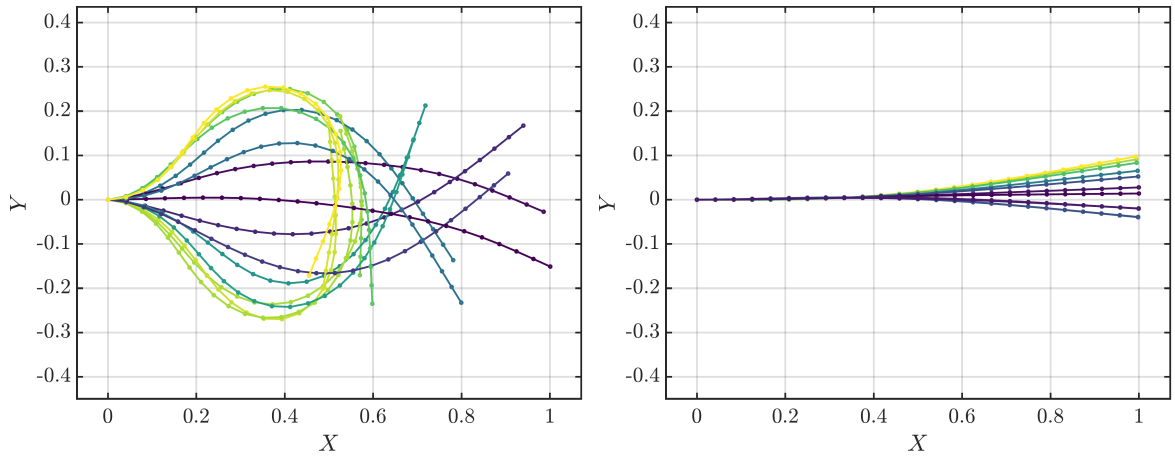


Figure 6.10: Locus of Floquet multipliers along the 12000 N FRC in Figure 6.9. (a) onset of NS1+ and subsequently SN1- (b) continued up to onset of $NS1^{X1}$ (c) continued up to after $NS1^{X2}$ and before SN2+ (d) continued to SN2+ then SN2- and eventually NS1-.

tilever have not been shown in other literature. This has been enabled by the $SE(2)$ beam formulation, which allows for a geometrically exact and kinematically accurate model of the beam deformations and displacements. The locus of the Floquet multipliers associated with the 12000 N FRC in Figure 6.9 can be seen in Figure 6.10. The figure is divided into subfigures, which show the evolution of the multipliers at different segments along the frequency response curve. The subfigures reveal how the pair of complex eigenvalues meet on the real axis, and the extent to which one of the eigenvalues moves to the right of the circle. They also depict how the eigenvalues lift from the real axis and become complex again, and how they re-enter the circle resulting in a recovery of the stability.

The shape of the deformed beam over a single period of forced motion, corresponding to the solution indicated by the square brown marker in Figure 6.9b, is shown in Figure 6.11a. It is seen that the periodic solution corresponds to large axial deformation of the beam, and cross sectional rotation at the tip of 115 degrees. The second mode shape of the cantilever is seen,



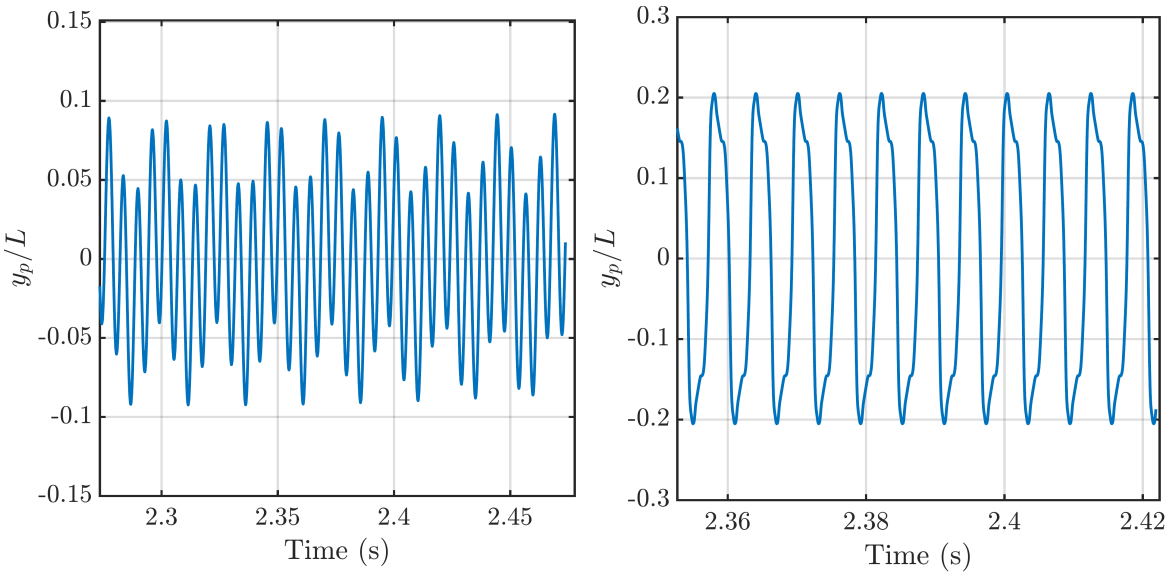
(a) One period of response.

(b) Steady state response.

Figure 6.11: Nonlinear deformed shape of the cantilever beam at over a period of forced motion for solution indicated by square brown marker in Figure 6.9b. (a) shows the solution over a single period, (b) shows the steady state solution after 80 periods.

however, the strong axial displacements towards the beam root, along with contributions from mode 1, results in the removal of the fixed node point typically seen in the second mode of a cantilever. As indicated in Figure 6.9b, this point corresponds to an unstable quasi-periodic solution with a pair of unstable Floquet multipliers. Figure 6.11b shows the steady state forced response of the same periodic solution, after 80 periods of motion. It is seen that the beam shape converges to a low-amplitude response, mostly dominated by the second mode, with no significant contribution from the axial modes.

The time histories of the solutions corresponding to the points indicated by the brown and pink square markers in Figure 6.9b are shown in Figure 6.12, which depicts the normalised transverse position of the beam tip over time. The brown marker solution corresponds to Neimark-Sacker instability with a complex pair of eigenvalues outside the unit circle. Quasi-periodic motion is expected for this solution, which is seen in the steady state response in Figure 6.12a. The normalised beam tip transverse oscillation amplitude of this steady state response is approximately equal to 0.1, which does not correspond to a solution point on the FRC depicted in Figure 6.9. It is possible that restarting the continuation algorithm from this steady state solution might reveal the existence of an isolated response curve at lower forcing amplitudes. Figure 6.12b shows the steady state response of the solution corresponding to the pink square marker in Figure 6.9b. As this unstable solution corresponds to a saddle node bifurcation alone, the steady state response is periodic, and converges to the stable branch immediately below the solution point at the same frequency level.



(a) Brown marker.

(b) Pink marker.

Figure 6.12: Time simulation of solution points in Figure 6.9b showing steady state oscillations. (a) corresponds to solution point indicated with square brown marker and (b) corresponds to solution point indicated with pink brown marker in Figure 6.9b. Normalised transverse position of beam tip shown.

6.6 3D Cantilever Beam

As a second test case, we compute the frequency response curves of a three-dimensional cantilever beam, which undergoes extremely large amplitude in-plane and out-of-plane vibrations. For a beam with symmetric cross section, the natural frequencies in both XY and XZ planes would be equal, where X denotes the local axis along the beam. As a result, there exists a 1:1 internal resonance between the first two nonlinear bending modes of the beam. This leads to different polarisations of the beam, whereby excitation in one plane leads to a response in both planes. This type of internal resonance has been shown on a clamped-clamped beam by Stoykov and Margenov [218], and Shen et al. [201], and on a cantilever beam by Debbuere et al. [59] and Farokhi and Erturk [68]. The extremely large amplitude motions of the cantilever require a geometrically exact beam model to fully capture the extreme displacements. The model by Farokhi and Erturk [68] is based on Euler angles describing the centreline rotation, which is used to formulate the element displacements, while keeping the trigonometric terms intact. As this model is based on Euler angles, it is not singularity free, however, it offers a simplified formulation for modelling cantilevers. Debeurre et al. [59] develop the geometrically exact beam equations, following the work by Cottanceau et al. [53], by using positions and rotations of centreline cross sections on $\mathbb{R}^3 \times SO(3)$, and computing the strains while maintaining the Lie group structure of rotations in the formulation. The rotations are further parametrised using quaternions, for a minimal representations avoiding singularities. The limitations of formulations built on $\mathbb{R}^3 \times SO(3)$ were discussed in Chapter 4. The $SE(3)$ model is employed here for the computation of FRCs of the cantilever, which, as discussed previously, offers greater kinematic accuracy and numerical benefits, and is able to capture the large displacements and

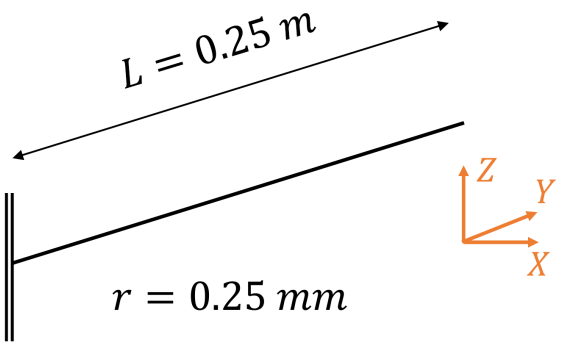


Figure 6.13: Configuration diagram of undeformed 3D cantilever beam.

rotations of the beam in three dimensions.

The cantilever beam studied by Farokhi and Erturk [68] was chosen in this section, and forced responses were computed using the single shooting and pseudo-arclength continuation methods described previously. The beam is modelled under the $SE(3)$ formulation, and is discretised with 21 finite elements along its length. The material properties of the beam are: Young's modulus $E = 210$ GPa, and density $\rho = 7850$ kg/m^3, and the geometric properties are: length $L = 0.25$ m, and cross-sectional radius $r = 0.25 \times 10^{-3}$ m. The configuration of the undeformed beam is shown in Figure 6.13. The natural frequency of the first bending mode in both planes is $\omega_1 = \omega_2 = 5.8$ Hz. The proportional damping model described in Section 6.3, which is proportional to the stiffness matrix and strain rates, is used when computing FRCs. A damping coefficient of 2.7×10^{-4} equivalent to a damping of 0.5% on the first bending modes was chosen.

The FRCs of the cantilever were computed for a range of external excitations. Uniform forcing was applied over the full length of the beam, and the forced response was computed using shooting and pseudo-arclength continuation. The responses in the primary resonance region for three forcing amplitudes of 0.001, 0.005, and 0.01 N over the full length of the beam are depicted in Figure 6.14. The beam response stays in the XZ plane, with bifurcations taking place near the resonance peaks of the FRCs. The deformed beam shape in the XZ plane over one period of oscillation at the peak of the FRC corresponding to a forcing amplitude of 0.005 N is shown in Figure 6.15. This corresponds to the first polarisation of the beam which deforms in the same plane as the applied force. It is seen that the $SE(3)$ model is able to accurately capture the large displacements and rotations of the beam as it bends backwards.

Figure 6.16 shows the locations of the bifurcation points near the resonance peak of the 0.005 N forcing amplitude. It is seen that a saddle node bifurcation takes place initially, characterised by the crossing of a Floquet multiplier through +1 to outside the unit circle. This is followed by a pitchfork bifurcation at the peak of the curve, again through the crossing of another Floquet multiplier through +1, which indicates the branching out of a new solution curve. This new branch corresponds to responses in the XY plane as the second vibration polarisation.

The solution branch which emerges after the pitchfork bifurcation may be computed by suitable branch switching techniques, as explained in Section 6.4.1. By computing the vector

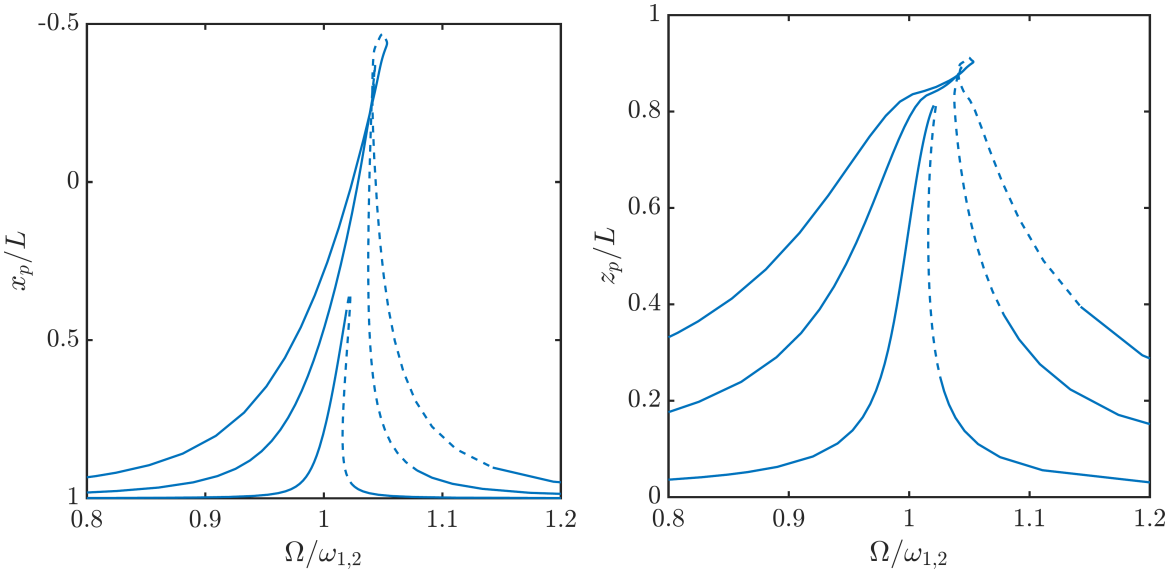


Figure 6.14: Frequency response curves of 3D cantilever beam in primary resonance showing beam tip maximum absolute axial and vertical positions, normalised with respect to beam length. Dashed lines indicate unstable solutions. Total forcing amplitude over the full length of the beam equals 0.001, 0.005, and 0.01 N from low to high amplitude. Beam discretised with 21 finite elements.

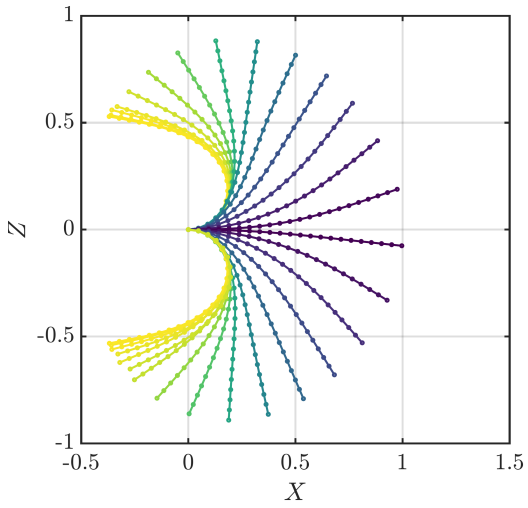


Figure 6.15: Beam shape of 3D cantilever over one period of oscillation at resonance peak of FRC with forcing amplitude of 0.005 N. First polarisation in XZ plane depicted.

orthogonal to the tangent vector at the pitchfork solution point, a prediction can be made along this vector for an initial point on the new branch. This can be then corrected to locate the branch, which can then be traced fully by pseudo-arclength continuation. Alternatively, a perturbation can be applied to the initial condition at the resonance peak, directed along the eigenvector associated with the unstable Floquet multiplier of the pitchfork bifurcation. A simpler approach, which is employed here, is to restart the continuation from the bifurcation point, while applying a small load in the Y direction of the beam, to encourage the continuation method to retrieve the coupled branch. This approach is similar to the one used by Shen et al. [201]. The choice of the direction for the small perturbing force is informed by the deformed shape of the beam, as determined by adding the unstable eigenvector to the initial conditions.

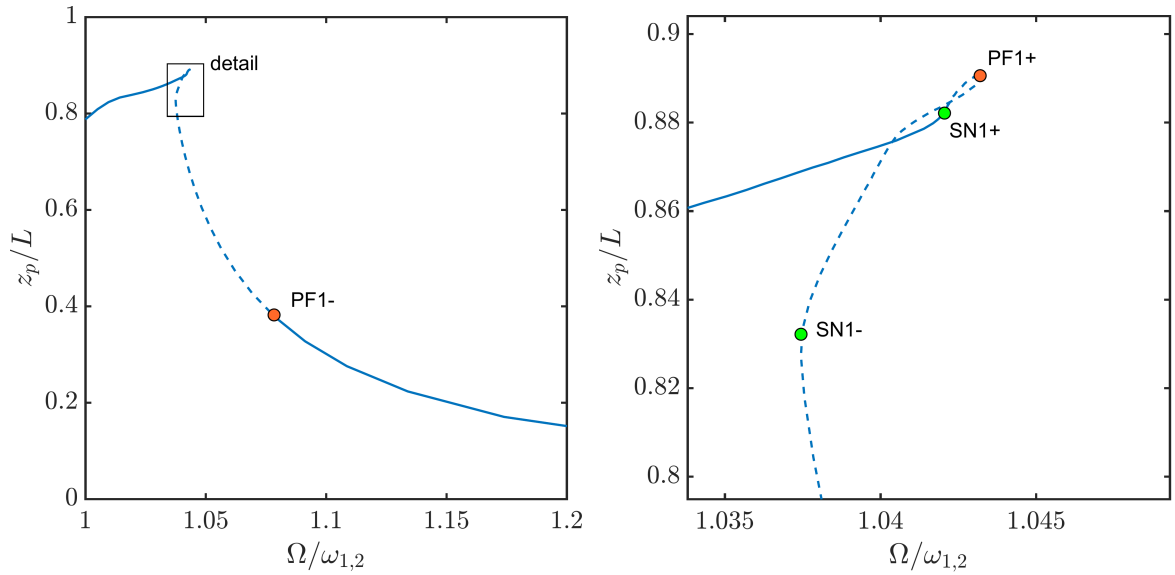


Figure 6.16: Bifurcation detail of FRC of 3D cantilever beam. Forcing amplitude over full length of beam equals 0.005 N. Vertical axis depicts beam tip maximum absolute normalised vertical position. Saddle Node (SN) and Pitchfork (PF) bifurcations shown. + indicates the corresponding eigenvalue leaving the unit circle, and - indicates the same eigenvalue returning inside the unit circle.

This ensures that the applied load aligns with the expected deformation direction on the coupled branch.

Taking into account the response curve for a forcing amplitude of 0.005 N, a small force with an amplitude of 2% of the main force, and in quadrature with the main force, is applied to the beam in the Y direction, and continuation is restarted from the pitchfork bifurcation at the resonance peak depicted in Figure 6.16. The complete FRC including the coupled solution branch is shown in Figure 6.17. It is seen that the coupled solution branch emanates out of the initial branch at the point of the pitchfork bifurcation, leading to periodic solutions with components in both the Y and the Z directions. The new branch also exhibits a Neimark-Sacker bifurcation, which leads to quasi-periodic solutions along a small section of the curve. The location of the bifurcation points are shown in Figure 6.18, which depicts 2D projections of the full FRC.

The deformed beam shapes at the solution points indicated with blue markers in Figure 6.18 are depicted in Figure 6.19. The 1:1 internal resonance between the first two bending modes is clearly seen, and the coupled response of the beam in both in-plane and out-of-plane motion is observed. The internal resonance results in the beam rotating along an elliptic trajectory at point I, which develops into a symmetric circular trajectory at the peak of the coupled solution branch at point III. It is confirmed that the $SE(3)$ model is able to capture the large displacements and rotations of the beam effectively, and that the shooting and pseudo-arclength continuation methods are able to trace the forced periodic solutions of the beam over a range of frequencies. Compared to the results by Farokhi and Erturk on the same beam [68], the $SE(3)$ formulation has been able to model larger amplitude displacements for comparable forcing levels, especially on the coupled bifurcated branch, which as seen in Figure 6.18, shows

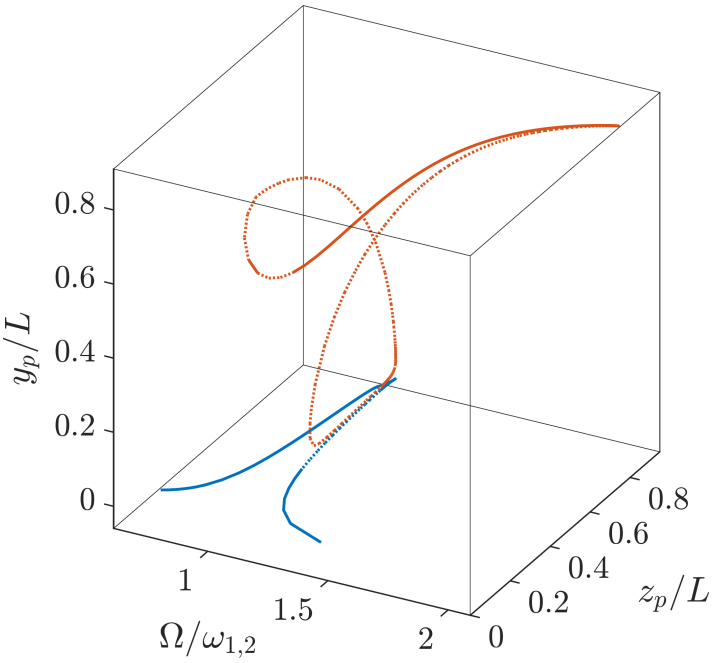


Figure 6.17: Frequency response curves of 3D cantilever with forcing amplitude of 0.005N, with 1:1 internal resonance. Blue curve depicts primary response in XZ plane, and orange curve depicts coupled response in 3D space. Axes show maximum absolute Y and Z position of beam tip over one period of oscillation, normalised with respect to beam length.

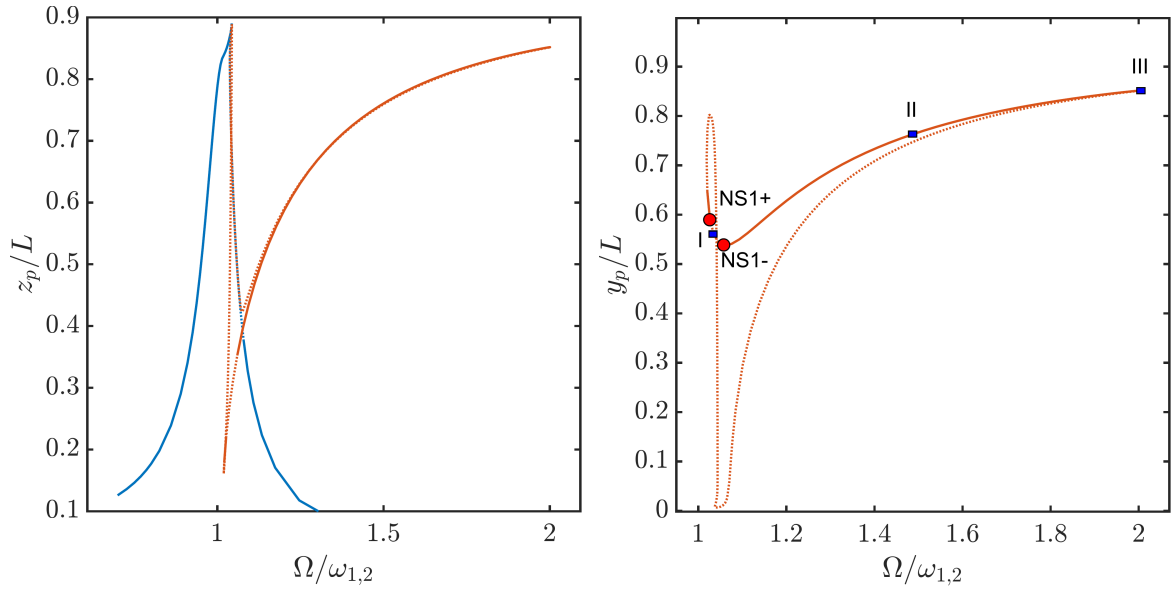
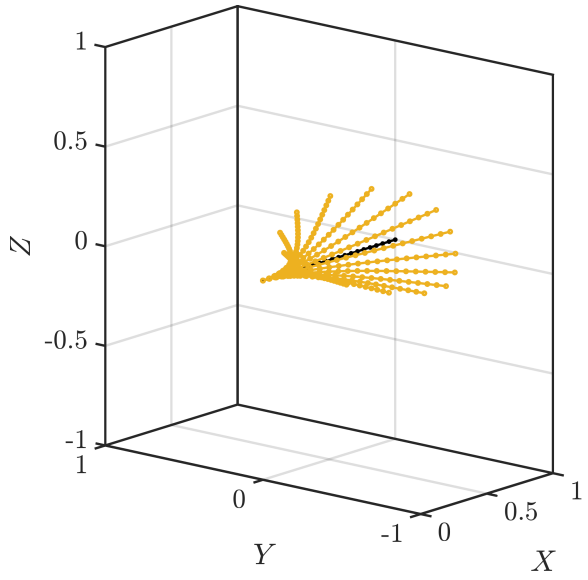
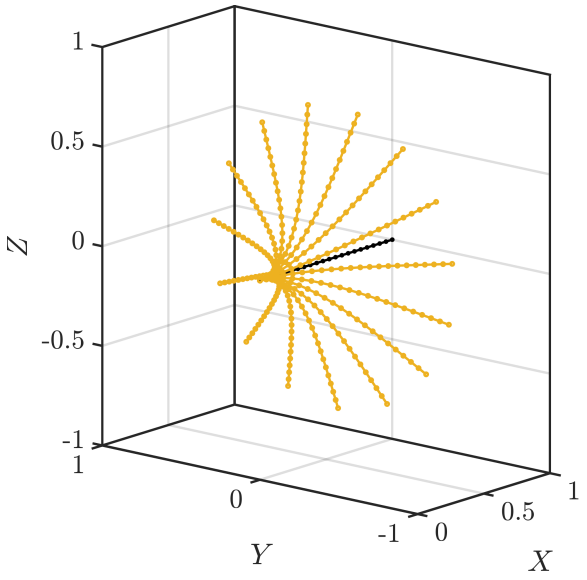


Figure 6.18: Frequency response curves of 3D cantilever with forcing amplitude of 0.005N, with 1:1 internal resonance. 2D projections of FRC in Figure 6.17. Neimark-Sacker (NS) bifurcations shown. + indicates the corresponding eigenvalue leaving the unit circle, and - indicates the same eigenvalue returning inside the unit circle. Dynamic response of beam at points I, II, and III shown in Figure 6.19.

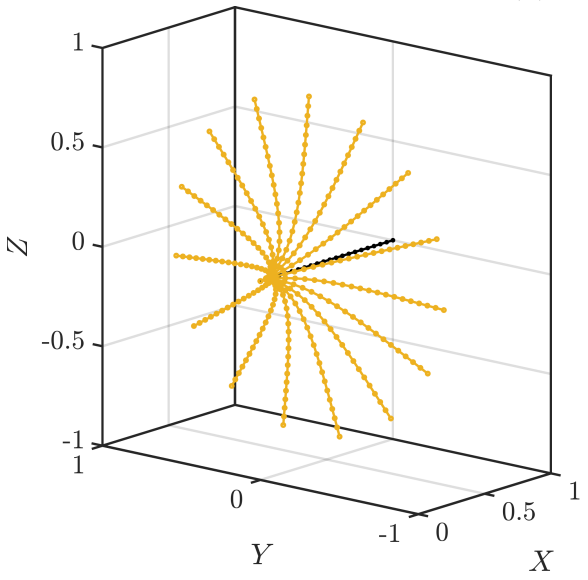
vibration amplitudes of 0.8 times the beam length in the vertical direction, near twice the beam's fundamental frequency.



(a) Point I.



(b) Point II.



(c) Point III.

Figure 6.19: Dynamic response of beam over one period of oscillation corresponding to points I, II, and III in Figure 6.18.

6.7 2D Vertical Cantilever Beam

As the final test case, a two-dimensional axially excited vertical cantilever beam with tip mass has been selected, which undergoes parametric resonance response under external load. This test case poses challenges due to the extremely large displacement amplitudes of the beam under loading, further augmented by the gravitational effect on the tip mass. This particular test case was studied by Farokhi et al. [70], who presented an experimental and numerical investigation of the model. Their geometrically exact numerical model is based on the centreline rotation as the

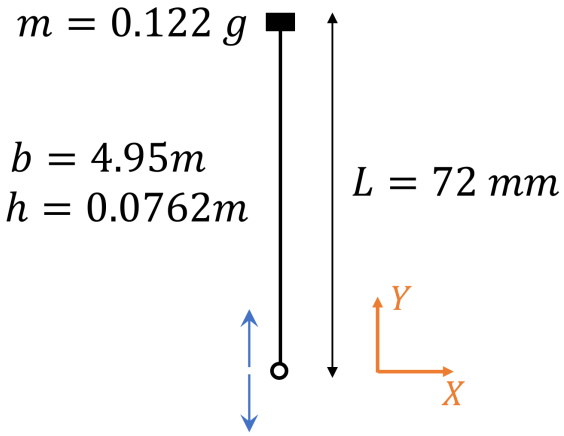


Figure 6.20: Configuration diagram of undeformed vertical cantilever beam.

main displacement variable of the FE equations. The transverse and longitudinal displacements are written in terms of the centreline slope, according to Euler-Bernoulli beam theory, while keeping the nonlinear trigonometric terms in the equations intact. The equations of motion are derived using variations of the strain and kinetic energies and using Hamilton's principle. The discretised equations of motion are obtained using the Galerkin method. The forced response of the beam is computed by pseudo-arclength continuation using the AUTO-07P code. This is accompanied by an experimental setup of the beam in a vacuum chamber, with prescribed base acceleration using a shaker, and high-speed videography to extract tip displacements and rotations. The frequency response of the cantilever was computed for three different levels of base excitation acceleration, and good agreement was observed with frequency sweep results from their experiments.

The material properties of the beam are: Young's modulus $E = 200$ GPa, and density $\rho = 7880$ kg/m^3, and the geometric properties are: length $L = 72$ mm, width $b = 4.95$ mm, and height $h = 0.0762$ mm. The tip mass is $m = 0.122$ g. The configuration of the undeformed beam is shown in Figure 6.20. The natural frequency of the first linear bending mode is computed as $\omega_1 = 6.4$ Hz. The beam is modelled based on the $SE(2)$ formulation and discretised with 21 finite elements of equal length. Base excitation is applied to the beam in the axial direction, and gravity is taken into account in the equations of motion.

6.7.1 Continuation Challenges

The computation of frequency responses for this test case using shooting and pseudo-arclength continuation faced some challenges. The beam is modelled with boundary conditions applied to the base restricting the transverse and rotational degrees of freedom. A constant load in the upward direction is also applied, to support the beam under its own weight. With this configuration, the continuation algorithm faced convergence issues, and the starting point on the FRC could not be computed. Owing to these challenges, the choice was made to investigate the dynamics of the beam using sine sweeps instead of continuation of forced periodic solutions. Sine sweep excitations of the main beam were carried out with axial excitation of its

base with the forcing term given by

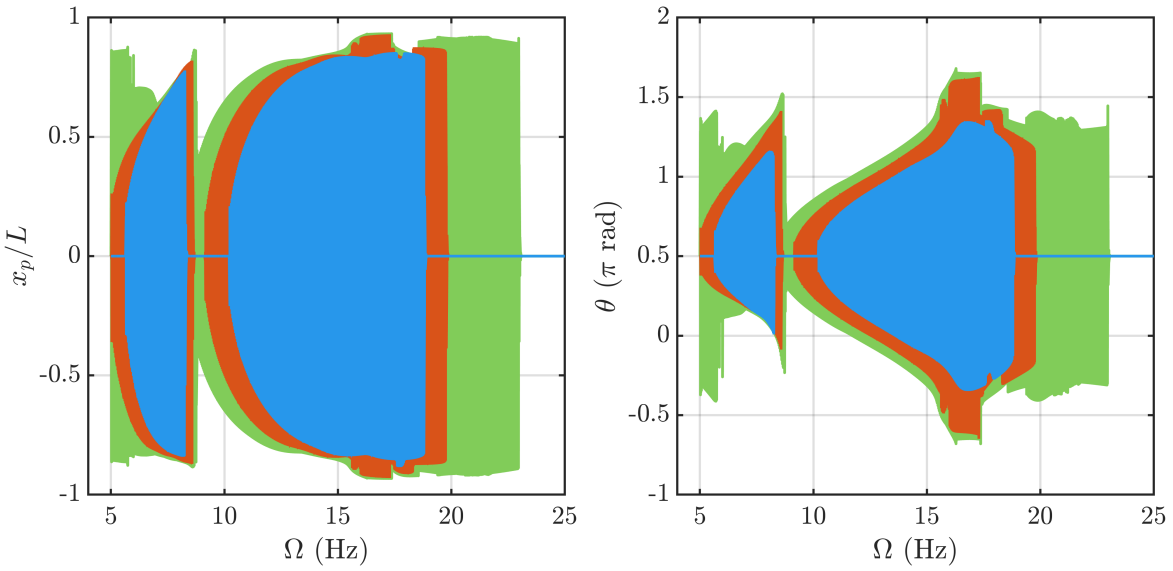
$$F_Y = f_0 \sin(\Omega t) \tag{6.9}$$

where f_0 is the prescribed forcing amplitude.

In addition to the challenge of continuation convergence, we were also unable to tune the damping parameter of our model to match exactly with the experimental results by Farokhi et al. [70] at all three levels of base acceleration. The damping model in their study is a combination of both Kelvin-Voigt damping proportional to strain rates, and linear viscous damping proportional to nodal velocities. They tune the parameters of their damping model to achieve the best match with their experimental results, motivated by matching the resonance peak at all three base excitation levels with the same damping coefficients. The displacement-based linear viscous damping model however is inherently not geometrically exact, as discussed in Section 6.3. For our study, we have used the stiffness-proportional damping based on the strain rates, thus maintaining objectivity of strains. The application of base excitation in their numerical model and experiments is based on prescribing a base acceleration level, which is not compatible with our implementation of prescribing a base forcing amplitude. In their computation of the beam forced responses, the displacement of the base node against the reference configuration is dependent on the forcing frequency since the acceleration is kept constant. This results in different base displacement levels through the range of frequencies considered in each FRC. The difference in the implementation of the external force between their numerical model and ours is a further contributing factor to our inability to tune our damping to match their experimental results. Therefore, a damping coefficient value was chosen such that the first bending mode of the beam is damped by 1%, and was kept constant for all sweep excitation levels. It is noted that damping is a nonlinear phenomenon, which has been experimentally shown to increase with the vibration amplitude during nonlinear oscillations of beams [4]. Damping in numerical FE models serves as an estimate, often calibrated to align with specific experimental results, and it is inherently an approximate method to introduce dissipation into the system. As our damping model is based on the strain rates, which are nonlinear in the geometrically exact $SE(2)$ formulation, the damping also becomes inherently nonlinear despite the fixed damping coefficient. We therefore believe that the strain-rate-based damping model used in the sine sweep simulations in this chapter is an appropriate choice, allowing for an effective study of the complex dynamics of the beam.

6.7.2 Sine Sweep Results

In this section, results are presented for a number of sine sweep excitations with increasing amplitudes, which were carried out on the $SE(2)$ beam near twice the beam's fundamental natural frequency in order to investigate the nonlinear dynamics. Principal parametric resonance occurs when the excitation frequency is close to twice the first natural frequency, and the forcing amplitude is larger than a given threshold. With these conditions, the occurrence of two

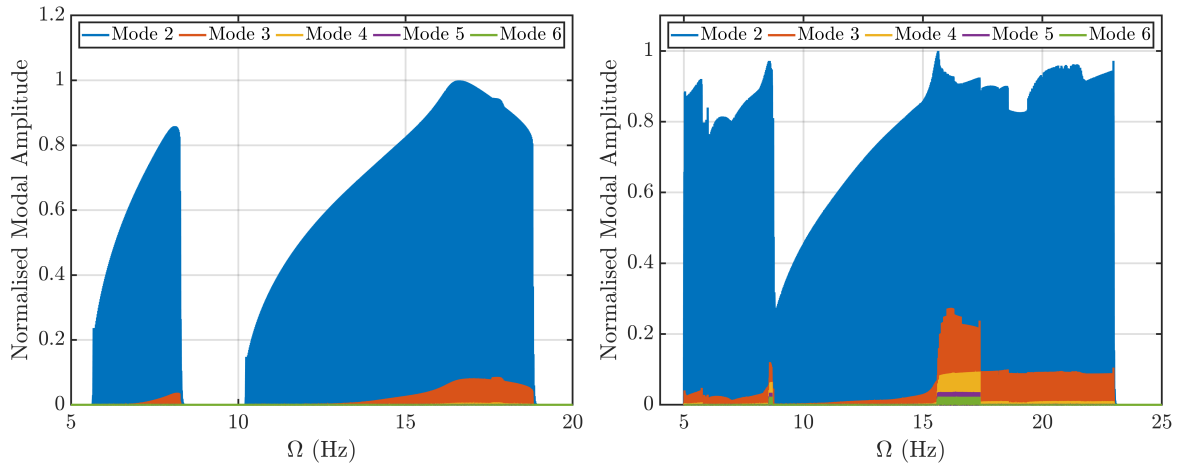


(a) Normalised transverse position. (b) Cross section rotation angle.

Figure 6.21: Response of vertical cantilever beam tip to sine sweep excitations. Forcing amplitudes equal 0.02, 0.03, and 0.04 N.

period-doubling bifurcations in the static branch gives rise to a stable and unstable periodic solution, which coincide at a fold bifurcation near the peak amplitude [70].

A sweep rate of 0.5 Hz/min was chosen for accurate simulations, and a range of three forcing amplitudes of f_0 equal to 0.02, 0.03, and 0.04 Newtons were chosen. The sampling frequency for the sweeps was set to 3000 Hz for the first two forcing levels, and 5000 Hz for the highest forcing amplitude. The transverse position of the beam tip, normalised with respect to the beam length, and the cross sectional rotation angle of the beam tip as a function of the sweep frequency Ω are depicted in Figure 6.21. The main resonance peak is seen at around 16 Hz, which is approximately twice the magnitude of the natural frequency of the first bending mode of the beam. Due to the hardening of the system, the resonance peaks are shifted to the right, resulting in maximum values at frequencies which are slightly larger than twice the first natural frequency. Sudden transitions from low to high amplitude, and back again to low amplitudes, commonly referred to as jumps, are observed. The asymmetric envelope of the sweep response, and the skewness around the resonance peak, are additional nonlinear phenomena, which can typically be seen in sine sweep excitation responses of geometrically nonlinear mechanical structures [152], [183]. A further resonance peak is also observed at approximately 8 Hz, which is close to the natural frequency of the first bending mode of the beam. The presence of two resonance peaks, one at the first natural frequency and the other from parametric resonance at twice the first natural frequency, was not reported by Farokhi [70]. The sweep response for the highest forcing level shows large amplitude motion at an extended range of frequencies, along with multiple modulations of the signal's envelope in the parametric resonance region. These modulations could indicate the occurrence of Neimark-Sacker bifurcations, and the attraction of the system dynamics towards a stable torus. Similar modulations were also observed in the sine sweep response of a cantilever beam by Kuether et al. [118].



(a) Forcing amplitude 0.02 N.

(b) Forcing amplitude 0.04 N.

Figure 6.22: Response to sine sweep excitations projected onto the linear modes of the beam. Modal amplitudes normalised by maximum amplitude of Mode 2 (first bending mode). Note that Mode 1 is the axial rigid body mode, and is omitted as a rigid body transformation is applied to the beam to move the base back to the origin before projecting onto the flexible modes.

Figure 6.22 shows the modal amplitudes of the sweep response to forcing excitations of 0.02 and 0.04 N, by projecting the sweep response onto the linear modes of the system. Before projecting onto the modes, a rigid body motion is applied to the deformed beam to fix the position of the beam base throughout the sweep excitation, and therefore remove the excitation displacement from the modal amplitudes. It is seen that, for the lower forcing amplitude of 0.02 N, there is a small contribution from the higher modes in the response. However, for the higher forcing amplitude of 0.04 N, the higher modes continue to contribute to the response throughout the higher sweep frequencies, in addition to having a greater contribution to the response close to the second resonance peak at approximately 16 Hz. Furthermore, the aforementioned modulation in the signal, as seen in Figure 6.21, is also present in the higher modes of the system, at the parametric resonance peak. The larger contributions from the higher modes in the 0.04 N sweep response could be a factor in the wider sweep profile corresponding to this forcing level in Figure 6.21. This large amplitude motion is multi-modal, with energy being transferred between the fundamental mode and the higher modes. In general, this energy exchange will not be trivial, as the decay in one mode might lead to a transfer of energy to another mode. Therefore, the system as a whole experiences a wider frequency response, as the energy transfer between the modes, and the presence of higher modes, offers a mechanism for overall energy to remain in the system for a longer time period. This however depends significantly on the degrees of freedom, as transferring energy from one mode to another can reduce or increase the motion in some physical DoFs. This was reported for a two degree of freedom mass spring system with cubic nonlinearity by Kerschen et al. [115], who demonstrated how the drop down in the peak response of the FRC of one degree of freedom coincides with a rapid increase in the peak amplitude of the other degree of freedom.

Another interesting feature of the sweep response for the cantilever is that the jump phe-

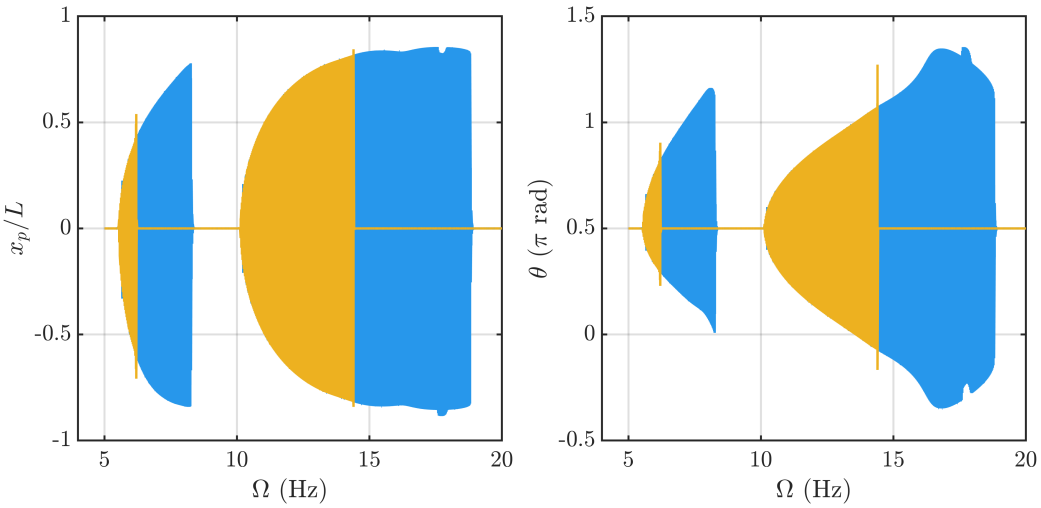
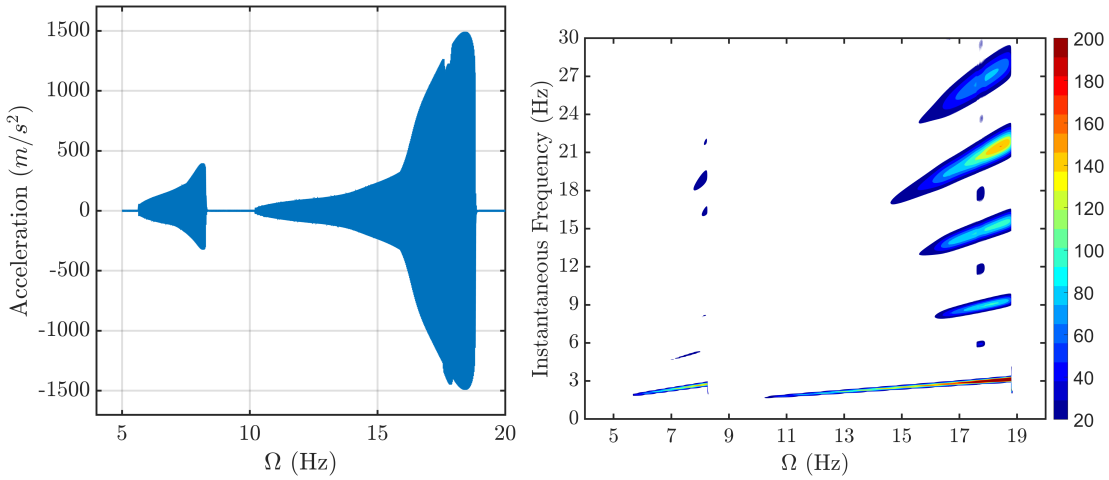


Figure 6.23: Response of vertical cantilever beam tip to sine sweep excitation with forcing amplitude of 0.02 N. Normalised transverse tip position and tip rotation shown. Positive sweep rate shown in blue, and negative sweep rate shown in yellow.



(a) Transverse acceleration amplitude. (b) Wavelet transform of acceleration signal.

Figure 6.24: Response of vertical cantilever beam tip transverse accelerations to sine sweep excitations with 0.02 N forcing amplitude. Note accelerations are expressed in the local frame of the beam tip, owing to the left-invariant formulation of the beam equations in the $SE(2)$ framework. Global accelerations may also be computed using the derivative of the Adjoint map on $SE(2)$, however, the qualitative response including the wavelet transformation remains similar.

nomena at low and high sweep frequencies completely envelope the full response, such that the jumps define the boundaries of where the response amplitudes are significant. The response to a sine sweep with decreasing frequency was computed for a forcing amplitude of 0.02 N, and is shown alongside the sweep up response in Figure 6.23. It is seen that the jumps enclose the sweep response for both sweep up and sweep down curves. The figures reveal the profile of the beam FRC, alongside the region of bi-stability in the response. This is consistent with the sharp resonance peaks demonstrated in the FRCs by Farokhi et al. [70], where the frequency curve abruptly turns and the system loses stability.

The time series of the transverse accelerations in the local frame of the beam tip in response

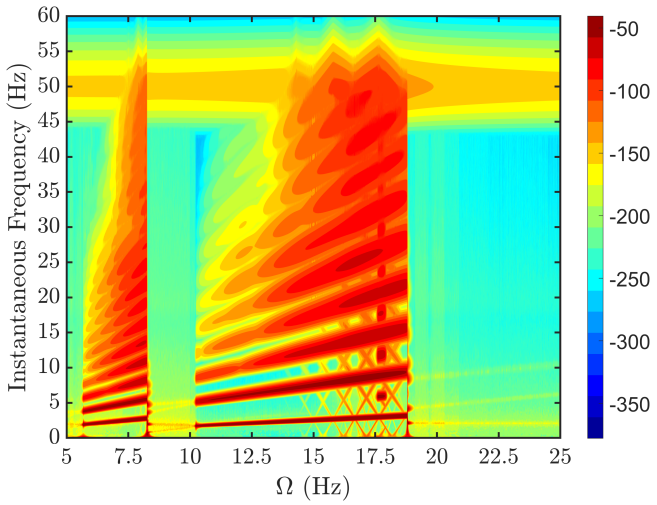
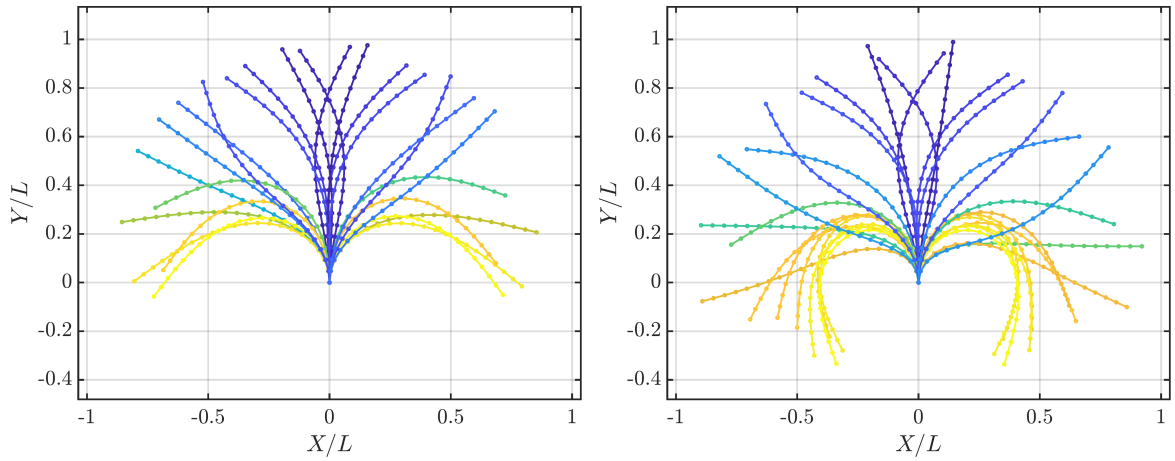


Figure 6.25: Wavelet transform of absolute beam tip transverse position for a sine sweep excitation amplitude of 0.02 N. Wavelet amplitude shown in decibels.

to the sine sweep excitation of 0.02 N is depicted in Figure 6.24a, along with the wavelet transform of the acceleration in Figure 6.24b. The wavelet amplitude shows the presence of significant harmonic components above the excitation frequency, along with subharmonics below the excitation frequency. The subharmonics are also present in the wavelet transform of the transverse beam tip position, shown in Figure 6.25, which corresponds to the response to the same sine sweep forcing amplitude as that in Figure 6.24b. The wavelet amplitude in Figure 6.25 is shown in a logarithmic scale, and depicts the appearance of wideband frequency components across the sweep frequency, which coincides with the jump locations seen in Figure 6.21a. As seen in Figure 6.25, two subharmonic responses exist in the region of the first peak between 6 and 8 Hz. Around the second peak in the region between 10 and 19 Hz, there is a single subharmonic response below the response from the parametric resonance, which itself occurs at half the sweep frequency. Additional responses at higher harmonics are also observed. The interaction of fundamental parametric resonance with subharmonic resonances has commonly been reported in literature, and was shown in a single degree of freedom system by Nayfeh [149]. Butikov also showed the occurrence of subharmonics in the dynamics of a parametrically driven pendulum [41]. There, it was shown that for certain ranges of the excitation amplitude and frequency, the pendulum can be trapped in an n-periodic limit cycle, locked in phase with the force, with a frequency equal to the driving frequency divided by n. In the case of the cantilever studied here, the presence of the lower harmonic responses in the wavelet transform in Figure 6.25 indicates the presence of subharmonic motion.

Finally, Figure 6.26 shows the deformed beam shape over one period of oscillation at the parametric resonance peak of the sweep response curves in Figure 6.21, corresponding to forcing levels of f_0 equal to 0.02 and 0.04 Newtons. Extremely large displacements and rotations of the beam are observed, which are greater in magnitude compared to the experimental and numerical results of Farokhi et al. [70]. The beam is bending below its root, and the shape of the deformed beam shows the presence of higher-order modes, as also depicted in Figure 6.22.



(a) $f_0 = 0.02$ N (b) $f_0 = 0.04$ N

Figure 6.26: Beam shape of vertical cantilever over one period of oscillation at parametric resonance peak of sine sweep excitations with forcing levels indicated.

6.8 Conclusion

In this chapter, we have effectively computed the forced responses of geometrically nonlinear beams modelled on the $SE(2)$ and $SE(3)$ Lie group formulations. Utilising an adapted shooting and pseudo-arclength continuation method, as detailed in Chapter 4, we have introduced a novel application of these methods to the Lie group beam formulations in computing forced periodic solutions. Our model incorporates geometrically exact damping, based on the strain rate and proportional to the stiffness matrix, which ensures invariance under Euclidean transformations, and effectively represents dissipative effects of the structure's dynamic behaviour.

We have demonstrated the capability to predict and model bifurcations and stability of periodic solutions. The analysis of a 2D cantilever beam under primary and secondary resonance conditions revealed that the $SE(2)$ model is capable of capturing extremely complex dynamics, including large displacements and rotations, more effectively and to a greater extent than previously reported in the literature.

Moreover, we have explored the forced responses of a 3D cantilever beam modelled under the $SE(3)$ formulation, and exhibiting 1:1 internal resonance between its first two bending modes. We demonstrate that the $SE(3)$ beam model can capture large-scale rotations and displacements in three dimensions, surpassing the capabilities reported on similar structures in existing studies. We have further demonstrated that the application of shooting and pseudo-arclength continuation methods, which have been adapted to work with models formulated on Lie groups, is effective in tracing periodic solution curves, assessing stability of solutions, detecting Neimark-Sacker and pitchfork bifurcations, and following the secondary resonance branch corresponding to the internal resonance.

Furthermore, we have demonstrated complex multi-modal dynamics and subharmonic responses on a 2D vertical cantilever under gravity, modelled under the $SE(2)$ formulation, which has not been previously documented. Some limitations were faced in the continuation of forced responses corresponding to the parametric excitation for this model, which need to be resolved

in future studies.

Overall, we have demonstrated, for the first time, that the combination of $SE(2)$ and $SE(3)$ beam formulations with shooting and pseudo-arclength continuation methods provides a robust framework for modelling the forced responses of geometrically nonlinear beams, and is capable of capturing extremely large displacements and rotations of such structures effectively.

Chapter 7

Nonlinear Dynamics of Flexible Aircraft Structures

Abstract

In this chapter, we explore the application of the $SE(3)$ beam formulation to the nonlinear analysis of a high-aspect-ratio wing and a box wing aircraft structure, highlighting the effectiveness of the $SE(3)$ model in capturing large displacements and rotations in multibody flexible structures commonly found in aeroelastic applications. Through forced response computations using the single shooting and pseudo-arclength continuation methods developed in previous chapters, various nonlinear dynamics phenomena such as modal interactions and bifurcations are demonstrated. The chapter's novel contribution lies in the application of the $SE(3)$ formulation to such structures, paving the way for future aeroelastic research by integrating aerodynamic models and flight dynamics solvers, to develop comprehensive aeroelastic analysis tools.

Chapter Acknowledgements

We gratefully acknowledge the research group at the University of Bristol, especially Professor Mark Lowenberg, Dr. Alessandro Pontillo, and Dr. Punsara Navaratna, for providing us with the geometry of the wing beam model for use in this chapter.

7.1 Introduction

High-aspect-ratio wings (HARWs) have seen increased interest in the civil aviation industry due to their aerodynamic efficiency. Owing to their slender design, they reduce effects from tip vortices which leads to lower induced drag and larger lift-to-drag ratios compared to lower aspect ratio wings. An additional driver for the design of these wings is the desire to keep the structural weight low, which leads to designs that are naturally very flexible and therefore more susceptible to aeroelastic effects. Due to their increased flexibility, they are more prone to higher deflections at lower air speeds, which could result in aeroelastic instabilities such as flutter and Limit Cycle Oscillations (LCO) [3], [166]. Therefore, accurate aeroelastic modelling of HARW is crucial in identifying phenomena such as aircraft stability characteristics, flutter, gust response and response to turbulence, in addition to the definition of flight control laws, and interactions between structural, aerodynamic, and flight dynamics [161].

A series of early pioneering studies on HARW include the works of Patil et al. [168] and Tang and Dowell [222], [223], which included experimental and theoretical research motivated by the use of HARW in high-altitude, long-endurance (HALE) aircraft. In the context of modelling the structural dynamics of HARW, and flexible aircraft in general, various geometrically exact beam formulations have been used in the literature. An early work by Cesnik et al. [48] used the strain based beam model for this purpose. Palacios et al. [159], [161] later expanded on that work by including shear strains as independent degrees of freedom in the strain based model. They also used the intrinsic beam model for comparison, and coupled it with the Vortex Lattice Method (VLM) for the aeroelastic analysis of a flexible aircraft. Su and Cesnik [220] applied the strain based beam formulation for modelling a joined beam and a split beam wing configuration, using relative displacement constraints for joint kinematics. The intrinsic beam model was later used by Cook et al. [52] to perform a gust load analysis on a range of flexible aircraft models with various wing aspect ratios, coupled with a linear unsteady strip theory aerodynamic model. They demonstrated the importance of correctly capturing the full dynamic behaviour of the axial and in-plane bending and shear loads on the aircraft wings for the nonlinear structural model, in addition to the torque loads, which showed significant nonlinear effects even for the lower aspect ratio wings. This coupling between the in-plane and out-of-plane bending modes (flapwise and chordwise) and the torsional mode for a HARW has also been documented by Hodges and Dowell [98]. Further coupling can also occur between structural modes and rigid body modes, particularly as the elastic modes, due to the flexibility of the wing, have low frequencies that are close to those of the rigid body modes. This phenomenon is thoroughly reviewed in the paper by Afonso et al. [3]. Artola et al. [9] further employed the intrinsic beam model to develop a low-order nonlinear aeroelastic model for the model predictive control of a HARW aimed at flutter suppression and gust alleviation. In other beam formulations, the ANCF model was used by Otsuka et al. [154] in the nonlinear aeroelastic analysis of HARW with a propeller, motivated by the systematic method through which the propeller cylinder coordinate system is obtained by the nodal gradient vectors. For a review of some further examples of numerical aeroelastic modelling of high-aspect-ratio wings and aircraft, along with

a review of the structural and flight dynamics modelling and aerodynamic tools in current use, see Palacios and Cesnik [160].

In this chapter, we apply the methods developed in the previous chapters to the nonlinear analysis of a high-aspect-ratio wing and a box wing aircraft structure. Our aim is to demonstrate the suitability of the $SE(3)$ beam model for the purpose of aeroelastic analysis. This chapter lays the groundwork for future research, serving as a starting point for both additional nonlinear dynamic analysis such as bifurcation tracking, and aeroelastic studies with the introduction of aerodynamic effects.

7.2 High-Aspect-Ratio Wing

A beam model of a HARW was created using the $SE(3)$ formulation and its forced response was computed for a range of excitation frequencies and amplitudes. The selected wing is one of three wings designed and manufactured by Navaratna et al. [15] at the University of Bristol. In their study, three 0.85 m (0.80 m wetted length) half-span cantilever wings with different flapwise bending stiffnesses were manufactured, chosen to have a static trim tip deflection of 5%, 10%, and 15% of the half-span. The wings are unswept and non-tapered with a chord length of 8.95 cm, giving them a half-span aspect ratio of 8.94. Of the three wings, we have chosen the most flexible wing with a static tip deflection 15% for the analysis in this chapter.

The schematic of the wing beam without aerofoils and ribs is shown in Figure 7.1. The full wing is modelled as a straight finite element beam with variable cross sectional dimensions along its length according to the design depicted in the schematic. The $SE(3)$ beam model was created using the nodal coordinates and element properties from the straight beam model used by the researchers at Bristol in their numerical computations conducted with NASTRAN. The offset properties incorporated in their model, such as shear centre and neutral axis offset, centre of gravity offsets of concentrated masses along the beam, and coordinate system offsets, are not modelled in the $SE(3)$ beam. Additionally, the tapered PBEAM elements in their model are averaged and added as elements with constant cross-sectional properties in the $SE(3)$ model. Figure 7.2 shows the static beam deflection under gravity for various tip masses for the beam model alone (without the wing assembly). The deflection computed in our $SE(3)$ model is greater than that recorded by Navaratna et al., due to the simplifications made in defining the beam properties, as described above. Despite this, a dynamic analysis on the model remains valid and provides valuable insight into the nonlinear dynamics of the structure, which is the focus of our study here.

The fully assembled wing comprises the beam shown in Figure 7.1 along with the aerofoil sections, rib attachments, and skin. These are modelled as concentrated masses that are distributed along the FE beam model, the details of which may be found in [15]. The concentrated masses are also added to the $SE(3)$ beam, and the forced response of the beam is computed for the fully assembled model. This is achieved with single shooting and pseudo-arclength continuation, as described and demonstrated in Chapter 6. The stiffness-proportional damping model based on the strain rate, as described in Chapter 6, is used, and is tuned to give a damping

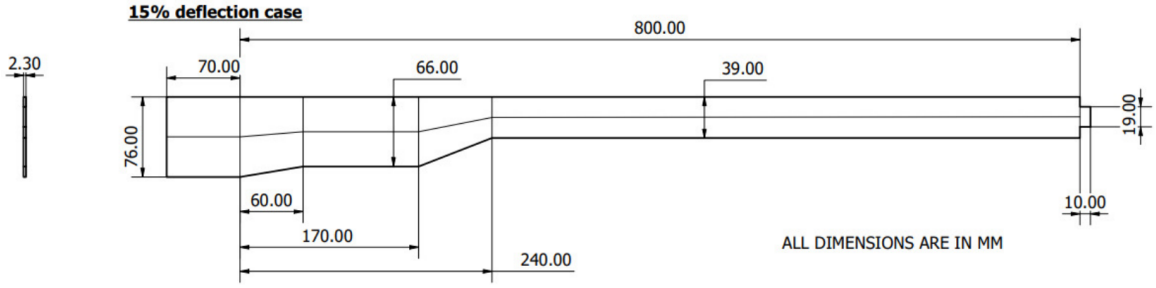


Figure 7.1: Schematic of wing design with 15% trim tip deflection [15].

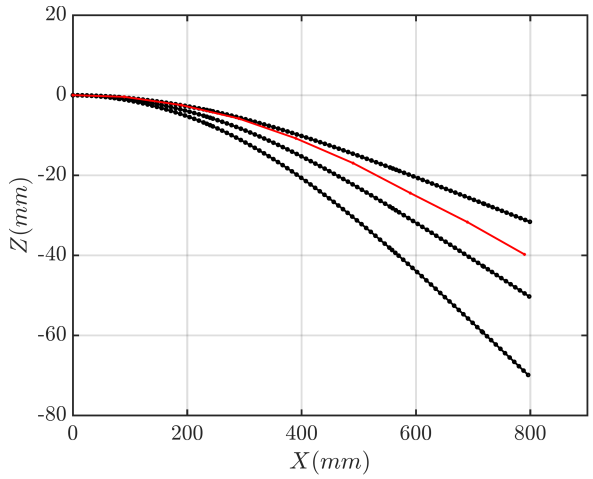
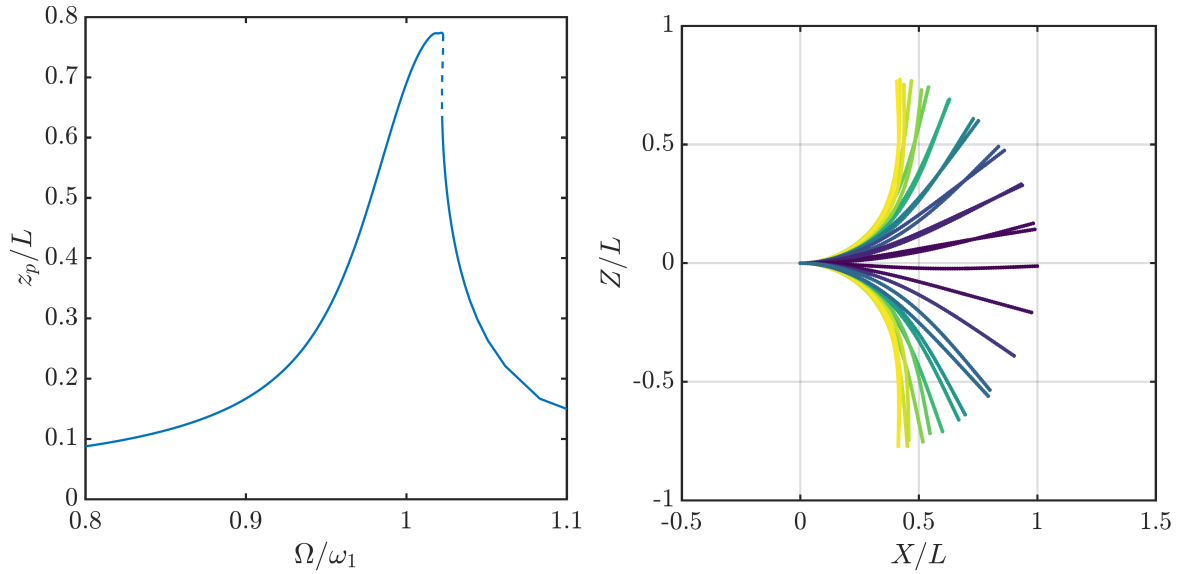


Figure 7.2: Static solution of beam only model under gravity with tip mass values 17.4, 42.7, and 88.0 grams. Red line indicates video gauge measurements for 88.0 grams tip mass from experimental results in [15].

value of 1% for the mode under consideration in the forced response. Figure 7.3 shows the FRC of the beam in primary resonance, which depicts the peak resonance of the beam under a uniformly distributed load of 1.275 N/m along its length. The hardening response characteristic of a cantilever in mode 1 bending is observed, similar to that found in Section 6.5 for the 2D cantilever. The system loses stability through a fold bifurcation at the resonance peak, which is regained further along the response curve. The beam shape corresponding to the peak resonance response is also shown, where very large tip displacements are observed.

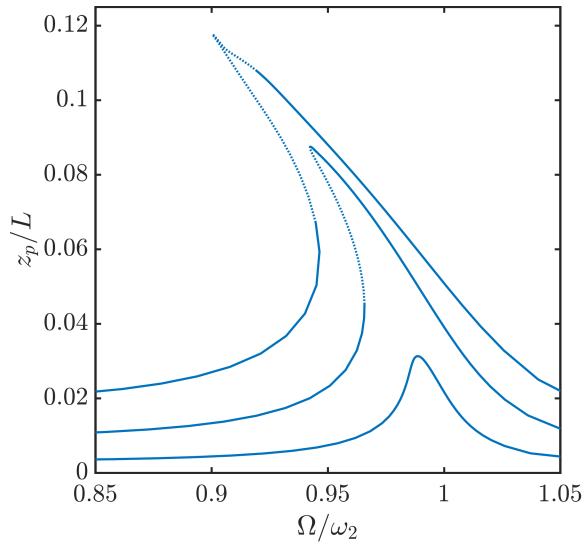
The FRC for mode 2, corresponding to the second flapwise bending mode, is shown in Figure 7.4 for a range of excitation amplitudes. The softening behaviour of the beam is observed, which increases for increasing force levels. The locus of the Floquet multipliers corresponding to the response curve for the highest forcing level is also shown. The system loses stability through a fold bifurcation, which occurs first as the forcing frequency is increased. Just before the peak of the response curve, another single eigenvalue leaves the unit circle through +1, which corresponds to a pitchfork bifurcation. Shortly after, the unstable eigenvalue from the fold bifurcation returns to the circle, whereas the multiplier associated with the pitchfork bifurcation remains outside. As seen in Figure 7.4, the magnitude of this eigenvalue grows rapidly as it moves to the right on the real axis, before it returns to the circle, and the system regains stability.



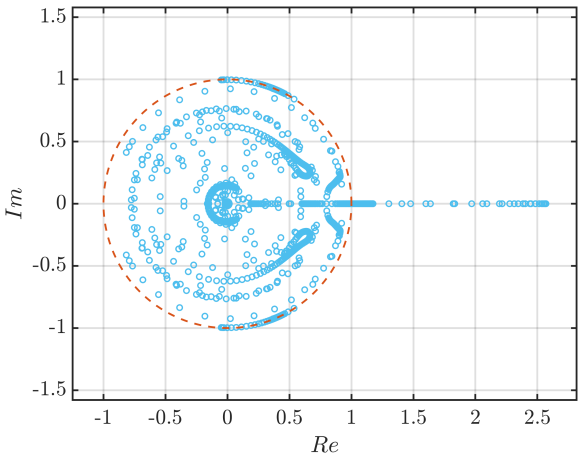
(a) FRC. (b) Beam shape at resonance peak.

Figure 7.3: Frequency response curve of fully assembled wing with forcing amplitude of 1.275 N/m showing maximum absolute beam tip vertical position. Solid and dashed lines indicate stable and unstable solutions respectively.

The eigenvector associated with this unstable eigenvalue corresponds to deformation of the beam in the out-of-plane (chordwise) direction. This corresponds to mode 4 of the structure, which is the first chordwise bending mode. The linear natural frequency of mode 4 for the $SE(3)$ beam is 47.7 Hz, which is almost an integer multiple of that of mode 2, at 11.9 Hz. The near commensurate natural frequencies, coupled with the direction of the unstable eigenvector, strongly indicates a 4:1 internal resonance between modes 2 and 4, and the branching out of the out-of-plane bending mode from the resonance peak of the in-plane mode depicted in Figure 7.4. The continuation was restarted from the resonance peak of the 7.65 N/m FRC in Figure 7.4, with the unstable eigenvector added to the initial condition vector corresponding to the peak solution. Note that the exponential map on $SE(3)$ is required for this purpose, to map the unstable eigenvector to an $SE(3)$ element which can be composed with the initial condition position vector. Unfortunately, the continuation process was not able to identify the secondary branch, and Newton corrections returned the initial condition vector back to the main branch. A secondary excitation was applied to the beam in the out-of-plane Y direction and in quadrature with the primary forcing, to encourage the continuation procedure to identify the coupled solution branch. The frequency of the chordwise forcing term was set at exactly 4 times that of the primary flapwise force, in line with the 4:1 frequency ratio between the modes in internal resonance. Unfortunately, the continuation was still unable to identify the secondary branch. As the wing has a non-symmetric cross section profile, with different in-plane and out-of-plane stiffness properties, finding the correct secondary excitation required to successfully excite the system to converge to the coupled branch is challenging. An additional challenge is from the damping term, which as discussed in Chapter 6, is stiffness-proportional and in proportion with the strain rate of the beam elements. This would result in higher dissipation for mode 4 which has a higher frequency than mode 2. Therefore, accurate and robust branch



(a) FRC.



(b) Floquet multipliers.

Figure 7.4: Frequency response curve of fully assembled wing with forcing amplitude of 1.275, 3.825, and 7.65 N/m showing maximum absolute beam tip vertical position. Locus of Floquet multipliers for the 7.65 N/m forcing amplitude response also shown. Solid and dashed lines indicate stable and unstable solutions respectively.

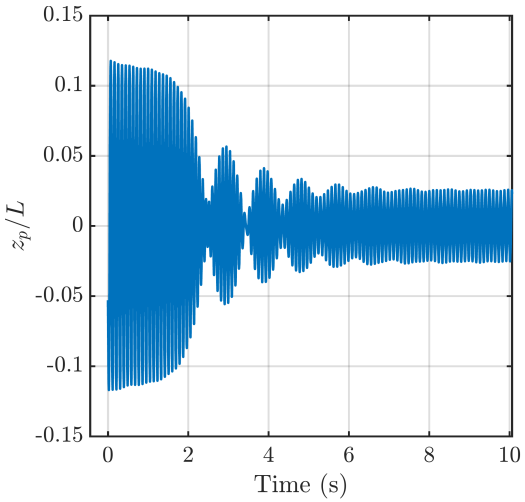


Figure 7.5: Time history of solution corresponding to the peak of 7.65 N/m forcing amplitude FRC in Figure 7.4, showing normalised beam tip vertical position. Steady state response converges to point on the lower branch of the FRC.

switching techniques are required, which rely on the computation of the tangent to the new branch, as described in Chapter 6. It is finally noted that a time simulation of the forced response starting from the unstable solution at the resonance peak will eventually jump down and converge to the stable solution at the same frequency on the lower section of the branch. This is depicted in Figure 7.5, which shows the time history of the solution at the resonance peak of the highest amplitude FRC in Figure 7.4

The forced responses computed in this section provide a preliminary study of the nonlinear dynamics of the HARW, demonstrating the efficacy of the $SE(3)$ model in capturing the large displacements and rotations, and internal resonance between the nonlinear modes. A final re-

mark is also made about the torsional coupling for limit-cycle oscillations, which, as highlighted by Navaratna et al. [15], is of interest in the subsequent wind tunnel testing phase of the wings. The current implementation of the $SE(3)$ beam model geometry yields a significantly higher natural frequency for the torsional mode compared to that reported in [15]. This is due to the omission of the shear centre offsets in the geometry definition of the $SE(3)$ model, as previously discussed. A more accurate representation of the torsional mode, and its possible coupling with the first flapwise bending mode, could be achieved by including the shear centre offsets in the $SE(3)$ beam definition, or by creating a structural model with multiple chordwise beams along the wing's length to model wing ribs, and is reserved for future studies.

7.3 Box Wing Aircraft Structure

As a second test case, we consider an aircraft structure with a closed box wing configuration. The structure is inspired by the Prandtl plane design of a box wing aircraft, which has garnered some interest in recent years as a design concept for civil aircraft [73], [251]. Due to the closed wing structure, these configurations reduce the effect of tip vortices, which in turn reduces the total induced drag and increases aerodynamic efficiency. Structurally, these wings are characterised by high aspect ratios and are therefore extremely flexible. In addition, the joined-wing configuration results in geometric nonlinearity even under small deformations due to the doubly clamped configuration of the wings. Moreover, the multi-beam structure could lead to modal interactions between the elements, which require accurate modelling. Finally, the complex design of the full structure with various joined and split beams requires special attention to the kinematic relations between the connected elements. As demonstrated in previous chapters, the $SE(3)$ beam formulation is capable of accurately modelling large displacements and rotations of geometrically nonlinear structures. Moreover, as discussed in Chapter 3, the underlying local frame approach of the Lie group model leads to kinematically accurate descriptions of joints based on the Lie subgroups, with kinematic constraints effectively managed through the Lagrange multiplier method. The box wing structure therefore presents an ideal test case to showcase the effectiveness of the $SE(3)$ formulation in modelling flexible aircraft structures.

The design of the box wing structure is taken from the PRP250 Prandtl Plane concept [55] with some dimensional modifications. The structural model of the box wing aircraft is shown in Figure 7.6, and the coordinates of the nodes can be found in Appendix D. The dimensional modifications were made to make the natural frequencies of the structure near-commensurate and closely distributed, in order to encourage interactions between the modes. The fuselage length is 1 m and the wingspan is 0.97 m. Isotropic properties were defined for the entire structure, and the relevant constants are: EA $= 5.25 \times 10^6$ N, GA $= 2 \times 10^6$ N throughout the aircraft. Bending stiffness EI $= 10.9$ Nm^2 for the fuselage and vertical tail, and EI $= 2.19$ Nm^2 for the front and rear wings. Two configurations of the aircraft are studied: one with a fully clamped nose and the other with a free-floating structure.

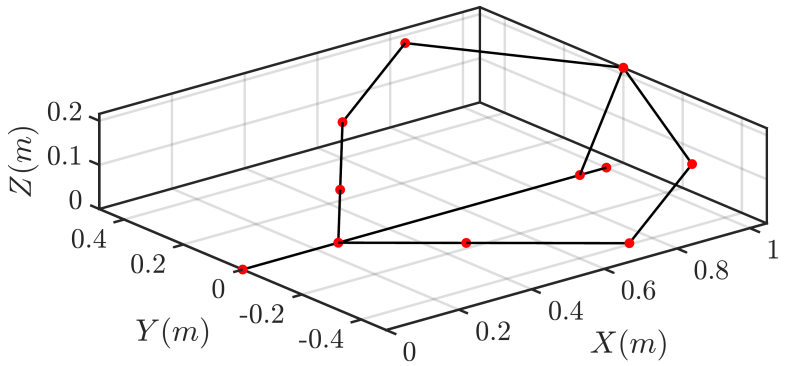


Figure 7.6: Geometry of box wing aircraft showing location of nodes before FE discretisation and connections between nodes. Nodal coordinates can be found in Appendix D.

7.3.1 Clamped Configuration

We first consider the aircraft with a fully clamped boundary condition on the fuselage nose, in line with other studies that have also investigated the dynamics of aircraft structures with a clamped nose configuration [161]. The full structure is discretised with 82 elements. The first 10 natural frequencies of the aircraft structure are given in Table 7.1. Figure 7.7 shows the static solution of the aircraft with constant uniform follower forces applied to the front and rear wings for a range of forcing levels.

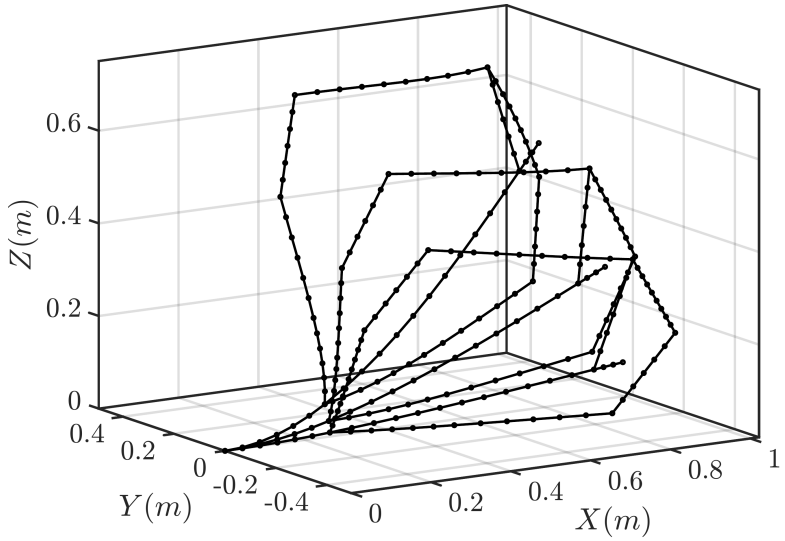


Figure 7.7: Static deformation of the box wing structure for follower distributed load on front and rear wings. Force levels equal 2.4, 9.6, and 21.6 N/m respectively.

Mode	1	2	3	4	5	6	7	8	9	10	11	12
ω_i (Hz)	2.07	2.19	3.43	7.62	13.97	14.96	21.81	24.99	25.22	31.49	35.37	40.32

Table 7.1: Natural frequencies of the first 12 modes of box wing aircraft with clamped nose.

The forced response of the box wing was computed using single shooting and pseudo-arclength continuation. To speed up calculations for this large system, the continuation equa-

tion in Eq. (2.6) was solved with a quasi-Newton method. The Jacobian was updated with Broyden's method, allowing it to be computed only once at each continuation step, thereby significantly reducing computational overhead. Using the notation

$$\begin{aligned} \Delta\boldsymbol{\psi}_j &= \boldsymbol{\psi}_j - \boldsymbol{\psi}_{j-1} \\ \Delta\mathbf{x}_j &= \mathbf{x}_j - \mathbf{x}_{j-1} \end{aligned} \tag{7.1}$$

Broyden's Jacobian update is given by

$$\mathbf{J}_j = \mathbf{J}_{j-1} + \frac{\Delta\boldsymbol{\psi}_j - \mathbf{J}_{j-1}\Delta\mathbf{x}_j}{\|\Delta\mathbf{x}_j\|^2}\Delta\mathbf{x}_j^T \tag{7.2}$$

where $\mathbf{x} = [\boldsymbol{X}(0)\ T]^T$ is the initial condition vector and initial period, $\boldsymbol{\psi}$ is the periodicity in Eq. (4.12), and the subscript j indicates the continuation step. It is noted that Broyden's method may be used with a Lie group formulation without any modification, as the initial condition vector contains twist increments and velocities, which are both elements of the Lie algebra $\mathfrak{se}(3)$, and may thus be subtracted in Euclidean space as in Eq. (7.1).

The FRC for mode 4 of the structure was computed for different forcing levels as depicted in Figure 7.8 and Figure 7.9. Mode 4 of the aircraft is symmetric about the XZ plane, and corresponds to the first mode of the structure where both the fuselage and front and rear wings undergo a first bending mode shape. Uniform distributed non-follower forcing was applied to the front and rear wings, and periodic solutions were computed. The strain-based damping coefficient was tuned to a damping value of 1% for the mode under consideration. Figure 7.8 shows the maximum absolute Z and X positions of the fuselage tail, over a single periodic response, and Figure 7.9 depicts the same for the rear right wing tip of the structure.

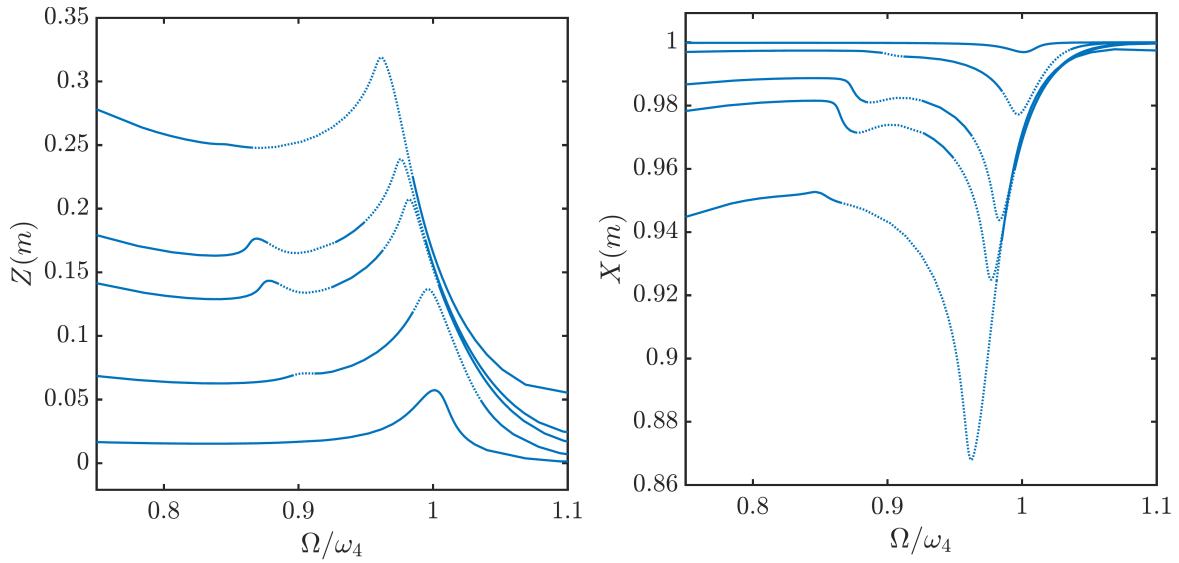


Figure 7.8: Frequency response curve of box wing for mode 4 showing maximum absolute vertical Z and longitudinal X position of fuselage tail, relative to undeformed structure. Forcing amplitudes are 2.4, 9.6, 19.2, 24, and 36 N/m respectively. Solid and dashed lines indicate stable and unstable solutions respectively.

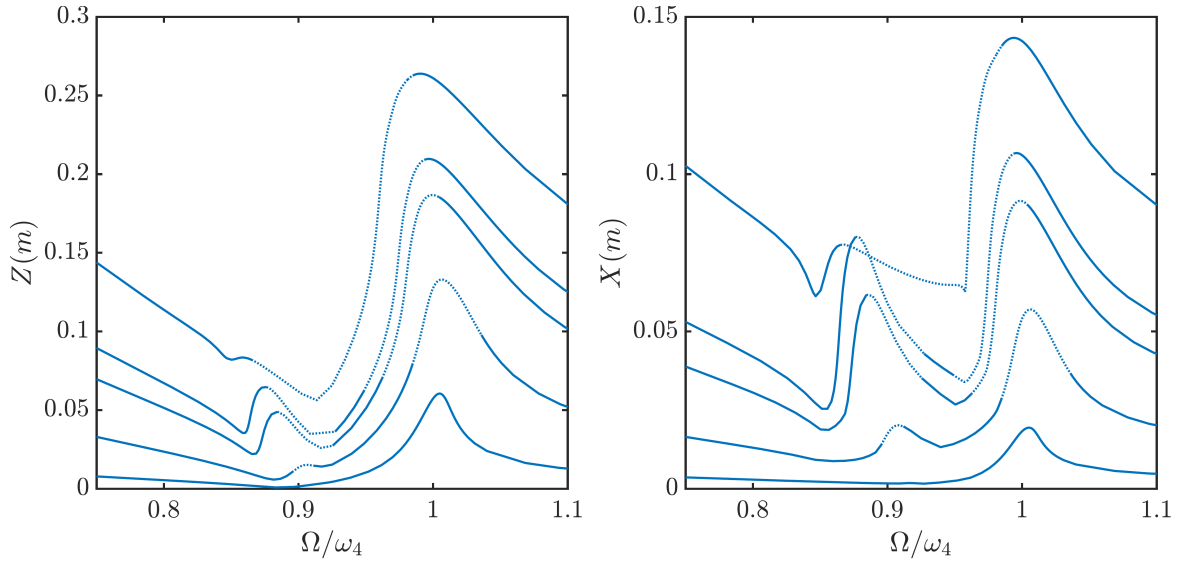


Figure 7.9: Frequency response curve of box wing for mode 4 showing maximum absolute vertical Z and longitudinal X position of rear right wing tip, relative to undeformed structure. Forcing amplitudes are 2.4, 9.6, 19.2, 24, and 36 N/m respectively. Solid and dashed lines indicate stable and unstable solutions respectively.

Several interesting nonlinear dynamics phenomena can be observed. It is seen from the FRCs that the aircraft exhibits softening behaviour, demonstrated by a slight shifting of the resonance peak to lower frequencies for higher forcing amplitudes. At lower forcing levels, the FRC shows a single peak at resonance corresponding to mode 4. As the forcing amplitude is increased, a secondary smaller peak appears at approximately $\Omega/\omega_4 = 0.9$ equal to 6.68 Hz, which also shifts to the left as the forcing amplitude is increased, in line with the softening behaviour of the structure. This peak is only manifested for the intermediary forcing amplitudes, and its magnitude diminishes at higher forcing levels. It corresponds to an internal resonance with other modes of the structure. MAC analysis was conducted using the linear eigenvectors of the system for FRC at a forcing amplitude of 24 N/m. The MAC quantifies the similarity between the deformation shape of the periodic solutions along the FRC branch and each linear eigenvector, as shown in Figure 7.10.

The presence of mode 12 in the forced response can be seen in the MAC plot at the frequency ratio of $\Omega/\omega_4 = 0.9$, corresponding to the location of the small resonance peak in Figures 7.8 and 7.9. The small FRC peak therefore corresponds to a 6:1 superharmonic internal resonance with mode 12, as the natural frequency of mode 12 is approximately 6 times the frequency of the peak at $\Omega/\omega_4 = 0.9$ equal to 6.68 Hz[1]. The MAC plot also shows the energy exchange between modes 4, 5, and 2 in the vicinity of the main resonance peak of the forced response.

Unstable periodic solutions are shown as dotted lines on the FRCs in Figures 7.8 and 7.9. Focusing on the FRC at a forcing amplitude of 24 N/m in Figure 7.8, the exchange of stability and bifurcations for this curve are illustrated in Figure 7.11. It is seen that a period-doubling bifurcation occurs shortly after the 6:1 small resonance peak, indicated by the crossing of

[1]Note the forced resonance peak of mode 12 will naturally shift from the linear eigenfrequency due to nonlinearity, and will be in an exact 6:1 ratio with the small resonance peak of mode 4.

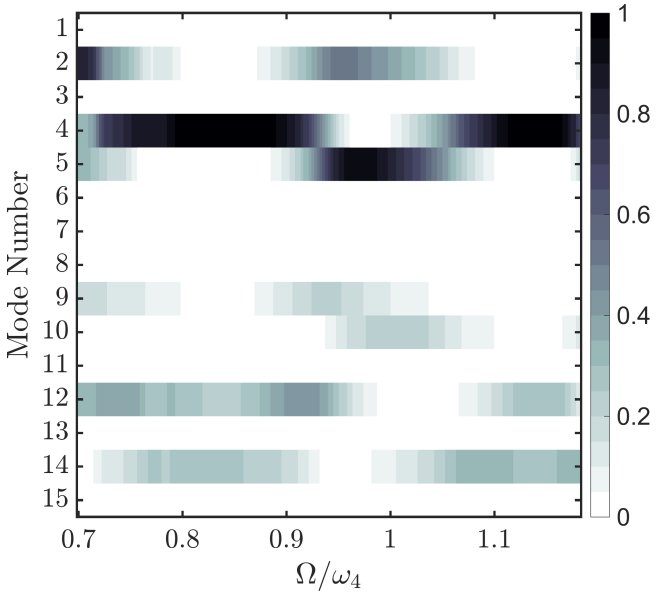


Figure 7.10: MAC plot of FRC at a forcing amplitude of 24 N/m in Figures 7.8 and 7.9, comparing solution initial conditions vector with linear eigenvectors of the system.

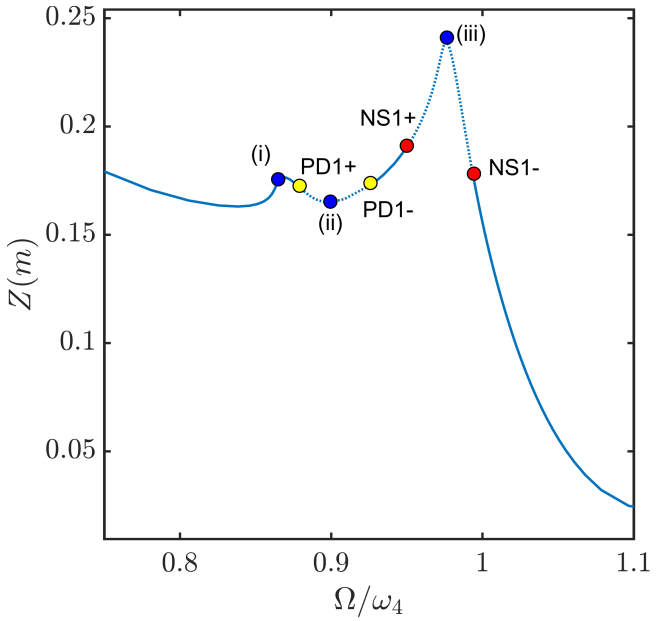
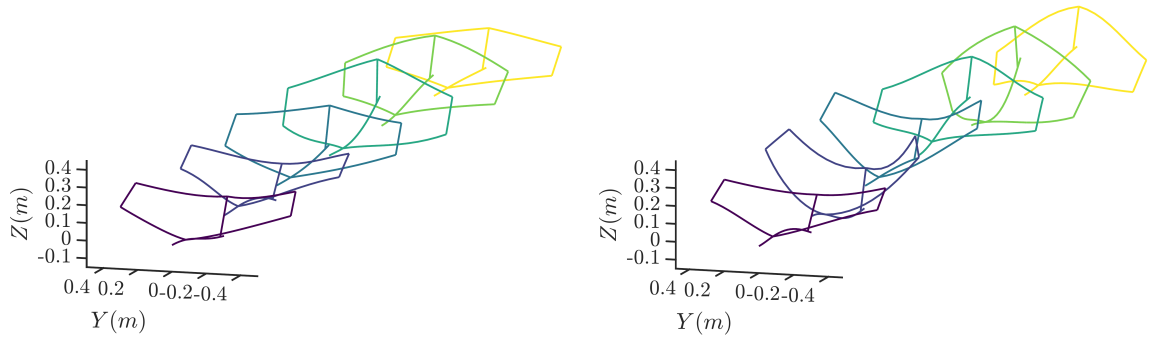


Figure 7.11: Bifurcations of FRC at a forcing amplitude of 24 N/m in Figure 7.8, showing maximum absolute vertical Z position of fuselage tail, relative to undeformed structure. Period doubling (PD) and Neimark-Sacker (NS) bifurcations shown, + indicates the corresponding eigenvalue leaving the unit circle, and - indicates the same eigenvalue returning inside the unit circle. Plots of aircraft shape at the two resonance peaks indicated by labels (i) and (iii) shown in Figure 7.12. Steady state times series of solution point labelled (ii) and (iii) shown in Figure 7.13 and Figure 7.14 respectively.

a Floquet multiplier through -1. The system briefly regains stability before losing it again through a Neimark-Sacker bifurcation before the main resonance peak. The system remains unstable throughout the resonance peak, and regains stability after the response starts falling back down. This behaviour is consistently observed across the FRCs corresponding to the other forcing amplitudes, with the stable region after the period-doubling bifurcation being wider at

lower forcing levels. Eventually, this region vanishes completely for the 36 N/m forcing level. On this curve, the unstable eigenvalue from the period-doubling bifurcation remains outside the unit circle as the Neimark-Sacker bifurcation occurs. The system therefore remains unstable after the single eigenvalue from the period doubling bifurcation returns to the circle, until the pair of eigenvalues from the Neimark-Sacker bifurcation also re-enter the unit circle further along the solution curve. The deformed aircraft shape through one period of oscillation at the solution points corresponding to both resonance peaks of the FRC is depicted in Figure 7.12.



(a) Solution at (i). (b) Solution at (iii).

Figure 7.12: Box wing aircraft deformation shape over one period of oscillation of FRC with amplitude 24 N/m in Figure 7.11. Snapshots distributed for clearer visualisation.

The results of the steady state time series simulations of the solution point labelled (ii) in Figure 7.11 is shown in Figure 7.13. The steady state Y and Z positions of the rear right wing tip over time are depicted, where the period doubling oscillations can be seen. An investigation of the shape of the aircraft over a single period of steady state oscillation shows the presence of mode 2 in the response, which also agrees with the MAC plot in Figure 7.10. This indicates the presence of a subharmonic interaction with mode 2 at a 1:3 ratio in the unstable period-doubling region.

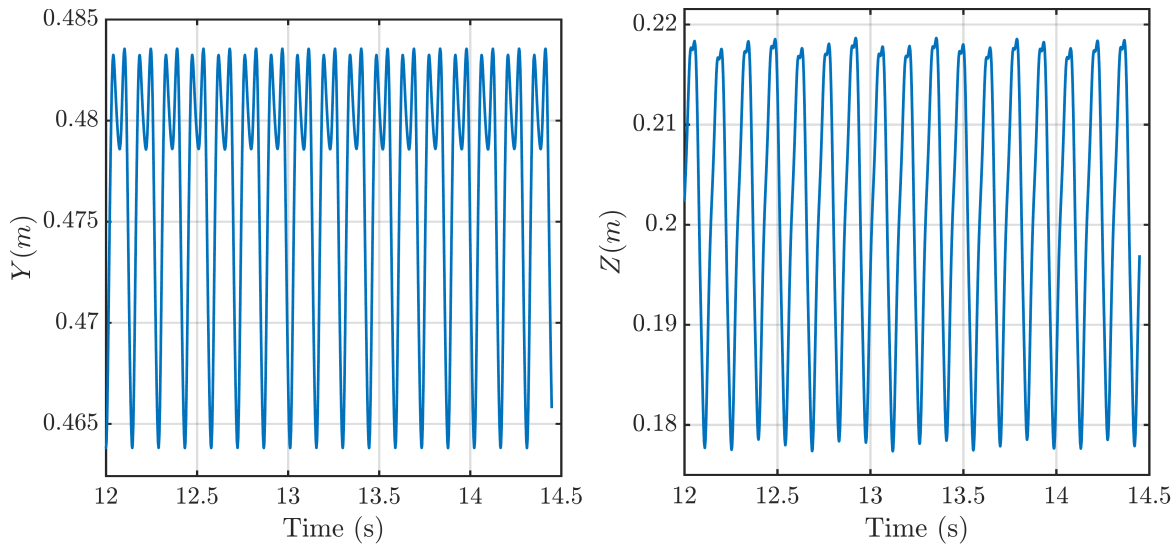


Figure 7.13: Box wing aircraft steady state response of point labelled (ii) in Figure 7.11. Absolute Y and Z positions of rear right wing tip shown, depicting double period oscillations.

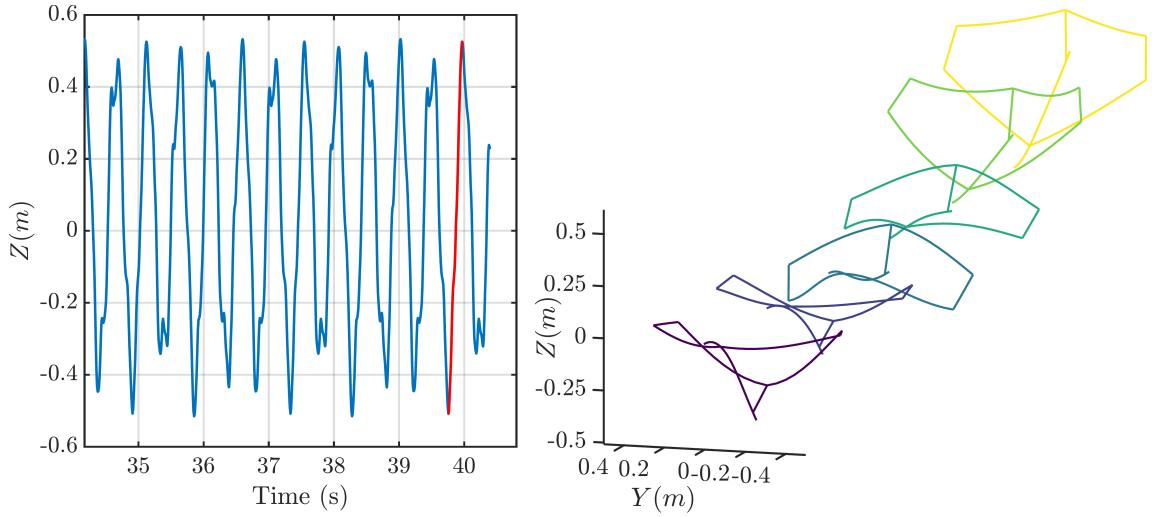


Figure 7.14: Box wing aircraft steady state response of point labelled (iii) in Figure 7.11. (a) shows absolute Z position of fuselage tail depicting quasi-periodic response. (b) shows deformed aircraft shape over the full range of oscillation of the steady state response (portion highlighted in red in (a)) Snapshots distributed for clearer visualisation.

The steady state response of the aircraft at the unstable solution labelled (iii) in the FRC in Figure 7.11 can be seen in Figure 7.14, along with the deformed aircraft shape over a full range of steady state oscillation. The quasi-periodic response associated with the Neimark-Sacker bifurcation of the unstable solution is seen. It is also observed that the response shows extremely large displacement of the fuselage, which is almost twice the amplitude of that of the FRC solution labelled (iii). The shape of the fuselage deformation is characteristically similar to the second bending mode of a cantilever at low amplitudes, which morphs into an extreme displacement similar to the first bending mode of a cantilever at high amplitudes. These translate to mode 5 and mode 2 of the full aircraft structure. The MAC plot in Figure 7.10 also confirms the presence of these modes in the response at point (iii), which is located at approximately $\Omega/\omega_4 = 0.98$. The motion of the fuselage is influenced by the inertia of the wings, causing extremely large steady state displacements which exceed the resonance peak of the FRC.

7.3.2 Free Configuration

As a second test case the aircraft is considered as a free-floating body with no boundary conditions on the nodes. The material properties of the aircraft remain the same. To aid with the convergence of the continuation solver auxiliary support elements were added to the structure, on which the aircraft is mounted. This was necessitated by the tendency of the continuation solver's Newton corrections in generating initial conditions that were excessively large not only in the rigid body displacements but also in other degrees of freedom. The support beam elements are placed in the XY plane, perpendicular to the fuselage, with two elements on either side of the fuselage nose and tail, resulting in a total of four support beams. These supports are connected to the nose and the tail node, and fully clamped at their free ends. The cross-sectional properties of the support elements are selected to ensure they offer

minimal resistance to bending and torsion, with values of EA = 10^4 N, GA = 3×10^{-2} N, and EI = 8×10^{-9} Nm^2. This ensures the effect of the supports on the natural frequencies of the deformation modes is minimised, such that the eigenvalues of the supported system are as close to possible to the fully free body. The natural frequencies of the first 12 modes of the true free floating aircraft and the supported aircraft are given in Table 7.2. Only 4 rigid body modes exist for the supported aircraft, as the axial stiffness of the support suppresses the rigid modes of translation along the Y axis and rotation about the Z axis. As a result, any potential coupling with these rigid modes will not be captured.

Mode	1	2	3	4	5	6	7	8	9	10	11	12
ω_i (Hz)	1×10^{-4}	1×10^{-4}	1×10^{-4}	2×10^{-4}	2×10^{-4}	3×10^{-4}	7.70	16.64	17.69	22.57	24.41	27.31
ω_i (Hz)	0.07	0.18	0.20	0.36	7.70	10.14	11.18	17.68	23.02	27.30	29.18	31.45

Table 7.2: Natural frequencies of the first 12 modes of box wing aircraft. Top row: free-free configuration, bottom row: free configuration with support beams on the XY plane.

The frequency response of the free aircraft was computed by prescribing a single harmonic single node load at the fuselage tip. The periodic solutions for a range of forcing frequencies were computed using shooting and pseudo-arclength continuation. Frequencies up to 20 Hz are considered, spanning the first 8 modes of the structure. Strain based damping was added to the model to give a damping coefficient of 1% for mode 6, which was kept constant throughout the continuation of the forced response solution. The computed FRCs for a non-follower external force of 20 N in the Z direction are shown in Figure 7.15, showing the maximum absolute vertical position of the rear right wing tip, relative to the undeformed structure, over a single oscillation. The MAC plot is also shown in Figure 7.17, which shows the presence of rigid body modes 2 and 4 in the response through the range of frequencies. A smaller contribution from mode 14 is also seen around the first resonant peak. The first peak corresponds to mode 5, and the second peak corresponds to mode 8 response. It is noted that the influence of the rigid body modes on the FRC may be reduced by performing a continuation downwards from the high frequency solutions, which is left for future investigation. The time history of the response over a single period of the solution for both peaks is shown as the shape of the deformed aircraft structure in Figure 7.18.

The forced response was also computed for a force applied at the nose and in the X direction, along the aircraft fuselage. This forcing also results in flapwise bending of the wings in the vertical direction. The FRC for a non-follower external force of 50 N in the X direction is shown in Figure 7.16, showing the maximum absolute vertical position of the rear right wing tip, relative to the undeformed structure, over a single oscillation. The MAC plot is also given in Figure 7.17, which shows the presence of rigid body mode 3 in the response through the range of frequencies. It is seen that the resonance peak around 17 Hz is smaller in amplitude compared to Figure 7.15, while the response is dominated by mode 8 in the vicinity of the peak.

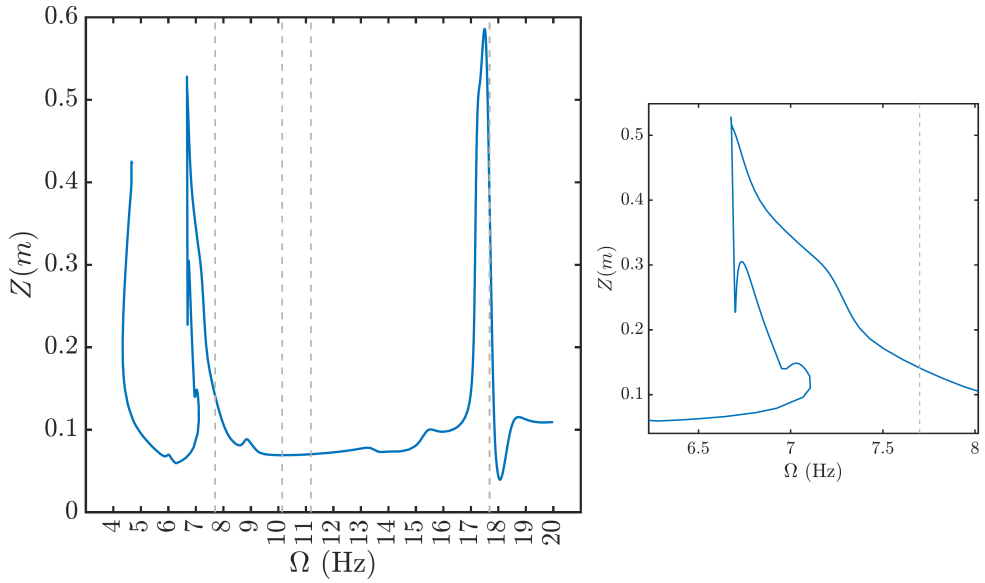


Figure 7.15: FRC of box wing aircraft in free configuration, depicting maximum absolute vertical position of the rear right wing tip, relative to the undeformed structure. (b) shows detail of first peak. Vertical lines correspond to locations of linear modes. Forcing amplitude of 20 N applied along Z axis at the aircraft nose.

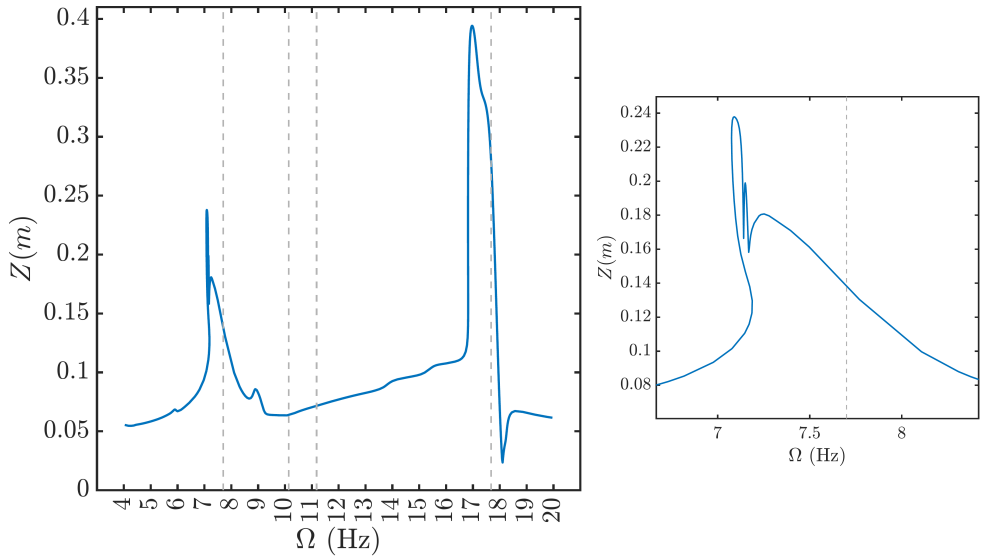


Figure 7.16: FRC of box wing aircraft in free configuration, depicting maximum absolute vertical position of the rear right wing tip, relative to the undeformed structure. (b) shows detail of first peak. Vertical lines correspond to locations of linear modes. Forcing amplitude of 50 N applied along X axis at the aircraft nose.

The time history of the response over a single period of the solution for both peaks is shown as the shape of the deformed aircraft structure in Figure 7.19.

As a final forcing case, a non-follower forcing was applied to the aircraft nose in the lateral direction along the Y axis, in order to excite the lateral bending modes, which were not captured in the previous responses. The support beams are now positioned on the XZ plane to allow for translation in the Y direction, while their material properties remain the same. The natural frequencies of the aircraft with the newly placed support beams are given in Table 7.3.

The FRC corresponding to a forcing amplitude of 5 N is shown in Figure 7.20, where the

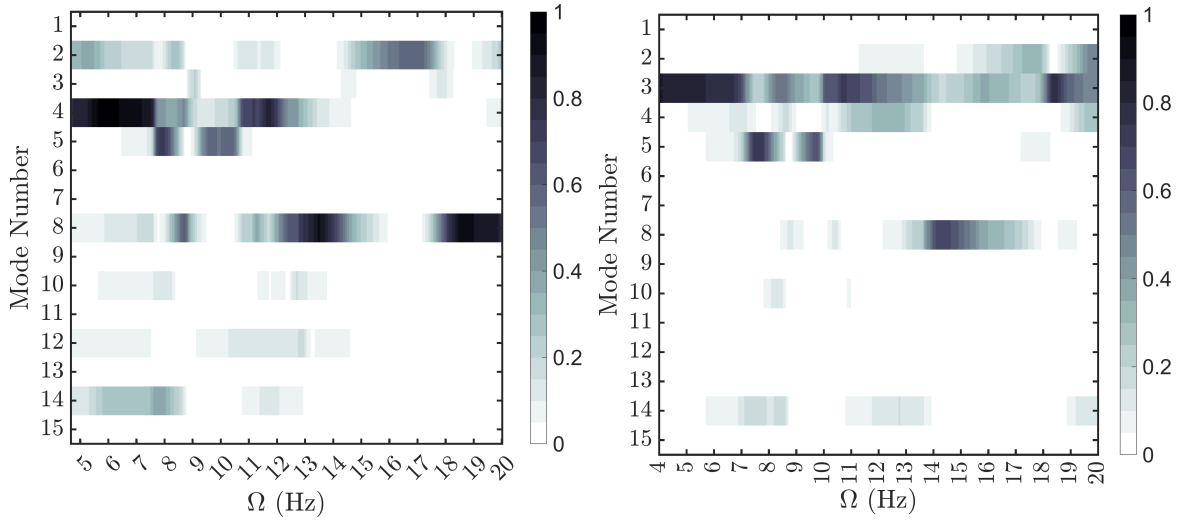
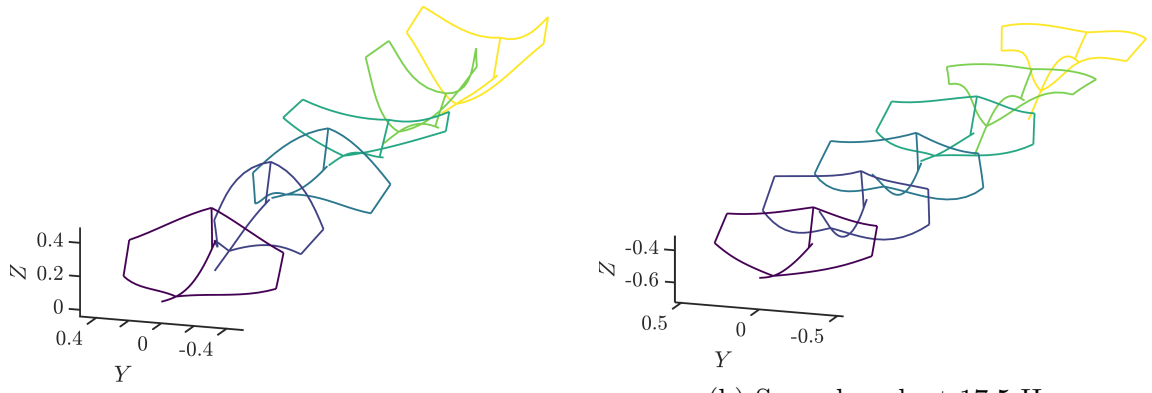


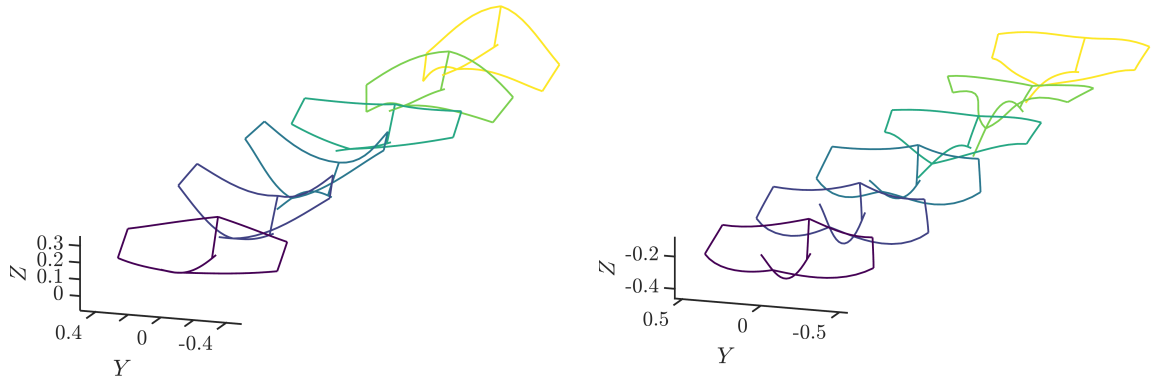
Figure 7.17: MAC of FRC comparing solution to linear eigenmodes. (a) Corresponds to Figure 7.15, and (b) to Figure 7.16 .



(a) First peak at 7 Hz.

(b) Second peak at 17.5 Hz.

Figure 7.18: Deformed aircraft shape over a single periodic motion corresponding to the peaks of the FRC in Figure 7.15.



(a) First peak at 7 Hz.

(b) Second peak at 17 Hz.

Figure 7.19: Deformed aircraft shape over a single periodic motion corresponding to the peaks of the FRC in Figure 7.16.

maximum absolute Z and Y positions of the fuselage tail and the rear right wing tip, relative to the undeformed structure, over a single oscillation period are illustrated. In order to compute

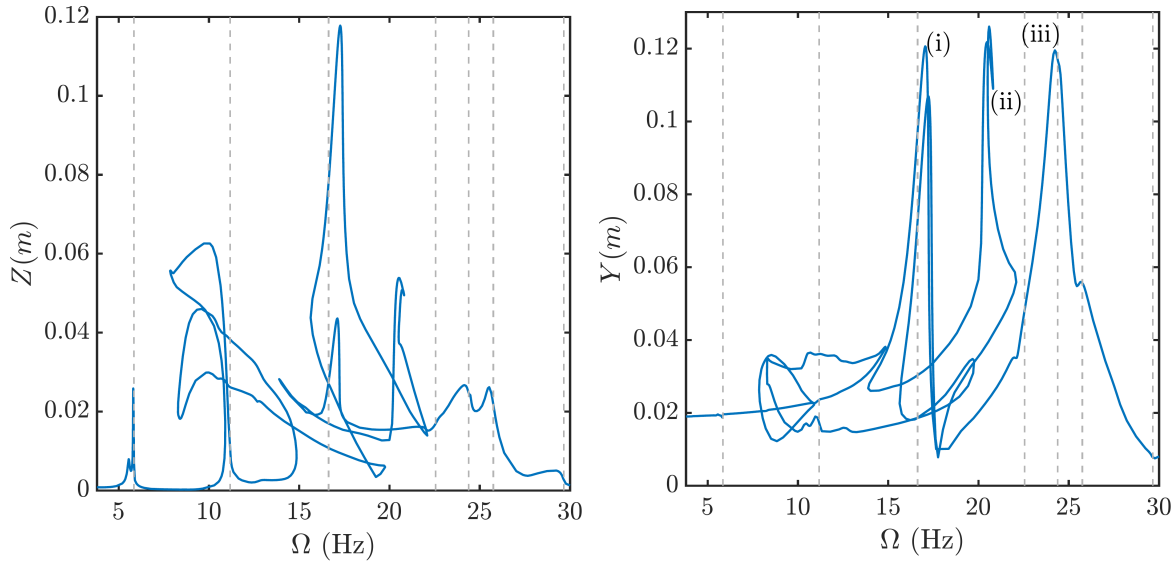
the absolute amplitudes for displaying the FRC for the lateral forcing, a rigid body transformation is first applied to the forced periodic solutions to bring the aircraft nose to the origin, and orient it with the global coordinate system. As the periodic solutions include rigid body motion of the aircraft with large rotations, applying the transformation enables the FRC amplitudes to be computed as deformations with reference to the undeformed configuration. The rigid body transformation can be applied very easily under the $SE(3)$ framework, by applying the composition of the inverse of the material frame at the fuselage nose to all the body-attached material frames of the structure.

Mode	1	2	3	4	5	6	7	8	9	10	11	12
ω_i (Hz)	0.07	0.19	0.20	0.28	5.85	11.18	16.63	22.56	24.39	25.75	29.66	34.98

Table 7.3: Natural frequencies of the first 12 modes of box wing aircraft in free configuration with support beams on the XZ plane.

The FRCs in Figure 7.20 reveal multiple resonance peaks and show coupling between the modes of the system. Due to the asymmetry of the box wing structure, the lateral forcing results in vertical and longitudinal motion, with the wings undergoing flapwise bending deformations. These can be also be seen in Figure 7.21 which shows the aircraft's motion over a single period of oscillation, corresponding to the solutions at the resonance peaks indicated in Figure 7.20. The presence of multiple loops and bent peaks in the FRC may be attributed to the influence of the support beams, which could have altered the dynamics of the structure. When large rigid body motions are present in the response, the support beams, though very flexible, still exert restoring force on the aircraft to pull it back towards its original position. This could potentially lead to broader and distorted peaks in the FRC. Other effects, such as the bending of the peak labelled (ii) in Figure 7.20, are likely nonlinear effects due to energy exchange between degrees of freedom of the system, to be investigated further.

An area of improvement would be to develop a more robust method for applying corrections to the starting point of the frequency response curve within the shooting and continuation routine. Currently, for free structures with no boundary conditions, the Newton iterations result in corrections to the initial condition vector that produce excessively large values, leading to significant rigid body motion and large deformations of the structure. This issue arises because the unrestricted nature of the rigid body motion allows the Newton iterations to converge to a large initial condition vector, which not only induces significant rigid body motion, but also leads to large deformations. As a result, the first continuation point often fails to converge. In this section, this problem was circumvented by introducing support elements to mount the aircraft, however, this approach is suboptimal, as evidenced by the emergence of large loops in the FRCs in Figure 7.20. A more effective solution would be to adapt the Newton solver to apply corrections that do not induce large rigid body motions, which could affect the other degrees of freedom. This could be achieved by either adding constrain equations to the problem or by redefining the initial conditions vector in terms of initial strains and velocities, as rigid



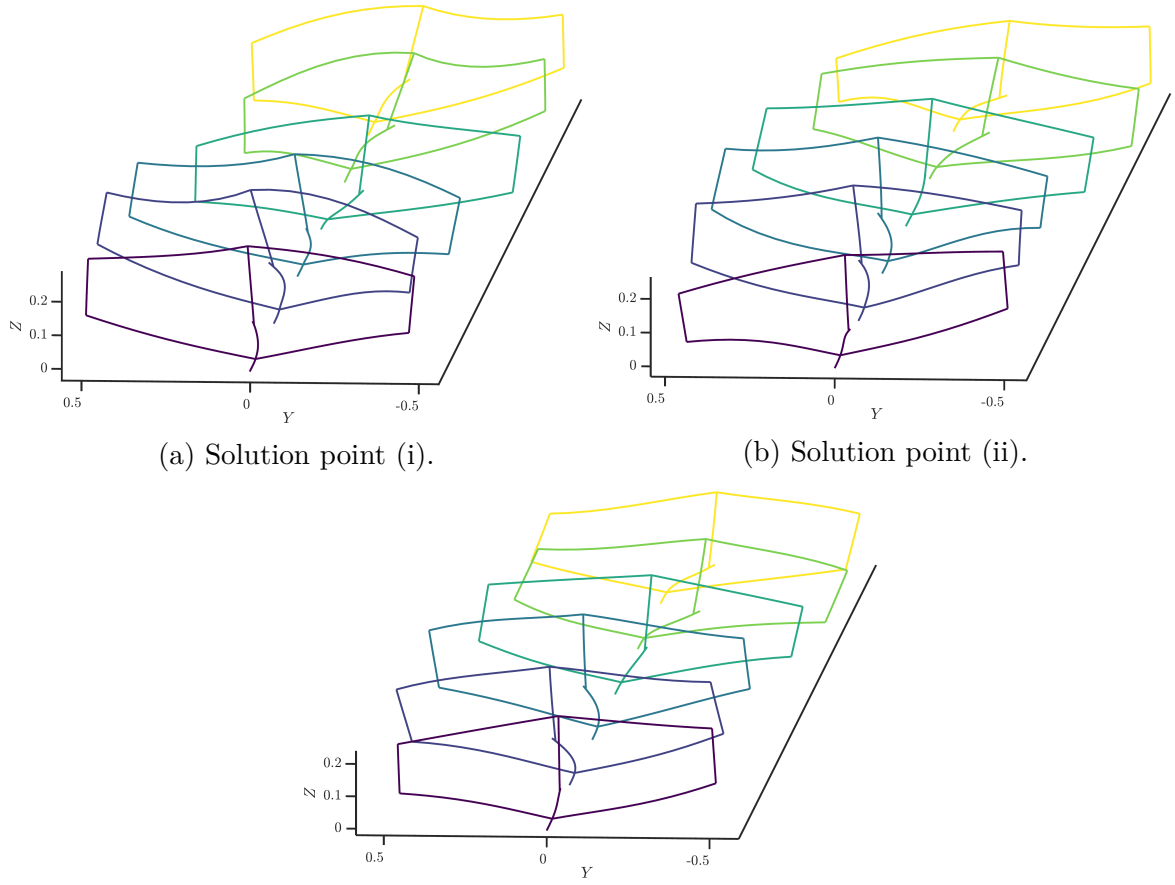
(a) Fuselage tail.

(b) Rear right wing tip.

Figure 7.20: FRC of box wing aircraft in free configuration, depicting maximum absolute vertical and lateral position of fuselage tail and rear right wing tip, relative to the undeformed structure. Forcing amplitude of 5 N applied along Y axis at the aircraft nose. Vertical lines correspond to locations of linear modes. Labels indicate solution points corresponding to the aircraft shapes in Figure 7.21.

body motions do not induce strains. This may be implemented easily on the $SE(3)$ formulation, as the beam equations of motion are in terms of strains and velocities, as discussed in Chapter 3. Alternatively, continuation could be performed on forcing amplitude instead of frequency, as is commonly done in computing S-curves. This would enable a solution curve at a low forcing frequency to be found for a range of forcing amplitudes, which could serve as initial conditions for frequency continuation for a range of fixed amplitudes. Developing such a method would be a significant improvement over the current approach and would offer additional functionality to the continuation code.

Regardless of altered dynamics of the system due to the support beams, the results for the box wing structure demonstrate the effectiveness of the $SE(3)$ formulation, combined with the shooting and pseudo-arclength continuation methods developed, in capturing large amplitude vibrations of complex structures, and in revealing complex nonlinear dynamics phenomena. Complementary studies are required to further explore the nonlinear dynamics of these complex structures, and pave the way for full aeroelastic analysis.



(a) Solution point (i).

(b) Solution point (ii).

(c) Solution point (iii).

Figure 7.21: FRC of box wing aircraft in free configuration, depicting maximum absolute vertical and lateral position fuselage tail and rear right wing tip, relative to the undeformed structure. Forcing amplitude of 5 N applied along Y axis at the aircraft nose. Rigid body transformation applied to the aircraft to move the nose to the origin. Labels indicate solution points corresponding to the aircraft shape in Figure 7.20.

7.4 Conclusion

In this chapter, we have explored the nonlinear dynamics of a high aspect ratio wing and a box wing aircraft modelled using the $SE(3)$ beam formulation. We have demonstrated that the $SE(3)$ formulation is able to effectively model the large displacements and rotations of very flexible structures which are commonly found in aeroelastic applications. Through the computation of forced responses using shooting and pseudo-arclength continuation, we have illustrated several nonlinear dynamics phenomena such as modal interactions and mode bifurcations. An additional benefit of the $SE(3)$ formulation in the effective implementation of joints and kinematic constraints enables the modelling of complex structures such as the box wing aircraft with multiple joints and split beam configurations. We have also discussed potential improvements which could be made to the continuation method to increase the robustness of modelling free-floating structures with rigid body motions.

The primary objective of this chapter was to showcase the suitability of the $SE(3)$ model for aeroelastic studies of highly flexible structures. To that end, the novel contribution of this

chapter lies in providing a preliminary study of the nonlinear dynamics of structures with potential aeroelastic applications. Laying the groundwork for future studies, the next steps would be to incorporate aerodynamic models and flight dynamics solvers to develop a comprehensive aeroelastic analysis tool. Aerodynamic methods such as unsteady strip theory or the Unsteady Vortex Lattice Method (UVLM) offer low to mid-fidelity tools for fluid flow, and have seen wide use in aeroelastic analysis [3], [160]. The $SE(3)$ model could be coupled with these aerodynamic solvers, in open source software packages such as SHARPy [45], or with higher fidelity flow solvers such as SU2 [65], to yield a robust tool for aeroelastic analysis of highly flexible structures.

Chapter 8

Conclusion

The primary objective of this thesis was to develop the theoretical and computational tools required to analyse vibrations of geometrically nonlinear structures formulated under the Lie group framework. Traditional methods in the analysis of nonlinear mechanical systems are built on linear vector spaces and, as such, cannot account for the nonlinear curved space of Lie group manifolds. To meet the aims of this thesis, state-of-the-art analysis methods in nonlinear dynamics were adapted to be compatible with the nonlinear configuration space of the Lie group models. To this end, in this thesis we have developed a shooting and pseudo-arclength continuation method for the computation of nonlinear normal modes and forced responses of geometrically nonlinear beams formulated on the Special Euclidean Lie group $SE(3)$. In order to make these methods compatible with the underlying Lie group formulation of the beam model, we have made adaptations to both the shooting and continuation algorithms and have demonstrated their effectiveness in computing periodic responses on a range of two and three dimensional geometrically nonlinear structures. We have further extended the simple shooting algorithm and developed a multiple shooting method suitable for use with Lie group models, which can be used for the analysis of large-scale dynamic systems.

The motivation for this work, as outlined in the Introduction, stems from the increasing need to accurately model and predict the complex nonlinear dynamic behaviour of flexible slender beams and geometrically nonlinear structures in industrial applications. Industries such as aerospace, automotive, and renewable energy, rely on precise simulation tools and accurate analysis methods for modelling the nonlinear behaviour of safety critical components. By developing a shooting and continuation method on Lie groups, we have made a significant and novel contribution to developing numerical methods, which enable highly accurate models such as the $SE(3)$ beam formulation, to be used in industrial design and analysis. This fills a critical gap in the current modelling capabilities available to industries, by creating a computational method for nonlinear vibration analysis of geometrically exact models formulated on Lie groups.

In Chapter 2, we reviewed the literature on nonlinear normal modes and geometrically exact beam models. We also developed the finite element equations of a nonlinear beam with von Kármán strains, which is used in subsequent chapters as a reference model in comparison with the $SE(3)$ beam. Following that, in Chapter 3 we presented a comprehensive introduction to

the theory of Lie groups, aiming to provide a clear and structured approach to explaining complex mathematical theory. This is followed by an in-depth introduction to the finite element formulation of the geometrically exact beam model on the $SE(3)$ Lie group. In Chapter 4, we developed the shooting and pseudo-arclength continuation methods with the necessary adaptations to enable their use on Lie group spaces. We demonstrated the effectiveness of this method in computing the nonlinear normal modes of a range of two-dimensional structures. The Lie group beam model was demonstrated to be able to accurately capture large rotations and displacements of a 2D cantilever beam, while the shooting and continuation methods were able to compute periodic solutions and capture interactions between the nonlinear modes of the structures. In Chapter 5 we developed a multiple shooting method for computing periodic responses on a 3D right-angled beam. Similarly to the standard shooting method, the multiple shooting method was also adapted to be used with the Lie group beam model. This adaptation involved formulating a suitable periodicity function on the Lie group which preserves the underlying nonlinear structure of the group. An alternative periodicity condition based on a global view of the problem was also presented and derived. We discussed the challenges of the multiple shooting method and motivated the need for future research to address these challenges. In Chapter 6 we extended the shooting and continuation methods to compute the forced responses of a range of nonlinear structures. We provided a discussion on the geometrically exact damping model used in the Lie group beam formulation, which preserves the invariance property of the beam model. We demonstrated the occurrence of internal resonances on a 3D cantilever beam, and discussed stability of periodic solutions in the context of bifurcation analysis. We demonstrated the effectiveness of the $SE(3)$ model in capturing large rotations and displacements of three-dimensional structures subject to large excitations. Finally, in Chapter 7, we applied the methods from previous chapters to test cases with aeroelastic relevance, including a high aspect ratio wing, and a box wing aircraft. We again showcased the suitability of the $SE(3)$ model in capturing large-amplitude motions of these structures which, due to their high aspect ratios, are increasingly flexible and thus prone to extreme oscillations. We have therefore met the main objective of this work in developing methods of nonlinear dynamic analysis that could be used with Lie group models, and we have laid the necessary foundational work on which future research efforts could be built.

Addressing the Research Questions

This thesis has aimed to address the following research questions, as outlined in the introduction. The answers are summarised below:

1. **How can numerical tools for nonlinear dynamic analysis be adapted to operate within the $SE(3)$ framework, enabling rigorous and efficient analysis of geometrically nonlinear structures with industrial relevance?**

   This thesis has demonstrated the adaptation of single and multiple shooting and pseudo-arclength continuation methods for use within the $SE(3)$ Lie group framework. These

adaptations ensure compatibility with the nonlinear configuration space of the $SE(3)$ manifold, and preserve the mathematical and geometric properties of the Lie group model. Local and global periodicity conditions, which adhere to the nonlinear configuration space of the Lie group, have been developed, and their sensitivities have been derived. These developments enable the rigorous analysis of periodic responses in geometrically nonlinear structures, including beams and aircraft models, formulated under the $SE(3)$ framework.

2. **To what extent does the $SE(3)$ formulation improve the modelling of nonlinear dynamic phenomena, such as large displacements, bifurcations, and modal interactions?**

   The formulation has been shown to accurately capture large-amplitude motions, including significant displacements and rotations, in both 2D and 3D geometrically nonlinear structures. Through its application in this thesis, and the adaptation of the numerical methods for nonlinear dynamic analysis, the $SE(3)$ model enabled the analysis of nonlinear normal modes and forced responses, capturing complex phenomena such as internal resonances, bifurcations, and modal interactions. Notably, the Lie group formulation facilitated the computation of beam motions with larger amplitudes and more complex dynamic phenomena than those previously reported in the literature, demonstrating an improvement in modelling capabilities.

Future Work

There exist two main directions for future work on the research conducted in this thesis. The first is the improvements which could be made to the methodologies presented and developed herein, and the second is related to more far-reaching and ambitious future goals, which could directly stem from this work.

Among the improvements which could be made we list the following:

- The continuation **phase condition** in computing nonlinear normal modes of conservative systems, as discussed in Chapter 4. In this work, we adopted a phase condition of velocities on all degrees of freedom as being zero. More advanced phase conditions, such as the integral and Poincaré conditions, need further adaptation to be used with Lie group models, which would constitute a valuable addition to the current approach.

- The **multiple shooting** method, as presented and discussed in Chapter 5 is currently unable to fully trace the full branch of periodic solutions for the right-angled beam. The challenges of the current implementation were discussed, which warrants further investigation in future work. These included the large dimensionality of the multiple shooting problem, robust strategies for continuation step size calculation and orthogonality condition, choice of relative increments in the prediction stage of the initial conditions, and the need for an accurate calculation of initial accelerations.

- A **global periodicity condition** was also developed and its advantages over the local periodicity condition were discussed. The global periodicity condition offers a fixed and consistent view of the periodicity. Additionally, the terms in the sensitivity of the global periodicity condition that are a result of the nonlinear configuration space of the Lie group vanish completely for a periodic solution. A numerical comparison between the two periodicity conditions and their effect on the computation of periodic solutions has not yet been undertaken and is left for future studies.

- A numerical study on the benefits of the **multiple shooting** method in terms of shorter computational time compared to the single shooting method, in addition to developing a fully **parallel implementation** of the multiple shooting algorithm, are also avenues worth exploring in the future. It is expected that the parallel multiple shooting method would require efficient management of computational memory, in addition to effective implementation of message passing on a parallel computing architecture. As a further benefit of the parallel multiple shooting method, the necessary parallel implementations could also be used in parallelisation of the continuation method as well, offering further computational advantages.

- The developed continuation method faces **stability issues** when used with models of free floating structures, such as the box wing aircraft presented in Chapter 7, and the vertical cantilever presented in Chapter 6. Improvements can be made to the continuation algorithm to encourage convergence on such structures which are characterised by having rigid body modes. These include adding constraints to the continuation equation to limit corrections to certain degrees of freedom, or formulating the initial conditions of the beam model in terms of initial strains and velocities.

In addition to the above, future research efforts could also focus on developing additional tools and more advanced analysis methods. Amongst these we list the following:

- Developing a Lie group specific **Harmonic Balance Method**. The harmonic balance method is a very popular tool in vibration analysis of nonlinear systems, and is well-suited to computing nonlinear modes of large scale systems exhibiting modal interactions. An incredibly powerful feature of this method is its ability to filter high frequencies through the selection of an appropriate number of harmonics. This addresses one of the main challenges of the shooting method, which, due to its inability to filter higher harmonics, leads to many interaction tongues being traced along the continuation path. However, the traditional harmonic balance method is not directly applicable to Lie group models, as the Fourier expansion on linear vector spaces is not a geometrically consistent operation on the Lie group framework. Future work could therefore be focused on developing a Lie group harmonic balance method, which could then be used for the analysis of more complex structures formulated on Lie groups.

- Exploration of geometrically exact **shell models**. Models of plates and shells have been developed on the $SE(3)$ framework for the analysis of flexible multibody dynamics [16]. The extension of the methods developed in this thesis to the analysis of shells would open up a range of possible applications, such as modelling fan blades, composites, and more accurate wing models. A significant challenge of this approach would be the increased dimensionality of the problems with a large number of degrees of freedom, which motivates the developments of reduced order models, as listed below.

- Further work could also be directed towards the efficient tracking of **bifurcations**, applying adaptations to make current methods compatible with the nonlinear Lie group space. In addition, effective **branch switching** methods could also be added to the current continuation code to offer greater functionality to the algorithm.

- **Model order reduction** methods such as modal derivatives, direct normal form, and spectral submanifolds, as discussed in Chapter 2, can also be adapted to be used with Lie group models. These are especially relevant for modelling large-scale systems, such as those with multiple beam configurations and shell elements. Although the computational efficiency of the $SE(3)$ method, such as the need for fewer finite elements, as discussed in Chapter 3, means these models take up less computational resources, the sheer scale of systems with large number of degrees of freedom necessitate the use of reduced order models. It is important that these reduced models preserve the underlying group structure, and are adapted to the nonlinear configuration space of the Lie group, so that they do not sacrifice mathematical rigour in the pursuit of better computational performance. It is envisaged that the quadratic nonlinearity of the $SE(3)$ beam formulation can be leveraged to efficiently reduce the dynamics with simple model reduction methods such as modal derivatives. Further simpler model reduction methods such as the Craig-Bampton method have been shown to be effective in $SE(3)$ floating frame formulations and corotational elements [192], [214], which can also be explored further.

- The extension of the $SE(3)$ beam and shell models to the **aeroelastic analysis** of aircraft structures, accounting for fluid-structure interactions and flight dynamics. Preliminary work on this area was conducted in Chapter 7, which needs to be developed further for full aeroelastic analysis of complex structures. This could also include addressing common challenges in computational fluid dynamics and fluid-structure interactions, such as mesh adaptation and refinement, handling of complex and interacting geometries, friction and contact nonlinearities, structural damping, and coupled thermal fluid-structure interaction.

Appendix A

Euler-Rodrigues Motion Parametrisation

The Euler-Rodrigues parametrisation of rotations is a vectorial parametrisation which offers a minimal set of three parameters to represent finite rotations [22], [23]. These are given by

$$\mathbf{p}_\theta = 2\boldsymbol{u}\sin\left(\frac{\theta}{2}\right) \in \mathbb{R}^3 \tag{A.1}$$

where $\boldsymbol{u}$ is a unit vector about which a rotation of magnitude θ takes place. In this formulation, $\mathbf{p}_\theta$ is a 3×1 vector which we shall term the rotation parameters. We also define the following parameter from $\mathbf{p}_\theta$

$$p_0 = \sqrt{1 - \frac{\mathbf{p}_\theta^T \mathbf{p}_\theta}{4}} = \cos\left(\frac{\theta}{2}\right) \tag{A.2}$$

The rotation parameters can be interpreted as the components of a unit quaternion $\mathbf{q}$ as

$$\mathbf{q} = \begin{bmatrix} p_0 \\ \frac{1}{2}\mathbf{p}_\theta \end{bmatrix} \in \mathbb{R}^4 \tag{A.3}$$

and they are closely related to Euler parameters as $e_0 = p_0$, and $\mathbf{e} = \frac{1}{2}\mathbf{p}$. Eq. (A.2) can be seen as a constraint equation which effectively sets the magnitude of the quaternion $\mathbf{q}$ to unity. Constraining the magnitude to unity therefore removes the dependence of the Euler parameters on e_0, enabling the representation of the rotation with the three Euler-Rodrigues parameters[1].

The axis-angle representation of $\boldsymbol{\omega} = \boldsymbol{u}\theta$ in Sections 3.2 and 3.3 may easily be converted to $\mathbf{p}_\theta$ using the sine of the half-angle and scaling by a factor of 2. As $\mathbf{p}_\theta$ is isomorphic to $\mathbb{R}^3$, we may still define $\widetilde{\mathbf{p}_\theta} \in \mathfrak{so}(3)$ as in Eq. (3.47).

The parameters $\mathbf{p}_\theta$ may be combined with translational parameters $\mathbf{p}_u$ to define the full motion parameters as

$$\boldsymbol{\mathcal{P}} = \begin{bmatrix} \mathbf{p}_u \\ \mathbf{p}_\theta \end{bmatrix} \in \mathbb{R}^6 \tag{A.4}$$

[1]For this reason, this parametrisation is sometimes termed the reduced Euler-Rodrigues parametrisation.

In this context, $\mathbf{p}_u$ is the same as the translational twist coordinates in Eq. (3.69), and we can write $\widetilde{\boldsymbol{\mathcal{P}}} \in \mathfrak{se}(3)$.

With the parametrisations in $\boldsymbol{\mathcal{P}}$, we first derive an expression for the exponential map on $SO(3)$ using the Euler-Rodrigues parameters $\mathbf{p}_\theta$. Recall from Eq. (3.49) that for the axis-angle representation $\boldsymbol{\omega} = \boldsymbol{u}\theta$ we have

$$\exp_{SO(3)}(\boldsymbol{\omega}) = \mathbf{I}_{3\times 3} + \left(\frac{\sin(\theta)}{\theta}\right)\widetilde{\boldsymbol{\omega}} + \left(\frac{1-\cos(\theta)}{\theta^2}\right)\widetilde{\boldsymbol{\omega}}^2 \tag{A.5}$$

which using $\boldsymbol{\omega} = \boldsymbol{u}\theta$ may be written as

$$\exp_{SO(3)}(\boldsymbol{\omega}) = \mathbf{I}_{3\times 3} + \sin(\theta)\widetilde{\boldsymbol{u}} + (1-\cos(\theta))\,\widetilde{\boldsymbol{u}}^2 \tag{A.6}$$

Using the sine and cosine double angle formulas, namely

$$\begin{aligned} \sin(\theta) &= 2\sin\left(\frac{\theta}{2}\right)\cos\left(\frac{\theta}{2}\right) \\ 1-\cos(\theta) &= 2\sin^2\left(\frac{\theta}{2}\right) \end{aligned} \tag{A.7}$$

the exponential can be written as

$$\exp_{SO(3)}(\boldsymbol{\omega}) = \mathbf{I}_{3\times 3} + 2\sin\left(\frac{\theta}{2}\right)\cos\left(\frac{\theta}{2}\right)\widetilde{\boldsymbol{u}} + 2\sin^2\left(\frac{\theta}{2}\right)\widetilde{\boldsymbol{u}}^2 \tag{A.8}$$

which using the parameters in Eq. (A.1) and Eq. (A.2) can be written as

$$\exp_{SO(3)}(\mathbf{p}_\theta) = \mathbf{I}_{3\times 3} + p_0\widetilde{\mathbf{p}_\theta} + \frac{1}{2}\widetilde{\mathbf{p}_\theta}\widetilde{\mathbf{p}_\theta} \tag{A.9}$$

which results in a rotation matrix. It is therefore evident that, with the Euler-Rodrigues rotation parameters, the expression for the exponential becomes increasingly simple, and all trigonometric terms are removed. Other equations on $SO(3)$ and $SE(3)$ can also be expressed in terms of the Euler-Rodrigues parameters, and can be derived in a similar way. Here we list some of the most important expressions which are used in this thesis.

The logarithm on $SO(3)$ which returns the Euler-Rodrigues rotation parameters from a rotation matrix $\mathbf{R}$ can be written as

$$\log_{SO(3)}(\mathbf{R}) = \frac{1}{\sqrt{\mathrm{tr}(\mathbf{R})+1}}\left(\mathbf{R}-\mathbf{R}^T\right)^\vee \tag{A.10}$$

The tangent operator and its inverse for the rotation parametrisation read

$$\mathbf{T}_{SO(3)}(\mathbf{p}_\theta) = \frac{1}{p_0}\mathbf{I}_{3\times 3} - \frac{1}{2}\widetilde{\mathbf{p}_\theta} + \frac{1}{4p_0}\widetilde{\mathbf{p}_\theta}\widetilde{\mathbf{p}_\theta} \tag{A.11}$$

$$\mathbf{T}^{-1}_{SO(3)}(\mathbf{p}_\theta) = p_0\mathbf{I}_{3\times 3} + \frac{1}{2}\widetilde{\mathbf{p}_\theta} \tag{A.12}$$

Finally, the directional derivative of the inverse tangent operator in the direction $\mathbf{v}_{3\times1} \in \mathbb{R}^3$ is

$$\mathrm{D}_{\mathbf{v}}\mathbf{T}^{-1}_{SO(3)}(\mathbf{p}_\theta) = -\frac{1}{2}\widetilde{\mathbf{v}} - \frac{1}{4p_0}\mathbf{v}\mathbf{p}_\theta^T \tag{A.13}$$

The following expressions can be listed for the motion parametrisation on $SE(3)$ where we have parameters $\boldsymbol{\mathcal{P}}$ from Eq. (A.4). The exponential map is given by

$$\exp_{SE(3)}(\boldsymbol{\mathcal{P}}) = \begin{bmatrix} \exp_{SO(3)}(\mathbf{p}_\theta) & \mathbf{T}^T_{SO(3)}(\mathbf{p}_\theta)\mathbf{p}_u \\ \mathbf{0}_{1\times3} & 1 \end{bmatrix} \tag{A.14}$$

The logarithm map which returns $\boldsymbol{\mathcal{P}}$ from an $SE(3)$ frame $\mathbf{H}$ is

$$\log_{SE(3)}(\mathbf{H}) = \begin{bmatrix} \mathbf{T}^{-T}_{SO(3)}(\mathbf{p}_\theta)\mathbf{x} \\ \log_{SO(3)}(\mathbf{R}) \end{bmatrix} \tag{A.15}$$

where $\mathbf{R}$ and $\mathbf{x}$ are the rotation matrix and position vector in $\mathbf{H}$ respectively, and $\mathbf{p}_\theta = \log_{SO(3)}(\mathbf{R})$.

The tangent operator and its inverse for the motion parametrisation are given by

$$\mathbf{T}_{SE(3)}(\boldsymbol{\mathcal{P}}) = \begin{bmatrix} \mathbf{T}_{SO(3)}(\mathbf{p}_\theta) & \mathbf{T}_+(\boldsymbol{\mathcal{P}}) \\ \mathbf{0}_{3\times3} & \mathbf{T}_{SO(3)}(\mathbf{p}_\theta) \end{bmatrix} \tag{A.16}$$

$$\mathbf{T}^{-1}_{SE(3)}(\boldsymbol{\mathcal{P}}) = \begin{bmatrix} \mathbf{T}^{-1}_{SO(3)}(\mathbf{p}_\theta) & \mathbf{T}_-(\boldsymbol{\mathcal{P}}) \\ \mathbf{0}_{3\times3} & \mathbf{T}^{-1}_{SO(3)}(\mathbf{p}_\theta) \end{bmatrix} \tag{A.17}$$

where

$$\mathbf{T}_+(\boldsymbol{\mathcal{P}}) = \frac{\rho}{4p_0^3}(\mathbf{I}_{3\times3} + \frac{1}{4}\widetilde{\mathbf{p}_\theta}\widetilde{\mathbf{p}_\theta}) - \frac{1}{2}\widetilde{\mathbf{p}_u} + \frac{1}{4p_0}(\widetilde{\mathbf{p}_\theta}\widetilde{\mathbf{p}_u} + \widetilde{\mathbf{p}_u}\widetilde{\mathbf{p}_\theta}) \tag{A.18}$$

$$\mathbf{T}_-(\boldsymbol{\mathcal{P}}) = \frac{-\rho}{4p_0}\mathbf{I}_{3\times3} + \frac{1}{2}\widetilde{\mathbf{p}_u} \tag{A.19}$$

and

$$\rho = \mathbf{p}_\theta^T\mathbf{p}_u \tag{A.20}$$

Finally, the directional derivative of the inverse tangent operator in the direction $\mathbf{v}_{6\times1} = [\mathbf{v}_u^T\ \mathbf{v}_\theta^T]^T \in \mathbb{R}^6$ is given by

$$\mathrm{D}_{\mathbf{v}}\mathbf{T}^{-1}_{SE(3)}(\boldsymbol{\mathcal{P}}) = \begin{bmatrix} \mathrm{D}_{\mathbf{v}_\theta}\mathbf{T}^{-1}_{SO(3)}(\mathbf{p}_\theta) & \mathrm{D}_{\mathbf{v}}\mathbf{T}^{-1}_-(\boldsymbol{\mathcal{P}}) \\ \mathbf{0}_{3\times3} & \mathrm{D}_{\mathbf{v}_\theta}\mathbf{T}^{-1}_{SO(3)}(\mathbf{p}_\theta) \end{bmatrix} \tag{A.21}$$

where

$$\mathrm{D}_{\mathbf{v}}\mathbf{T}^{-1}_-(\boldsymbol{\mathcal{P}}) = -\frac{1}{2}\widetilde{\mathbf{v}_u} - \frac{1}{4p_0}\left(\frac{\rho}{4p_0^2}\mathbf{v}_\theta\mathbf{p}_\theta^T + \mathbf{v}_\theta\mathbf{p}_u^T + \mathbf{v}_u\mathbf{p}_\theta^T\right) \tag{A.22}$$

Appendix B

Derivative of Joint Motion Frames

Consider a joint $\mathbf{H}_J$ belonging to a subgroup of $SE(3)$[1], written as the exponential of $\mathbf{n}$ as

$$\mathbf{H}_J = \exp_{SE(3)}(\mathbf{n}) = \exp_{SE(3)}(\mathbf{A}\mathbf{n}_j) \tag{B.1}$$

where $\mathbf{n}_j \in \mathbb{R}^l$ represents the relative joint coordinates corresponding to its degrees of freedom, and $\mathbf{A} \in \mathbb{R}^{6\times l}$ is a full-rank matrix whose columns form a basis for the Lie subalgebra associated with the joint's motion. Consider now the derivative of $\mathbf{H}_J$

$$\mathrm{d}(\mathbf{H}_J) = \mathbf{H}_J\widetilde{\mathbf{h}} = \mathbf{H}_J\widetilde{\mathbf{A}\mathbf{h}}_j \tag{B.2}$$

written using the left-invariant vector field $\mathbf{h}$. From Eq. (3.43), the derivative of $\mathbf{H}_J$, namely $\mathbf{h}$, can be related to $\mathbf{n}$ through the tangent operator written in vector form, as

$$\mathbf{h} = \mathbf{T}_{SE(3)}(\mathbf{n})\,\mathrm{d}(\mathbf{n}) \tag{B.3}$$

Using the relationships $\mathbf{n} = \mathbf{A}\mathbf{n}_j$ and $\mathbf{h} = \mathbf{A}\mathbf{h}_j$, the above can be written as

$$\mathbf{A}\mathbf{h}_j = \mathbf{T}_{SE(3)}(\mathbf{n})\mathbf{A}\,\mathrm{d}(\mathbf{n}_j) \tag{B.4}$$

For the abelian prismatic and revolute joints, it can be shown that $\mathbf{T}_{SE(3)}(\mathbf{n})\mathbf{A}$ reduces to $\mathbf{A}$. Therefore, the above can be written as

$$\mathbf{A}\mathbf{h}_j = \mathbf{A}\,\mathrm{d}(\mathbf{n}_j) \tag{B.5}$$

which, as $\mathbf{A}$ is full rank, can be simplified to give

$$\mathbf{h}_j = \mathrm{d}(\mathbf{n}_j) \tag{B.6}$$

Therefore, it is shown that $\mathbf{h}_j$, which is the left-invariant vector field resulting from the derivative of $\mathbf{H}_J$, is equal to the derivative of the vector of the exponentiated joint coordinates $\mathbf{n}_j$.

[1] Same applies to $SE(2)$.

Appendix C

Some Lie Group Identities and Relationships

C.1 Identity

The following identity holds for the tangent operator on any Lie group $\mathcal{G}$ with a Lie algebra $\mathfrak{g}$, for any $\mathbf{d}$ in $\mathfrak{g}$. Its proof may be found in [209].

$$\mathbf{T}^{-1}(-\mathbf{d}) - \mathbf{T}^{-1}(\mathbf{d}) + \widehat{\mathbf{d}} = \mathbf{0} \tag{C.1}$$

where the hat operator is derived from the adjoint (as given in Eq. (3.32)). The tangent operator may therefore be viewed as the series expansion of the adjoint map.

C.2 Identity

The following identity holds for any $\mathbf{d}$ in $\mathfrak{g}$. Its proof may be found in [209].

$$\mathrm{Ad}_{\exp(-\mathbf{d})} + \mathbf{T}(\mathbf{d})\left(\mathbf{T}^{-1}(\mathbf{d}) - \mathbf{T}^{-1}(-\mathbf{d})\right) = \mathbf{I} \tag{C.2}$$

C.3 Identity

The following identity holds for any $\mathcal{X}$ in $\mathcal{G}$ and $\mathbf{d}$ in $\mathfrak{g}$

$$\mathrm{Ad}_{\mathcal{X}}\mathbf{T}^{-1}(\mathbf{d})\mathrm{Ad}_{\mathcal{X}}^{-1} = \mathbf{T}^{-1}(\mathrm{Ad}_{\mathcal{X}}\mathbf{d}) \tag{C.3}$$

C.4 Derivative of the Adjoint

The derivative of the Adjoint map, as given in Eq. (3.23) can be evaluated as

$$\mathrm{dAd}_{\mathcal{X}}(\widetilde{\boldsymbol{\tau}}) = \mathrm{d}\left(\mathcal{X}\widetilde{\boldsymbol{\tau}}\mathcal{X}^{-1}\right) \tag{C.4}$$

Expanding the right hand side gives

$$\mathrm{dAd}_{\mathcal{X}}(\widetilde{\boldsymbol{\tau}}) = \left(\mathrm{d}\mathcal{X}\widetilde{\boldsymbol{\tau}}\mathcal{X}^{-1} + \mathcal{X}\,\mathrm{d}\widetilde{\boldsymbol{\tau}}\mathcal{X}^{-1} + \mathcal{X}\widetilde{\boldsymbol{\tau}}\,\mathrm{d}\mathcal{X}^{-1}\right) \tag{C.5}$$

Writing the derivatives of $\mathcal{X}$ and $\mathcal{X}^{-1}$ using the left-invariant vector field representation yields

$$\mathrm{dAd}_{\mathcal{X}}(\widetilde{\boldsymbol{\tau}}) = \left(\mathcal{X}\widetilde{\mathbf{x}}\widetilde{\boldsymbol{\tau}}\mathcal{X}^{-1} + \mathcal{X}\,\mathrm{d}\widetilde{\boldsymbol{\tau}}\mathcal{X}^{-1} - \mathcal{X}\widetilde{\boldsymbol{\tau}}\widetilde{\mathbf{x}}\mathcal{X}^{-1}\right) \tag{C.6}$$

The $\mathcal{X}$ and $\mathcal{X}^{-1}$ may now be factorised to give

$$\mathrm{dAd}_{\mathcal{X}}(\widetilde{\boldsymbol{\tau}}) = \mathcal{X}\left(\widetilde{\mathbf{x}}\widetilde{\boldsymbol{\tau}} + \mathrm{d}\widetilde{\boldsymbol{\tau}} - \widetilde{\boldsymbol{\tau}}\widetilde{\mathbf{x}}\right)\mathcal{X}^{-1} \tag{C.7}$$

which may be re-written using the Adjoint. The terms inside the parentheses represent the Lie bracket between $\widetilde{\mathbf{x}}$ and $\widetilde{\boldsymbol{\tau}}$, and may be also written using the adjoint map (Eq. (3.30)), to give

$$\mathrm{dAd}_{\mathcal{X}}(\widetilde{\boldsymbol{\tau}}) = \mathrm{Ad}_{\mathcal{X}}\left(\mathrm{d}\widetilde{\boldsymbol{\tau}} + \mathrm{ad}_{\widetilde{\mathbf{x}}}(\widetilde{\boldsymbol{\tau}})\right) \tag{C.8}$$

which may also be written in vector form as

$$\mathrm{dAd}_{\mathcal{X}}(\boldsymbol{\tau}) = \mathrm{Ad}_{\mathcal{X}}\left(\mathrm{d}\boldsymbol{\tau} + \mathrm{ad}_{\mathbf{x}}(\boldsymbol{\tau})\right) \tag{C.9}$$

or using the hat operator $\widehat{(\bullet)}$ in Eq. (3.32) as

$$\mathrm{dAd}_{\mathcal{X}}(\boldsymbol{\tau}) = \mathrm{Ad}_{\mathcal{X}}\left(\mathrm{d}\boldsymbol{\tau} + \widehat{\mathbf{x}}(\boldsymbol{\tau})\right) \tag{C.10}$$

Appendix D

Box Wing Aircraft Geometry Data

Table D.1: Coordinates and Directional Vectors for Nodes in the Box Wing Model

Label	X	Y	Z
Node Positions			
Node 0	0.000000	0.000000	0.000000
Node 1	0.262840	0.000000	0.000000
Node 2	0.927120	0.000000	0.000000
Node 3	1.000000	0.000000	0.000000
Node 4	0.441308	0.212690	0.018608
Node 5	0.441308	-0.212690	0.018608
Node 6	0.668856	0.483871	0.042333
Node 7	0.668856	-0.483871	0.042333
Node 8	0.841201	0.483871	0.181814
Node 9	0.841201	-0.483871	0.181814
Node 10	1.046592	0.000000	0.215650
Unit Vectors Along the Beams (Subscripts show nodal connections)			
U_{0-1}	1.000000	0.000000	0.000000
U_{1-4}	0.641349	0.764330	0.066870
U_{1-5}	0.641349	-0.764330	0.066870
U_{1-2}	1.000000	0.000000	0.000000
U_{4-6}	0.641349	0.764330	0.066870
U_{5-7}	0.641349	-0.764330	0.066870
U_{6-8}	0.777325	0.000000	0.629099
U_{7-9}	0.777325	0.000000	0.629099
U_{8-10}	0.389924	-0.918604	0.064235
U_{9-10}	0.389924	0.918604	0.064235
U_{2-10}	0.484609	0.000000	0.874731
U_{2-3}	1.000000	0.000000	0.000000
Unit Vectors Normal to the Beams (Subscripts show nodal connections)			
W_{0-1}	0.000000	1.000000	0.000000
W_{1-4}	-0.765249	0.643532	-0.016144
W_{1-5}	0.493931	0.478002	0.726324
W_{1-2}	0.000000	1.000000	0.000000
W_{4-6}	-0.765249	0.643532	-0.016144
W_{5-7}	0.493931	0.478002	0.726324
W_{6-8}	-0.100946	0.987042	0.124730
W_{7-9}	-0.266371	0.905935	0.329133
W_{8-10}	0.765467	0.362116	0.531914
W_{9-10}	-0.851101	0.332882	0.405977
W_{2-10}	-0.055651	0.997974	0.030831
W_{2-3}	0.000000	1.000000	0.000000

References

[1] Abbasbandy, S. and Hajiketabi, M., "A simple efficient and accurate new Lie–group shooting method for solving nonlinear boundary value problems," en, *International Journal of Nonlinear Analysis and Applications*, vol. 12, no. 1, Feb. 2021. DOI: 10.22075/ijnaa.2019.1543.1403.

[2] Abeloos, G., Renson, L., Collette, C., and Kerschen, G., "Stepped and swept control-based continuation using adaptive filtering," en, *Nonlinear Dynamics*, vol. 104, no. 4, pp. 3793–3808, Jun. 2021, ISSN: 0924-090X, 1573-269X. DOI: 10.1007/s11071-021-06506-z.

[3] Afonso, F., Vale, J., Oliveira, É., Lau, F., and Suleman, A., "A review on non-linear aeroelasticity of high aspect-ratio wings," en, *Progress in Aerospace Sciences*, vol. 89, pp. 40–57, Feb. 2017, ISSN: 03760421. DOI: 10.1016/j.paerosci.2016.12.004.

[4] Amabili, M., "Derivation of nonlinear damping from viscoelasticity in case of nonlinear vibrations," en, *Nonlinear Dynamics*, vol. 97, no. 3, pp. 1785–1797, Aug. 2019, ISSN: 0924-090X, 1573-269X. DOI: 10.1007/s11071-018-4312-0.

[5] Amabili, M., "Nonlinear damping in nonlinear vibrations of rectangular plates: Derivation from viscoelasticity and experimental validation," en, *Journal of the Mechanics and Physics of Solids*, vol. 118, pp. 275–292, Sep. 2018, ISSN: 00225096. DOI: 10.1016/j.jmps.2018.06.004.

[6] Apiwattanalunggarn, P., Shaw, S. W., Pierre, C., and Jiang, D., "Finite-Element-Based Nonlinear Modal Reduction of a Rotating Beam with Large-Amplitude Motion," en, *Journal of Vibration and Control*, vol. 9, no. 3-4, pp. 235–263, Mar. 2003, ISSN: 1077-5463, 1741-2986. DOI: 10.1177/107754603030751.

[7] Arnold, M., Brüls, O., and Cardona, A., "Error analysis of generalized-alpha Lie group time integration methods for constrained mechanical systems," en, *Numerische Mathematik*, vol. 129, no. 1, pp. 149–179, Jan. 2015, ISSN: 0029-599X, 0945-3245. DOI: 10.1007/s00211-014-0633-1.

[8] Arquier, R., Bellizzi, S., Bouc, R., and Cochelin, B., "Two methods for the computation of nonlinear modes of vibrating systems at large amplitudes," en, *Computers & Structures*, vol. 84, no. 24-25, pp. 1565–1576, Sep. 2006, ISSN: 00457949. DOI: 10.1016/j.compstruc.2006.01.011.

[9] Artola, M., Goizueta, N., Wynn, A., and Palacios, R., "Aeroelastic Control and Estimation with a Minimal Nonlinear Modal Description," en, *AIAA Journal*, vol. 59, no. 7, pp. 2697–2713, Jul. 2021, ISSN: 0001-1452, 1533-385X. DOI: 10.2514/1.J060018.

[10] Artola, M., Wynn, A., and Palacios, R., "A Nonlinear Modal-Based Framework for Low Computational Cost Optimal Control of 3D Very Flexible Structures," en, in *2019 18th European Control Conference (ECC)*, Naples, Italy: IEEE, Jun. 2019, pp. 3836–3841, ISBN: 978-3-907144-00-8. DOI: 10.23919/ECC.2019.8796151.

[11] Artola, M., Wynn, A., and Palacios, R., "Generalized KelvinVoigt Damping for Geometrically Nonlinear Beams," en, *AIAA Journal*, vol. 59, no. 1, pp. 356–365, Jan. 2021, ISSN: 0001-1452, 1533-385X. DOI: 10.2514/1.J059767.

[12] Artola, M., Wynn, A., and Palacios, R., "Modal-Based Nonlinear Model Predictive Control for 3-D Very Flexible Structures," en, *IEEE Transactions on Automatic Control*, vol. 67, no. 5, pp. 2145–2160, May 2022, ISSN: 0018-9286, 1558-2523, 2334-3303. DOI: 10.1109/TAC.2021.3071326.

[13] Avramov, K. V. and Mikhlin, Y. V., "Review of Applications of Nonlinear Normal Modes for Vibrating Mechanical Systems," en, *Applied Mechanics Reviews*, vol. 65, no. 2, p. 020 801, Mar. 2013, ISSN: 0003-6900, 2379-0407. DOI: 10.1115/1.4023533.

[14] Bagheri, A. K., Sonneville, V., and Renson, L., "Nonlinear normal modes of highly flexible beam structures modelled under the SE(3) Lie group framework," en, *Nonlinear Dynamics*, vol. 112, no. 3, pp. 1641–1659, Feb. 2024, ISSN: 0924-090X, 1573-269X. DOI: 10.1007/s11071-023-09106-1.

[15] Banneheka Navaratna, P. D., Pontillo, A., Rezgui, D., Lowenberg, M. H., Neild, S. A., and Cooper, J. E., "Design and assessment of subscale flexible high aspect ratio cantilever wings," in *AIAA SCITECH 2022 Forum*, American Institute of Aeronautics and Astronautics, Jan. 2022. DOI: 10.2514/6.2022-1305.

[16] Bauchau, O. and Sonneville, V., "Formulation of shell elements based on the motion formalism," *Applied Mechanics*, vol. 2, no. 4, pp. 1009–1036, Dec. 2021, ISSN: 2673-3161. DOI: 10.3390/applmech2040059.

[17] Bauchau, O. A., Betsch, P., Cardona, A., Gerstmayr, J., Jonker, B., Masarati, P., and Sonneville, V., "Validation of flexible multibody dynamics beam formulations using benchmark problems," en, *Multibody System Dynamics*, vol. 37, no. 1, pp. 29–48, May 2016, ISSN: 1384-5640, 1573-272X. DOI: 10.1007/s11044-016-9514-y.

[18] Bauchau, O. A., Han, S., Mikkola, A., and Matikainen, M. K., "Comparison of the absolute nodal coordinate and geometrically exact formulations for beams," en, *Multibody System Dynamics*, vol. 32, no. 1, pp. 67–85, Jun. 2014, ISSN: 1384-5640, 1573-272X. DOI: 10.1007/s11044-013-9374-7.

[19] Bauchau, O. A., Lao, Z., and Linn, J., "Formulations of Viscoelastic Constitutive Laws for Beams in Flexible Multibody Dynamics," en, in *Volume 6: 11th International Conference on Multibody Systems, Nonlinear Dynamics, and Control*, Boston, Massachusetts, USA: American Society of Mechanical Engineers, Aug. 2015, V006T10A032, ISBN: 978-0-7918-5716-8. DOI: 10.1115/DETC2015-47233.

[20] Bauchau, O. A. and Nemani, N., "Modeling viscoelastic behavior in flexible multibody systems," en, *Multibody System Dynamics*, vol. 51, no. 2, pp. 159–194, Feb. 2021, ISSN: 1384-5640, 1573-272X. DOI: 10.1007/s11044-020-09767-5.

[21] Bauchau, O. A. and Sonneville, V., "The Motion Formalism for Flexible Multibody Systems," en, *Journal of Computational and Nonlinear Dynamics*, vol. 17, no. 3, p. 030 801, Mar. 2022, ISSN: 1555-1415, 1555-1423. DOI: 10.1115/1.4053148.

[22] Bauchau, O. A. and Trainelli, L., "The Vectorial Parameterization of Rotation," *Nonlinear Dynamics*, vol. 32, no. 1, pp. 71–92, 2003, ISSN: 0924-090X. DOI: 10.1023/a:1024265401576.

[23] Bauchau, O. A., *Flexible multibody dynamics* (Solid mechanics and its applications 176), eng. Dordrecht Heidelberg: Springer, 2011, ISBN: 978-94-007-0334-6.

[24] Behdinan, K., Stylianou, M., and Tabarrok, B., "Co-rotational dynamic analysis of flexible beams," en, *Computer Methods in Applied Mechanics and Engineering*, vol. 154, no. 3-4, pp. 151–161, Mar. 1998, ISSN: 00457825. DOI: 10.1016/S0045-7825(97)00124-2.

[25] Bekhoucha, F., Rechak, S., Duigou, L., and Cadou, J.-M., "Nonlinear forced vibrations of rotating anisotropic beams," en, *Nonlinear Dynamics*, vol. 74, no. 4, pp. 1281–1296, Dec. 2013, ISSN: 0924-090X, 1573-269X. DOI: 10.1007/s11071-013-1040-3.

[26] Belytschko, T., Liu, W. K., Moran, B., and Elkhodary, K. I., *Nonlinear finite elements for continua and structures*, Second edition. Chichester, West Sussex, United Kingdon: Wiley, 2014, ISBN: 978-1-118-63270-3.

[27] Betsch, P. and Steinmann, P., "Frame-indifferent beam finite elements based upon the geometrically exact beam theory," *International Journal for Numerical Methods in Engineering*, vol. 54, pp. 1775–1788, 12 Aug. 2002, ISSN: 0029-5981. DOI: 10.1002/nme.487.

[28] Beyn, W.-J., Champneys, A., Doedel, E., Govaerts, W., Kuznetsov, Y. A., and Sandstede, B., "Numerical Continuation, and Computation of Normal Forms," en, in *Handbook of Dynamical Systems*, vol. 2, Elsevier, 2002, pp. 149–219, ISBN: 978-0-444-50168-4. DOI: 10.1016/S1874-575X(02)80025-X.

[29] Bidhendi, M. R. T., "Nonlinear dynamics of a cantilevered beam with a tip mass and elastic-damping support," en, *International Journal of Non-Linear Mechanics*, vol. 125, p. 103 541, Oct. 2020, ISSN: 00207462. DOI: 10.1016/j.ijnonlinmec.2020.103541.

[30] Bilbao, S., Thomas, O., Touzé, C., and Ducceschi, M., "Conservative numerical methods for the Full von Kármán plate equations," en, *Numerical Methods for Partial Differential Equations*, vol. 31, no. 6, pp. 1948–1970, Nov. 2015, ISSN: 0749-159X, 1098-2426. DOI: 10.1002/num.21974.

[31] Bock, H. and Plitt, K., "A Multiple Shooting Algorithm for Direct Solution of Optimal Control Problems *," en, *IFAC Proceedings Volumes*, vol. 17, no. 2, pp. 1603–1608, Jul. 1984, ISSN: 14746670. DOI: 10.1016/S1474-6670(17)61205-9.

[32] Bock, H. G., Kostina, E., and Schlöder, J. P., "Numerical Methods for Parameter Estimation in Nonlinear Differential Algebraic Equations," en, *GAMM-Mitteilungen*, vol. 30, no. 2, pp. 376–408, Aug. 2007, ISSN: 09367195, 15222608. DOI: 10.1002/gamm.200790024.

[33] Borst, R. d. and Crisfield, M. A., Eds., *Nonlinear finite element analysis of solids and structures*, 2nd ed. Hoboken, NJ: Wiley, 2012, ISBN: 978-0-470-66644-9.

[34] Boyer, F., Gotelli, A., Tempel, P., Lebastard, V., Renda, F., and Briot, S., "Implicit Time-Integration Simulation of Robots With Rigid Bodies and Cosserat Rods Based on a NewtonEuler Recursive Algorithm," en, *IEEE Transactions on Robotics*, vol. 40, pp. 677–696, 2024, ISSN: 1552-3098, 1941-0468. DOI: 10.1109/TRO.2023.3334647.

[35] Brockett, R. W., "Robotic manipulators and the product of exponentials formula," in *Mathematical Theory of Networks and Systems*. Springer-Verlag, pp. 120–129, ISBN: 354013168X. DOI: 10.1007/bfb0031048.

[36] Brüls, O., Arnold, M., and Cardona, A., "Two Lie Group Formulations for Dynamic Multibody Systems With Large Rotations," en, in *Volume 4: 8th International Conference on Multibody Systems, Nonlinear Dynamics, and Control, Parts A and B*, Washington, DC, USA: ASMEDC, Jan. 2011, pp. 85–94, ISBN: 978-0-7918-5481-5. DOI: 10.1115/DETC2011-48132.

[37] Brüls, O. and Cardona, A., "On the Use of Lie Group Time Integrators in Multibody Dynamics," en, *Journal of Computational and Nonlinear Dynamics*, vol. 5, no. 3, p. 031 002, Jul. 2010, ISSN: 1555-1415, 1555-1423. DOI: 10.1115/1.4001370.

[38] Brüls, O., Cardona, A., and Arnold, M., "Lie group generalized-alpha time integration of constrained flexible multibody systems," en, *Mechanism and Machine Theory*, vol. 48, pp. 121–137, Feb. 2012, ISSN: 0094114X. DOI: 10.1016/j.mechmachtheory.2011.07.017.

[39] Brüls, O. and Eberhard, P., "Sensitivity analysis for dynamic mechanical systems with finite rotations," en, *International Journal for Numerical Methods in Engineering*, vol. 74, no. 13, pp. 1897–1927, Jun. 2008, ISSN: 0029-5981, 1097-0207. DOI: 10.1002/nme.2232.

[40] Burger, L., Dörlich, V., Burger, M., Linn, J., and Schneider, F., "Estimation of cable bundle stiffness based on gaussian process regression," in *Progress in Industrial Mathematics at ECMI 2021*. Springer International Publishing, 2022, pp. 329–335, ISBN: 9783031118180. DOI: 10.1007/978-3-031-11818-0_43.

[41] Butikov, E. I., "Subharmonic resonances of the parametrically driven pendulum," en, *Journal of Physics A: Mathematical and General*, vol. 35, no. 30, pp. 6209–6231, Aug. 2002, ISSN: 03054470. DOI: 10.1088/0305-4470/35/30/301.

[42] Calderon, D. E., Cooper, J. E., Lowenberg, M., Neild, S. A., and Coetzee, E. B., "Sizing high-aspect-ratio wings with a geometrically nonlinear beam model," *Journal of Aircraft*, vol. 56, no. 4, pp. 1455–1470, Jul. 2019, ISSN: 1533-3868. DOI: 10.2514/1.c035296.

[43] Callejo, A., Sonneville, V., and Bauchau, O. A., "Discrete Adjoint Method for the Sensitivity Analysis of Flexible Multibody Systems," en, *Journal of Computational and Nonlinear Dynamics*, vol. 14, no. 2, p. 021 001, Feb. 2019, ISSN: 1555-1415, 1555-1423. DOI: 10.1115/1.4041237.

[44] Cardona, A. and Geradin, M., "A beam finite element non-linear theory with finite rotations," en, *International Journal for Numerical Methods in Engineering*, vol. 26, no. 11, pp. 2403–2438, Nov. 1988, ISSN: 0029-5981, 1097-0207. DOI: 10.1002/nme.1620261105.

[45] Carre, A. del, Muñoz-Simón, A., Goizueta, N., and Palacios, R., "Sharpy: A dynamic aeroelastic simulation toolbox for very flexible aircraft and wind turbines," *Journal of Open Source Software*, vol. 4, no. 44, p. 1885, Dec. 2019, ISSN: 2475-9066. DOI: 10.21105/joss.01885.

[46] Cebeci, T. and Keller, H. B., "Shooting and parallel shooting methods for solving the Falkner-Skan boundary-layer equation," en, *Journal of Computational Physics*, vol. 7, no. 2, pp. 289–300, Apr. 1971, ISSN: 00219991. DOI: 10.1016/0021-9991(71)90090-8.

[47] earek, P., Saje, M., and Zupan, D., "Kinematically exact curved and twisted strain-based beam," en, *International Journal of Solids and Structures*, vol. 49, no. 13, pp. 1802–1817, Jun. 2012, ISSN: 00207683. DOI: 10.1016/j.ijsolstr.2012.03.033.

[48] Cesnik, C. and Brown, E., "Modeling of high aspect ratio active flexible wings for roll control," in *43rd AIAA/ASME/ASCE/AHS/ASC Structures, Structural Dynamics, and Materials Conference*, American Institute of Aeronautics and Astronautics, Apr. 2002. DOI: 10.2514/6.2002-1719.

[49] Chan, T. F. C. and Keller, H. B., "Arc-length continuation and multigrid techniques for nonlinear elliptic eigenvalue problems," *SIAM Journal on Scientific and Statistical Computing*, vol. 3, pp. 173–194, 2 Jun. 1982, ISSN: 0196-5204. DOI: 10.1137/0903012.

[50] Chevallier, D., "Lie algebras, modules, dual quaternions and algebraic methods in kinematics," *Mechanism and Machine Theory*, vol. 26, no. 6, pp. 613–627, Jan. 1991, ISSN: 0094-114X. DOI: 10.1016/0094-114x(91)90043-4.

[51] Cho, H., Jeong, B., Yu, M.-F., Vakakis, A. F., McFarland, D. M., and Bergman, L. A., "Nonlinear hardening and softening resonances in micromechanical cantilever-nanotube systems originated from nanoscale geometric nonlinearities," *International Journal of Solids and Structures*, vol. 49, no. 1516, pp. 2059–2065, Aug. 2012, ISSN: 0020-7683. DOI: 10.1016/j.ijsolstr.2012.04.016.

[52] Cook, R. G., Calderon, D. E., Cooper, J. E., Lowenberg, M. H., and Neild, S. A., "Industrially Inspired Gust Loads Analysis of Various-Aspect-Ratio Wings Featuring Geometric Nonlinearity," en, *Journal of Aircraft*, vol. 57, no. 1, pp. 13–28, Jan. 2020, ISSN: 1533-3868. DOI: 10.2514/1.C035294.

[53] Cottanceau, E., Thomas, O., Véron, P., Alochet, M., and Deligny, R., "A finite element/quaternion/asymptotic numerical method for the 3D simulation of flexible cables," en, *Finite Elements in Analysis and Design*, vol. 139, pp. 14–34, Feb. 2018, ISSN: 0168874X. DOI: 10.1016/j.finel.2017.10.002.

[54] Crisfield, M. A. and Jeleni; G., "Objectivity of strain measures in the geometrically exact three-dimensional beam theory and its finite-element implementation," en, *Proceedings of the Royal Society of London. Series A: Mathematical, Physical and Engineering Sciences*, vol. 455, no. 1983, pp. 1125–1147, Mar. 1999, ISSN: 1364-5021, 1471-2946. DOI: 10.1098/rspa.1999.0352.

[55] Dal Canto, D., Frediani, A., Ghiringhelli, G. L., and Terraneo, M., "The lifting system of a prandtlplane, part 1: Design and analysis of a light alloy structural solution," in *Variational Analysis and Aerospace Engineering: Mathematical Challenges for Aerospace Design*. Springer US, 2012, pp. 211–234, ISBN: 9781461424352. DOI: 10.1007/978-1-4614-2435-2_9.

[56] Debeurre, M., "Nonlinear dynamics of highly flexible slender beams : Efficient numerical strategies in the frequency domain," Ph.D. dissertation, 2023.

[57] Debeurre, M., Benacchio, S., Grolet, A., Grenat, C., Giraud-Audine, C., and Thomas, O., "Phase resonance testing of highly flexible structures: Measurement of conservative nonlinear modes and nonlinear damping identification," en, *Mechanical Systems and Signal Processing*, vol. 215, p. 111 423, Jun. 2024, ISSN: 08883270. DOI: 10.1016/j.ymssp.2024.111423.

[58] Debeurre, M., Grolet, A., Cochelin, B., and Thomas, O., "Finite element computation of nonlinear modes and frequency response of geometrically exact beam structures," *Journal of Sound and Vibration*, vol. 548, Mar. 2023, ISSN: 10958568. DOI: 10.1016/j.jsv.2022.117534.

[59] Debeurre, M., Grolet, A., and Thomas, O., "Quaternion-based finite-element computation of nonlinear modes and frequency responses of geometrically exact beam structures in three dimensions," en, *Multibody System Dynamics*, Jun. 2024, ISSN: 1384-5640, 1573-272X. DOI: 10.1007/s11044-024-09999-9.

[60] Denis, V., Jossic, M., Giraud-Audine, C., Chomette, B., Renault, A., and Thomas, O., "Identification of nonlinear modes using phase-locked-loop experimental continuation and normal form," en, *Mechanical Systems and Signal Processing*, vol. 106, pp. 430–452, Jun. 2018, ISSN: 08883270. DOI: 10.1016/j.ymssp.2018.01.014.

[61] Detroux, T., Noël, J.-P., Virgin, L. N., and Kerschen, G., "Experimental study of isolas in nonlinear systems featuring modal interactions," en, *PLOS ONE*, vol. 13, no. 3, Garikipati, K., Ed., e0194452, Mar. 2018, ISSN: 1932-6203. DOI: 10.1371/journal.pone.0194452.

[62] Detroux, T., Renson, L., Masset, L., and Kerschen, G., "The harmonic balance method for bifurcation analysis of large-scale nonlinear mechanical systems," en, *Computer Methods in Applied Mechanics and Engineering*, vol. 296, pp. 18–38, Nov. 2015, ISSN: 00457825. DOI: 10.1016/j.cma.2015.07.017.

[63] Doedel, E. J., "Lecture notes on numerical analysis of nonlinear equations," in *Numerical Continuation Methods for Dynamical Systems: Path following and boundary value problems*, Krauskopf, B., Osinga, H. M., and Galán-Vioque, J., Eds., Dordrecht: Springer Netherlands, 2007, pp. 1–49, ISBN: 978-1-4020-6356-5. DOI: 10.1007/978-1-4020-6356-5_1.

[64] Dwivedy, S. K. and Eberhard, P., "Dynamic analysis of flexible manipulators, a literature review," en, *Mechanism and Machine Theory*, vol. 41, no. 7, pp. 749–777, Jul. 2006, ISSN: 0094114X. DOI: 10.1016/j.mechmachtheory.2006.01.014.

[65] Economon, T. D., Palacios, F., Copeland, S. R., Lukaczyk, T. W., and Alonso, J. J., "Su2: An open-source suite for multiphysics simulation and design," *AIAA Journal*, vol. 54, no. 3, pp. 828–846, Mar. 2016, ISSN: 1533-385X. DOI: 10.2514/1.j053813.

[66] Elliott, A. J., Cammarano, A., Neild, S. A., Hill, T. L., and Wagg, D. J., "Comparing the direct normal form and multiple scales methods through frequency detuning," en, *Nonlinear Dynamics*, vol. 94, no. 4, pp. 2919–2935, Dec. 2018, ISSN: 0924-090X, 1573-269X. DOI: 10.1007/s11071-018-4534-1.

[67] Escalona, J. L. and Mohammadi, N., "Advances in the modeling and dynamic simulation of reeving systems using the arbitrary lagrangianeulerian modal method," *Nonlinear Dynamics*, vol. 108, no. 4, pp. 3985–4003, Mar. 2022, ISSN: 1573-269X. DOI: 10.1007/s11071-022-07357-y.

[68] Farokhi, H. and Erturk, A., "Three-dimensional nonlinear extreme vibrations of cantilevers based on a geometrically exact model," en, *Journal of Sound and Vibration*, vol. 510, p. 116 295, Oct. 2021, ISSN: 0022460X. DOI: 10.1016/j.jsv.2021.116295.

[69] Farokhi, H. and Ghayesh, M. H., "Geometrically exact extreme vibrations of cantilevers," en, *International Journal of Mechanical Sciences*, vol. 168, p. 105 051, Feb. 2020, ISSN: 00207403. DOI: 10.1016/j.ijmecsci.2019.105051.

[70] Farokhi, H., Kohtanen, E., and Erturk, A., "Extreme parametric resonance oscillations of a cantilever: An exact theory and experimental validation," en, *Mechanical Systems and Signal Processing*, vol. 196, p. 110 342, Aug. 2023, ISSN: 08883270. DOI: 10.1016/j.ymssp.2023.110342.

[71] Felippa, C., *Nonlinear Finite Element Methods*. University of Colorado, Boulder, 2001.

[72] Fontanela, F., Vizzaccaro, A., Auvray, J., NiedergesäSS, B., Grolet, A., Salles, L., and Hoffmann, N., "Nonlinear vibration localisation in a symmetric system of two coupled beams," en, *Nonlinear Dynamics*, vol. 103, no. 4, pp. 3417–3428, Mar. 2021, ISSN: 0924-090X, 1573-269X. DOI: 10.1007/s11071-020-05760-x.

[73] Frediani, A., Cipolla, V., and Rizzo, E., "The prandtlplane configuration: Overview on possible applications to civil aviation," in *Variational Analysis and Aerospace Engineering: Mathematical Challenges for Aerospace Design*. Springer US, 2012, pp. 179–210, ISBN: 9781461424352. DOI: 10.1007/978-1-4614-2435-2_8.

[74] Gallier, J. and Quaintance, J., *Differential Geometry and Lie Groups: A Computational Perspective* (Geometry and Computing), en. Cham: Springer International Publishing, 2020, vol. 12, ISBN: 978-3-030-46039-6. DOI: 10.1007/978-3-030-46040-2.

[75] Gallo, E., *The SO(3) and SE(3) Lie Algebras of Rigid Body Rotations and Motions and their Application to Discrete Integration, Gradient Descent Optimization, and State Estimation*, en, Aug. 2023.

[76] Georgiades, F., Peeters, M., Kerschen, G., Golinval, J. C., and Ruzzene, M., "Modal Analysis of a Nonlinear Periodic Structure with Cyclic Symmetry," en, *AIAA Journal*, vol. 47, no. 4, pp. 1014–1025, Apr. 2009, ISSN: 0001-1452, 1533-385X. DOI: 10.2514/1.40461.

[77] Georgiades, F. and Vakakis, A. F., "Passive targeted energy transfers and strong modal interactions in the dynamics of a thin plate with strongly nonlinear attachments," en, *International Journal of Solids and Structures*, vol. 46, no. 11-12, pp. 2330–2353, Jun. 2009, ISSN: 00207683. DOI: 10.1016/j.ijsolstr.2009.01.020.

[78] Géradin, M. and Cardona, A., *Flexible multibody dynamics: a finite element approach*. New York: John Wiley, 2001, ISBN: 978-0-471-48990-0.

[79] Géradin, M., Rixen, D., and Farhat, C., *Mechanical vibrations: theory and applications to structural dynamics*, eng, Third Edition. Chichester, West Suxxes: Wiley, 2015, ISBN: 978-1-118-90020-8.

[80] Géradin, M. and Sonneville, V., "A two-field approach to multibody dynamics of rotating flexible bodies," en, *Multibody System Dynamics*, vol. 60, no. 3, pp. 375–415, Mar. 2024, ISSN: 1384-5640, 1573-272X. DOI: 10.1007/s11044-023-09912-w.

[81] Gerstmayr, J., Sugiyama, H., and Mikkola, A., "Review on the absolute nodal coordinate formulation for large deformation analysis of multibody systems," en, *Journal of Computational and Nonlinear Dynamics*, vol. 8, no. 3, p. 031 016, Jul. 2013, ISSN: 1555-1415, 1555-1423. DOI: 10.1115/1.4023487.

[82] Ghasemi, K., Ghaisari, J., and Abdollahi, F., "Robust formation control of multiagent systems on the lie group se(3)," *International Journal of Robust and Nonlinear Control*, vol. 30, no. 3, pp. 966–998, Dec. 2019, ISSN: 1099-1239. DOI: 10.1002/rnc.4806.

[83] Ghayesh, M. H. and Amabili, M., "Nonlinear dynamics of an axially moving Timoshenko beam with an internal resonance," en, *Nonlinear Dynamics*, vol. 73, no. 1-2, pp. 39–52, Jul. 2013, ISSN: 0924-090X, 1573-269X. DOI: 10.1007/s11071-013-0765-3.

[84] Ghosh, S. and Roy, D., "Consistent quaternion interpolation for objective finite element approximation of geometrically exact beam," en, *Computer Methods in Applied Mechanics and Engineering*, vol. 198, no. 3-4, pp. 555–571, Dec. 2008, ISSN: 00457825. DOI: 10.1016/j.cma.2008.09.004.

[85] Giusti, A., "A nonlinear model for the dynamics of moored floating platforms," Ph.D. dissertation, University of Braunschweig, University of Florence, 2016.

[86] Givois, A., Grolet, A., Thomas, O., and Deü, J.-F., "On the frequency response computation of geometrically nonlinear flat structures using reduced-order finite element models," en, *Nonlinear Dynamics*, vol. 97, no. 2, pp. 1747–1781, Jul. 2019, ISSN: 0924-090X, 1573-269X. DOI: 10.1007/s11071-019-05021-6.

[87] Givois, A., Tan, J.-J., Touzé, C., and Thomas, O., "Backbone curves of coupled cubic oscillators in one-to-one internal resonance: Bifurcation scenario, measurements and parameter identification," en, *Meccanica*, vol. 55, no. 3, pp. 481–503, Mar. 2020, ISSN: 0025-6455, 1572-9648. DOI: 10.1007/s11012-020-01132-2.

[88] Gonzalez, J. L. and Mireles James, J. D., "High-Order Parameterization of Stable/Unstable Manifolds for Long Periodic Orbits of Maps," en, *SIAM Journal on Applied Dynamical Systems*, vol. 16, no. 3, pp. 1748–1795, Jan. 2017, ISSN: 1536-0040. DOI: 10.1137/16M1090041.

[89] Govaerts, W. J. F., *Numerical methods for bifurcations of dynamical equilibria*. Philadelphia, Pa: Society for Industrial and Applied Mathematics, 2000, ISBN: 978-0-89871-442-5.

[90] Guillot, L., Lazarus, A., Thomas, O., Vergez, C., and Cochelin, B., "A purely frequency based Floquet-Hill formulation for the efficient stability computation of periodic solutions of ordinary differential systems," en, *Journal of Computational Physics*, vol. 416, p. 109 477, Sep. 2020, ISSN: 00219991. DOI: 10.1016/j.jcp.2020.109477.

[91] Gupta, M., Sarkar, K., and Hodges, D. H., "Dynamic Analysis of Nonlinear Composite Beams with 3-D Structural Damping," en, in *AIAA Scitech 2019 Forum*, San Diego, California: American Institute of Aeronautics and Astronautics, Jan. 2019, ISBN: 978-1-62410-578-4. DOI: 10.2514/6.2019-0211.

[92] Hall, B. C., *Lie Groups, Lie Algebras, and Representations: An Elementary Introduction* (Graduate Texts in Mathematics), en. Cham: Springer International Publishing, 2015, vol. 222, ISBN: 978-3-319-13466-6. DOI: 10.1007/978-3-319-13467-3.

[93] Haller, G. and Ponsioen, S., "Nonlinear normal modes and spectral submanifolds: Existence, uniqueness and use in model reduction," en, *Nonlinear Dynamics*, vol. 86, no. 3, pp. 1493–1534, Nov. 2016, ISSN: 0924-090X, 1573-269X. DOI: 10.1007/s11071-016-2974-z.

[94] Harsch, J., Sailer, S., and Eugster, S. R., "A total Lagrangian, objective and intrinsically locking-free Petrov-Galerkin SE(3) Cosserat rod finite element formulation," en, *International Journal for Numerical Methods in Engineering*, vol. 124, no. 13, pp. 2965–2994, Jul. 2023, ISSN: 0029-5981, 1097-0207. DOI: 10.1002/nme.7236.

[95] Hill, T., Cammarano, A., Neild, S., and Wagg, D., "Interpreting the forced responses of a two-degree-of-freedom nonlinear oscillator using backbone curves," en, *Journal of Sound and Vibration*, vol. 349, pp. 276–288, Aug. 2015, ISSN: 0022460X. DOI: 10.1016/j.jsv.2015.03.030.

[96] Hodges, D. H., "A mixed variational formulation based on exact intrinsic equations for dynamics of moving beams," en, *International Journal of Solids and Structures*, vol. 26, no. 11, pp. 1253–1273, 1990, ISSN: 00207683. DOI: 10.1016/0020-7683(90)90060-9.

[97] Hodges, D. H., "Geometrically exact, intrinsic theory for dynamics of curved and twisted anisotropic beams," *AIAA Journal*, vol. 41, pp. 1131–1137, 6 Jun. 2003, ISSN: 0001-1452. DOI: 10.2514/2.2054.

[98] Hodges, D. H. and Dowell, E. H., "Nonlinear equations of motion for the elastic bending and torsion of twisted nonuniform rotor blades," 1974.

[99] Holzinger, S., Arnold, M., and Gerstmayr, J., "Evaluation and implementation of Lie group integration methods for rigid multibody systems," en, *Multibody System Dynamics*, Mar. 2024, ISSN: 1384-5640, 1573-272X. DOI: 10.1007/s11044-024-09970-8.

[100] Hong, D., Hill, T. L., and Neild, S. A., "Efficient energy balancing across multiple harmonics of nonlinear normal modes," en, *Nonlinear Dynamics*, vol. 108, no. 4, pp. 2935–2959, Jun. 2022, ISSN: 0924-090X, 1573-269X. DOI: 10.1007/s11071-022-07428-0.

[101] Hoskoti, L., Misra, A., and Sucheendran, M. M., "Bifurcation of nonlinear normal modes of a cantilever beam under harmonic excitation," en, *Archive of Applied Mechanics*, vol. 90, no. 6, pp. 1247–1266, Jun. 2020, ISSN: 0939-1533, 1432-0681. DOI: 10.1007/s00419-019-01647-5.

[102] Ibrahimbegovi, A., "On finite element implementation of geometrically nonlinear reissner's beam theory: Three-dimensional curved beam elements," *Computer Methods in Applied Mechanics and Engineering*, vol. 122, pp. 11–26, 1-2 Apr. 1995, ISSN: 00457825. DOI: 10.1016/0045-7825(95)00724-F.

[103] Iserles, A., Munthe-Kaas, H. Z., Nørsett, S. P., and Zanna, A., "Lie-group methods," en, *Acta Numerica*, vol. 9, pp. 215–365, Jan. 2000, ISSN: 0962-4929, 1474-0508. DOI: 10.1017/S0962492900002154.

[104] Jain, S. and Haller, G., "How to compute invariant manifolds and their reduced dynamics in high-dimensional finite element models," en, *Nonlinear Dynamics*, vol. 107, no. 2, pp. 1417–1450, Jan. 2022, ISSN: 0924-090X, 1573-269X. DOI: 10.1007/s11071-021-06957-4.

[105] Jain, S., Tiso, P., and Haller, G., "Exact nonlinear model reduction for a von Kármán beam: Slow-fast decomposition and spectral submanifolds," en, *Journal of Sound and Vibration*, vol. 423, pp. 195–211, Jun. 2018, ISSN: 0022460X. DOI: 10.1016/j.jsv.2018.01.049.

[106] Jain, S., Tiso, P., Rutzmoser, J. B., and Rixen, D. J., "A quadratic manifold for model order reduction of nonlinear structural dynamics," en, *Computers & Structures*, vol. 188, pp. 80–94, Aug. 2017, ISSN: 00457949. DOI: 10.1016/j.compstruc.2017.04.005.

[107] Jeleni, G. and Crisfield, M., "Geometrically exact 3d beam theory: Implementation of a strain-invariant finite element for statics and dynamics," *Computer Methods in Applied Mechanics and Engineering*, vol. 171, pp. 141–171, 1-2 Mar. 1999, ISSN: 00457825. DOI: 10.1016/S0045-7825(98)00249-7.

[108] Jeong, B., Cho, H., Yu, M.-F., Vakakis, A. F., McFarland, D. M., and Bergman, L. A., "Modeling and measurement of geometrically nonlinear damping in a microcantilevernanotube system," *ACS Nano*, vol. 7, no. 10, pp. 8547–8553, Sep. 2013, ISSN: 1936-086X. DOI: 10.1021/nn402479d.

[109] Jiang, D., Pierre, C., and Shaw, S., "The construction of non-linear normal modes for systems with internal resonance," en, *International Journal of Non-Linear Mechanics*, vol. 40, no. 5, pp. 729–746, Jun. 2005, ISSN: 00207462. DOI: 10.1016/j.ijnonlinmec.2004.08.010.

[110] *Joint training on numerical modelling of highly flexible structures for industrial applications: Thread project: European commission.* https://cordis.europa.eu/project/id/860124/results, 2019.

[111] Jonghoon Park and Wan-Kyun Chung, "Geometric integration on Euclidean group with application to articulated multibody systems," en, *IEEE Transactions on Robotics*, vol. 21, no. 5, pp. 850–863, Oct. 2005, ISSN: 1552-3098. DOI: 10.1109/TRO.2005.852253.

[112] Jonker, J. and Meijaard, J., "A geometrically non-linear formulation of a three-dimensional beam element for solving large deflection multibody system problems," en, *International Journal of Non-Linear Mechanics*, vol. 53, pp. 63–74, Jul. 2013, ISSN: 00207462. DOI: 10.1016/j.ijnonlinmec.2013.01.012.

[113] Keller, H. B., *Numerical methods for two-point boundary-value problems*. Dover Publications, Dec. 2018, ISBN: 9780486828343.

[114] Kerschen, G., Peeters, M., Golinval, J. C., and Stéphan, C., "Nonlinear Modal Analysis of a Full-Scale Aircraft," en, *Journal of Aircraft*, vol. 50, no. 5, pp. 1409–1419, Sep. 2013, ISSN: 0021-8669, 1533-3868. DOI: 10.2514/1.C031918.

[115] Kerschen, G., Peeters, M., Golinval, J., and Vakakis, A., "Nonlinear normal modes, Part I: A useful framework for the structural dynamicist," en, *Mechanical Systems and Signal Processing*, vol. 23, no. 1, pp. 170–194, Jan. 2009, ISSN: 08883270. DOI: 10.1016/j.ymssp.2008.04.002.

[116] Kerschen, G., Ed., *Modal Analysis of Nonlinear Mechanical Systems* (CISM International Centre for Mechanical Sciences). Vienna: Springer Vienna, 2014, vol. 555, ISBN: 978-3-7091-1791-0. DOI: 10.1007/978-3-7091-1791-0.

[117] Kobilarov, M. B. and Marsden, J. E., "Discrete geometric optimal control on lie groups," *IEEE Transactions on Robotics*, vol. 27, no. 4, pp. 641–655, Aug. 2011, ISSN: 1941-0468. DOI: 10.1109/tro.2011.2139130.

[118] Kuether, R., Renson, L., Detroux, T., Grappasonni, C., Kerschen, G., and Allen, M., "Nonlinear normal modes, modal interactions and isolated resonance curves," en, *Journal of Sound and Vibration*, vol. 351, pp. 299–310, Sep. 2015, ISSN: 0022460X. DOI: 10.1016/j.jsv.2015.04.035.

[119] Kuether, R. J. and Allen, M. S., "A numerical approach to directly compute nonlinear normal modes of geometrically nonlinear finite element models," en, *Mechanical Systems and Signal Processing*, vol. 46, no. 1, pp. 1–15, May 2014, ISSN: 08883270. DOI: 10.1016/j.ymssp.2013.12.010.

[120] Kuether, R. J. and Allen, M. S., "Computing Nonlinear Normal Modes Using Numerical Continuation and Force Appropriation," en, in *Volume 1: 24th Conference on Mechanical Vibration and Noise, Parts A and B*, Chicago, Illinois, USA: American Society of Mechanical Engineers, Aug. 2012, pp. 329–340, ISBN: 978-0-7918-4500-4. DOI: 10.1115/DETC2012-71257.

[121] Kuznecov, J. A., *Elements of applied bifurcation theory* (Applied mathematical sciences 112), eng, 3. ed. New York, NY: Springer, 2010, ISBN: 978-1-4419-1951-9.

[122] Lacarbonara, W., *Nonlinear Structural Mechanics: Theory, Dynamical Phenomena and Modeling*, en. Boston, MA: Springer US, 2013, ISBN: 978-1-4419-1275-6. DOI: 10.1007/978-1-4419-1276-3.

[123] Lakshmi, M. V., Fantuzzi, G., Chernyshenko, S. I., and Lasagna, D., "Finding unstable periodic orbits: A hybrid approach with polynomial optimization," en, *Physica D: Nonlinear Phenomena*, vol. 427, p. 133 009, Dec. 2021, ISSN: 01672789. DOI: 10.1016/j.physd.2021.133009.

[124] Le, T.-N., Battini, J.-M., and Hjiaj, M., "A consistent 3D corotational beam element for nonlinear dynamic analysis of flexible structures," en, *Computer Methods in Applied Mechanics and Engineering*, vol. 269, pp. 538–565, Feb. 2014, ISSN: 00457825. DOI: 10.1016/j.cma.2013.11.007.

[125] Le Cunff, C., Heurtier, J.-M., Piriou, L., Berhault, C., Perdrizet, T., Teixeira, D., Ferrer, G., and Gilloteaux, J.-C., "Fully coupled floating wind turbine simulator based on nonlinear finite element method: Part i methodology," in *Volume 8: Ocean Renewable Energy*, ser. OMAE2013, American Society of Mechanical Engineers, Jun. 2013. DOI: 10.1115/omae2013-10780.

[126] Lee, K.-H., Han, H.-S., and Park, S., "Bifurcation analysis of coupled lateral/torsional vibrations of rotor systems," en, *Journal of Sound and Vibration*, vol. 386, pp. 372–389, Jan. 2017, ISSN: 0022460X. DOI: 10.1016/j.jsv.2016.10.002.

[127] Lens, E. V. and Cardona, A., "A nonlinear beam element formulation in the framework of an energy preserving time integration scheme for constrained multibody systems dynamics," en, *Computers & Structures*, vol. 86, no. 1-2, pp. 47–63, Jan. 2008, ISSN: 00457949. DOI: 10.1016/j.compstruc.2007.05.036.

[128] Li, M., Jain, S., and Haller, G., "Nonlinear analysis of forced mechanical systemswith internal resonance using spectral submanifolds, Part I: Periodic response and forced response curve," en, *Nonlinear Dynamics*, vol. 110, no. 2, pp. 1005–1043, Oct. 2022, ISSN: 0924-090X, 1573-269X. DOI: 10.1007/s11071-022-07714-x.

[129] Linn, J., Lang, H., and Tuganov, A., "Geometrically exact Cosserat rods with KelvinVoigt type viscous damping," en, *Mechanical Sciences*, vol. 4, no. 1, pp. 79–96, Feb. 2013, ISSN: 2191-916X. DOI: 10.5194/ms-4-79-2013.

[130] Liu, C.-S., "The Lie-Group Shooting Method for Solving Multi-dimensional Nonlinear Boundary Value Problems," en, *Journal of Optimization Theory and Applications*, vol. 152, no. 2, pp. 468–495, Feb. 2012, ISSN: 0022-3239, 1573-2878. DOI: 10.1007/s10957-011-9913-4.

[131] Liu, X. and Wagg, D. J., "Simultaneous normal form transformation and model-order reduction for systems of coupled nonlinear oscillators," en, *Proceedings of the Royal Society A: Mathematical, Physical and Engineering Sciences*, vol. 475, no. 2228, p. 20 190 042, Aug. 2019, ISSN: 1364-5021, 1471-2946. DOI: 10.1098/rspa.2019.0042.

[132] Lust, K., "Numerical bifurcation analysis of periodic solutions of partial differential equations," English, Ph.D. dissertation, KU Leuven, 1997.

[133] Lynch, K. M. and Park, F. C., *Modern robotics: mechanics, planning, and control*. Cambridge, UK: Cambridge University Press, 2017, ISBN: 978-1-107-15630-2.

[134] Ma, Z., Liu, Z., and You, P., "A 3D corotational beam element formulated on the special Euclidean group SE(3)," en, *Computers & Structures*, vol. 281, p. 107 011, Jun. 2023, ISSN: 00457949. DOI: 10.1016/j.compstruc.2023.107011.

[135] Mahmoodi, S. N., Jalili, N., and Ahmadian, M., "Subharmonics analysis of nonlinear flexural vibrations ofăpiezoelectrically actuated microcantilevers," *Nonlinear Dynamics*, vol. 59, no. 3, pp. 397–409, Jul. 2009, ISSN: 1573-269X. DOI: 10.1007/s11071-009-9546-4.

[136] Martin, A., Opreni, A., Vizzaccaro, A., Debeurre, M., Salles, L., Frangi, A., Thomas, O., and Touzé, C., "Reduced-order modeling of geometrically nonlinear rotating structures using the direct parametrisation of invariant manifolds," en, *Journal of Theoretical, Computational and Applied Mechanics*, p. 10 430, Jun. 2023, ISSN: 2726-6141. DOI: 10.46298/jtcam.10430.

[137] Al-Mdallal, Q. M., Syam, M. I., and Anwar, M., "A collocation-shooting method for solving fractional boundary value problems," en, *Communications in Nonlinear Science and Numerical Simulation*, vol. 15, no. 12, pp. 3814–3822, Dec. 2010, ISSN: 10075704. DOI: 10.1016/j.cnsns.2010.01.020.

[138] Meier, C., "Geometrically exact finite element formulations for slender beams and their contact interaction," Ph.D. dissertation, Technical University of Munich, Germany, 2016.

[139] Meier, C., Popp, A., and Wall, W. A., "Geometrically Exact Finite Element Formulations for Slender Beams: KirchhoffLove Theory Versus SimoReissner Theory," en, *Archives of Computational Methods in Engineering*, vol. 26, no. 1, pp. 163–243, Jan. 2019, ISSN: 1134-3060, 1886-1784. DOI: 10.1007/s11831-017-9232-5.

[140] Mélot, A., Denimal Goy, E., and Renson, L., "Control of isolated response curves through optimization of codimension-1 singularities," en, *Computers & Structures*, vol. 299, p. 107 394, Aug. 2024, ISSN: 00457949. DOI: 10.1016/j.compstruc.2024.107394.

[141] Mikhlin, Y. and Avramov, K., "Nonlinear Normal Modes of Vibrating Mechanical Systems: 10 Years of Progress," en, *Applied Mechanics Reviews*, vol. 76, no. 5, p. 050 801, Sep. 2024, ISSN: 0003-6900, 2379-0407. DOI: 10.1115/1.4063593.

[142] Mikhlin, Y. V. and Avramov, K. V., "Nonlinears Normal Modes for Vibrating Mechanical Systems. Review of Theoretical Developments," en, *Applied Mechanics Reviews*, vol. 63, no. 6, p. 060 802, Nov. 2010, ISSN: 0003-6900, 2379-0407. DOI: 10.1115/1.4003825.

[143] Mladenova, C. D., *Group Theory in the Problems of Modeling and Control of Multi-Body Systems*. 2012. DOI: 10.7546/jgsp-8-2006-17-121.

[144] Müller, A., *Multibody System Dynamics*, vol. 9, no. 4, pp. 311–352, 2003, ISSN: 1384-5640. DOI: 10.1023/a:1023321630764.

[145] Müller, A., "Review of the exponential and Cayley map on SE(3) as relevant for Lie group integration of the generalized Poisson equation and flexible multibody systems," en, *Proceedings of the Royal Society A: Mathematical, Physical and Engineering Sciences*, vol. 477, no. 2253, p. 20 210 303, Sep. 2021, ISSN: 1364-5021, 1471-2946. DOI: 10.1098/rspa.2021.0303.

[146] Müller, A., "Screw and Lie group theory in multibody kinematics: Motion representation and recursive kinematics of tree-topology systems," en, *Multibody System Dynamics*, vol. 43, no. 1, pp. 37–70, May 2018, ISSN: 1384-5640, 1573-272X. DOI: 10.1007/s11044-017-9582-7.

[147] Müller, A., "Singularity-Free Lie Group Integration and Geometrically Consistent Evaluation of Multibody System Models Described in Terms of Standard Absolute Coordinates," en, *Journal of Computational and Nonlinear Dynamics*, vol. 17, no. 5, p. 051 003, May 2022, ISSN: 1555-1415, 1555-1423. DOI: 10.1115/1.4053368.

[148] Murray, R. M., Li, Z., and Sastry, S., *A mathematical introduction to robotic manipulation*. Boca Raton: CRC Press, 1994, ISBN: 978-0-8493-7981-9.

[149] Nayfeh, A., "Interaction of fundamental parametric resonances with subharmonic resonances of order one-half," en, *Journal of Sound and Vibration*, vol. 96, no. 3, pp. 333–340, Oct. 1984, ISSN: 0022460X. DOI: 10.1016/0022-460X(84)90360-2.

[150] Neild, S. A. and Wagg, D. J., "Applying the method of normal forms to second-order nonlinear vibration problems," en, *Proceedings of the Royal Society A: Mathematical, Physical and Engineering Sciences*, vol. 467, no. 2128, pp. 1141–1163, Apr. 2011, ISSN: 1364-5021, 1471-2946. DOI: 10.1098/rspa.2010.0270.

[151] Neukirch, S., Yavari, M., Challamel, N., and Thomas, O., "Comparison of the von Kármán and Kirchhoff models for the post-buckling and vibrations of elastic beams," en, 2021.

[152] Noël, J., Renson, L., and Kerschen, G., "Complex dynamics of a nonlinear aerospace structure: Experimental identification and modal interactions," en, *Journal of Sound and Vibration*, vol. 333, no. 12, pp. 2588–2607, Jun. 2014, ISSN: 0022460X. DOI: 10.1016/j.jsv.2014.01.024.

[153] Ntarladima, K., Pieber, M., and Gerstmayr, J., "A model for contact and friction between beams under large deformation and sheaves," *Nonlinear Dynamics*, vol. 111, no. 22, pp. 20 643–20 660, Oct. 2023, ISSN: 1573-269X. DOI: 10.1007/s11071-023-08973-y.

[154] Otsuka, K., Del Carre, A., and Palacios, R., "Nonlinear Aeroelastic Analysis of High-Aspect-Ratio Wings with a Low-Order Propeller Model," en, *Journal of Aircraft*, vol. 59, no. 2, pp. 293–306, Mar. 2022, ISSN: 1533-3868. DOI: 10.2514/1.C036285.

[155] Otsuka, K., Makihara, K., and Sugiyama, H., "Recent Advances in the Absolute Nodal Coordinate Formulation: Literature Review From 2012 to 2020," en, *Journal of Computational and Nonlinear Dynamics*, vol. 17, no. 8, p. 080 803, Aug. 2022, ISSN: 1555-1415, 1555-1423. DOI: 10.1115/1.4054113.

[156] Otsuka, K., Wang, Y., Palacios, R., and Makihara, K., "Strain-Based Geometrically Nonlinear Beam Formulation for RigidFlexible Multibody Dynamic Analysis," en, *AIAA Journal*, vol. 60, no. 8, pp. 4954–4968, Aug. 2022, ISSN: 0001-1452, 1533-385X. DOI: 10.2514/1.J061516.

[157] Pak, C., "Synge's concept of stability applied to non-linear normal modes," en, *International Journal of Non-Linear Mechanics*, vol. 41, no. 5, pp. 657–664, Jun. 2006, ISSN: 00207462. DOI: 10.1016/j.ijnonlinmec.2006.01.007.

[158] Palacios, R., "Nonlinear normal modes in an intrinsic theory of anisotropic beams," *Journal of Sound and Vibration*, vol. 330, pp. 1772–1792, 8 Apr. 2011, ISSN: 0022460X. DOI: 10.1016/j.jsv.2010.10.023.

[159] Palacios, R. and Cesnik, C., "Structural Models for Flight Dynamic Analysis of Very Flexible Aircraft," en, in *50th AIAA/ASME/ASCE/AHS/ASC Structures, Structural Dynamics, and Materials Conference*, Palm Springs, California: American Institute of Aeronautics and Astronautics, May 2009, ISBN: 978-1-60086-975-4. DOI: 10.2514/6.2009-2403.

[160] Palacios, R. and Cesnik, C. E. S., *Dynamics of Flexible Aircraft: Coupled Flight Mechanics, Aeroelasticity, and Control*, 1st ed. Cambridge University Press, Jun. 2023, ISBN: 978-1-108-42060-0. DOI: 10.1017/9781108354868.

[161] Palacios, R., Murua, J., and Cook, R., "Structural and Aerodynamic Models in Nonlinear Flight Dynamics of Very Flexible Aircraft," en, *AIAA Journal*, vol. 48, no. 11, pp. 2648–2659, Nov. 2010, ISSN: 0001-1452, 1533-385X. DOI: 10.2514/1.J050513.

[162] Park, F., "Computational aspects of the product-of-exponentials formula for robot kinematics," *IEEE Transactions on Automatic Control*, vol. 39, no. 3, pp. 643–647, Mar. 1994, ISSN: 0018-9286. DOI: 10.1109/9.280779.

[163] Park, F., Bobrow, J., and Ploen, S., "A lie group formulation of robot dynamics," *The International Journal of Robotics Research*, vol. 14, no. 6, pp. 609–618, Dec. 1995, ISSN: 1741-3176. DOI: 10.1177/027836499501400606.

[164] Pastor, M., Binda, M., and Harik, T., "Modal Assurance Criterion," en, *Procedia Engineering*, vol. 48, pp. 543–548, 2012, ISSN: 18777058. DOI: 10.1016/j.proeng.2012.09.551.

[165] Patil, M. and Hodges, D., "On the importance of aerodynamic and structural geometrical nonlinearities in aeroelastic behavior of high-aspect-ratio wings," *Journal of Fluids and Structures*, vol. 19, no. 7, pp. 905–915, Aug. 2004, ISSN: 0889-9746. DOI: 10.1016/j.jfluidstructs.2004.04.012.

[166] Patil, M., Hodges, D., and Cesnik, C., "Limit cycle oscillations in high-aspect-ratio wings," en, in *40th Structures, Structural Dynamics, and Materials Conference and Exhibit*, St. Louis,MO,U.S.A.: American Institute of Aeronautics and Astronautics, Apr. 1999. DOI: 10.2514/6.1999-1464.

[167] Patil, M. J. and Hodges, D. H., "Flight Dynamics of Highly Flexible Flying Wings," en, *Journal of Aircraft*, vol. 43, no. 6, pp. 1790–1799, Nov. 2006, ISSN: 0021-8669, 1533-3868. DOI: 10.2514/1.17640.

[168] Patil, M. J., Hodges, D. H., and Cesnik, C. E. S., "Nonlinear aeroelasticity and flight dynamics of high-altitude long-endurance aircraft," *Journal of Aircraft*, vol. 38, no. 1, pp. 88–94, Jan. 2001, ISSN: 1533-3868. DOI: 10.2514/2.2738.

[169] Peeters, M., Kerschen, G., and Golinval, J., "Dynamic testing of nonlinear vibrating structures using nonlinear normal modes," en, *Journal of Sound and Vibration*, vol. 330, no. 3, pp. 486–509, Jan. 2011, ISSN: 0022460X. DOI: 10.1016/j.jsv.2010.08.028.

[170] Peeters, M., Viguié, R., Sérandour, G., Kerschen, G., and Golinval, J.-C., "Nonlinear normal modes, part ii: Toward a practical computation using numerical continuation techniques," *Mechanical Systems and Signal Processing*, vol. 23, pp. 195–216, 1 Jan. 2009, ISSN: 08883270. DOI: 10.1016/j.ymssp.2008.04.003.

[171] Peeters, M., "Theoretical and experimental modal analysis of nonlinear vibrating structures using nonlinear normal modes," Ph.D. dissertation, University of Liège: Liège, Belgium, 2010.

[172] Perdrizet, T., Gilloteaux, J.-C., Teixeira, D., Ferrer, G., Piriou, L., Cadiou, D., Heurtier, J.-M., and Le Cunff, C., "Fully coupled floating wind turbine simulator based on nonlinear finite element method: Part ii validation results," in *Volume 8: Ocean Renewable Energy*, ser. OMAE2013, American Society of Mechanical Engineers, Jun. 2013. DOI: 10.1115/omae2013-10785.

[173] Perroni, A. P. and Bussamra, F. L. S., "Effects of geometric nonlinearity on flexible wing structures," *Journal of Aircraft*, vol. 58, no. 1, pp. 85–97, Jan. 2021, ISSN: 1533-3868. DOI: 10.2514/1.c035745.

[174] Pieber, M., Ntarladima, K., Winkler, R., and Gerstmayr, J., "A hybrid arbitrary lagrangian eulerian formulation for the investigation of the stability of pipes conveying fluid and axially moving beams," *Journal of Computational and Nonlinear Dynamics*, vol. 17, no. 5, Mar. 2022, ISSN: 1555-1423. DOI: 10.1115/1.4053505.

[175] Ranjbar, M., kec, L., Jeleni, G., and Ribari, D., "Mixedmode delamination of layered structures modeled as timoshenko beams with linked interpolation," *International Journal for Numerical Methods in Engineering*, vol. 124, no. 8, pp. 1773–1797, Dec. 2022, ISSN: 1097-0207. DOI: 10.1002/nme.7187.

[176] Raze, G., Volvert, M., and Kerschen, G., "Tracking amplitude extrema of nonlinear frequency responses using the harmonic balance method," en, *International Journal for Numerical Methods in Engineering*, vol. 125, no. 2, e7376, Jan. 2024, ISSN: 0029-5981, 1097-0207. DOI: 10.1002/nme.7376.

[177] Reddy, J. N., *An Introduction to Nonlinear Finite Element Analysis: with applications to heat transfer, fluid mechanics, and solid mechanics*. Oxford University Press, Oct. 2014, ISBN: 9780199641758. DOI: 10.1093/acprof:oso/9780199641758.001.0001.

[178] Reissner, E., "On finite deformations of space-curved beams," en, *ZAMP Zeitschrift für angewandte Mathematik und Physik*, vol. 32, no. 6, pp. 734–744, 1981, ISSN: 0044-2275, 1420-9039. DOI: 10.1007/BF00946983.

[179] Reissner, E., "On one-dimensional finite-strain beam theory: The plane problem," en, *Zeitschrift für angewandte Mathematik und Physik ZAMP*, vol. 23, no. 5, pp. 795–804, Sep. 1972, ISSN: 0044-2275, 1420-9039. DOI: 10.1007/BF01602645.

[180] Renda, F., Giorgio-Serchi, F., Boyer, F., Laschi, C., Dias, J., and Seneviratne, L., "A unified multi-soft-body dynamic model for underwater soft robots," en, *The International Journal of Robotics Research*, vol. 37, no. 6, pp. 648–666, May 2018, ISSN: 0278-3649, 1741-3176. DOI: 10.1177/0278364918769992.

[181] Renson, L., Hill, T. L., Ehrhardt, D. A., Barton, D. A. W., and Neild, S. A., "Force appropriation of nonlinear structures," en, *Proceedings of the Royal Society A: Mathematical, Physical and Engineering Sciences*, vol. 474, no. 2214, p. 20 170 880, Jun. 2018, ISSN: 1364-5021, 1471-2946. DOI: 10.1098/rspa.2017.0880.

[182] Renson, L., Kerschen, G., and Cochelin, B., "Numerical computation of nonlinear normal modes in mechanical engineering," *Journal of Sound and Vibration*, vol. 364, pp. 177–206, Mar. 2016, ISSN: 0022460X. DOI: 10.1016/j.jsv.2015.09.033.

[183] Renson, L., Noël, J. P., and Kerschen, G., "Complex dynamics of a nonlinear aerospace structure: Numerical continuation and normal modes," en, *Nonlinear Dynamics*, vol. 79, no. 2, pp. 1293–1309, Jan. 2015, ISSN: 0924-090X, 1573-269X. DOI: 10.1007/s11071-014-1743-0.

[184] Renson, L., "Nonlinear modal analysis of conservative and nonconservative aerospace structures," Ph.D. dissertation, University of Liège: Liège, Belgium, 2014.

[185] Romero, I., "A comparison of finite elements for nonlinear beams: The absolute nodal coordinate and geometrically exact formulations," en, *Multibody System Dynamics*, vol. 20, no. 1, pp. 51–68, Aug. 2008, ISSN: 1384-5640, 1573-272X. DOI: 10.1007/s11044-008-9105-7.

[186] Rong, B., Rui, X., Tao, L., and Wang, G., "Theoretical modeling and numerical solution methods for flexible multibody system dynamics," en, *Nonlinear Dynamics*, vol. 98, no. 2, pp. 1519–1553, Oct. 2019, ISSN: 0924-090X, 1573-269X. DOI: 10.1007/s11071-019-05191-3.

[187] Rosenberg, R., "On Nonlinear Vibrations of Systems with Many Degrees of Freedom," en, in *Advances in Applied Mechanics*, vol. 9, Elsevier, 1966, pp. 155–242, ISBN: 978-0-12-002009-6. DOI: 10.1016/S0065-2156(08)70008-5.

[188] Sánchez, J. and Net, M., "On the multiple shooting continuation of periodic orbits by newtonkrylov methods," en, *International Journal of Bifurcation and Chaos*, vol. 20, no. 01, pp. 43–61, Jan. 2010, ISSN: 0218-1274, 1793-6551. DOI: 10.1142/S0218127410025399.

[189] Sarrouy, E., Grolet, A., and Thouverez, F., "Global and bifurcation analysis of a structure with cyclic symmetry," en, *International Journal of Non-Linear Mechanics*, vol. 46, no. 5, pp. 727–737, Jun. 2011, ISSN: 00207462. DOI: 10.1016/j.ijnonlinmec.2011.02.005.

[190] Sayed, M., Mousa, A. A., Alzaharani, D. Y., Mustafa, I. H., and El-Bendary, S. I., "Bifurcation analysis of a composite cantilever beam via 1:3 internal resonance," en, *Journal of the Egyptian Mathematical Society*, vol. 28, no. 1, p. 45, Dec. 2020, ISSN: 2090-9128. DOI: 10.1186/s42787-020-00102-7.

[191] Schäfer, A., Kühl, P., Diehl, M., Schlöder, J., and Bock, H. G., "Fast reduced multiple shooting methods for nonlinear model predictive control," en, *Chemical Engineering and Processing: Process Intensification*, vol. 46, no. 11, pp. 1200–1214, Nov. 2007, ISSN: 02552701. DOI: 10.1016/j.cep.2006.06.024.

[192] Schilder, J., "Flexible multibody dynamics: Superelements using absolute interface coordinates in the floating frame formulation," English, PhD Thesis - Research UT, graduation UT, University of Twente, Netherlands, Nov. 2018, ISBN: 978-90-365-4653-9. DOI: 10.3990/1.9789036546539.

[193] Selig, J. M., *Geometric Fundamentals of Robotics* (Monographs in Computer Science), eng, 2nd edition. New York, NY: Springer New York, 2005, ISBN: 978-0-387-27274-0.

[194] Seydel, R., *Practical Bifurcation and Stability Analysis*. Springer New York, 2010, vol. 5, ISBN: 978-1-4419-1739-3. DOI: 10.1007/978-1-4419-1740-9.

[195] Shabana, A. A., Hussien, H. A., and Escalona, J. L., "Absolute Nodal Coordinate Formulation," en, in *Volume 1A: 16th Biennial Conference on Mechanical Vibration and Noise*, Sacramento, California, USA: American Society of Mechanical Engineers, Sep. 1997, V01AT06A016, ISBN: 978-0-7918-8040-1. DOI: 10.1115/DETC97/VIB-4227.

[196] Shabana, A. A. and Yakoub, R. Y., "Three Dimensional Absolute Nodal Coordinate Formulation for Beam Elements: Theory," en, *Journal of Mechanical Design*, vol. 123, no. 4, pp. 606–613, Dec. 2001, ISSN: 1050-0472, 1528-9001. DOI: 10.1115/1.1410100.

[197] Shami, Z. A., Shen, Y., Giraud-Audine, C., Touzé, C., and Thomas, O., "Nonlinear dynamics of coupled oscillators in 1:2 internal resonance: Effects of the non-resonant quadratic terms and recovery of the saturation effect," en, *Meccanica*, vol. 57, no. 11, pp. 2701–2731, Nov. 2022, ISSN: 0025-6455, 1572-9648. DOI: 10.1007/s11012-022-01566-w.

[198] Shaw, S. and Pierre, C., "Non-linear normal modes and invariant manifolds," en, *Journal of Sound and Vibration*, vol. 150, no. 1, pp. 170–173, Oct. 1991, ISSN: 0022460X. DOI: 10.1016/0022-460X(91)90412-D.

[199] Shaw, S. and Pierre, C., "Normal Modes for Non-Linear Vibratory Systems," en, *Journal of Sound and Vibration*, vol. 164, no. 1, pp. 85–124, Jun. 1993, ISSN: 0022460X. DOI: 10.1006/jsvi.1993.1198.

[200] Shaw, S. and Pierre, C., "Normal Modes of Vibration for Non-Linear Continuous Systems," en, *Journal of Sound and Vibration*, vol. 169, no. 3, pp. 319–347, Jan. 1994, ISSN: 0022460X. DOI: 10.1006/jsvi.1994.1021.

[201] Shen, Y., Vizzaccaro, A., Kesmia, N., Yu, T., Salles, L., Thomas, O., and Touzé, C., "Comparison of Reduction Methods for Finite Element Geometrically Nonlinear Beam Structures," en, *Vibration*, vol. 4, no. 1, pp. 175–204, Mar. 2021, ISSN: 2571-631X. DOI: 10.3390/vibration4010014.

[202] Shi, J., Shariati, A., Abad, S.-A., Liu, Y., Dai, J. S., and Wurdemann, H. A., "Stiffness modelling and analysis of soft fluidic-driven robots using Lie theory," en, *The International Journal of Robotics Research*, vol. 43, no. 3, pp. 354–384, Mar. 2024, ISSN: 0278-3649, 1741-3176. DOI: 10.1177/02783649231200595.

[203] Simo, J., "A finite strain beam formulation. the three-dimensional dynamic problem. part i," *Computer Methods in Applied Mechanics and Engineering*, vol. 49, pp. 55–70, 1 May 1985, ISSN: 00457825. DOI: 10.1016/0045-7825(85)90050-7.

[204] Simo, J. and Vu-Quoc, L., "A three-dimensional finite-strain rod model. part II: Computational aspects," en, *Computer Methods in Applied Mechanics and Engineering*, vol. 58, no. 1, pp. 79–116, Oct. 1986, ISSN: 00457825. DOI: 10.1016/0045-7825(86)90079-4.

[205] Simo, J. and Vu-Quoc, L., "On the dynamics in space of rods undergoing large motions A geometrically exact approach," en, *Computer Methods in Applied Mechanics and Engineering*, vol. 66, no. 2, pp. 125–161, Feb. 1988, ISSN: 00457825. DOI: 10.1016/0045-7825(88)90073-4.

[206] Solà, J., Deray, J., and Atchuthan, D., *A micro Lie theory for state estimation in robotics*, en, Dec. 2021.

[207] Sombroek, C., Tiso, P., Renson, L., and Kerschen, G., "Numerical computation of nonlinear normal modes in a modal derivative subspace," *Computers & Structures*, vol. 195, pp. 34–46, Jan. 2018, ISSN: 00457949. DOI: 10.1016/j.compstruc.2017.08.016.

[208] Sonneville, V., Cardona, A., and Brüls, O., "Geometrically exact beam finite element formulated on the special euclidean group," *Computer Methods in Applied Mechanics and Engineering*, vol. 268, pp. 451–474, Jan. 2014, ISSN: 00457825. DOI: 10.1016/j.cma.2013.10.008.

[209] Sonneville, V., "A geometric local frame approach for flexible multibody systems," Ph.D. dissertation, University of Liège: Liège, Belgium, 2015.

[210] Sonneville, V. and Brüls, O., "A Few Good Reasons to Consider a Beam Finite Element Formulation on the Lie Group SE(3)," en, in *Volume 7B: 9th International Conference on Multibody Systems, Nonlinear Dynamics, and Control*, Portland, Oregon, USA: American Society of Mechanical Engineers, Aug. 2013, V07BT10A008, ISBN: 978-0-7918-5597-3. DOI: 10.1115/DETC2013-13099.

[211] Sonneville, V. and Brüls, O., "A Formulation on the Special Euclidean Group for Dynamic Analysis of Multibody Systems," en, *Journal of Computational and Nonlinear Dynamics*, vol. 9, no. 4, p. 041 002, Oct. 2014, ISSN: 1555-1415, 1555-1423. DOI: 10.1115/1.4026569.

[212] Sonneville, V. and Brüls, O., "Sensitivity analysis for multibody systems formulated on a lie group," *Multibody System Dynamics*, vol. 31, pp. 47–67, 1 Jan. 2014, ISSN: 1384-5640. DOI: 10.1007/s11044-013-9345-z.

[213] Sonneville, V., Cardona, A., and Brüls, O., "Geometric Interpretation of a Non-Linear Beam Finite Element on The Lie Group SE(3)," en, *Archive of Mechanical Engineering*, vol. 61, no. 2, pp. 305–329, Aug. 2014, ISSN: 2300-1895. DOI: 10.2478/meceng-2014-0018.

[214] Sonneville, V., Scapolan, M., Shan, M., and Bauchau, O. A., "Modal reduction procedures for flexible multibody dynamics," en, *Multibody System Dynamics*, vol. 51, no. 4, pp. 377–418, Apr. 2021, ISSN: 1384-5640, 1573-272X. DOI: 10.1007/s11044-020-09770-w.

[215] Sotoudeh, Z. and Hodges, D. H., "Modeling Beams With Various Boundary Conditions Using Fully Intrinsic Equations," *Journal of Applied Mechanics*, vol. 78, no. 3, Feb. 2011, ISSN: 0021-8936. DOI: 10.1115/1.4003239.

[216] Sracic, M. W. and Allen, M. S., "Numerical Continuation of Periodic Orbits for Harmonically Forced Nonlinear Systems," en, in *Civil Engineering Topics, Volume 4*, Proulx, T., Ed., New York, NY: Springer New York, 2011, pp. 51–69, ISBN: 978-1-4419-9315-1. DOI: 10.1007/978-1-4419-9316-8_5.

[217] Stillwell, J., *Naive lie theory* (Undergraduate texts in mathematics). New York ; London: Springer, 2008, ISBN: 978-0-387-78214-0.

[218] Stoykov, S. and Margenov, S., "Numerical computation of periodic responses of nonlinear large-scale systems by shooting method," en, *Computers & Mathematics with Applications*, vol. 67, no. 12, pp. 2257–2267, Jul. 2014, ISSN: 08981221. DOI: 10.1016/j.camwa.2014.01.023.

[219] Stuelpnagel, J., "On the Parametrization of the Three-Dimensional Rotation Group," en, *SIAM Review*, vol. 6, no. 4, pp. 422–430, Oct. 1964, ISSN: 0036-1445, 1095-7200. DOI: 10.1137/1006093.

[220] Su, W. and Cesnik, C. E., "Strain-based geometrically nonlinear beam formulation for modeling very flexible aircraft," en, *International Journal of Solids and Structures*, vol. 48, no. 16-17, pp. 2349–2360, Aug. 2011, ISSN: 00207683. DOI: 10.1016/j.ijsolstr.2011.04.012.

[221] Szalai, R., Ehrhardt, D., and Haller, G., "Nonlinear model identification and spectral submanifolds for multi-degree-of-freedom mechanical vibrations," en, *Proceedings of the Royal Society A: Mathematical, Physical and Engineering Sciences*, vol. 473, no. 2202, p. 20 160 759, Jun. 2017, ISSN: 1364-5021, 1471-2946. DOI: 10.1098/rspa.2016.0759.

[222] Tang, D. and Dowell, E., "Effects of geometric structural nonlinearity on flutter and limit cycle oscillations of high-aspect-ratio wings," *Journal of Fluids and Structures*, vol. 19, no. 3, pp. 291–306, Apr. 2004, ISSN: 0889-9746. DOI: 10.1016/j.jfluidstructs.2003.10.007.

[223] Tang, D. and Dowell, E. H., "Experimental and theoretical study on aeroelastic response of high-aspect-ratio wings," *AIAA Journal*, vol. 39, no. 8, pp. 1430–1441, Aug. 2001, ISSN: 1533-385X. DOI: 10.2514/2.1484.

[224] Teh, L. H. and Clarke, M. J., "Co-rotational and Lagrangian formulations for elastic three-dimensional beam finite elements," en, *Journal of Constructional Steel Research*, vol. 48, no. 2-3, pp. 123–144, Nov. 1998, ISSN: 0143974X. DOI: 10.1016/S0143-974X(98)00200-4.

[225] Thomas, O. and Bilbao, S., "Geometrically nonlinear flexural vibrations of plates: In-plane boundary conditions and some symmetry properties," en, *Journal of Sound and Vibration*, vol. 315, no. 3, pp. 569–590, Aug. 2008, ISSN: 0022460X. DOI: 10.1016/j.jsv.2008.04.014.

[226] Thomas, O., Sénéchal, A., and Deü, J.-F., "Hardening/softening behavior and reduced order modeling of nonlinear vibrations of rotating cantilever beams," en, *Nonlinear Dynamics*, vol. 86, no. 2, pp. 1293–1318, Oct. 2016, ISSN: 0924-090X, 1573-269X. DOI: 10.1007/s11071-016-2965-0.

[227] Todesco, J. and Brüls, O., "Highly accurate differentiation of the exponential map and its tangent operator," en, *Mechanism and Machine Theory*, vol. 190, p. 105 451, Dec. 2023, ISSN: 0094114X. DOI: 10.1016/j.mechmachtheory.2023.105451.

[228] Touzé, C., "A normal form approach for nonlinear normal modes," 2015.

[229] Touzé, C., Vizzaccaro, A., and Thomas, O., "Model order reduction methods for geometrically nonlinear structures: A review of nonlinear techniques," en, *Nonlinear Dynamics*, vol. 105, no. 2, pp. 1141–1190, Jul. 2021, ISSN: 0924-090X, 1573-269X. DOI: 10.1007/s11071-021-06693-9.

[230] Tumiotto, D. and Arnold, M., "Local coordinates on Lie groups for half-explicit time integration of Cosserat-rod models with constraints," en, *Multibody System Dynamics*, Jun. 2024, ISSN: 1384-5640, 1573-272X. DOI: 10.1007/s11044-024-10002-8.

[231] Umbría, J. S. and Net, M., "Numerical continuation methods for large-scale dissipative dynamical systems," en, *The European Physical Journal Special Topics*, vol. 225, no. 13-14, pp. 2465–2486, Nov. 2016, ISSN: 1951-6355, 1951-6401. DOI: 10.1140/epjst/e2015-50317-2.

[232] Vadcard, T., Thouverez, F., and Batailly, A., "On the detection of nonlinear normal mode-related isolated branches of periodic solutions for high-dimensional nonlinear mechanical systems with frictionless contact interfaces," en, *Computer Methods in Applied Mechanics and Engineering*, vol. 419, p. 116 641, Feb. 2024, ISSN: 00457825. DOI: 10.1016/j.cma.2023.116641.

[233] Vakakis, A., "Non-Linear Normal Modes (nnms) and Their Applications in Vibration Theory: An Overview," en, *Mechanical Systems and Signal Processing*, vol. 11, no. 1, pp. 3–22, Jan. 1997, ISSN: 08883270. DOI: 10.1006/mssp.1996.9999.

[234] Vakakis, A. F., Manevitch, L. I., Mlkhlin, Y. V., Pilipchuk, V. N., and Zevin, A. A., *Normal Modes and Localization in Nonlinear Systems*, en, 1st ed. Wiley, Jul. 1996, ISBN: 978-0-471-13319-3. DOI: 10.1002/9783527617869.

[235] Vaurigaud, B., Ture Savadkoohi, A., and Lamarque, C.-H., "Targeted energy transfer with parallel nonlinear energy sinks. Part I: Design theory and numerical results," en, *Nonlinear Dynamics*, vol. 66, no. 4, pp. 763–780, Dec. 2011, ISSN: 0924-090X, 1573-269X. DOI: 10.1007/s11071-011-9949-x.

[236] Vizzaccaro, A., Givois, A., Longobardi, P., Shen, Y., Deü, J.-F., Salles, L., Touzé, C., and Thomas, O., "Non-intrusive reduced order modelling for the dynamics of geometrically nonlinear flat structures using three-dimensional finite elements," en, *Computational Mechanics*, vol. 66, no. 6, pp. 1293–1319, Dec. 2020, ISSN: 0178-7675, 1432-0924. DOI: 10.1007/s00466-020-01902-5.

[237] Vizzaccaro, A., Shen, Y., Salles, L., Blaho, J., and Touzé, C., "Direct computation of nonlinear mapping via normal form for reduced-order models of finite element nonlinear structures," en, *Computer Methods in Applied Mechanics and Engineering*, vol. 384, p. 113 957, Oct. 2021, ISSN: 00457825. DOI: 10.1016/j.cma.2021.113957.

[238] Volvert, M. and Kerschen, G., "Phase resonance nonlinear modes of mechanical systems," en, *Journal of Sound and Vibration*, vol. 511, p. 116 355, Oct. 2021, ISSN: 0022460X. DOI: 10.1016/j.jsv.2021.116355.

[239] Wagg, D. J., "Normal form transformations for structural dynamics: An introduction for linear and nonlinear systems.," en, *Journal of Structural Dynamics*, 2022, ISSN: 2684-6500. DOI: 10.25518/2684-6500.84.

[240] Wang, L., Liu, X., Renevier, N., Stables, M., and Hall, G. M., "Nonlinear aeroelastic modelling for wind turbine blades based on blade element momentum theory and geometrically exact beam theory," *Energy*, vol. 76, pp. 487–501, Nov. 2014, ISSN: 0360-5442. DOI: 10.1016/j.energy.2014.08.046.

[241] Wang, Q., Liu, Y., Liu, H., Fan, H., and Jing, M., "Parallel numerical continuation of periodic responses of local nonlinear systems," en, *Nonlinear Dynamics*, vol. 100, no. 3, pp. 2005–2026, May 2020, ISSN: 0924-090X, 1573-269X. DOI: 10.1007/s11071-020-05619-1.

[242] Wasfy, T. M. and Noor, A. K., "Computational strategies for flexible multibody systems," en, *Applied Mechanics Reviews*, vol. 56, no. 6, pp. 553–613, Nov. 2003, ISSN: 0003-6900, 2379-0407. DOI: 10.1115/1.1590354.

[243] Wiser, J. and Golubitsky, M., "Bifurcations in Forced Response Curves," en, *SIAM Journal on Applied Dynamical Systems*, vol. 14, no. 4, pp. 2013–2029, Jan. 2015, ISSN: 1536-0040. DOI: 10.1137/14096846X.

[244] Wriggers, P., *Nonlinear finite element methods*, en. Berlin: Springer, 2008, ISBN: 978-3-540-71000-4.

[245] Wright, J., Cooper, J., and Desforges, M., "Normal-mode force appropriationtheory and application," en, *Mechanical Systems and Signal Processing*, vol. 13, no. 2, pp. 217–240, Mar. 1999, ISSN: 08883270. DOI: 10.1006/mssp.1998.1214.

[246] Wu, L. and Tiso, P., "Nonlinear model order reduction for flexible multibody dynamics: A modal derivatives approach," en, *Multibody System Dynamics*, vol. 36, no. 4, pp. 405–425, Apr. 2016, ISSN: 1384-5640, 1573-272X. DOI: 10.1007/s11044-015-9476-5.

[247] Yu, W. and Pan, Z., "Dynamical equations of multibody systems on Lie groups," en, *Advances in Mechanical Engineering*, vol. 7, no. 3, p. 168 781 401 557 595, Mar. 2015, ISSN: 1687-8140, 1687-8140. DOI: 10.1177/1687814015575959.

[248] Yuan, J., Sun, Y., Schwingshackl, C., and Salles, L., "Computation of damped nonlinear normal modes for large scale nonlinear systems in a self-adaptive modal subspace," en, *Mechanical Systems and Signal Processing*, vol. 162, p. 108 082, Jan. 2022, ISSN: 08883270. DOI: 10.1016/j.ymssp.2021.108082.

[249] Zhou, X., Huang, K., and Li, Z., "Geometrically nonlinear beam analysis of composite wind turbine blades based on quadrature element method," *International Journal of Non-Linear Mechanics*, vol. 104, pp. 87–99, Sep. 2018, ISSN: 0020-7462. DOI: 10.1016/j.ijnonlinmec.2018.05.007.

[250] Zienkiewicz, O. C., Taylor, R. L., and Fox, D., *The finite element method for solid and structural mechanics*, en, 7th ed. Amsterdam ; Boston: Elsevier/Butterworth-Heinemann, 2014, ISBN: 978-1-85617-634-7.

[251] Zohlandt, C., "Conceptual design of high subsonic prandtl planes," M.S. thesis, Delft University of Technology, Netherlands, 2016.

[252] Zupan, D. and Saje, M., "Finite-element formulation of geometrically exact three-dimensional beam theories based on interpolation of strain measures," en, *Computer Methods in Applied Mechanics and Engineering*, vol. 192, no. 49-50, pp. 5209–5248, Dec. 2003, ISSN: 00457825. DOI: 10.1016/j.cma.2003.07.008.

[253] Zupan, E., Saje, M., and Zupan, D., "The quaternion-based three-dimensional beam theory," *Computer Methods in Applied Mechanics and Engineering*, vol. 198, pp. 3944–3956, 49-52 Nov. 2009, ISSN: 00457825. DOI: 10.1016/j.cma.2009.09.002.

[254] Zupan, E., Saje, M., and Zupan, D., "On a virtual work consistent three-dimensional ReissnerSimo beam formulation using the quaternion algebra," en, *Acta Mechanica*, vol. 224, no. 8, pp. 1709–1729, Aug. 2013, ISSN: 0001-5970, 1619-6937. DOI: 10.1007/s00707-013-0824-3.